Technische Universität München

Max-Planck-Institut für Physik
(Werner-Heisenberg-Institut)

Performance of Cryogenic Light detectors in the CRESST-II Dark Matter Search

Emilija Pantić

Vollständiger Abdruck der von der Fakultät für Physik der Technischen Universität München zur Erlangung des akademischen Grades eines

Doktors der Naturwissenschaften

genehmigten Dissertation.

Vorsitzender:	Univ.-Prof. Dr. Alejandro Ibarra
Prüfer der Dissertation:	1. Priv.-Doz. Dr. Rainer Kotthaus
	2. Univ.-Prof. Dr. Lothar Oberauer

Die Dissertation wurde am 31.07.2008 bei der Technischen Universität München eingereicht und durch die Fakultät für Physik am 26.09.2008 angenommen.

Kurzfassung

Im CRESST-II Experiment sollen hypothetische, schwach wechselwirkende, massive Teilchen (WIMPs), welche ein gut motivierter Kandidat für Dunkle Materie sind, über Streuung an Atomkernen eines $CaWO_4$-Kristalls nachgewiesen werden.

WIMPs können an Kernen elastisch streuen. Die dabei auf einen Kern übertragene Energie (wenige 10 keV) und die erwartete Streuerate (weniger als 10 Ereignisse pro Jahr und kg Detektormasse) sind extrem gering. Daher sind die Hauptanforderungen an ein Experiment zum Nachweis Dunkler Materie eine niedrige Energieschwelle, eine hohe Energieauflösung und eine hohe Effizienz bei der Unterscheidung zwischen Signal und Untergrund.

Die im CRESST-II Experiment eingesetzten Detektormodule bestehen aus einem 300 g schweren, szintillierenden $CaWO_4$-Kristall, welcher als Tieftemperaturkalorimeter betrieben wird und die im Kristall deponierte Rückstoßenergie misst. Dieser Detektor befindet sich in unmittelbarer Nähe zu einem zweiten, deutlich kleineren Kalorimeter, welches als Lichtdetektor eingesetzt wird. Durch gleichzeitige Messung des Phononensignals und des Lichtsignals ist man in der Lage, zwischen Wechselwirkungen von WIMPs und solchen des radioaktiven β- und γ-Untergrunds zu unterscheiden. Während β- und γ-Strahlung vor allem Energie auf Elektronen der Kristallatome überträgt, führen WIMPs zu Kernrückstößen, inbesondere von Wolframkernen. Da der Energieanteil des Szintillationslichts typischerweise nur wenigen Prozent der Energie entspricht, welche im Phononendetektor deponiert wurde, hängt die Diskriminierungseffizienz des Detektormoduls stark von der Energieschwelle und Auflösung des Lichtdetektors ab.

Die Lichtdetektoren bestehen aus einem runden ($\oslash$ = 40 mm) Substrat aus Saphir, welches zur Lichtabsorption einseitig, dünn mit Silizium beschichtet ist (Silicon-On-Saphire, SOS). Die Signale des Lichtdetektors werden mit einem supraleitenden Phasenübergangsthermometer aus Wolfram ausgelesen. Die Geometrie des Thermometers wird dabei durch große Aluminiumflächen zu beiden Seiten des Wolframfilms bestimmt, welche Kollektoren für nichtthermische Phononen darstellen. Ein dünner, schmaler Goldfilm dient ferner zur schwachen thermischen Kopplung an das Wärmebad. Durch entsprechend lange Relaxationszeiten wird das Signal des Szintillazionslichts integriert.

Die vorliegende Arbeit erläutert die laufenden Entwicklungen der Tieftemperaturkalorimeter, welche zum Nachweis des Szintillazionslichts der $CaWO_4$-Kristalle genutzt werden. Zunächst wurde der Einfluss verschiedener Ausführungen des Thermometers auf das Verhalten des Detektors untersucht. Um die Lichtabsorption zu optimieren, wurde als Alternative zur absorbierenden Siliziumschicht eine supraleitende Bleischicht getestet.

Die Ergebnisse der ersten Messungen des CRESST-II Experiments mit SOS-Lichtdetektoren werden in dieser Arbeit präsentiert und das Detektorverhalten wird untersucht. Besondere Aufmerksamkeit wurde dabei auf Studien der Empfindlichkeit und der Energieabhängigkeit der Auflösung im relevanten Bereich gelegt. Signal-zu-Rausch-Verhältnisse, die verschiedenen Quellen des Rauschens und ihr Beitrag zum gesamten Rauschspektrum der Baseline wurden für verschiedene Arbeitspunkte des Detektors analysiert, was letztendlich die Einstellung eines optimierten Arbeitspunktes ermöglichte.

Abstract

The CRESST-II experiment attempts to detect hypothetical Weakly Interacting Massive Particles (WIMPs), a class of well-motivated Dark Matter candidates, using scintillating $CaWO_4$ cryodetectors. A WIMP interacts in the detector via elastic scattering off a target nucleus. The energy transferred to the nucleus (a few tens of keV) and the expected event rate of WIMP-nucleus scattering (less than ten per year and per kg of detector mass) are extremely low. Hence challenges in a Dark Matter search are a low energy threshold and a high energy resolution of the detectors as well as a high efficiency for discrimination between signal and background.
A detector module developed for CRESST-II consists of a scintillating 300 g $CaWO_4$ crystal operated as a cryogenic calorimeter measuring the deposited recoil energy (by detection of a phonon signal). A second, much smaller cryogenic calorimeter is used to detect the scintillation light produced in the target crystal in coincidence with the phonon signal. Measuring simultaneously the phonon and the scintillation light signal, CRESST-II detector modules are able to discriminate nuclear recoils, in particular tungsten recoils expected from WIMP interactions, from radioactive γ and β background processes down to recoil energies of about 10 keV. Since the energy emitted in the form of scintillation light is typically only a few percent of the energy deposited in the target crystal, the discrimination efficiency depends strongly on the sensitivity and the resolution of the detectors which measure the scintillation light yield.
The light detectors have circular (40 mm diameter) silicon-on-sapphire wafers as absorbers for the scintillation light and are read out by tungsten superconducting phase transition thermometers. The geometry of the thermometer is characterized by large Al pads on each side of the tungsten film used for efficient collection of non-thermal phonons and by a thin film thermal coupling to the heat sink for a relaxation time long enough to allow for the integration of the scintillation light pulse.
The present work reports on the ongoing development of these cryogenic light detectors.
The effect of different thermometer layouts on the performance of the detector has been investigated. With the aim to improve the absorption of the light detector substrate, a superconductive lead layer has been tested as an alternative to a silicon light absorber.
Results of first measurements with the silicon-on-sapphire light detectors in the Gran Sasso setup are presented and their performance is studied and discussed in detail. Particular attention is given to the investigation of their sensitivity and of the energy dependence of their resolution in the relevant signal range. Signal-to-noise ratios and baseline noise spectra obtained at different operating points have been analyzed, yielding the optimal operation point and the noise components which limit the resolution of the light detectors.

Contents

1 Introduction **1**
- 1.1 Dark Matter . . . 1
  - 1.1.1 Observational evidence for Dark Matter . . . 2
  - 1.1.2 Cold Dark Matter candidates . . . 6
  - 1.1.3 Direct detection of WIMPs . . . 8
- 1.2 Dark Matter searches with cryogenic detectors . . . 15
  - 1.2.1 Cryogenic detector principle . . . 15
  - 1.2.2 Motivation for cryogenic detectors . . . 18
  - 1.2.3 Sources of background . . . 21
- 1.3 Direct searches with active background rejection . . . 24
  - 1.3.1 Charge-phonon detectors . . . 25
  - 1.3.2 Light-phonon detectors . . . 27
  - 1.3.3 Light-charge detectors . . . 29
  - 1.3.4 Perspectives . . . 32

2 CRESST-II with Light-Phonon Detectors **35**
- 2.1 Experimental setup . . . 35
  - 2.1.1 Cryostat . . . 35
  - 2.1.2 Background considerations . . . 37
- 2.2 Light-phonon technique . . . 40
  - 2.2.1 Quenching factors for different target nuclei . . . 41
- 2.3 Detector module . . . 45
  - 2.3.1 Phonon detector . . . 45
  - 2.3.2 Light detector . . . 48
  - 2.3.3 Holder and light collection . . . 50
- 2.4 Readout and data acquisition . . . 54
  - 2.4.1 Biasing and readout circuit . . . 54
  - 2.4.2 Data acquisition system . . . 56

3 Detector model **61**
- 3.1 Signal evolution . . . 61
  - 3.1.1 Heat capacities . . . 61

3.1.2 Energy down-conversion . . . 63
3.1.3 Energy propagation . . . 64
3.1.4 Electron-phonon coupling . . . 65
3.2 Detector model for pulse formation . . . 67
3.2.1 Calorimeter model . . . 67
3.2.2 Phonon collectors . . . 72
3.3 Noise and energy resolution . . . 76
3.3.1 Basic thermometer model . . . 76
3.3.2 Noise sources . . . 81
3.3.3 Energy resolution . . . 85

4 Detector operation and data analysis 89
4.1 Detector operation . . . 89
4.1.1 Transition curve measurements . . . 89
4.1.2 Stability control . . . 92
4.2 Data analysis . . . 93
4.2.1 Pulse height evaluation . . . 94
4.2.2 Energy calibration . . . 96
4.2.3 Event cuts . . . 99
4.2.4 Acceptance regions for recoiling nuclei . . . 99

5 Light detector study 103
5.1 Thermometer layout . . . 103
5.1.1 Influence of thermometer geometry on detector response . 104
5.1.2 Performance of two thermometers on one substrate . . . 108
5.2 Light detector substrate . . . 112
5.2.1 Lead absorber on the sapphire substrate . . . 113
5.2.2 Elemental, structural and optical studies of lead film . . . 114
5.2.3 Performance of the lead-on-sapphire light detector . . . 117

6 Light detector performance in Gran Sasso 127
6.1 Light detector layout and operation . . . 127
6.1.1 Thermometer layout . . . 127
6.1.2 Transition curves . . . 129
6.1.3 Operating point . . . 130
6.2 Results . . . 133
6.2.1 Light detector energy resolution . . . 133
6.2.2 Energy dependence of the light detector resolution . . . 136
6.2.3 Pulse shape . . . 148
6.2.4 Optimal operation point . . . 154
6.2.5 Noise spectra . . . 159

7 Conclusion and Perspectives 165

Chapter 1

Introduction

According to our present knowledge of cosmology we are living in a flat Universe which consists of two major components: 72 % is an energy of unknown nature, named Dark Energy, and 23 % is a non-baryonic matter of unknown identity, called Dark Matter. The ordinary baryonic matter which is visible to us represents only about 5 % of the total density of the Universe.
Indirect evidence for the existence of Dark Matter, through its gravitational action, is present on all astrophysical scales. Differently, direct evidence for Dark Matter, through its elastic scattering off nuclei, is still missing despite a considerable experimental effort throughout the world. Candidates for Dark Matter particles arise from many extensions of the Standard Model of particle physics, particulary from the concept of Supersymmetry.
This chapter briefly reviews arguments for the existence of Dark Matter and gives an introduction of the main Dark Matter candidates. Then, a more detailed account of Weakly Interacting Massive Particles (WIMPs) and the principles of their direct detection is given.
In the last part of the chapter cryogenic detectors principles and their application in direct Dark Matter searches are introduced and a short overview of the common background sources and the main direct detection experiments is given.

1.1 Dark Matter

Understanding the evolution of the Universe provides an insight into the nature of Dark Matter. The well established theory for the origin and evolution of the Universe is the Standard Cosmological Model[1] that is based upon the hot Big Bang. The most important observations supporting the Big Bang Model are: Hubble's observation of an expanding Universe, the observed relative abundance of light elements and the discovery of the Cosmic Microwave Background

[1]More information can be found in text books on cosmology, such as [Boerner, 2003] or in the Particle Data Group's reviews [Yao et al., 2006].

(CMB)[Penzias & Wilson, 1965].
The theoretical framework of the Cosmological Model is based on general relativity and on the idea that the geometry of space-time is determined by the energy content of the Universe. The metric of a homogeneous, isotropic and expanding Universe is described by the Friedmann-Robertson-Walker (FRW) metric

$$ds^2 = -c^2dt^2 + a^2(t)\left[\frac{dr^2}{(1-kr^2)} + r^2\left(d\theta^2 + \sin^2\theta d\phi^2\right)\right], \tag{1.1}$$

where the scale factor $a(t)$ determines the physical size and the constant k characterizes the spatial curvature of the Universe ($k = -1,\ 0,\ +1$ for a spatially open, flat or closed Universe respectively).
The global dynamics of the Universe is described by the Friedmann equation, which can be written in the form of a cosmic density sum rule [Garcia-Bellido, 2005]

$$\Omega_m + \Omega_k + \Omega_\Lambda = 1\,, \tag{1.2}$$

where Ω_m is the cosmological density parameter that describes the matter content of the Universe, Ω_k expresses its curvature and Ω_Λ accounts for the contribution of vacuum energy, which is called Dark Energy or, assuming its spatial uniformity and time-independence, Cosmological Constant[2]. The matter density contains Dark Matter density, baryon density and neutrino density.
The cosmological density parameter of a given component Ω_i is defined as the ratio of its actual density (ρ_i) to the critical density (ρ_c)

$$\Omega_i \equiv \frac{\rho_i}{\rho_c}\,. \tag{1.3}$$

The critical density is the matter density needed for a flat spatial geometry ($k = 0$) in the absence of a cosmological constant. For the total energy density higher than critical, the spatial cosmic geometry is closed ($k = 1$), while for the total energy density lower than critical the geometry is open ($k = -1$).

1.1.1 Observational evidence for Dark Matter

The presence of Dark Matter had a profound influence on the evolution of the Universe and has observable effects on its present characteristics. This provides numerous indirect evidences of the existence of undetected Dark Matter on all astrophysical scales.

[2]The contribution of the radiation component Ω_r to the total density of the Universe today can be safely neglected [Garcia-Bellido, 2005].

Cosmological scale and large scale structure

The CMB radiation is the background of photons created in the early Universe. When the temperature of the expanding Universe decreased below a few eV photons at thermal equilibrium had no longer sufficient energy to ionize hydrogen such that and protons and electrons recombined into neutral hydrogen (recombination time). Soon after, the further expansion of the Universe diluted the density of the remaining free electrons enough that the photons could no longer interact. Thus the photons decoupled from matter and were free to propagate without interaction (matter-radiation decoupling). These photons, measured today as CMB radiation, give an image of the matter density distribution at the time of decoupling. After decades of experimental investigation the CMB is known to be isotropic with fluctuations at the 10^{-5} level (see figure 1.1) and to follow the energy spectrum of a black body corresponding to a temperature $T = 2.725 \pm 0.001\,\mathrm{K}$ [Mather et al., 1999].

In order to explain how the large scale structures observed today [SDDS, 2008]

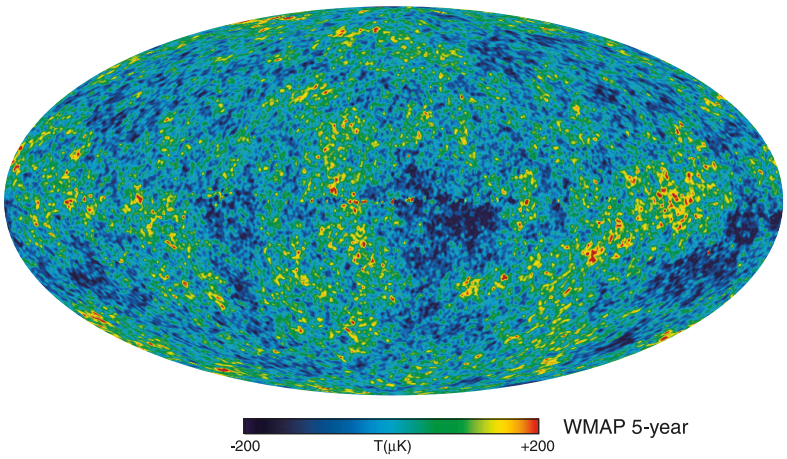

Figure 1.1: CMB temperature fluctuations observed by WMAP. The anisotropies of the CMB are at the level of a few parts in 10^5. Figure from http://map.gsfc.nasa.gov/.

evolved from the isotropic early Universe, a large fraction of the matter density is assumed to be weakly interacting Dark Matter, since weakly interacting particles decouple earlier allowing time for larger density fluctuations to develop. Radiation and the known baryonic matter alone are insufficient to provide the adequate growth of the observed structure.

This weakly interacting Dark Matter component is usually divided into Cold Dark Matter (CDM), corresponding to particles that were non-relativistic at the time of decoupling, and Hot Dark Matter (HDM) representing relativistic particles at decoupling. When the Universe became matter dominated and galaxy formation started, CDM particles were slow enough to be bound in regions of higher mass density on the galactic scale. Therefore CDM models explain the

formation of structure in the Universe starting from small-scale structures evolving to larger scales. On the contrary, HDM relativistic particles would stop only in very large size overdensities and as a consequence the first structures formed would be clouds of HDM particles of supergalactic size followed by the infall of baryonic matter after recombination. HDM models yield therefore to a ¨top-down¨ scenario where supergalaxies are formed first and galaxy clusters later on from their internal gravitation. N-body simulations of huge parts of the Universe showed that a consistent scenario for structure formation results in a substantial CDM component and a subdominant HDM component [Springel et al., 2005].

Today the analysis of CMB anisotropies enables to accurate testing of cosmological models and puts strong constraints on cosmological parameters. The WMAP 5-year CMB data taken in combination with the distance measurements from Type Ia supernovae and the Baryon Acoustic Oscillations (BAO) indicate that the Universe is flat, with $\Omega_{tot} = 1.0052 \pm 0.0064$, and yield the cosmological densities of different components as shown in table 1.1 [Komatsu et al., 2008]. This combined result indicates that a large fraction of the matter density is due

Description	Symbol	WMAP+BAO+SN
Dark Energy density	Ω_Λ	0.721 ± 0.015
Dark Matter density	Ω_c	0.233 ± 0.013
Baryon density	Ω_b	0.0462 ± 0.0015
Neutrino density	$\Omega_\nu h^2$	$< 0.0065(95\% CL)$

Table 1.1: Relevant cosmological densities of the Universe today and the corresponding 68% confidence intervals for the Standard ΛCDM model (Concordance model) with Ω_{tot} assumed to be one [Komatsu et al., 2008]. Some cosmological densities are written in terms of the Hubble parameter h, which is commonly used to express the value of Hubble constant as $H = h \cdot 100\,\mathrm{km\,s^{-1}\,Mpc^{-1}}$ in terms of the present value $h = 0.701 \pm 0.013$.

to non-baryonic Dark Matter. A stringent upper limit on the neutrino density excludes currently known neutrinos from being a major constituent of Dark Matter. Moreover observations of large scale structures allow to derive relevant information on the neutrino contribution to HDM [**?**], [**?**].

Galaxy Clusters scale

Clusters of galaxies are the largest gravitationally bound systems in the Universe and from the observation of the velocity dispersion of galaxies in the Coma cluster in 1933, Zwicky Zwicky [1933] first inferred the existence of Dark Matter. Additional evidence comes from the present day observations. The mass of clusters inferred from their luminosity is much smaller then the mass of the

entire clusters estimated by applying the virial theorem[3], by fitting the measured X-ray temperatures and luminosity of the hot gas to a model assuming hydrostatic equilibrium or by observing gravitational distortion of light from distant background galaxies (gravitational lensing). The additional non-visible mass is interpreted as being due to Dark Matter.

Moreover, the galaxy cluster 1E0657-56, also known as the bullet cluster, provides direct evidence for the existence of Dark Matter [Clowe et al., 2006]. This cluster is composed of two merging clusters (see figure 1.2). The constituent galaxies of both clusters interact only gravitationally and, as observed in the optical spectrum, their path is hardly affected by the collision. The intergalactic gas, which represents most of the clusters mass, interacts electromagnetically causing it to slow down and fall behind the galaxies, as observed with X-ray telescopes. The cluster mass distribution, measured by weak gravitational lensing, does not follow the cluster gas but is distributed similarly to the visible galaxies, as it is expected from weakly interacting Dark Matter.

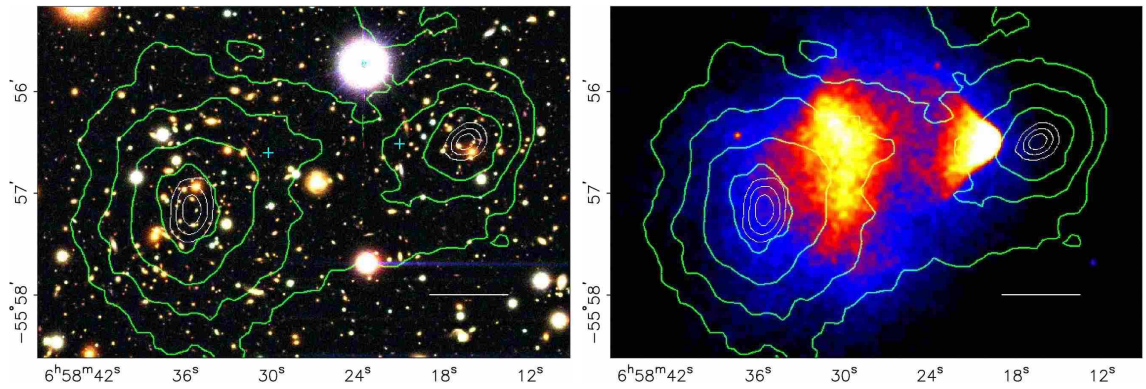

Figure 1.2: The bullet cluster in the optical spectrum, X-ray spectrum and weakly lensed. The main cluster is on the left side of each figure and the subcluster on the right. An overlay of weak lensing mass contours is shown in green in both figures. The white contour lines indicate 1σ, 2σ and 3σ confidence interval on the mass centers of the clusters. The left figure shows an optical image of the bullet cluster. The right figure shows the X-ray image, where the hot gas in the subcluster exhibits a bowed shock front indicative of an encounters with matter not seen otherwise. The hot gas centers, marked on the left figure by the blue crosses, are separated from the mass centers by about 8σ. Figures from [Clowe et al., 2006].

Besides Dark Matter a proposed solution for the observed deviations of bodies in clusters and, as well, galaxies is MOdified Newtonian Dynamics (MOND) [Milgrom, 1983]. Nowadays the cold Dark Matter is the most favored solution

[3]The virial theorem states that in closed system of particles in stable statistical equilibrium under its own gravitation, the time average of potential energy of the system equals twice the time average of the total kinetic energy of the particles.

but its existence does not preclude non-standard gravity.

The Galactic scale

Evidence for Dark Matter on galactic scales comes from observations of the flat rotation curves[4] of spiral galaxies out to large distances from the galaxy centers (see figure 1.3). This evidence is particulary important for laboratory searches for direct Dark Matter interactions.
According to Newtonian dynamics, the rotational velocity of the galaxy at radius r is given by

$$v(r) = \sqrt{\frac{G_N\, M(r)}{r}}, \tag{1.4}$$

where G_N is the Newton's gravitational constant and $M(r)$ is the mass enclosed within the radius r, which is given as $M(r) \equiv 4\pi \int_0^r \rho(r')r'^2 dr'$ with $\rho(r')$ being the mass density profile. Beyond the optical disc, the circular velocity should fall proportionally to $1/\sqrt{r}$. The observed flat rotational curves at large radii indicate that $M(r) \propto r$ and $\rho \propto 1/r^2$, which is explained with a halo extending beyond the optical disc.

1.1.2 Cold Dark Matter candidates

Currently, the two leading generic candidates for CDM are: non-thermal axions and WIMPs (Weakly Interacting Massive Particles).

Axions

Axions are hypothetical light pseudoscalar particles introduced in the attempt to solve the so-called strong-CP problem of quantum chromodynamics, which includes in its Lagrangian a CP violating term, which is experimentally limited to an unnaturally small value [Peccei & Quinn, 1977], [**?**], [**?**].
Axions are divided into thermal axions, produced by thermal processes in the early Universe, which provide a hot Dark Matter candidate analogous to neutrinos, and non-thermal axions which are produced as non-relativistic and thus are a cold Dark Matter candidate. CDM axions have masses between $\sim 1\mu$eV and ~ 1meV, while HDM axions occupy the higher mass range. The present CDM axion energy density, that is a decreasing function of the axion mass, compared to the observed DM energy density implies a lower limit on the axion mass of about 10μeV. Astrophysics establishes the upper bound on the HDM axion mass of about 1eV by arguments based on the observations of the cosmological large-scale structures [**?**], [**?**].

[4]Rotation curves are graphs of rotational velocities of stars and gas as a function of their distance from the galactic center.

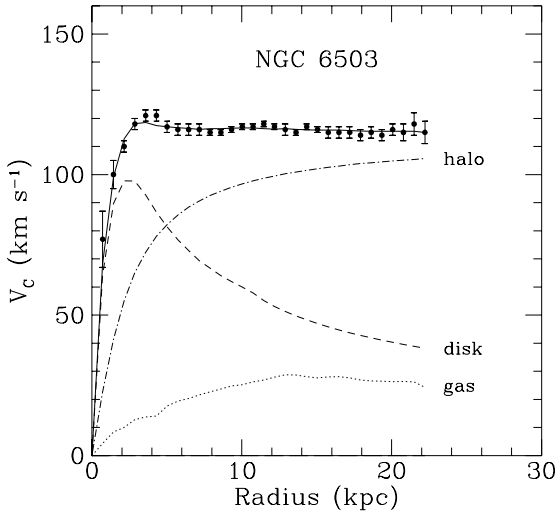

Figure 1.3: Observed rotation curve for the spiral galaxy NGC6503. The points are the measured circular rotation velocities as a function of distance from the center of the galaxy. The dashed and dotted curves are the contribution to the rotational velocity due to the observed disk and gas, respectively, and the dot-dash curve is the contribution from the dark halo. Figure taken from [Begeman et al., 1991].

Axion searches are mostly based on measuring its coupling to a pair of photons due to the Primakoff effect, where a pseudoscalar can convert in an external electromagnetic field to a single real photon. Among them, the most promising are the microwave cavity searches for cold Dark Matter axions and helioscope searches for solar axions, that are produced in the core of the Sun by means of the Primakoff conversion of the plasma photons. Combination of experimental, astrophysical, and cosmological limits indicate that CDM axions are likely very light, $m_A \lesssim 10$ meV [Yao et al., 2006].

Supersymmetric candidates - WIMPs

WIMPs are hypothetical weakly interacting massive stable neutral particles left over from the Big Bang. Typically their masses are presumed to be between a few GeV and a few TeV.
In the early Universe WIMPs are in thermal equilibrium with ordinary particles and their abundance is proportional to the Boltzmann factor $e^{-m/T}$, where m is the WIMP mass and T is the ambient temperature. As the Universe expands and the temperature becomes smaller than the WIMP mass, the gas of WIMPs, still in thermal equilibrium, dilutes faster (due to their higher mass) than the gas of standard model particles. As the Universe expands further, WIMPs become

so rare that they cease to annihilate and they fall out of equilibrium. From then on the number of WIMPs per comoving volume, i.e. WIMP relic density, remains constant. At the time of decoupling WIMP velocities are typically some appreciable fraction of the speed of light. In order to have the relic WIMP density in the range of the observed Dark Matter density of the Universe, the annihilation cross section is expected to be in the order of magnitude of the typical electroweak interaction cross section.

The best motivated WIMP candidate is the lightest supersymmetric particle (LSP) which arises in supersymmetric (SUSY) extensions of the Standard Model. Supersymmetry is a symmetry of space-time that has been introduced in the process of unifying the fundamental forces of nature. SUSY theories hypothesize the existence of a SUSY partner for each particle of the Standard Model establishing symmetry between fermions and bosons. They are characterized by a new quantum number called R-parity, where R = 1 for Standard Model particles and R = - 1 for SUSY particles. The Minimal Supersymmetric extension of the Standard Model (MSSM) is minimal in the sense that it contains the smallest possible field content to give rise and mass to all fields of the Standard Model. One assumption of the MSSM is the conservation of the R-parity. It follows that supersymmetric particles can only decay into an odd number of supersymmetric particles implying the existence of a stable lightest supersymmetric particle (LSP), which can only be destroyed via pair annihilation. The LSP in the MSSM cannot have a non-zero electric charge or color, otherwise it would have condensed with baryonic matter producing heavy isotopes, in conflict with observations.
The most general SUSY Dark Matter candidate is the lightest neutralino χ, a linear combination of the supersymmetric partners of the photon, Z^0 and Higgs bosons.

1.1.3 Direct detection of WIMPs

Astrophysical observations probe the existence of Dark Matter only by its gravitational interaction with ordinary matter. In order to detect Dark Matter particles directly via their scattering with ordinary matter, a huge effort is being carried out by many different direct detection experiments.
The basic idea, on which all direct detection experiments are based, relies on the fact that WIMPs cluster gravitationally with ordinary matter in galactic halos and therefore must be present in our own galaxy. As a consequence there will be a flux of these particles on the Earth, making possible the detection of the interaction of such particles with ordinary matter.
In addition to detecting WIMPs directly, there are methods for the indirect detection by looking for evidence of WIMP annihilations in the galactic halo, in the center of the Sun or other astronomical regions and methods for detecting

WIMP candidates in accelerator experiments [Bertone, 2007], in particular at the Large Hadron Collider (LHC) expected to come into operation soon.
Direct and indirect Dark Matter searches are complementary to the accelerator searches in the sense that they provide a different set of information related to the mass, interactions and distribution of Dark Matter. If the collider experiments identify a long-lived, weakly interacting particle which could be a Dark Matter candidate, they would still need direct or indirect detection of Dark Matter particle in the galactic halo, with the expected mass to prove its cosmological stability and abundance. One method alone is not sufficient and the strategy is to combine all these different methods to conclusively identify the nature of Dark Matter.

The Local Halo

Experiments attempting to detect the scattering of a WIMP with the material of a detector placed on the Earth depend on the knowledge of the local density ρ_0 and the velocity distribution of Dark Matter particles. Rotation curves, that are the most important observational quantities, are much better known for external galaxies than for the Milky Way due to the position of the Earth inside the galaxy. Recent measurements of the rotational velocities for radii longer than the Solar circle ($\approx$8.0 kpc) indicate the existence of a local Dark Matter halo [Battaglia et al., 2005, Xue et al., 2008].
Using an isothermal sphere model [Binney & Tremaine, 1987] for the Dark Matter halo, at the position of the Sun the mean density of particles trapped in the gravitational potential well of the galaxy is expected[5] to be $\rho_0 \approx 5 \times 10^{-25}\,\mathrm{g{\cdot}cm^{-3}} \simeq 0.3\,\mathrm{GeV{\cdot}cm^{-3}}$. In this model the local velocity distribution in the galactic rest frame (the halo is assumed to be non rotating) is Maxwellian

$$f(v)d^3v = (1/v_0^3\pi^{3/2})\exp(-v^2/v_0^2)d^3v\,, \tag{1.5}$$

where v_0 is the local rotational velocity. The velocity distribution of the halo is truncated at the escape velocity from the galaxy, estimated to be $v_{esc} \approx 650\,\mathrm{km{\cdot}s^{-1}}$ [Bottino et al., 1997]. In the Milky Way the rotation curve appears to be already flat at the local position with $v_0 = 220 \pm 20\,\mathrm{km{\cdot}s^{-1}}$ [Kerr & Lynden-Bell, 1986]. The velocity dispersion $\overline{v}$ of the Dark Matter particles in the halo is then given as $\overline{v} = \sqrt{3/2}v_0 = 270 \pm 25\,\mathrm{km{\cdot}s^{-1}}$ [Binney & Tremaine, 1987].
To evaluate the WIMP interaction rate on Earth, equation 1.5 has to be transformed to the rest frame of the Earth, which moves through the galaxy with a velocity $v_E \approx 226\,\mathrm{km{\cdot}s^{-1}}$. Taking into account the motion of the Earth around

[5]The uncertainty comes from the uncertainty in the measured rotation curve, from the uncertainty in the dark halo model considered and from the uncertainty in the contribution of the disk to the rotation curve. A comprehensive numerical study [Gates et al., 1995] results in the (conservative) range $0.1 \lesssim \rho_0 \lesssim 0.7\,\mathrm{GeV{\cdot}cm^{-3}}$.

the Sun with the orbital speed of 30 km·s^{-1} leads to

$$v_E = v_0 \left\{ 1.05 + 0.07 \cos \left[\frac{2\pi(t - t_m)}{1\ year} \right] \right\} , \tag{1.6}$$

where t_m=June 2± 1.3 days [6]. This annual modulation of the velocity of the Earth in the galactic frame produces an event rate variation of about few % over the course of the year.

WIMP elastic scattering

The observed signal due to the elastic WIMP-nucleus scattering in a detector is the recoil energy spectrum in the target[7]. As WIMP velocities are non-relativistic, the recoil energy E_r of the target nucleus due to the WIMP nucleus elastic scattering is expressed as

$$E_r = \frac{q^2}{2m_N} = \frac{m_\chi^2 m_N}{(m_\chi + m_N)^2} v^2 (1 - \cos\theta) , \tag{1.7}$$

where q is the momentum transfer, m_N is the mass of the target nucleus, m_χ is the WIMP mass, v is the WIMP velocity and θ is the scattering angle in the center of mass frame. From equation 1.7 the maximum momentum is transferred for cos θ=-1, therefore the minimum velocity to get a recoil of given energy E_r is

$$v_{min} = \sqrt{\frac{E_r m_N}{2\mu^2}} , \tag{1.8}$$

where μ is the reduced mass ($\mu = (m_\chi m_N)/(m_\chi + m_N)$).

Elastic scattering cross section and Form Factor

WIMP scattering off nuclei is commonly discussed in the context of two classes of couplings. Spin dependent (axial) interactions result from the coupling to the spin content of a nucleon. The cross section for spin dependent scattering is proportional to $J(J+1)$ where J is the spin of the nucleus whereas in the case of spin independent (scalar) interaction the cross section is proportional to the number of nucleons. Here only spin independent interaction will be considered[8].

[6] t_m is the time relative to January first when the Earth's orbital velocity achieves maximal alignment with the Sun's velocity.

[7] In the case of inelastic scattering the WIMP interacts with orbital electrons in the target, either exciting them or ionizing the target. Alternatively the WIMP could interact with a target nucleus leaving it in an excited nuclear state. In the latter case the signature is a recoil followed by a photon emission that has to compete with the background.

[8] A generic WIMP will have both scalar and axial interactions with the nucleus. The total event rate will therefore be the sum of the event rates for the two interactions.

When the momentum transfer to the nucleus q is such that the de Broglie wavelength $\lambda = h/q$ is bigger than the size of the nucleus ($R_N \propto A^{1/3}$), a coherent WIMP interaction with all the nucleons occurs and the cross section is proportional to A^2.
For higher momentum transfer or higher A nuclei, the spin independent interaction begins to loose its coherence. The loss of coherence due to the structure of the nucleus, as the energy of the WIMP and thus the moment transfer increases, is described by a form factor $F(E_r)$, which is defined as the Fourier transform of the nuclear matter distribution.
The effective cross section can, in general, be written as

$$\sigma_{\chi N} = \sigma_0 F^2(E_r), \tag{1.9}$$

where σ_0 is the zero momentum transfer cross section which contains all dependencies on the specific interaction and for spin independent WIMP interaction is related to the mass of the target nucleus by the relation [Lewin & Smith, 1996]

$$\sigma_0 \propto \mu^2 m_N^2 \,. \tag{1.10}$$

Equation 1.10 implies that, for coherently interacting WIMPs, massive nuclei are desirable since the interaction cross section scales as the nucleus mass squared.

Scattering rate

The rate of WIMP scatter events expected per unit detector mass is

$$R = \frac{n_\chi \sigma_{\chi N} \langle v \rangle}{m_N} \,, \tag{1.11}$$

where m_N is the mass of the detector's nucleus, $n_\chi = \rho_0/m_\chi$ is the local number density of WIMPs, $\sigma_{\chi N}$ is the cross section for the elastic scattering of WIMPs off nucleus and $\langle v \rangle$ is the mean WIMP velocity with respect to the detector[9].
Using equations 1.11, 1.9, 1.7 and 1.8 the differential rate per unit detector mass for the elastic WIMP-nucleus scattering can be written as [Jungman et al., 1996]

$$\frac{dR}{dE_r} = \frac{\rho_0 \sigma_0}{2 m_\chi \mu^2} F^2(E_r) \int_{v_{min}}^{v_{esc}} \frac{f_1(v)}{v} dv \,, \tag{1.12}$$

where $f_1(v)$ is the laboratory velocity distribution, found by integrating over angles the three-dimensional velocity distribution in equation 1.5.
The total event rate is computed integrating dR over deposited energies between the detector threshold E_{thr} and $E_{max} = 2\mu^2 v_{esc}^2/m_N$.

[9] When there are several target nuclei species present in the detector, the total rate is given by a sum of all different target nuclei rates.

Neglecting for simplicity the motion of the Earth and the WIMP escape velocity and integrating over angles the Maxwellian velocity distribution of WIMPs in equation 1.5 to find the distribution $f_1(v)dv$, equation 1.12 becomes

$$\frac{dR}{dE_r} = \frac{\rho_0 \sigma_0}{\sqrt{\pi} v_0 m_\chi \mu^2} F^2(E_r) \exp\left(-\frac{E_r m_N}{2\mu^2 v_0^2}\right). \tag{1.13}$$

The integration to obtain the total event rate requires the knowledge of the dependency of the form factor on the deposited energy [Lewin & Smith, 1996]. The event rate is significantly influenced by the mass of the target nucleus and the WIMP mass.
Figure 1.4 illustrates the effect of changing the target material by showing the integrated scattering rate for 30 GeV and 300 GeV WIMPs incident on several prominent target materials.

Experimental requirements

The described characteristics of the WIMP-nucleus elastic scattering determine the main experimental requirements for direct detection experiments based on this interaction.
Target mass is needed as high as possible in order to compensate for the small cross section of WIMP-nucleus elastic scattering. Heavier nuclei benefit from the A^2 elastic cross section scaling, leading to higher interaction rates with WIMPs (see figure 1.4).
Energy threshold should be as low as possible due to the quasi exponential decrease of the signal as a function of the recoil energy (see figure 1.4). The interaction rate decreases more rapidly with deposited energy for heavier nuclei due to the more rapid decrease of the nuclear form factor. Thus a low energy threshold is needed to take advantage of the A^2 cross section scaling for heavier nuclei.
Background has to be highly suppressed and rejected in order to allow a spectrum of rare nuclear recoils to be observed. As can be seen from figure 1.4, for a year of exposure of 1kg target mass, using the standard value of ρ_0 and the WIMP-nucleon cross section of $1{\times}10^{-44}\,cm^2$ only few events are expected.
Background suppression and rejection are particulary important due to the fact that the sensitivity of a WIMP search is determined by the ability to detect the WIMP energy spectrum on top of a background spectrum of unknown shape. For that purpose different experimental strategies have been developed (see subsection 1.3).

Signatures for direct detection

Today three experimental signatures are considered feasible for direct WIMP detection:

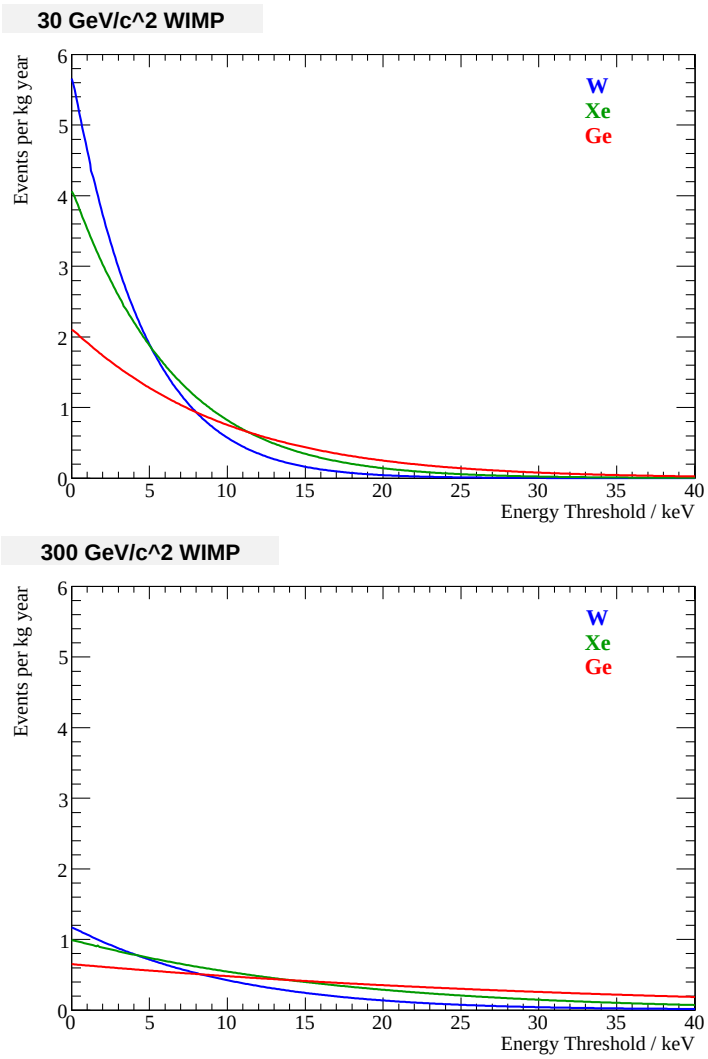

Figure 1.4: The integrated scattering rates on W, Xe and Ge targets per kg and per year of exposure for WIMP mass of 30 GeV and 300 GeV. The x axis shows the energy threshold of the integration. For low energy threshold (less than 5 keV), the integrated scattering rate for W (A=184) is higher than for Xe (A=131) or Ge (A=73) due to the A^2 dependence of the cross section. As the energy threshold increases, the rate drops more rapidly for the heavier nuclei as elastic scattering processes lose coherence due to the large size of the nucleus. The cross section for a WIMP scatter on a nucleon is assumed to be $1{\times}10^{-44}\,cm^2$. The standard value of ρ_0, a time averaged value of the velocity of Earth from equation 1.6 and the Helm form factor were used [Lang, 2008].

Annual modulation of the event rate is due to the motion of the Earth around the Sun (see equation 1.6). Since the expected amplitude of the modulation is in the order of few %, only direct detection experiments based on this signature need large statistics.

Up to the present days only one experiment has exploited the possibility to detect Dark Matter using this signature. The DAMA experiment reports an annual modulation in the signal ascribing it to Dark Matter [Bernabei et al., 2008]. However this is not compatible with the observations of other experiments.
Detector material dependence (see equation 1.13 and figure 1.4) results in different WIMP rates and spectral shapes for different target materials. Experiments that use different target materials in the same setup and have a positive signal exceeding the expected background could identify the WIMP signal by comparing rates and spectra.
Diurnal modulation of the event directional distribution is due to the rotation of the Earth about its axis. In a direction sensitive detector a daily directional periodicity is expected due to rotation in the WIMP flux expected to primarily come from one direction. The experiments aiming at measuring the recoil direction are still in the development phase and the most sensitive experiments nowadays measure only the recoil energy.

WIMP exclusion limits

The difficulty of direct detection experiments in measuring the WIMP interaction cross section arises from the fact that for a given WIMP mass only the shape of the expected energy spectrum is known whereas the normalization has to be determined experimentally in the presence of background contributions of unknown shape.
To set an upper limit for the cross section the value of σ is varied until the resulting theoretical event rate becomes incompatible with the observed event rate and this is done for all possible WIMP masses (m_χ). Any set (σ, m_χ) of the parameter space which produces a theoretical event rate exceeding this limit is then excluded to a given confidence level (usually 90% CL) without any assumption on the background shape. As a first step in the calculation procedure the theoretical WIMP recoil spectrum for a given mass has to be convoluted with the experimental resolution and then compared with the observed spectrum applying criteria that would produce 90% CL exclusion limits. Different criteria for deciding the compatibility of expected and observed spectra have been applied by the various experiments ([Green, 2002], [Tovey et al., 2000], [Angloher et al., 2002], [Yellin, 2002]).
Since various target nuclei are used in direct WIMP searches, in order to facilitate comparison of results, the quoted cross section limit is typically normalized to a single nucleon (see figure 1.8).

1.2 Dark Matter searches with cryogenic detectors

A cryogenic detector measures the energy deposited by an incident particle, independent of the type of interaction, through the consequent temperature rise. The second generation of cryogenic detectors developed for Dark Matter searches measure additionally one more quantity (charge or light) that depends strongly on the interaction type. Simultaneous measurement of the two signals allows to distinguish event by event nuclear from electron recoils. This feature, combined with a low energy threshold and very good energy resolution, is the main advantage of cryogenic detectors for the detection of low energetic nuclear recoils resulting from a WIMP interaction.

1.2.1 Cryogenic detector principle

Basic model

A cryogenic detector (figure 1.5) consists of an absorber with a heat capacity C, a thermometer and a weak thermal link with a thermal conductance G to the heat bath of infinitive heat capacity. In thermal equilibrium the absorber temperature $T(t)$ is equal to the bath temperature T_{bath}. If an incident particle

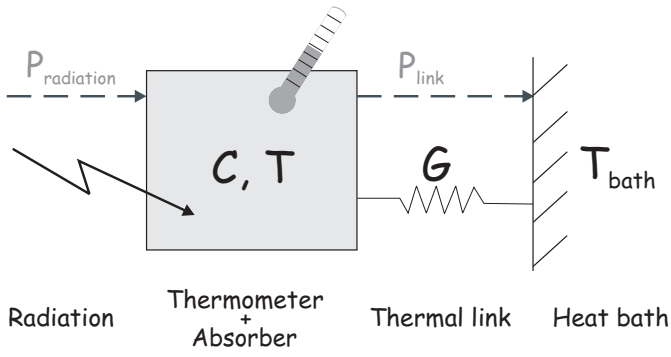

Figure 1.5: Schematic view of a cryogenic detector. An absorber with a heat capacity C at a temperature T is connected to a heat bath at temperature T_{bath} through a weak thermal link . An incident radiation of power $P_{radiation}$ heats up the absorber, which then cools down via a thermal link transmitting power P_{link} to a heat sink. The temperature rise is measured by a thermometer.

hits the absorber and deposits an energy E the temperature of the absorber rises and then cools back to the bath temperature via the thermal link. The temperature rise, proportional to the deposited energy ($\Delta T \sim E/C$), is measured by a thermometer.

The total power flow through the detector can be written as

$$P_{radiation} = C\frac{dT(t)}{dt} + P_{link}\,, \tag{1.14}$$

where the incoming power $P_{radiation}$ causes a temperature rise above the bath temperature and leads to a power flow P_{link} from the absorber to the bath. In the simplified case where the incoming particle deposits the energy instantaneously, then the incoming power is given by $P_{radiation} = E\delta(t)$. The power flowing out of absorber through the weak link into the cold bath can be written as $P_{link}\,(T(t), T_{bath}) = G\cdot(T(t) - T_{bath})$. The thermal equation 1.14 is then given by

$$E\delta(t) = C\frac{dT(t)}{dt} + G\cdot(T(t) - T_{bath})\,. \tag{1.15}$$

It follows that the time development of the detector temperature is described by

$$T(t) = \frac{E}{C}\,e^{-\frac{t}{\frac{C}{G}}} + T_{bath}\,. \tag{1.16}$$

The detector temperature returns exponentially to its equilibrium value T_{bath}, where the time constant of decay is given by the ratio of the heat capacity of the detector and the thermal conductance of the thermal link.
The temperature signal in the calorimeter, as seen in equation 1.16, is inversely proportional to the heat capacity. Due to the temperature rise of the heat capacity (linear for metals and cubic for dielectrics or semiconductors), the sensitivity of a calorimeter of any absorber material is greatly enhanced at low temperatures.

Absorber

The choice of the absorber depends on the nature of the incoming radiation and is at the same time constrained by requirements related to the experimental technique[10]. An ideal absorber should completely absorb the incoming radiation and quickly convert all the deposited energy to heat. The transfer of the heat to the temperature sensor should be without losses which can be realized in many different schemes depending on which excitation of the absorber is used (electrons, phonons, quasiparticles).
In cryogenic direct Dark Matter searches dielectrics and semiconductors are used as target material. The small cross section of the WIMP-nucleus elastic scattering requires the use of high mass target nuclei and of large absorber mass. As previously mentioned for coherently interacting WIMPs absorbers with very massive nuclei are desirable (see equation 1.10).

[10]That means the material has to be suitable as absorber in cryogenic calorimeters (i.e. has to be heat leak free) and it has to have a high melting point to allow the deposition of thin films with high melting temperature such as tungsten.

Thermometer

A thermometer is a sensor which converts a temperature signal into any temperature dependent physical parameter. There is a huge variety of available thermometers for different cryogenic detectors[11]. The most common are thermometers measuring the change of electrical resistance with temperature. In the low temperature region this class includes both standard doped semiconductor thermometers and superconducting phase transition thermometers (SPT), also called superconducting transition edge sensors (TES).
In semiconductor thermometers doped below the so-called metal-insulator transition (MIT) the charge transport takes place by phonon-assisted tunneling between impurity sites. In this regime the resistance shows a strong temperature dependence [Mott & Davies, ????]

$$\rho = \rho_0 \, exp(T_0/T)^n \,, \tag{1.17}$$

where ρ_0, T_0 and n are material parameters depending on the doping. Neutron transmutation doped (NTD) germanium thermometers are frequently used in cryogenic experiments since their uniformity[12] and reproducibility facilitates the construction of large arrays of detectors. An alterative to NTD films are thin film sensors in the MIT, e.g. Nb_xSi_{1-x} alloys exhibit a metal-insulator transition at a composition which depends on the manufacturing process. Over a limited temperature and composition range, the resistivity is well-described by equation 1.17.
An SPT consists of a thin film stabilized in the transition range from the normal to the superconducting phase, where a small temperature rise leads to a large increase in resistance. The temperature-to-resistance conversion factor of SPT can be more than an order of magnitude higher than that of semiconductor thermometers. This allows a smaller detectable energy but has the drawback of a lower saturation limit given by the narrow temperature range of the transition.
SPTs can be produced with the use of elemental superconductors, proximity multilayers and magnetically doped superconductors. There are 18 elements with bulk transition temperature below 2 K. Among them, α-W (α-tungsten[13]) is the most appropriate since it has a rather low transition temperature ($T_c \sim 15$ mK), but still achievable with conventional dilution refrigerators. In many cases thin films do not have the same T_c as the bulk material and show a dependence

[11] A comprehensive review of cryogenic particle detectors can be found in Enss [2005].

[12] NTD-Ge is obtained by irradiation of Ge with thermal neutrons, which induce nuclear reactions on the various target isotopes leading to the formation of n- and p-dopants. Since the isotope distribution is homogenous, the resulting doping is uniform.

[13] Thin tungsten films can exhibit one or two crystal structures: α-W, which is the stable crystal structure, and β-W, which is the metastable configuration. The transition temperature of pure α-W films is about 15 mK, while for pure β-W films transition temperatures range from 1 K to 4 K [Lita et al., 2005].

on the deposition and processing parameters which allows ¨tuning¨ the T_c. In proximity multilayers a composite superconductor is formed by depositing layers of both a superconductor and a normal metal. With layers thinner than the superconducting coherence length[14], the composite film exhibits a reduced transition temperature compared to the superconducting film. This effect, known as proximity effect, has been first applied in Ir/Au bilayers [Nagel et al., 1993]. Proximity multilayer SPTs are widely used due to their transition temperature tunability in a wide temperature range (tens to hundreds of mK) with changing the thickness ratio of the individual layers. Another technique to adjust the transition temperature is magnetic doping of elemental superconductors, first demonstrated with the suppression of T_c in thin tungsten films by implanted iron ions [Young et al., 1999].

Low temperature calorimetric measurements (with a dielectric or semiconducting absorber) are performed in two rather different phonon collection modes, depending on the choice of the thermometer. In the literature they are referred to as equilibrium and non-equilibrium mode. After a particle interaction with the absorber the deposited energy is shared between the electron and the phonon system. Depending on the absorber material, thermal equilibrium between thermometer and absorber needs some time to be established. Equilibrium thermal detectors measure the temperature rise in the absorber after the non-thermal phonons have reached thermal equilibrium within the absorber. In this case the temperature rise is determined by the total heat capacity of absorber and thermometer. In non-equilibrium mode the non-thermal phonons, that are quickly distributed within the absorber volume, are collected by the thermometer before they are thermalized. In the thermometer they cause a temperature rise corresponding to the heat capacity of the thermometer only. This is the dominant part of the signal while an additional component due to the thermalized phonons shows up as a small superposition. Non-equilibrium cryogenic detectors are faster compared to equilibrium devices, but can show a position dependence of the signal. Detectors with SPTs or thin MIT films are sensitive to non-thermal phonons, while detectors measuring the phonon signal in the thermal regime are equipped with NTD thermometers. In Dark Matter searches non-equilibrium detectors are more commonly used since they allow for larger absorber volumes.

1.2.2 Motivation for cryogenic detectors

Cryogenic detectors for Dark Matter detection have been developed by many groups [Chardin, 2004]. The main motivation for their application is the possibility to measure a very small energy deposition that is the only signal expected

[14]The coherence length ξ represents the distance over which the number density of the superconducting electrons changes, and is a measure of the intrinsic non-local nature of the superconducting state

from coherent WIMP interactions.
The excellent sensitivity of cryogenic detectors is mostly due to the decrease of the heat capacity at low temperatures combined with a decrease of the noise. Furthermore the fraction of energy, deposited by the WIMP-nucleus elastic scattering in form of heat ($\approx$ 70% to $\approx$100%) compares favorably to that in form of ionization ($\approx$30%) and scintillation light (few %). In addition, cryogenic detectors measure the heat that is carried by phonons, the excitation energy of which (typically meV) is roughly three of four orders of magnitude lower than that of electron-hole pairs in semiconductor detectors or scintillation photons in scintillators. For this reason the reachable recoil energy thresholds in cryogenic detectors are smaller and ¨quantum noise¨ is negligible. Energy thresholds below 1 keV of recoil energy have already been achieved with massive cryogenic detectors in Dark Matter searches [Angloher et al., 2002].
The theoretical limit of the energy resolution of cryogenic detectors is primarily determined by the thermodynamical fluctuations in the energy content of the detector. The full width at half maximum of the energy distribution is given by

$$\Delta E_{FWHM} \approx 2.35\sqrt{k_B C T^2}\,, \tag{1.18}$$

where k_B is the Boltzmann constant, T is the operating temperature and C is the appropriate heat capacity of the detector[15]. As an example, a calorimeter with typical heat capacity of $1pJ/K$ at an operating temperature of 15mK has $\Delta E_{FWHM} \approx 1eV$.
Another advantage of cryogenic detectors in Dark Matter searches is the large choice of different absorbers that would allow to identify a possible WIMP signal by comparing rates and spectra in different target materials.

Cryogenic detectors with background rejection capabilities

The main limitation of cryogenic detectors is due to radioactive background events which superimpose the spectrum of WIMP induced events. Cryogenic detectors can not discriminate between them since they measure an energy deposition and no further characteristics of the incoming radiation. Thus only statistical rejection can be used to discriminate the background.
A statistical estimate of a possible WIMP contribution to a measured energy spectrum can be made by comparing the overall distribution of all observed events to the expected distributions due to the various backgrounds. However, this is limited by the statistical uncertainties on the number of signal and background events and by systematic uncertainties of the expected distributions. Optimal statistical rejection requires well-identified types of background

[15] As explained in subsection 1.2.1 for detectors measuring, non-thermal phonons the thermometer heat capacity determines the temperature signal, while for detectors measuring thermal phonons the total heat capacity has to be taken into account.

and strongly depends on the theoretical predictions about the signal induced by WIMPs. Experiments using statistical rejection, after some measuring time will be limited by systematic uncertainties and are not sensitive to Dark Matter signals much smaller than the background.

A more effective method of background rejection is from the possibility to measure simultaneously more than one signal for energy deposition, where the different channels refer to the various forms of detector excitations like phonons, free charge due to ionizations, photons or quasi-particles. Simultaneous measurement of two channels allows to discriminate between electron recoil events, expected from γ and β radioactive background, and nuclear recoil events induced by neutrons or WIMPs.
The ionization detection channel can be employed in "active" semiconductor absorbers applying a electrical drift field and read out electrodes. Incident radiation ionizes atoms and the charge collected on the electrodes is a measure of the amount of energy leading to ionization. A photon, for example, entering a detector interacts with bound electrons. The energy transfer leads to electron recoils with a range of the order of the μm and possibly produces secondary electrons. Differently, neutrons interact with a nucleus the recoil range of which is only of the order of nm and a substantial part of the energy is transferred directly into the lattice. Therefore, there is a different ionization efficiency for electron recoils and nuclear recoils that is usually expressed as the quenching factor. The *ionization quenching factor* has been defined as the ratio of the number of the charge carriers produced by a nuclear recoil to that produced by an electron recoil for the same deposited energy.
To exploit the photon detection channel, scintillating crystals are used as absorbers. A particle interaction inside such a crystal excites mainly phonons, but a small amount of the deposited energy is converted into scintillation light in the luminescent centers of the crystal. Nuclear recoils produce less scintillation light than electron recoils. This is due to a different ionization density between electron and nuclear recoils, that translates into a different scintillation efficiency. For an electron, the specific energy loss is small and the spacing between successive ionizations is several molecular distances, so the interaction between ionization sites is negligible. For a recoiling nuclei, the specific energy loss is large and the high density of ions lead to overlapping excitations and a reduced light emission[16]. The *scintillation quenching factor* is defined as the ratio between the light produced by an electron recoil and the light produced by a nuclear recoil for the same deposited energy[17].

[16]The mechanism of the energy transfer to the luminescent centers is quite complex. More information can be found in Birks [1967].

[17]There is no unified definition of the quenching factor as used in Dark Matter search experiments. Ionization quenching factor and scintillation quenching factor are inversely proportional. In the next chapters the definition of the scintillation quenching factor will be used.

Another approach for background rejection is based on a possibly different pulse shape for nuclear recoil and electron recoil events. For instance, in many scintillators the decay time of light pulses due to nuclear recoils is different from that due to electron recoils. Thus some experiments exploit the additional information from the decay times of the signals. Although being powerful, the pulse shape discrimination (PSD) technique at low energies, due to the limited resolution and discrimination power, allows only for a statistical background rejection.

Due to the efficient background rejection of the γ and β interactions on an event-by-event basis down to low energy recoils ($\sim 10\,keV$), most of the direct WIMP detection experiments nowadays use detectors with a combined measurement of two signals. In the last section a short description of the main WIMP direct detection experiments with background rejection techniques will be presented.

1.2.3 Sources of background

Rare event searches are limited by radioactive background signals due to cosmic rays, natural and induced radioactivity. Various techniques are applied to obtain a suppression of background, like passive suppression with appropriate shielding installed, veto system or already mentioned active suppression with two signals combined. An extensive overview of background and shielding concerns for low-background experiments can be found in Formaggio & Martoff [2004].

Cosmic rays

Cosmic radiation at sea level is composed of about 70% muons, nearly 30% electrons and less than 1% protons and neutrons. Muons represent the most penetrating component. Approximately 10^9 cosmic muons pass through the Earth's surface per square meter and per year. Effective shielding against cosmic radiation and radioactivity at the Earth surface is achieved by installing the experimental setup in a deep underground site. In the most prominent underground laboratories the sea level muon flux is reduced by a factor varying from 10^4 to 10^7 (see figure 1.6).
Muons contribute to the detector background in different ways. They cause ionization in traversing the detector or produce energetic electrons, which induce secondary electrons and gamma radiation. These events can be rejected with the active background discrimination technique. Muons also generate neutrons, gamma radiation and radioactive isotopes through spallation processes. Neutrons are of a major concern in direct Dark Matter searches as they produce nuclear recoils similar to those produced in WIMP collisions. The secondary neutrons produced by high energy muons interacting in the shielding material or in the detector itself can be tagged by surrounding the shield with a muon detector (active veto). Veto efficiencies of 99% can be achieved such that this

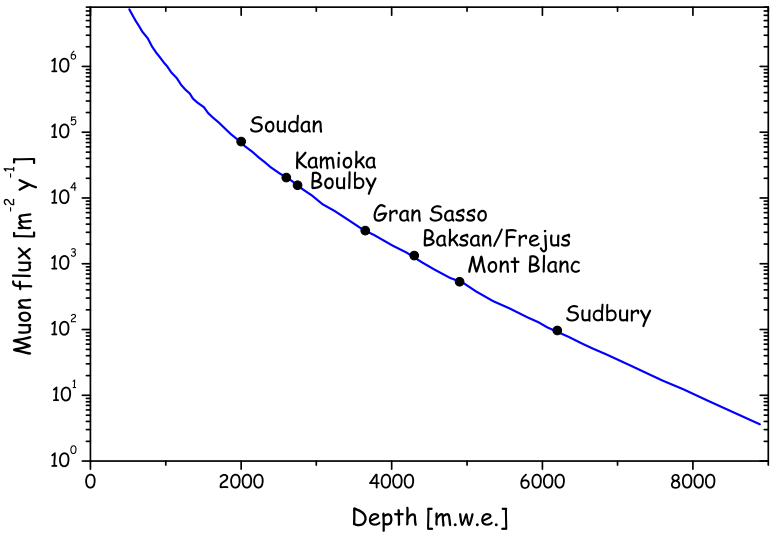

Figure 1.6: Cosmic Muon flux at some of the large depth underground laboratories. The depth is given in meters of water equivalent. Figure adapted from [Koshiba, 1992].

background should not limit an experiment. On the contrary, the secondary neutrons produced by high energy muons interaction in the nearby rock, which are not necessarily in time coincidence with the incident muon, are not easily tagged and rejected. Passive neutron shields made of materials with a high density of hydrogen, such as polyethylene or water are used to moderate and (in combination with absorbers for low energy neutrons) absorb such muon induced neutrons. Neutrons produced by cosmic muons in the detector vicinity may represent a limiting background that only deeper experimental sites can reduce.

Environmental radioactivity

Environmental radioactivity consists of cosmogenic radionuclides, primordial radionuclides and man-made radioisotopes.
Cosmogenic radionuclides are produced by the interaction of cosmic rays with atoms in the atmosphere through spallation processes or neutron capture. The most relevant ones are: ^{3}H, ^{14}C, ^{7}Be and ^{22}Na. Primordial radionuclides are long-lived isotopes originating mainly from the star remnants that formed the Solar system. The most important ones are ^{40}K, ^{87}Rb and those belonging to the natural radioactive chains of ^{238}U and ^{232}Th. ^{40}K and ^{87}Rb are β beta emitters with a half-life of $\geq 10^9$ y. Uranium and thorium are usually present in nature with an abundance ranging from a few to several tens of ppm (parts per million), depending on the type of rocks. Among the man-made radionuclides,

mainly originating from nuclear fallout, the most important ones are the β emitters ^{90}Sr and ^{137}Cs with half-lifes of 28.5 y and 30.2 y, respectively.
The environmental γ activity is mainly originating from the the radioactive isotopes present in the rock around the underground laboratory and in the walls of the laboratory. The γ sources are primarily the ^{238}U and ^{232}Th decay chains, with photon energies up to 2.6 MeV and ^{40}K, which emits a 1.46 MeV photon. The shielding is achieved by surrounding the detector with thick walls of absorbing material. High Z materials are very effective for stopping γ rays with energies in the MeV range. Typically lead shielding is used to reduce γ background. In addition the inner part of lead shielding is made of lead with low content of ^{210}Pb ($T_{1/2}$=22y) to reduce the contribution from bremsstrahlung (from ^{210}Bi β decay). The innermost shielding is made from radiopure copper to shield the radioactivity from the lead.
In addition to muon induced neutrons, other sources for neutrons are spontaneous fission and (α,n) reactions due to natural radioactivity of the rock or residual radioactivity of the shielding material. The secondary neutrons produced in the rock are moderated with low Z material shields. Residual radioactivity of the shielding and especially of all the parts inside the shielding, like detectors themselves and the surfaces facing them, is kept low with the use of intrinsically high purity materials and controlled manufacture that excludes intentional or accidental contamination. In order to prevent cosmic activation, all parts which belong to the innermost part of the shielding are stored underground in a clean room environment when not in use. Additionally, the storage place is kept at slight overpressure and flushed with a radiopure gas to avoid any further contamination (like radon).

Radon

A special treatment is needed for gaseous ^{222}Rn originating from ^{226}Ra α-decay (^{238}U decay chain) which is widely present in rock and soil. Due to its long life time ($T_{1/2}$=3.8d), ^{222}Rn is normally found in the air and groundwater, being degassed from materials containing radium. Therefore radon can be deposited on the surfaces of detectors or in their vicinity, while its daughters can be implanted even slightly below the surfaces by the parent decay. This background contamination is considered the most problematic one for Dark Matter experiments. A common contaminant originating from radon is α-archived ^{210}Po

$$^{210}Po \rightarrow {}^{206}Pb + \alpha\,. \tag{1.19}$$

The ^{206}Po nucleus is left with an energy of 104 keV, while the α carries 5.3 MeV. When the ^{210}Po on the surface of detector or in its vicinity decays, it can occur that the α moves away from detector while the ^{206}Pb nucleus enters the detectors and deposits an energy of $\sim$ 100 keV (see picture 1.7). Without additional energy

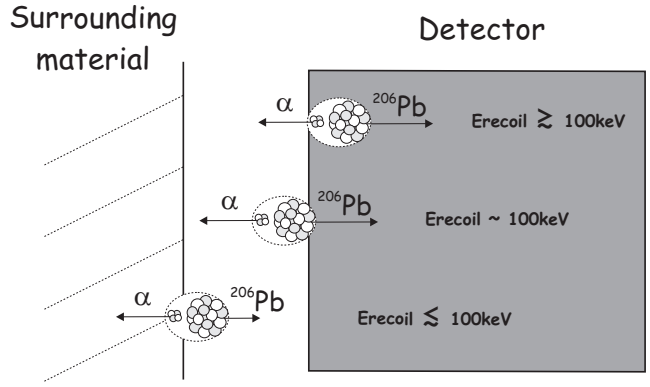

Figure 1.7: ^{210}Po contamination of the detector and surrounding material. In a process where polonium decays with the α moving away from the detector and the ^{206}Pb nucleus going into the detector, only the recoil energy of the heavy lead nucleus ($\sim 100\,\mathrm{keV}$) is detected. Depending on the exact position of ^{210}Po nucleus this energy deposition can be $\gtrsim$100 keV if the mother nucleus is inside the detector and there is a partial contribution of the α or <100 keV if the decay occurs on the surface of the surrounding material and the lead nucleus looses energy on the way to the detector.

deposition from α this heavy nucleus recoil can not be easily distinguished from a WIMP interaction.
There are two particular situations which can occur depending on the position of the decaying ^{210}Po nucleus. When the ^{210}Po is implanted on the surface of the detector, the escaping α looses some energy inside the detector leading to an energy deposition $\gtrsim$100 keV. Conversely, if the ^{210}Po is implanted on the surface of the surrounding material the nucleus looses some energy on the way to the detector and deposits energies <100 keV. These events can extend down to the interesting energy range and mimic a WIMP event.
The activity due to ^{222}Rn and its daughters can be efficiently reduced and controlled the entire shielding hermetically and by maintaining a slight overpressure inside by flushing it with a radon-free gas.

1.3 Direct searches with active background rejection

The ongoing direct Dark Matter searches can be divided into experiments with and without active background discrimination[18].
Non-discriminating experiments are the first ones that have searched for Dark

[18]For a detailed description of direct detection experiments past, present and future see [Enss, 2005][Gaitskell, 2004][Chardin, 2004].

Matter evidence. In the past their sensitivity was limited by the residual background. Currently these experiments are developing large scale detectors with self shielding and position reconstruction that will allow a better suppression of the background. Additionally the radiopurity of the setup is constantly being improved.
Discriminating experiments, which make use of the combined detection of two channels (charge-phonon, light-phonon or light-charge), show much better background discrimination on an event-by-event basis. Today they have achieved the best sensitivity for direct Dark Matter search. A considerable number of discriminating experiments makes use of cryogenic detectors. Apart of them, discriminating experiments with liquid noble gases have shown promising sensitivity. Worth mentioning is also an attempt to utilize a bubble chamber filled with a superheated heavy liquid (CF_3I) for Dark Matter detection [Behnke et al., 2008].

1.3.1 Charge-phonon detectors

Charge-phonon detectors provide active background discrimination by simultaneous detection of phonon and charge signals. These detectors, operated at sub-kelvin temperatures, are equipped with temperature sensors measuring the heat deposited due to a particle interaction. Additionally, ionization charges ($\sim 1/3$ of the deposited energy) are drifted by applying an electrical field to thin film electrodes on the detector surface giving rise to a charge signal. The charge-phonon technique restricts possible targets to semiconductor materials, of which high intrinsic purity germanium and silicon are the most commonly used ones.
As previously mentioned, the discrimination between electron recoils and nuclear recoils is based on their different ionization efficiency (also called ionization yield). The ionization efficiency in Ge (Si) for nuclear recoils is typically about a factor of 4 (3) lower than for electron recoils and depends on the deposited energy[19] [Simon et al., 2003]. The charge-phonon detectors presently show discrimination efficiencies against γ and β background of $> 99.9\%$ down to recoil energy of $\sim$10keV [Chardin, 2004].
Incomplete charge collection for the electron recoil events occurring very close to the surface of detectors is a problem for the detectors since these events can mimic the reduced ionization efficiency of nuclear recoil events. One of the ways to decrease the dead surface layer is by improving electrode/absorber surface

[19]The ionization yield for electron recoil events shows only a slight energy dependence in the relevant energy range (0 - 100 keV).

with intermediate amorphous layers[20]. A similar degradation of the charge signal occurs when charge carriers are trapped on impurities within the bulk of the detector. To prevent this, the impurity sites need to be kept neutral. This is achieved by exposing the detectors to photons of energies slightly higher than the gap of the semiconductor producing electron-hole pairs. Without external electrical field, electron-hole pairs diffuse through the volume of the detector and fall into impurity traps, neutralizing them. In addition, to avoid the accumulation of space charge during detector exposure to radiation, a regeneration process is periodically required.
CDMS[21] [CDMS Collaboration, 2008] and EDELWEISS[22] [Sanglard et al., 2005] are two experiments using the charge-phonon technique.

The **CDMS-II** experiment, located at the Soudan mine, operates Ge and Si cryogenic detectors designated as Z (depth)-sensitive Ionization and Phonon (ZIP) detector. ZIP detectors are cylindrically shaped (m_{Ge}=250 g, m_{Si}=100 g) and equipped with two concentric ionization electrodes and four SPTs. The SPT thermometer consists of superconducting W films with Fe ions implanted for optimizing the transition temperature ($\sim$ 70 mK) and with additional superconducting Al fins for improved phonon collection. These thermometers detect the non-thermal phonons from particle interactions on time scales of $\sim$ 1-100 μs. The combined timing and relative amplitude information of the four SPTs are used to reconstruct the event location in x-y plane (parallel to phonon sensors) with a resolution of $\sim$1 mm. This information is used to improve the energy resolution by correcting for the position dependence of the phonon signal.
The phonon signal of an event occurring near the surface is faster than of an event away from the surface[23]. Thus the rise time of the phonon signal as well as the time difference between the charge and phonon signals are used to discriminate between bulk nuclear and surface electron recoil events at the expense of an energy-dependent fiducial volume cut. According to Akerib et al. [2005] surface events are rejected by this "timing parameter" cut with $> 96\%$ efficiency, while over one half of all nuclear recoil events are kept. In addition, statistical substraction of neutron background can be achieved by comparing the interaction rates and recoil spectra shapes in two different target material (Ge and Si).

[20]Incomplete charge collection occurs when charge carriers diffuse, against the electric field, to the opposite electrode. This effect can be reduced significantly by the addition of a thin layer of amorphous Si to the surface of the detector. This provides a barrier against charge diffusion away from the collecting electrode [Shutt et al., 2000].

[21]Cryogenic Dark Matter Search.

[22]Experience pour DEtecter Les Wimps En Site Souterrain.

[23]For events occurring sufficiently near the surface of the crystal, the interaction between the initial quasi-diffuse phonon population and the metal films results in a very rapid down-conversion of the phonons into the ballistic regime [Akerib et al., 2005].

The most recent published results from the CDMS-II experiment are from combined data collected between 2003 and 2007 with a total exposure of 174.7 kg d for the Ge target [CDMS Collaboration, 2008]. Two nuclear recoil events are present in the 10-100 keV range in agreement with the expected background from residual surface events. Based on these data, a 90% C.L. upper limit on the spin-independent WIMP-nucleon cross section in Ge of 4.6×10^{-8} pb for a WIMP mass of 60 GeV/c^2 has been obtained [Ahmed et al., 2008]. The experiment shows the best sensitivity in the WIMP mass region above 40 GeV/c^2 (see figure 1.8).
The CDMS collaboration is presently preparing a SuperCDMS-25 experiment at SNO-Lab with new 2.5 cm thick ZIP detectors [Akerib et al., 2008], lower background rates, improved background rejection and advanced timing analysis.
The **EDELWEISS-II** experiment, in the Modane underground laboratory, operates cylindrical germanium (m=320 g and 400 g) charge-phonon detectors at $\sim$20 mK. A thermal phonon signal is detected with glued NTD temperature sensors on the time scale of $\sim$ 100 ms. A ionization signal (time scale $\sim$ 50 μs) is simultaneously collected on Al-sputtered electrodes polarized with a few Volts. For thermal phonon signals there is neither a position dependence, no timing information that could be used to discriminate surface events. To reject surface events the collaboration has developed a new fast phonon readout scheme based on NbSi films which show large differences in pulse shape depending on the interaction depth [Marnieros et al., 2008]. Another approach for discrimination of surface events are Ge/NTD detectors with special electrodes consisting of parallel stripes (instead of classical disk-shaped electrodes) that allow to infer the depth of an event from a comparison of the ionization signals on the different strips [Broniatowski et al., 2008].
The last published results [Sanglard et al., 2005], shown in figure 1.8, represent a total exposure of 62 kg d (collected between 2000-2003). The data show 40 nuclear recoils between 15 and 200 keV, that are compatible with a leakage of surface electron scatters and a residual neutron background. EDELWEISS-II, after a significant upgrade including a new cryostat, new detector, electronics and DAQ, is running 28 detectors (Ge/NTD and Ge/NbSi) with the aim to reach a sensitivity to WIMP-nucleon cross section of $\sim 10^{-7}$ pb for a WIMP mass of 100 GeV/c^2 in 2008 [Chantelauze, 2007].

1.3.2 Light-phonon detectors

Light-phonon cryogenic detectors measure simultaneously scintillation light and phonons providing another technique to discriminate nuclear recoils from electron recoils. The absorber (phonon detector) consists of a scintillating dielectric crystal equipped with a temperature sensor (SPT or NTD) for detecting the heat signal. In a scintillating crystal a particle interaction mostly excites phonons, but

a few percent of the deposited energy is emitted as scintillation light. Photons escaping from the crystal are absorbed in a separate detector (light detector). Since conventional photodetectors are not suitable at very low temperatures[24], a light detector consists of a calorimeter, which is read out by a thermometer with a very small heat capacity to allow the detection of the small number of emitted photons. Besides commonly used germanium and silicon thin wafer absorbers, thin crystal wafers covered with an absorber film (like silicon-on-sapphire substrates) matched to the scintillation light spectrum have been developed. The heat produced by the absorption of scintillation light in the light detector is detected with SPT or NTD thermometers. In order to enhance the light collection efficiency both detectors are enclosed in a highly reflective housing.
The active background discrimination technique, which is based on the different scintillation efficiencies of nuclear and electron recoils, works with many scintillating crystals (BGO, BaF_2, $PbWO_4$, $CaWO_4$, $ZnW0_4$, doped Al_2O_3) light output of which has been studied at low temperature [Meunier et al., 1999][Bavykina et al., 2008][Luca, 2007]. Thus, a variety of different targets materials for WIMP interactions is available. An important difference to charge-phonon detectors is, that there are several target nuclei present in the absorber and the response of each recoiling nucleus must be taken into account. For $CaWO_4$ systematic specific studies of the scintillation quenching factor for different recoiling nuclei as a function of temperature and energy are already under way, whereas for other scintillators, such investigations still have to be carried out. Another relevant characteristic of the light-phonon detectors is no significant surface effect for electron recoil interactions, meaning that surface and bulk events have the same quenching factor [Angloher et al., 2005].
The light-phonon technique shows comparable background discrimination efficiency for electron recoil events as the charge-phonon technique. The main challenge is the detection of the small energy fraction that is converted to light. Presently two experiments are probing WIMP cross sections with the light-phonon technique: CRESST[25] [Angloher et al., 2005] employing $CaWO_4$ crystals and ROSEBUD[26] [Calleja et al., 2008] with multi-absorber targets.

The **CRESST-II experiment**, located in the Gran Sasso National Laboratory (LNGS), employs $CaWO_4$ cylindrical crystals (300 g) and associated silicon or silicon-on-sapphire light detectors of a size matching the crystal size (ϕ= 40 mm). Both detectors are read out by tungsten SPT thermometers stabilized at ∼15 mK. The light detector thermometers have additional Al pads for improved phonon collection. The non-thermal phonons are detected within ∼

[24]Due to various effects, the detection efficiency of standard photodetectors is notably reduced at low temperatures.
[25]Cryogenic Rare Event Search with Superconducting Thermometers.
[26]Rare Objects SEarch with Bolometers UndergrounD.

10 ms and ∼100 μs after energy deposition, for phonon and light detector respectively. A scintillating polymeric foil with very high reflectivity[27] surrounding the detectors contributes to an enhanced light collection efficiency. In addition, its scintillation light due to α particle interactions provides an information to veto recoils of heavy nuclei induced by α decays of radon daughters (see discussion in section 1.2.3 and figure 1.7).
For a detailed understanding of the detector response to nuclear recoils of all constituents, measurements with neutron scattering and ion impingement have been performed for $CaWO_4$ crystals at room temperature. The results show a strong dependence of the light output on the mass of the recoiling nucleus. A quenching factor of ∼ 10 for oxygen recoils and ∼ 40 for tungsten recoils has been measured [Ninković et al., 2006]. Besides, it has been shown that the light output for both electron and nuclear recoils are weakly energy dependent in the relevant energy range from ∼10 keV to 40 keV resulting in the practically energy independent quenching factor [Moszyński et al., 2005, Bavykina et al., 2007]. Quenching factor measurements for $CaWO_4$ crystals are currently carried out at mK temperatures with a monoenergetic pulsed neutron source.
The latest published results [Angloher et al., 2005] present the data collected with one detector module in 2004 and total exposure of 6.2 kg d for tungsten nuclei. The data show no nuclear recoil events in the region 12-40 keV yielding the 90% C.L. limit shown in figure 1.8. After a major upgrade which includes the installation of a neutron shielding, a muon veto system, the mounting system and readout for 33 detector modules (66 detectors), the experiment in the commission phase has been running three detector modules during 2007. The analysis of the data collected with two detector modules during this commission phase is in progress. Another run with more detector modules installed has been started in April 2008.
In the next phase, the CRESST and EDELWEISS collaborations are planning to cooperate in building a 100 kg to 1 t cryogenic detector EURECA[28], based on the existing technology, but with better background rejection capabilities [Kraus et al., 2007].

1.3.3 Light-charge detectors

The light-charge detector technique is presently exploited by two-phase liquid noble gas detectors consisting of a scintillating liquid target and a gas phase above the liquid. Intrinsic scintillators (neon, argon and xenon) are used as liquid absorbers. The use of liquid absorbers as a target material allows for higher operating temperatures (22 K for LNe, 87 K for LAr and 165 K for LXe) and an

[27] The reflectivity of the foil is greater than 98% at the wave length of the $CaWO_4$ emission peak (∼ 420 nm).
[28] European Underground Rare Event search with Calorimeter Array.

easier upgrade to larger masses than possible with cryogenic detectors. A particle interaction in the liquid noble gas produces excitation and ionization. The relaxation of the excited molecules produces prompt scintillation light that is detected using arrays of photomultipliers (PMTs). Produced electron-ion pairs can recombine and form excitation states which also contributes to primary scintillation light output. In a high electric field ($\sim$1 kV/cm), part of the ionization electrons are prevented from recombination and are drifted towards the gas phase. Once the electrons reach the liquid surface they are extracted into the gas phase by the presence of a stronger electric field ($\sim$10 kV/cm). Extracted electrons excite and ionize gas atoms along their path resulting in electroluminescence and in a multiplication the charges. These secondary photons (proportional light) are also detected in photodetectors. The delay time between primary and secondary light, due to the drift time of the electrons, provides information about the depth (z position) of the event. The x-y position can be inferred from the relative sizes of the signal in the PMTs. The 3D reconstruction allows geometric fiducial volume cuts for further suppression of the background.
High performance diffusive reflector housing is used to improve the collection of the liquid xenon UV scintillation light[29]. For the far UV light of liquid neon and argon[30], in addition to the reflector, a wavelength shifter is required to provide a match to the photomultiplier sensitivity spectrum.
In the charge-light technique, both the scintillation and the ionization signals for nuclear recoils are quenched with respect to electron recoils, but by different amounts. Therefore the ratio of the two signals can be used for discrimination between electron and nuclear recoils (nuclear recoils show smaller secondary to primary signal ratios). Both scintillation and ionization quenching factors depend on the drift field and on the energy of the recoil. An electron recoil discrimination efficiency of 98.5% with a 50% nuclear recoil acceptance down to 20 keV recoil energy has been achieved with a small two-phase LXe detector [Aprile et al., 2006].
Additional background discrimination is possible by exploiting the shape of the primary signal where nuclear recoils show faster rise time than electron recoils.
An important challenge for detectors using liquid noble gases is the identification and suppression of the radioactive contamination of the detector material itself, such as ^{85}Kr in LXe (25 ppm Kr in natural Xe) or ^{39}Ar in LAr, and of the surface radioactivity from the container.
Two experiments, XENON10 [31][Angle et al., 2008] and ZEPLIN-II[32] [Alner et al., 2007], are using light-charge technique with liquid xenon as Dark Matter target.

[29] $\lambda = 174$ nm (Xe)
[30] $\lambda = 85$ nm (Ne) and $\lambda = 128$ nm (Ar)
[31] ¨ 10¨ designates the LXe absorber mass of the order of 10Kg.
[32] ZonEd Proportional scintillation in LIquid Noble gases.

The WARP[33] [WARP Collaboration, 2008] collaboration is employing a similar technique with liquid argon. Future dual phase liquid noble gas experiments are XENON100, ZEPLIN-III and XMASSII with LXe and ArDM with LAr [Baudis, 2007].

The **XENON10** experiment, located in LNGS, has operated a 15 kg dual phase xenon time projection chamber with 3D position sensitivity. Two arrays of UV-sensitive PMTs detect both the prompt and the proportional light signals. The large refractive index of liquid xenon makes it difficult to efficiently detect the scintillation in a dual phase detector, with light detectors only in the gas phase, due to total reflection in the liquid-gas interface. Therefore a bottom array of PMTs is completely immersed in LXe and mainly detects the prompt light signal, while a top array of PMTs is located in the gas and measures the proportional light. Self-shielding of LXe, due to its high density ($3\,g/cm^3$) and atomic number (Z=54), reduces the background rate in the central region of the target by more than one order of magnitude in the relevant energy range. Combined with 3D position information ($\sigma_{xy} \sim 1\,mm$, $\sigma_z < 1\,mm$) it provides high background rejection.
The scintillation quenching factor, measured with a tagged neutron beam, for nuclear recoils with energy between 10.4 and 56.5 keV, was found to be 0.130 ± 0.024 and 0.227 ± 0.016 for the lowest and highest energy recoils, respectively. In the same experiment the dependence of the scintillation efficiency on the applied electric field has been measured for 56.5keV nuclear recoils showing a slight decrease with an increase of the drift field [Aprile et al., 2005]. The ionization yield of nuclear recoils, here defined as the number of observed electrons per unit recoil energy, was measured to be between 5.5 and $2.5\,e^-/keV$ at a drift field of 2kV/cm in the energy range 10 - 100 keV, showing an increase with a decrease of recoil energy and exhibiting only a weak field dependence [Aprile et al., 2006].
The collaboration recently published a result for a fiducial mass of 5.4 kg in a 136 kg d exposure showing 10 nuclear recoil events in the energy range 4.5 keV to 26.9 keV. One group of events is clustered at higher energies and in the lower part of the fiducial volume and the remainder is statistically consistent with the leakage from electron recoils. Thus, none of the observed events are likely WIMP interactions. At present, this experiment gives the most sensitive 90% C.L. upper limit for the spin-independent WIMP-nucleon cross-section in the lower WIMP mass region (up to 40 GeV/c^2) with a value of 8.8×10^{-8} pb for a WIMP mass of 100 GeV/c^2 [Angle et al., 2008]. The very high sensitivity of XENON10, in particular to low WIMP masses, is mainly due to the very low energy threshold (~ 5 keV) (see figure 1.4). LXe dual phase detectors allow for comparatively easy and cost-effective upgrades to higher masses.
The XENON100 detector with a technique similar to XENON10 and with the

[33] WIMP Argon Programme.

target mass of 170 kg is already installed and is presently in the commissioning phase at LNGS.

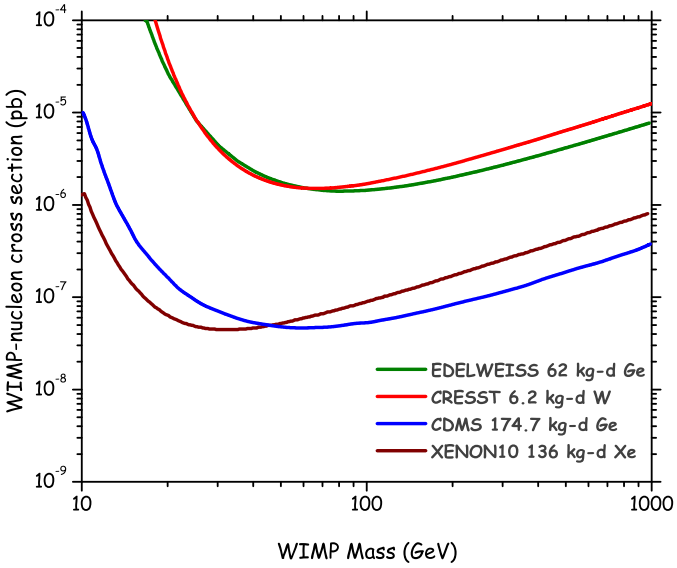

Figure 1.8: The current limits on the spin-independent WIMP-nuclei (normalized per nucleon) elastic scattering cross section, as a function of the WIMP mass, for several leading direct detection experiments. The regions above the curves are excluded with 90% C.L.

1.3.4 Perspectives

Direct Dark Matter searches have started to probe interesting regions in the parameter space predicted by some supersymmetric models, but up to now there is no solid evidence of Dark Matter detection. At the current stage, these experiments are mainly focused on how to clearly identify a WIMP signal from the background. The combined results of different target materials with different signatures appear as the most promising way to verify the existence of WIMPs. Furthermore, measurement of the WIMP recoil spectrum with a good statistics would allow to determine the particle mass. However as previously mentioned, only the combination of different detection techniques: direct, indirect and accelerator searches will provide all the different information needed to fully identify the Dark Matter.
The cryogenic detectors have made significant progress in the last few years.

Presently their results are among the world's best exclusion limits for the spin-independent WIMP interaction (see figure 1.8). The future cryogenic Dark Matter experiments will face technical challenges and the high cost of a large mass modular detector. The major tasks are further improvements of the discrimination power, radiopurity and size of the individual detectors, as well as long-term stability requirement due to the significant increase of the number of readout and DAQ channels.
The two phase liquid noble gas detectors have proven to be very successful detectors for direct Dark Matter searches, at present providing one of the best sensitivities to coherent WIMP interactions. The future liquid noble gas experiments have the advantage of being better suited to extensions to a very massive detector with a self shielding feature, but they need to prove that the detector concept still works once the detector is scalled.

Despite all the efforts made in neutron background reduction it seems likely that the residual neutron flux will be a limiting factor in future setups. Therefore, the direct Dark Matter experiments have to address the issue of neutron background identification. The different strategies include the study of the multiple scatter neutron interactions in an array of densely packed detectors or in a compact 3D position sensitive detector; comparison of the neutron flux spectra on different target materials or active discrimination of neutron events in a multitarget scintillating absorber due to their different scintillation efficiency compared to WIMP induced events.

It is reasonable to expect that in the near future direct Dark Matter searches, by scaling the target mass up to 100 kg - 1 t, by optimizing the detectors performance and by minimizing residual background contributions, will reach the sensitivity to probe WIMP cross sections down to a level of 10^{-9} pb.

Chapter 2

CRESST-II with Light-Phonon Detectors

The aim of the CRESST experiment is to detect WIMP Dark Matter particles via their elastic scattering on target nuclei in the absorber of a cryogenic detector. In this chapter, a characterization of the setup in Gran Sasso and an overview of the detector module, developed for the second phase of the CRESST experiment, are presented.

2.1 Experimental setup

The CRESST facility is located in Hall A of the Laboratori Nazionali del Gran Sasso in Italy. The laboratory is situated in the highway tunnel of the Gran Sasso mountain at an average depth of about 3500 m.w.e (see figure 1.6) with a minimum rock overburden of ∼3150 m.w.e. (1400 m). This reduces the cosmic muon flux by 6 orders of magnitude to about $1\mu/\mathrm{hm}^2$ [Cribier et al., 1997].

2.1.1 Cryostat

The central part of the setup for the CRESST experiment at the LNGS is the cryostat. The design combines the requirements of low temperatures for the operation of detectors with those of low background for the rare events search. A standard dilution refrigerator is made of various materials which do not necessarily satisfy radiopurity requirements. To avoid any line of sight between detectors and non-radiopure materials, a low background cold box (experimental volume) housing the detectors is well separated from a commercial dilution refrigerator, as shown in figure 2.1. The low temperature of the dilution refrigerator is transferred to the cold box by a 1.5 m long cold finger.
A 20 cm thick lead shield (Plombum lead with a ^{210}Pb activity of $3.6\,\mathrm{Bq{\cdot}kg^{-1}}$) inside a copper can, which transmits the cooling power, is placed between the

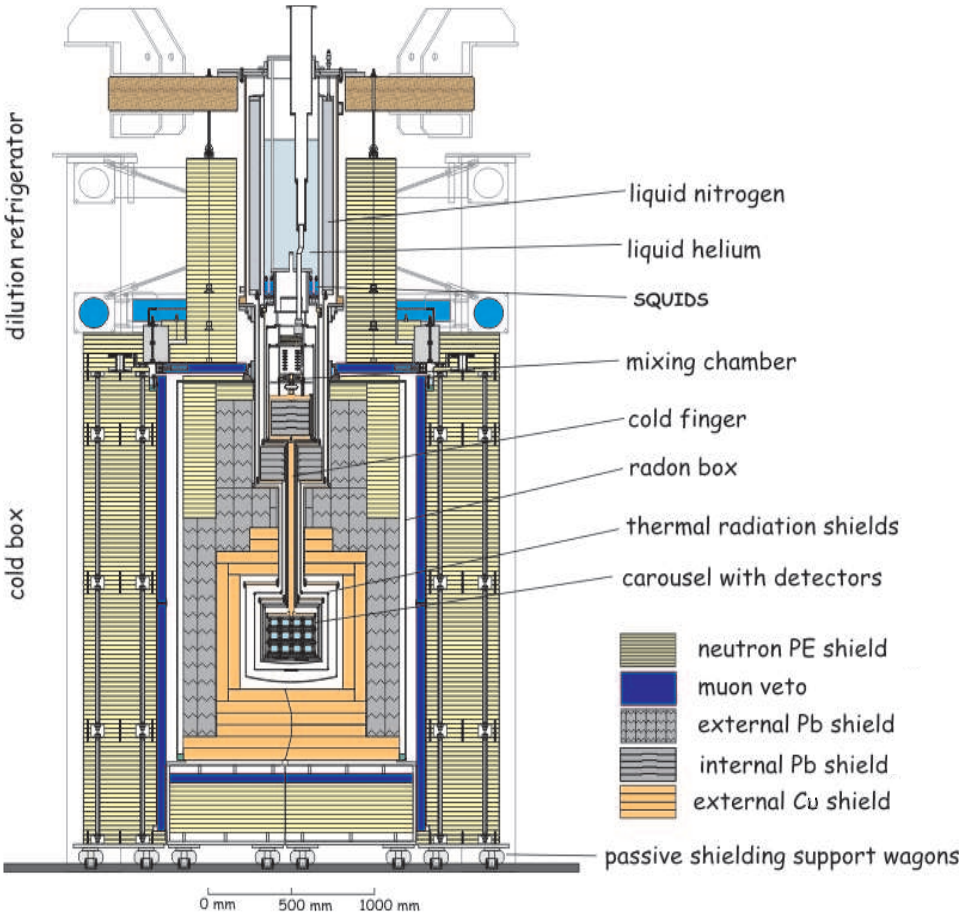

Figure 2.1: Schematic view of the CRESST cryostat and passive shielding.

mixing chamber and the cold finger. This shield, combined with another one at liquid nitrogen temperature surrounding the cold finger, blocks radiation coming from the dilution refrigerator into the experimental volume. The cold box consists of five concentric radiation shields which surround the experimental volume and the cold finger: a room temperature vacuum can; a first shield thermally anchored to the liquid nitrogen dewar of the refrigerator; an inner vacuum can thermally sunk at the temperature of the liquid helium dewar; two inner radiation shields at 600 mK and 80 mK. The cold finger and the shields are made of radiopure copper, which has been electro-polished after machining to remove residual surface contaminations and to reduce the risk of recontamination. High purity lead is used for vacuum seals [Bühler et al., 1996].
The cryostat rests on air dampers in order to isolate it from external vibrations. To reduce the effect of vibrations created inside the cryostat by boiling cryogenic liquids, the detectors in the cold box are mounted onto a spring loaded support structure (carousel) hanging from the cold finger.

The whole setup is housed in a three level building (figure 2.2). A two level

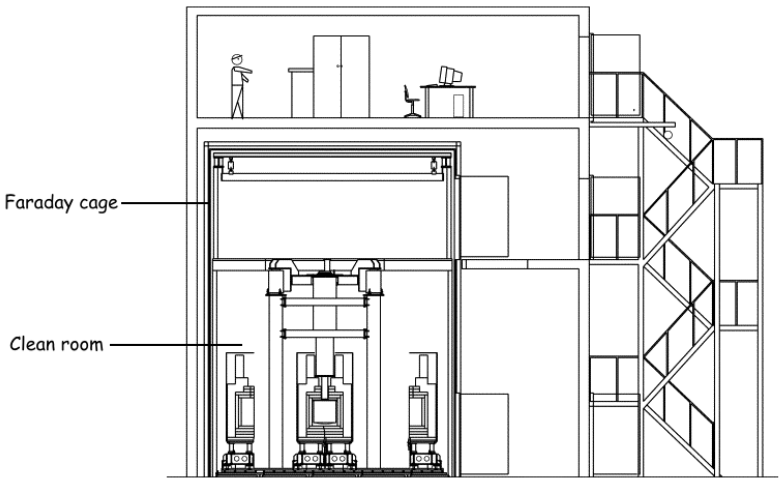

Figure 2.2: Cross section of CRESST building. The external passive shielding is shown in both its open and closed positions.

Faraday cage which surrounds the experiment has been chosen large enough so that all work on the low-background components can be performed inside this cage. Furthermore, to provide clean conditions while mounting detectors, the ground floor of the Faraday cage, housing the cold box and the lower part of the cryostat, is equipped as a class 100 clean room. The upper level of the Faraday cage is outside the clean room and allows access to the top of the cryostat and to the electronics so that maintenance can be done without entering the clean environment. The gas handling and the pumping system of the cryostat, as well as the data acquisition system, are located outside the Faraday cage. On the third floor there is a small chemistry laboratory and a laminar flow area where detectors are prepared before being mounted in the cryostat.

2.1.2 Background considerations

The activity from a sample of rock from the laboratory Hall A has been measured and results are reported in table 2.1. The integral gamma flux calculated for all natural chains is $\sim 1\,\gamma{\cdot}\mathrm{cm}^{-2}{\cdot}\mathrm{s}^{-1}$ [Arpesella, 1992]. As mentioned before, the gamma ray activity from the rock and concrete of the underground lab can be suppressed by means of high Z and high density materials like lead and radiopure materials like copper. The CRESST passive shielding is composed of 20 cm of Boliden lead with a ^{210}Pb activity of $35\,\mathrm{Bq}{\cdot}\mathrm{kg}^{-1}$ [Bühler et al., 1996] followed by 14 cm of radiopure copper surrounding the cold box that hosts the experimental volume. This arrangement suppresses gamma rays from the ^{238}U/^{232}Th/^{210}Pb

Sample	γ activity [Bq·kg^{-1}]			
	^{232}Th	^{238}U	^{40}K	^{214}Bi
Hall A Rock	8.8±0.3	84.7±8.4	224±6	41.9±0.6

Table 2.1: Activity of a sample of rock from Hall A of Gran Sasso underground laboratory [Arpesella, 1992].

activity in the lead shielding. The shielding is made of two snugly fitting halves that can be opened without handling the individual pieces.
The entire shielding is housed in an air tight aluminium container (radon-box) which is constantly flushed with nitrogen gas and maintained at a slight overpressure in order to prevent radon from penetrating the shielding. The activity due to ^{222}Rn and its daughters in the underground laboratory, with the present ventilation system, is between 10 and 20 Bq·m^{-3} [Bucci, 2007].
The neutron flux in the Hall A (see table 2.2) mostly consists of thermal neutrons (E $<$ 1 MeV), which mainly scatter elastically off the target in this way simulating a WIMP signal. The major part of the neutron flux in the experimental site

Hall *A*	
Energy interval (MeV)	Neutron flux (10^{-6}·cm^{-2}·s^{-1})
$< 50 \times 10^{-9}$	1.07 ± 0.05
$50 \times 10^{-9} \div 10^{-3}$	1.99 ± 0.05
$10^{-3} \div 2.5$	0.53 ± 0.008
$2.5 \div 5$	0.18 ± 0.04
$5 \div 10$	0.04 ± 0.01
$10 \div 15$	$(0.7 \pm 0.2)10^{-3}$
$15 \div 20$	$(0.1 \pm 0.3)10^{-6}$

Table 2.2: Integrated neutron fluxes measured in the given energy intervals (BF_3 counters [Bellotti et al., 1985]).

is expected to be due to neutrons from radioactivity in the rock and concrete. A simulation of the expected signal due to the different background contributions and of the influence of different shielding materials has been performed. Conservative estimates of the recoil spectra induced by neutrons from different sources in $CaWO_4$ crystals are presented in figure 2.3 [Wulandari et al., 2004b,a].
To moderate the neutrons before entering the experimental volume of the cryostat, a neutron shield of 50 cm thick polyethylene (PE) is installed outside the radon-box. According to the simulation, the neutron shield is expected to reduce the neutron background by more than three orders of magnitude (see figure 2.3).

With the moderator installed, the remaining neutron flux is dominated by muon induced neutrons in the experimental setup. Such a background is suppressed by a muon veto system, which consists of plastic scintillators panels read out by photomultiplier tubes[1]. The panels are installed between the neutron shield and the

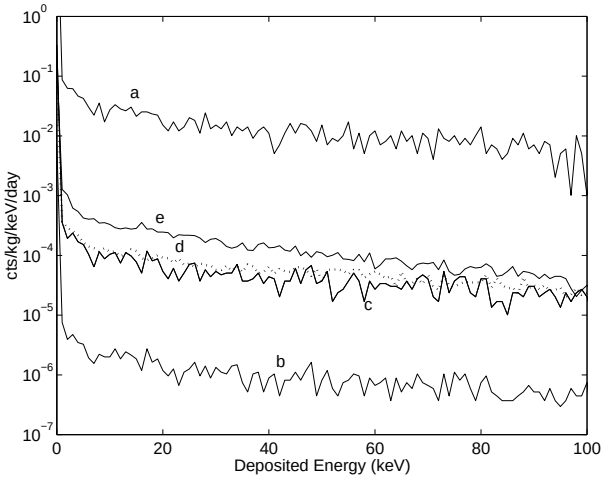

Figure 2.3: Simulated recoil spectra in a $CaWO_4$ detector in different scenarios: (a) low energy neutrons from the rock/concrete without neutron moderator; (b) low energy neutrons from the rock/concrete moderated by 50 cm of polyethylene; (c) low energy neutrons from fission reactions due to 0.1 ppb ^{238}U contamination in the lead shield; (d) high energy neutrons induced by muons in the rock; (e) high energy neutron induced by muons in the experimental setup. Figure from [Wulandari et al., 2004a].

radon-box (see figure 2.1) and grouped into functional units representing the six faces of the cube formed by the radon box. An incoming muon passing through the veto system deposits some energy in the scintillator. An event recorded by the CRESST detectors is rejected a posteriori if it comes in coincidence with a signal in the muon veto system.
The residual neutron background, with neutron shield and muon veto installed, comes from high energy neutrons produced by muons that are not tagged by the veto system and by the neutrons from ^{238}U fission in the lead shielding. The further reduction of the neutron background can be achieved with an array of detectors by rejecting the neutrons scattered in more than one detector.

[1]The muon detectors are made of Bicron BC-408 plastic scintillator panels whose scintillation light is detected by a green-extended photomultiplier with a sidewall sensitivity for a wide-angle light detection (end-window PMT) [Nikolodi, D., 2006].

2.2 Light-phonon technique

As discussed in the previous chapter (see 1.2.2), the residual radioactive background represents the main limitation of the sensitivity of direct Dark Matter experiments. The possibility to actively discriminate the radioactive background from γ and β interactions in the absorber allows significant improvement in sensitivity. Therefore for its second phase the CRESST experiment is employing active background rejection based on the simultaneous detection of a phonon and a light signal.
A first simultaneous measurement of scintillation light and phonons, using $CaWO_4$ crystals as absorber, has been performed with a proof-of-principle detector module [Meunier et al., 1999]. A schematic view of the module for coincident phonon and light measurement is shown in figure 2.4.

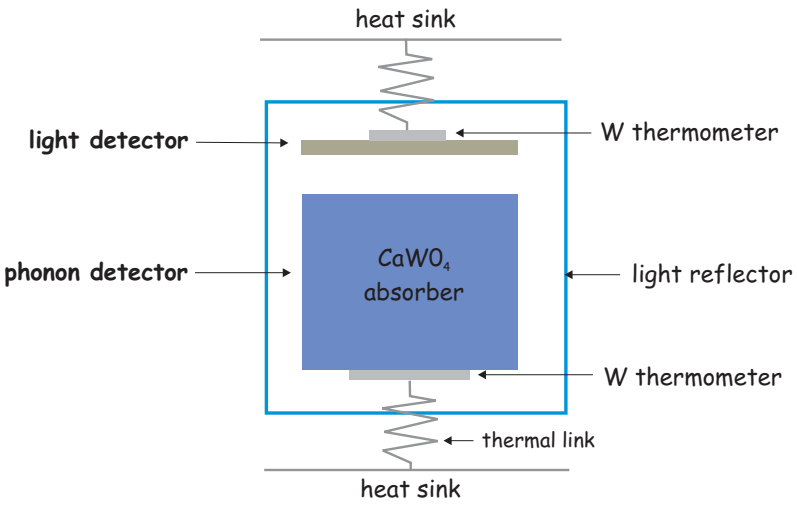

Figure 2.4: Schematic view of a detector module for coincident light and phonon measurements. The heat signal from a particle interaction in the $CaWO_4$ crystal is detected by a phonon detector, while the emitted scintillation light is measured by a separate light detector. Both detectors are read out by tungsten SPTs. High reflectivity material is encapsulating the detectors.

The proof-of-principle detector module was made from a 6 g ($20\times10\times5\,mm^3$) $CaWO_4$ absorber and a much smaller sapphire substrate ($20\times10\times0.5$)mm^3 with one side silicon coated[2] as a light detector absorber.

The results from this experiment are shown in figure 2.5. The signal in the phonon detector provides a measurement of the total energy deposited in the $CaWO_4$ absorber independent of the type of interaction. In contrast, the light output of the scintillating crystal associated with electron recoils is significantly

[2]Standard sapphire substrates are transparent for scintillation light in the visible spectrum, therefore an absorption layer is required.

higher than the one associated with nuclear recoils. This property is quantita-

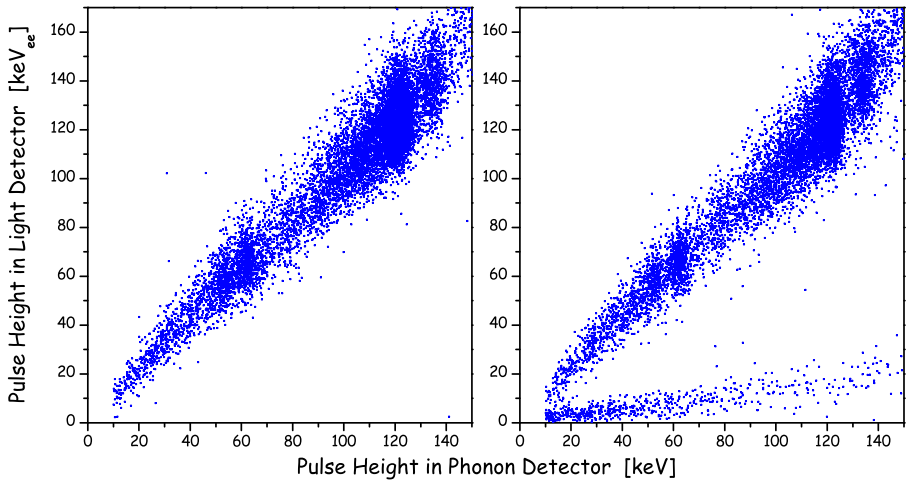

Figure 2.5: Scatter plot of the pulse height in the light detector versus the pulse height in the phonon detector for the proof-of-principle module [Meunier et al., 1999]. The crystal was irradiated with a ^{57}Co γ source together with a ^{90}Sr β source (left panel) and an Am - Be neutron source added (right panel). The pulse height in the light detector is converted to energy using the calibration of the phonon detector, i.e. the energy scale of the light detector corresponds to the energy deposition in the phonon detector.

tively expressed by the scintillation quenching factor. In the proof-of-principle experiment the quenching factor for nuclear recoils induced by incident neutrons has been found to be nearly constant within the WIMP relevant energy interval with values of QF_n=10.0±0.8 in the energy range 10 to 20 keV and QF_n=8.9±0.4 from 20 to 40 keV [3] [Angloher et al., 2005].
A discrimination for γ and β radioactive background of 98% in the energy range 10 to 20 keV and better than 99.9% above 20 keV has been achieved.

2.2.1 Quenching factors for different target nuclei

Interactions of different nature (due to α, β, γ, n irradiation) in the scintillator have different quenching of the light output (electron recoil events produce more light than nuclear recoil events). Moreover, as observed experimentally, for a given scintillator different recoiling nuclei lead to different quenching factors (for

[3] The quenching factor for nuclear recoils induced by incoming neutrons shows a small variation with energy in the energy range 10-150 keV.

example QF ~ 5 for Na recoils and QF ~ 10 for I recoils in NaI target [Simon et al., 2003]). Since there are different nuclei present in the $CaWO_4$ scintillator, it is expected to have different quenching factors depending on which nucleus was struck by the incident particle. For an effective background suppression, the quenching factors for the different recoiling nuclei present in the absorber have to be measured.
Given the spectrum of neutrons at Gran Sasso laboratory [Wulandari et al., 2004a], neutron induced recoils, which appear in the relevant energy range, are mainly oxygen and calcium. In contrast, WIMPs mainly scatter off tungsten nuclei due to the A^2 scaling of the WIMP-nucleus scalar cross section (see equation 1.10). Therefore the different quenching of oxygen and tungsten recoils in the scintillator can be used for a discrimination of the neutron background.
To further exploit the background rejection capabilities of the detector, a detailed study of the quenching factor for different recoiling nuclei has been carried out using different techniques, which are described below.

Low temperature QF measurements with light-phonon technique

A γ calibrated cryogenic detector module for coincident light and phonon detection, exposed to a neutron source of known energy spectrum, can be directly used for quenching factor measurements. If the resolution of the light channel is high enough the quenching factors for different recoiling nuclei could be inferred from well separated bands in the light vs phonon channel scatter plot. In the case of $CaWO_4$ absorbers the nuclear recoil band has contributions from three different nuclei (O, Ca and W) with oxygen being dominant. The contributions from these different nuclei depend on the incident neutron energy spectrum and on the recoil energy interval. At present, the resolution of the light detectors does not allow to separate the light output for different recoiling nuclei[4]. This, combined with the multiple scattering of neutrons, raises a lot of uncertainties in the measurements of different nuclear recoil quenching factors.

Neutron scattering experiments

One possibility to overcome the uncertainties resulting from the neutron multiple scattering and the overlapping of the response bands for different recoiling nuclei is to perform a tagged neutron scattering experiments [Jagemann et al., 2005]. A scintillating crystal is first calibrated with a known γ source. The scintillation light from the crystal is detected by a commercial photomultiplier at room temperature or by a cryogenic light detector at low temperatures. The scintillator

[4]The result quoted for QF_n (section 2.2.1) are thus weighted (by the appropriate n cross sections) averages of O, Ca and W quenching factor for incident neutrons.

is then exposed to neutrons. The scattered neutrons are detected by an array of neutron detectors covering a certain range of scattering angles with respect to the neutron beamline. The energy of the scattered neutrons is measured via their time-of-flight between the scintillator and the neutron detectors, which are read out in coincidence. Assuming elastic scattering, the energy of the recoiling nucleus is then determined by the energy and the scattering angle[5] of neutron. In the case of a continuous energy spectrum of the incident neutrons (like from a Am-Be source) also the spectrum of scattered neutrons (and thus the spectrum of nuclear recoils) at a fixed angle is continuous. If several target elements are involved, it is difficult to extract information about individual quenching factors of target elements from a continuous spectrum. Therefore such measurements require the use of monochromatic incident neutrons.
The quenching factors for oxygen and calcium recoils in the $CaWO_4$ crystal measured with a monoenergetic pulsed neutron beam[6] at room temperature are presented in figure 2.6 [Jagemann et al., 2006]. The large quenching factor for tungsten could not be obtained because the signal was hidden in the background. Since the $CaWO_4$ light output is temperature dependent [Mikhailik et al., 2007], the neutron scattering experiment has recently been extended to low temperatures [Coppi, 2007].

Ion impingement experiments

Instead of detecting the light produced by the recoiling nuclei of the target material, as done in neutron scattering experiments, in this technique the light emitted when single ions impinge onto the scintillating crystal is measured [Ninković et al., 2006].
Ions are produced with a Laser Desorption/Ionization source (LDI). The selection of ions with a certain mass is done with a time-of-flight mass spectrometer. The light produced in the $CaWO_4$ target by the impinging ions is detected with a commercial photomultiplier. The electron recoil reference measurement for the determination of the quenching factors is made with 5.9 keV X-rays from an ^{55}Fe source.
The main advantage of such a technique compared to a neutron scattering experiment is the possibility to choose the type and energy of the recoiling nuclei. The impinging ions are absorbed near the surface of the scintillator. Therefore, a possible surface effect where the light output for energy depositions close to the crystal surface differs from that for bulk depositions could limit the technique. In the case of $CaWO_4$ crystals no significant change of the light output near the

[5] The energy of the recoiling nucleus is given by $E_r \approx \frac{4AE_n}{(A+1)^2}\cos^2\theta$, where A is the nucleus mass number, E_n is the energy of the incident neutron and θ is the recoil angle in the laboratory coordinate system, assuming the target nucleus is at rest.

[6] 11 MeV neutrons are produced via the reaction $p(^{11}B, n)^{11}C$.

surface has been observed. This is supported by the absence of splitting of the gamma-electron recoil band in cryogenic measurements (see figure 2.5). If there were surface effects, electrons interacting mainly near the surface and photons mostly in the interior would have a different light output.
The quenching factor for different recoiling nuclei measured at room temperature shows a strong dependence on the mass of the nucleus, as shown in figure 2.6. With this technique it was possible for the first time to determine the large

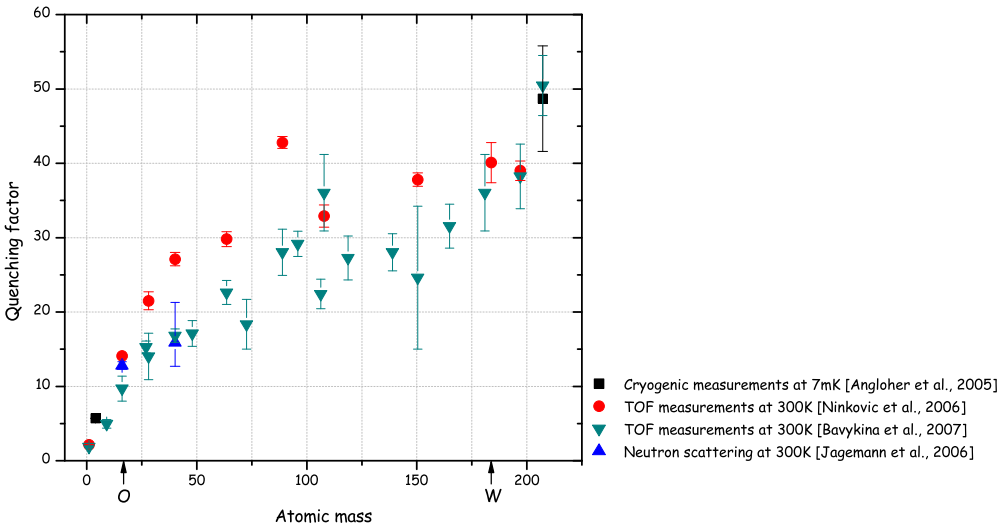

Figure 2.6: Dependence of the quenching factor of $CaWO_4$ on the atomic mass of selected elements. The neutron scattering result measured at room temperature are shown in blue. Two different sets of ion impingement measurements (E_{ion}=18 keV), at room temperature, are shown in red and green. For the measurements in Ninković et al. [2006] (red points) only statistical errors are plotted, while for the measurements in Bavykina et al. [2007] (green points) also the systematic errors are given. The black squares refer to a measurement with a cryogenic detector at a temperature of 7mK. Tungsten recoils, expected from a WIMP interaction in the $CaWO_4$ absorber, show a QF of about 40, while oxygen recoils, mainly originating from neutron interaction, show a QF of about 10.

quenching factor of tungsten recoils in $CaWO_4$. The light from tungsten recoils is quenched four times more than that from oxygen recoils. Hence, the discrimination between these two nuclear recoils is achievable.

QF for the Pb nucleus and α particle at low temperatures

During one of the Dark Matter runs in Gran Sasso, the detector's response on the irradiation from the ^{210}Po surface contamination was used to determine the quenching factor for the nuclear recoils of lead (see 1.2.3). A group of events

in the energy region from 80 to 110 keV have been identified as ^{210}Po α-decays with only ^{206}Pb recoils detected [Angloher et al., 2005]. The obtained value of 48.7 ± 7.1 for the quenching factor of ^{206}Pb at millikelvin temperature is shown in the figure 2.6. The quenching factor of He with value of (5.70±0.01), derived from the 2.3MeV alpha-peak in [Angloher et al., 2005, fig.7], is as well shown.

The data presented in figure 2.6, although obtained with quite different techniques at different temperatures and for different energies, show reasonable agreement. This demonstrates the absence of a significant temperature and energy dependence of the quenching factors in $CaWO_4$ and provides good support to the ion impingement method as a technique to measure quenching factors.

2.3 Detector module

Starting from the 6 g proof-of-principle detector, during the prototyping phase of CRESST II, 300 g prototype modules have been developed with the goal to operate 33 modules for a total absorber mass of $\sim$10 kg. An open detector module for CRESST phase II is shown in figure 2.12.

2.3.1 Phonon detector

The phonon detectors developed for the second phase of the CRESST experiment consist of a 300g cylindrical $CaWO_4$ crystals with 40 mm diameter and 40 mm height equipped with a tungsten superconducting phase transition thermometer for the readout. The main requirements for the large phonon detectors are a high light output of scintillation light combined with a good energy resolution and an excellent level of radiopurity.

$CaWO_4$ crystal

$CaWO_4$ has been chosen as scintillator because of its relatively high light yield at low temperatures [Meunier et al., 1999] and the large atomic mass of tungsten (A_W=183.86) which enhances the WIMP-nucleus coherent interaction. In addition it shows no noticeable degradation of the light yield for events near the crystal surface.
The scintillation properties of $CaWO_4$ crystals have been thoroughly investigated in Ninković [2005]. The main scintillation emission spectrum of $CaWO_4$ has a Gaussian-like shape ranging from $\sim$ 300 nm to $\sim$ 650 nm with a peak at about 425 nm at room temperature. A temperature decrease leads to an increase of the emission intensity and narrowing of the width of the emission spectrum, while the peak position shows very little variation over the temperature range from

300 K to 8 K [Ninković, 2005]. On the other hand, light output and energy resolution have been observed to strongly depend on the crystal sample[7].
$CaWO_4$ crystals have a rather slow light signal response, that is even slower (in the range of hundreds of microseconds) at low temperatures [Blasse & Bokkers, 1983, Ninković, 2005] as it can be seen from the figure 2.7.
Although the radiopurity level of crystals varied depending on the manufacturer, a low level of radioactive contamination from the natural decay chains (∼1 mBq/kg) for 300 g $CaWO_4$ crystals could be obtained.

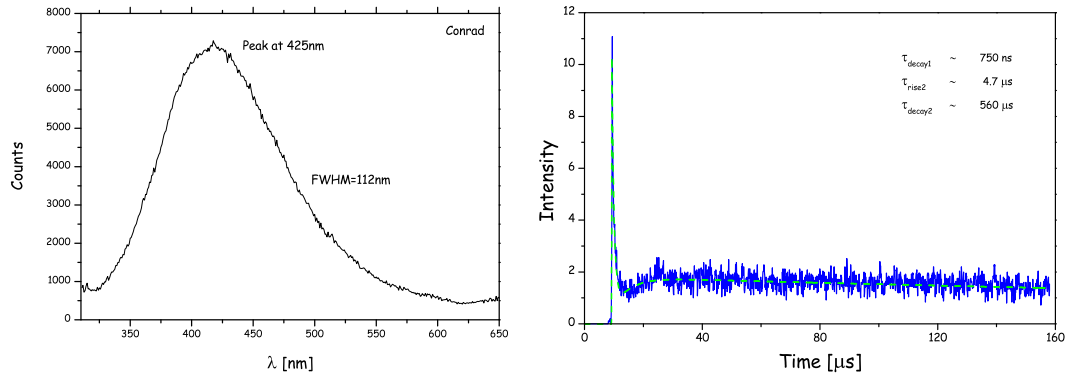

Figure 2.7: Figure on the left shows a typical $CaWO_4$ emission spectrum at room temperature. Figure on the right shows light emission curve of $CaWO_4$ measured at 6 K using a time-of-flight mass spectrometer. Two components in the scintillation time of $CaWO_4$ are visible. The slow component with a decay time of about 560μ s is attributed to the intrinsic emission of the pure $CaWO_4$ crystal, while the fast component (decay time about 700 ns) is due to the impurities present in the crystal [Ninković, 2005].

Thermometer

Thermometer used for the phonon readout of the $CaWO_4$ crystal is a $5.9\times7.5\,mm^2$ superconducting tungsten film (see figure 2.8), which is evaporated on the crystal surface and has a thickness in the range 1.2-2kÅ. Thin tungsten films evaporated directly on $CaWO_4$ crystals show superconducting transition temperatures around 50 mK that is much higher than the transition temperature of α-W (15 mK). This is probably due to a reaction between the thin film and the substrate at the high temperatures (about 500°C) during the evaporation process.

[7]The light yield of the scintillator, defined as the number of photons produced in the crystal per unit of absorbed energy (photons/MeV), is an inherent property of the type of scintillator material. On the other hand, the light output, that is a fraction of scintillation light which leaves the crystal, can differ from sample to sample. Light output depends on optical properties (transmissivity, refraction), size, geometry and surface quality of the crystal.

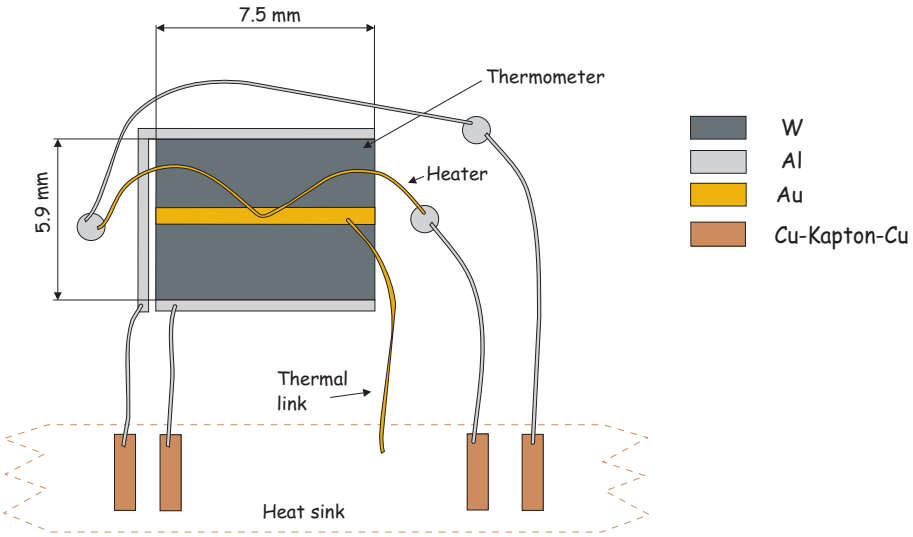

Figure 2.8: Layout of a superconducting phase transition thermometer realized on a $CaWO_4$ crystal.

To prevent diffusion between the film and the crystal, a SiO_2 buffer layer was introduced and transition temperatures in the order of 10 mK have been obtained. Additional aluminum and gold structures are needed for the electrical and thermal connections of the thermometer (see figure 2.8). Electrical connections to the read out circuit are made by 25 μm diameter superconducting aluminum wires, bonded between the aluminum pads on each end of the thermometer and the electrically insulated contact pads on the copper holder. Thermometers are stabilized at the operating point within a few μK by a heater, consisting of a gold structure coupled to the tungsten film. In the phonon detector the heater consists of a 25 μm diameter gold wire bonded from two small aluminium pads on either side of the thermometer onto a gold pad in its center. The thermal coupling of the sensor to the heat bath is provided via a gold wire connecting the central gold pad to the detector holder.

Studying the properties of the crystals, it was discovered that they show a decrease in scintillation light output up to 50% after the thermometer deposition [Ninković, 2005]. One possible explanation could be the formation of a surface layer with a reduced scintillation yield or an absorbing layer at the crystal surface due to the exposure of the $CaWO_4$ crystal to the high temperatures and high vacuum needed for the W film evaporation. Therefore, there is an ongoing research to avoid the degradation of the light output of the $CaWO_4$ crystals by producing thermometers on small $CaWO_4$ samples which are then glued to the big crystals [Kiefer, M., 2007].

A significant improvement in energy resolution and light output after the thermometer deposition has been achieved by roughening the crystal surface facing the light detector to a scale of about 10μm. This reduces the internal total reflection observed in crystals with high index of refraction ($n_{CaWO_4} = 1.92$) and enhances the escape of the scintillation light.

2.3.2 Light detector

The detection of the light emitted by the scintillating absorber is achieved by using cryogenic light detectors which consist of a non-transparent absorber for the scintillation light, equipped with a tungsten thermometer. The main challenge for the light detectors is the low intensity of scintillation light. Therefore, the energy threshold of the light detector needs to be as low as possible and the total amount of collected light has to be maximized.

Substrate

Silicon and silicon-on-sapphire (SOS) wafers are used as light detector absorbers in the CRESST II experiment.
During the prototyping phase of CRESST II experiment light detectors with $(30\times30\times0.45)\,\mathrm{mm}^3$ pure n-type silicon absorbers with 200 Å SiO_2 layers on both surfaces were used[8]. In order to minimize the thermalization of high frequency phonons in the transmission to the thermometer film through the SiO_2 [Dietsche & Kinder, 1979], later on SOS substrates consisting of a 1 μm thick layer of silicon (001), epitaxially grown on the r-plane of a 46μm thick sapphire substrate, were employed[9].
The light absorption of the SOS substrate at room temperature, estimated from the transmission and reflectivity measurements[10] and averaged over the whole emission spectrum of $CaWO_4$, was found to be ∼70% for direct illumination of the silicon surface and ∼80% for illumination from the sapphire side [Petricca, 2005]. In the present detector module geometry (see figure 2.10) the major fraction of the light is absorbed by the side of the light detector facing the $CaWO_4$ [Frank, 2002]. This gives an additional motivation for orienting the sapphire side (on which the thermometer is grown) towards the scintillating crystal.

[8]The oxide layer of a controlled thickness is deposited on the silicon wafer to prevent its uncontrolled natural growth. The naturally grown silicon oxide is of undefined thickness and quality. Additionally silicon oxide is used as interdiffusion barrier between silicon and tungsten for obtaining tungsten transition temperatures in the order of 10 mK [Di Stefano et al., 2003].

[9]SOS substrates have naturally grown silicon oxide only on one side of the wafer.

[10]The transmission measurements are done at normal incidence and the reflectivity measurements at 45° to the surface.

The size of the light detector substrate should be optimized to absorb the maximum amount of light. The observation that the scintillation light does not escape the crystal with a uniform distribution but with higher intensity on its edges and well defined patterns that depend on the crystal sample[11], favors a larger size of light detector substrates. Thus the present light detectors have circular substrates the size of which (Ø=40 mm) match the size of the $CaWO_4$ crystals.

Thermometer

To achieve a very good sensitivity and low energy threshold of the light detectors, a small heat capacity of both the absorber and the thermometer is required.

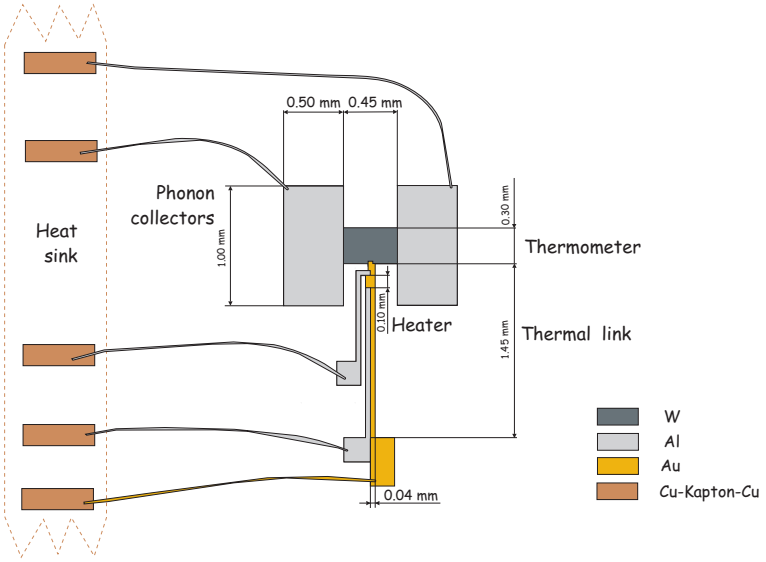

Figure 2.9: Layout of a light detector thermometer in the second phase of CRESST.

The layout of a light detector thermometer is presented in figure 2.9. The tungsten film of $(0.45\times0.3)\,mm^2$ area and 1.2-2kÅ thickness is located between two aluminium/tungsten bilayers of $0.5\,mm^2$ area and 10kÅ/2 kÅ thickness. At the typical operating temperatures the Al/W bilayers are superconducting and do not contribute to the heat capacity of the thermometer. These bilayers provide the main collection area for the non-thermal phonons from the substrate and therefore they are called phonon collectors. Their working principle is explained in section 3.2.2.

[11] Tests have been performed with some crystals having a small radioactive α source attached to one crystal surface and recording the emitted scintillation light with a photographic film [Ninković, 2007].

The phonon collectors are also used as electrical contact pads for the read out. Superconducting aluminum wires (25 μm diameter), which have negligible thermal conductance at the operating temperature, are bonded between the phonon collectors and the insulated pads on the detector holder[12]. In order to minimize additional contributions to the heat capacity of thermometer, the heater and the thermal coupling to the heat sink are provided by the same gold structure (see figure 2.9). The gold film of $(1.5\times0.08)\,\mathrm{mm}^2$ area and 500-1000 Å thickness is deposited on a thin underlying sputtered tungsten layer (100-200 Å), used to improve the adhesion between the film and the substrate. One side of the film is electrically shortened with a superconducting Al film leaving only a small portion uncovered $(0.1\times0.04)\,\mathrm{mm}^2$, that acts as a heater. The electrical connection for the heater is also made with superconducting aluminum wires bonded from the pads placed at the end of the aluminum structures to the insulated pads on the detector holder. The thermal coupling of light detectors is provided by the other side of the gold structure $(1.5\times0.04)\,\mathrm{mm}^2$ which overlaps at one end with the tungsten film. The connection to the heat bath is made via a 25 μm diameter gold wire bonded between the gold pad and an electrically insulated pad on the detector holder (see figure 2.9). In this way the thermal coupling strength (G) is defined by the gold structure[13] allowing to adjust the thermal relaxation time of light detector thermometers (see equation 1.16) by modifying the gold film conductance. Long time constants are needed in the light detector to be able to integrate the energy of the $CaWO_4$ scintillation photons, which are emitted on the time scale of a few hundred microseconds (see figure 2.7).

2.3.3 Holder and light collection

Holder

The detector module holder (see figure 2.10) consists of two copper rings and three copper rods which hold the scintillating crystal and two end-caps in one of which the light detector is housed. The open structure of copper was chosen to allow background rejection of multiple scattering events in a multi detector setup. An open detector module can be seen in figure 2.12.

The crystal is held by six pairs of CoSn6-bronze clamps. Due to the elasticity of the bronze even at low temperatures the clamps can keep the crystal tightly preventing its vibrations without introducing too much stress in the contact area that would result in the formation of cracks on the crystal surface [Majorovits et al., 2008].

The circular substrate of light detectors is held by three CoSn6-bronze clamps, which keep the detector $\sim$5 mm away from the end-cap allowing its full exposure

[12]The electrical insulation of the pads reduces of the common mode interferences.

[13]The conductance defined by the series of the two resistances is dominated by the much larger resistance of the film structure.

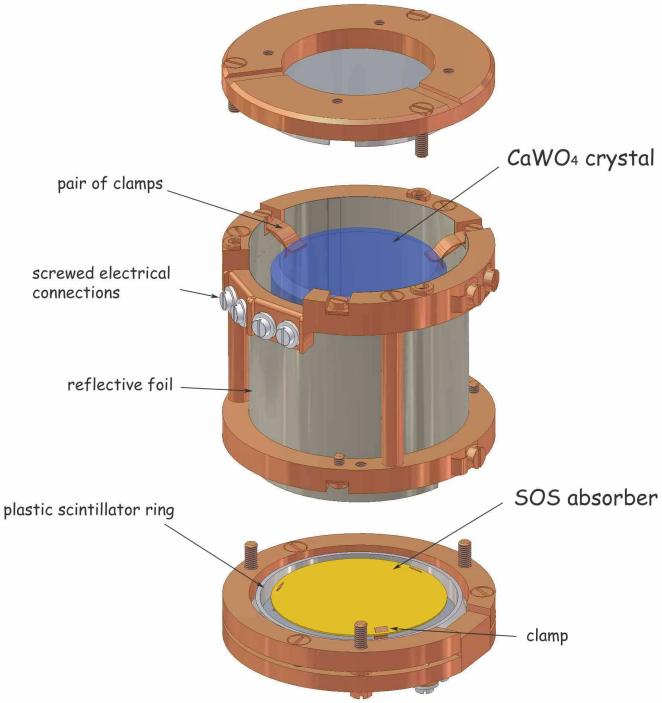

Figure 2.10: Exploded view of a detector module.

to scintillation light. The clamps for both phonon detector and light detector are specially designed to have a small contact area with the substrate to prevent parasitic thermalization of non-thermal phonons.
In order to avoid soldering[14], screwed electrical connections have been chosen to provide a reliable contact at low temperatures (see figure 2.11). To connect detectors to the readout circuit, superconducting wires are screwed onto electrically insulated copper pads on the holder from where aluminium bond wires lead into the inner part of the holder and contact the thermometers.

Light collection

The crucial point in the detector module design is its light collection efficiency. The measured fraction of the scintillation light yield is typically about 2% of the total energy deposited in $CaWO_4$ [Frank, 2002] [Stark, 2005]. A 10 keV energy deposition in the crystal then corresponds to 200 eV in scintillation light that is only about 66 photons.
To be able to detect the light of low energetic interactions the scintillation light

[14]The presence of lead in soldering alloys requires to avoid solder joints in the vicinity of detectors.

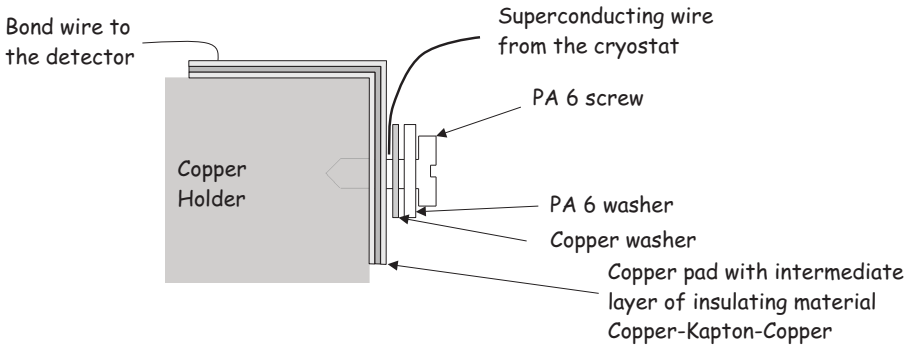

Figure 2.11: Schematic view of screwed electrical connections. For reliable contacts at low temperatures a careful choice of materials that takes into account the effect of thermal shrinkage is important. PA6 stands for polyamide 6.

escaping from the crystal first must reach the light detector, where it is then efficiently absorbed. The solution adopted by CRESST consists in having both calorimeters inside a reflector that allows to have a fully exposed light detector. Due to the unfavorable ratio of areas of the light detector and the reflecting surface of the holder, a photon on the average has to undergo many reflections before hitting the light detector. Therefore the use of a reflector with a high overall reflectivity is needed.
The reflecting housing is made of a high reflectivity polymeric multilayer foil VM2000a[15], the transparent polyethylenenaphthalate (PEN) support layer of which scintillates, allowing to discriminate background events originating from alpha decays of nuclei implanted on the crystal or reflector surface (see chapter 1.2.3). The reflectivity of the polymeric foil and the luminescence properties of the PEN layer have been measured [Ninković, 2005, figures 5.36-5.38]. The VM2000a foil shows a reflectivity >98% at the wavelength of the emission peak of $CaWO_4$. The emission spectrum of the foil overlaps with the intrinsic emission of $CaWO_4$, while the excitation spectrum is in the ultraviolet range. The reflectivity of the VM2000a polymeric multilayer foil measured at the wavelength of 476 nm shows no noticeable dependence on the angle of incidence [Brunoldi et al., 2007].
The interface between the cylindrical reflector around the crystal and the reflector covering the end-caps is provided by overlapping plastic scintillator rings (see figure 2.10), that are coated on the outer side with an aluminum reflective layer. The reflector has two small gaps needed to provide the access for electrical connections for both detectors. To optimize light collection and discrimination against radioactive surface contaminations the part of the clamps extending inside the reflector are also covered with the reflective and scintillating polymeric

[15]3M Radiant Mirror Film VM2000a is a registered trade mark of 3M, also called VM2002 or 3M adhesive foil.

foil[16].

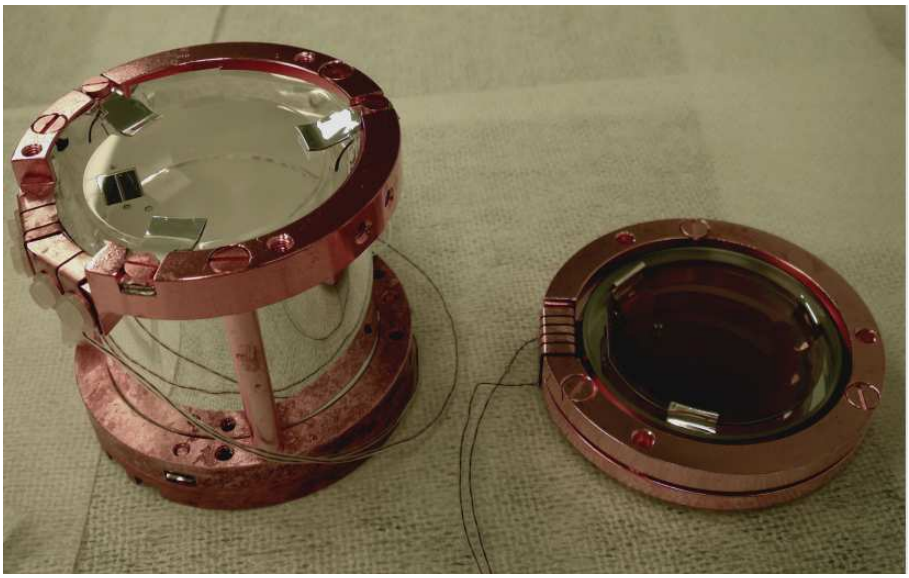

Figure 2.12: Picture of an open detector module for CRESST phase II (Run29 and Run30).

The carousel

For the second phase of CRESST a total target mass of 10 kg with 33 detector modules is foreseen [Altmann et al., 2001]. To allow the installation of all detector modules a special detector holder structure (carousel) has been constructed and mounted at the end of the cold finger (see figure 2.1). The carousel provides mechanical support for the detectors and electrical connections (see figure 2.13). The 33 detector modules are arranged in 12 towers, where each tower holds two or three detector modules. The design allows each detector module to be manipulated individually.

Another important function of the carousel is to supply the thermal coupling of the detectors (via the cold finger) to the mixing chamber of the cryostat. Copper holders which house the detectors have strong thermal coupling to the carousel, while the carousel is only weakly coupled to the mixing chamber. The weak coupling provides an efficient filter to fast temperature fluctuations of the mixing chamber and thus allows a better temperature stabilization of the detectors. In addition, a CoSn6-bronze spring suspension between the cold finger and the carousel provides the decoupling of vibrations from the cryostat.

[16]In order to achieve an even better surface covering of the clamps and easier mass production, for the next setup the clamps are coated with a reflective aluminum layer and then with a thin layer of araldit 2011 glue, which has been found to scintillate both at room and low temperature [Schäffner, 2007].

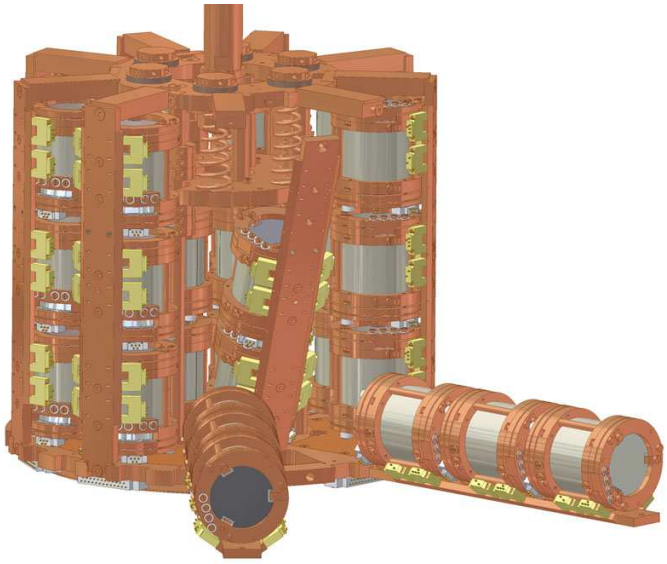

Figure 2.13: Schematic view of the open detector holder structure constructed for CRESST phase II. It can house 33 detector modules arranged in 12 towers. Each detector module is individually exchangeable. Spring suspension is used to decouple the detectors from the vibrations of the cryostat.

To reduce environmental background, all the materials used in the vicinity of the detectors have been tested and selected for their radiopurity [Majorovits et al., 2008][Frank, 2002, page 40][Majorovits, 2007].

2.4 Readout and data acquisition

The change of a resistance caused by a temperature rise in a thermometer following an event needs to be converted to an electrical signal that is fed into the readout circuit and recorded by the data acquisition system (DAQ).

2.4.1 Biasing and readout circuit

The circuit used to bias and read out thermometers is shown in figure 2.14. A constant bias current I_0, supplied by a floating current source, is shared between the branch containing the temperature dependent resistance of the film $R_f(T)$ and the branch containing two constant reference (shunt) resistances in series with the input coil of the dc SQUID[17]. Reference resistors (each 20 mΩ) with

[17]A dc Superconducting QUantum Interference Device consists of a superconducting coil with two Josephson junctions. The device is named dc SQUID because it operates with a steady current bias [Rose-Innes & Rhoderick, 1978].

a total resistance R_s=40 mΩ are used for the second phase of CRESST[18]. The

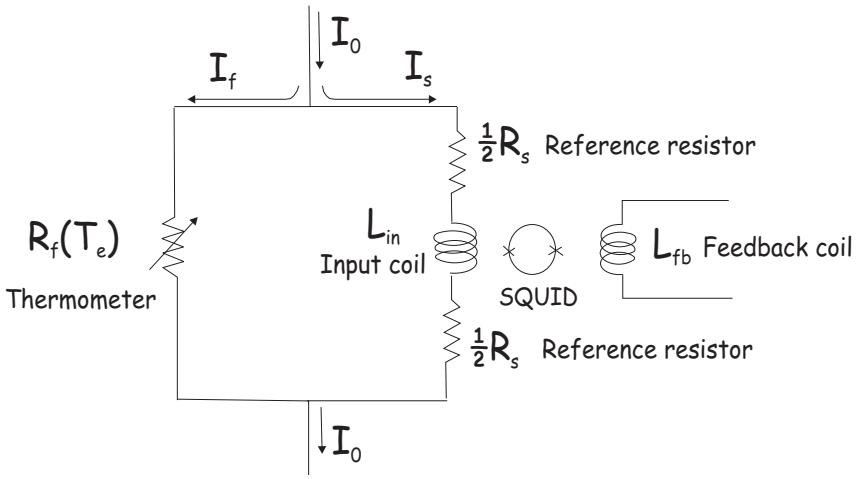

Figure 2.14: Schematic view of the readout circuit. An increase of I_s due to an increase of R_f changes the magnetic flux through the SQUID, which converts the magnetic flux variations to a voltage pulse.

currents through the thermometer branch and the SQUID branch are given by

$$I_f = I_0 \frac{R_s}{R_f(T) + R_s}\,, \qquad I_s = I_0 \frac{R_f(T)}{R_f(T) + R_s} \tag{2.1}$$

Any change in the film resistance causes a change in the branching of the bias current I_0 and consequently a change in the current passing through the SQUID given by

$$\Delta\, I_s = -\Delta\, I_f = I_0 \frac{R_s}{(\Delta\, R_f + R_f + R_s)(R_f + R_s)}\, \Delta\, R_f. \tag{2.2}$$

In a small signal approximation ($\Delta R_f \ll R_f$) the equation 2.2 can be linearized to

$$\Delta\, I_s = I_0 \frac{R_s}{(R_f + R_s)^2}\, \Delta\, R_f = \frac{I_f}{(R_f + R_s)}\, \Delta\, R_f. \tag{2.3}$$

The increase ΔI_s of the current I_s, that results from an increase ΔR_f of the resistance of the film following an energy deposition, is converted into a magnetic flux change by the input coil with inductance L_{in}. The input coil is magnetically coupled to the SQUID loop. The SQUID acts as an amplifier, that converts a magnetic flux change to a voltage pulse. For the applied magnetic flux Φ the output voltage of the SQUID has a periodic behavior, with a period equal to one flux quantum $\phi_0 \equiv h/2e \approx 2 \times 10^{-15}\, Wb$ [Clarke, 1989]. To overcome

[18]Two reference resistors are used to balance the circuit [Henry et al., 2007].

the ambiguity due to the periodicity of the response, SQUIDs are used as null detectors. This is realized by operating them in a flux locked mode (Flux Locked Loop (FLL)) with a separate feedback coil used to keep the flux through the loop constant. The output voltage of the SQUID electronics is then proportional to the feedback current. In the FLL mode there is a linear relation between the applied magnetic flux Φ, defined by the current I_s flowing through the input coil, and the output voltage given by

$$V_{out} = \xi(\Phi + n\phi_0) \tag{2.4}$$

where ξ is the flux to voltage transfer coefficient of the SQUID system.
This techniques enables the measurements of changes in flux ranging from much less than a single flux quantum to many flux quanta. Due the periodicity of the flux-voltage characteristics of the SQUID there is a sequence of stable operating points. If the input signal changes faster than the response of the feedback loop, the operating point of the SQUID will change resulting in the different output voltage (different value of n in equation 2.4). As a consequence, this readout scheme is limited by the maximum rate of flux change that the feedback electronics can compensate (slew rate).
The advantage of using SQUIDs for the readout of the detectors, besides their extreme sensitivity, is the fact that their input impedance is essentially inductive, which matches the small impedance of the biasing circuit.
SQUIDs used for the CRESST phase II are commercially available Supracon dc SQUIDs.

2.4.2 Data acquisition system

The electronic chain is here described by following the path of the analog signals from the detectors to the digital information stored on hard drives. A block diagram of the electronic of one detector module is shown in figure 2.15. Each detector (two per module) requires two pairs of wires to supply the bias current and the heater current. As already mentioned, electrical connections from the thermometer to the contact pads are done with bonded superconducting aluminum wires. From the detectors contact pads electrical connections are then realized with twisted pairs of superconducting wires combined into woven cables[19].

The bias wires run up along the cold finger until the shunt boxes placed at the level of the mixing chamber. The reference (shunt) resistors of the biasing circuit are mounted inside the shunt boxes having a good thermal contact with the mixing chamber to minimize their Johnson noise. From the shunt boxes bias

[19]Each woven cable carries 12 superconductive NbTi wire pairs, that are twisted in alternate directions to prevent pickup noise and reduce crosstalk. The NbTi wires are covered with an external CoNi shielding to improve the thermal coupling at the various temperature stages to ensure that there is no heat load on the detectors [Henry et al., 2007].

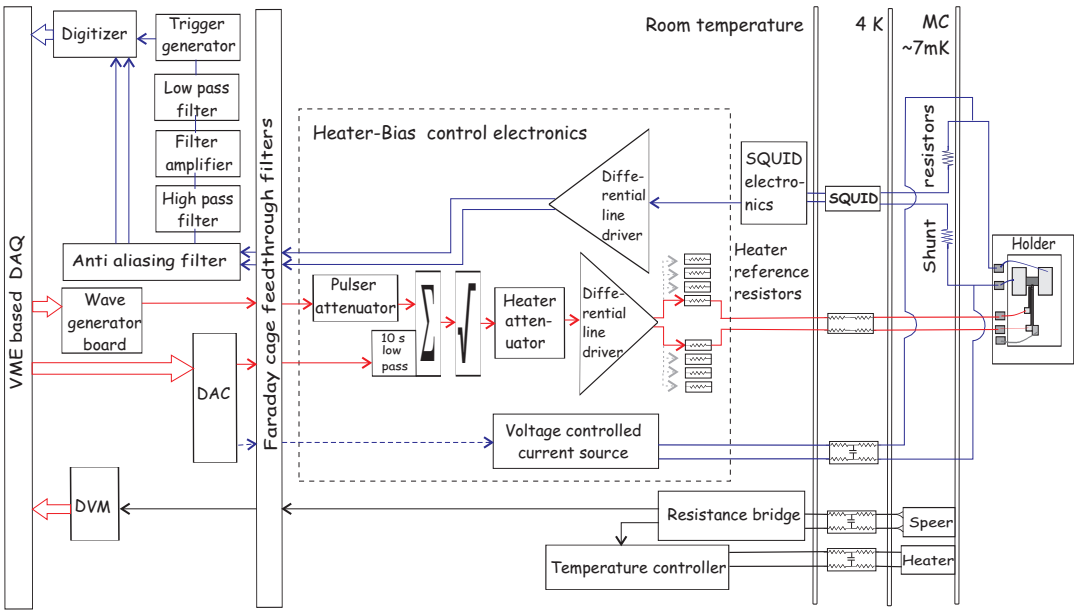

Figure 2.15: Block diagram of the readout circuit (blue lines) and the heater circuit (red lines) for one detector, together with the data acquisition system. Continuous lines connecting devices represent analog signals while block arrows represent digital transmission of data.

wires run to the current sources outside of cryostat and to the SQUID sensors mounted in the liquid helium bath. In order to reduce high frequency noise from outside H-type low pass filters (ν_{cutoff}=50kHz) are installed on the bias lines at the 4.2K level between the reference resistors and the current sources. The bias current for the detector readout is provided by voltage controlled floating current sources with a set of current defining resistors. During normal operation the voltage is internally provided[20].The current sources are an integrated part of the Heater-Bias control electronics, that is placed in the Faraday cage.

As already mentioned, film heaters are used to individually stabilize the detectors at the operating point. The same heaters are also used to inject periodic heater pulses to monitor the detector stability (see section 4.1.2).

The heater wires follow the bias wires along the cold finger. They pass the series of high ohmic resistances arranged in H-shape[21] at the 4K stage and are connected to an external heater power supply placed within the Heater-Bias control electronics. The heater power supply is a feedback unit, which sums the voltage for regulating the temperature and the voltage corresponding to heater

[20]The voltage can be also externally provided by the DAC located outside the Faraday cage.

[21]This helps reducing the effect of possible differential-mode voltage interferences developed at the input outside of cryostat.

pulses. The summed voltage is passed through an analog square-rooter which linearizes the dependence of the heating power with respect to the input voltage. The output voltage is then connected via series heater reference resistors to the heater on the film. Phonon and light detectors have different resistance values of the heaters and different thermal coupling. In order to allow discrete adjustment of the heater output current, different series resistors are installed. An additional attenuator provides further continuous adjustment of the heating demands. The heating power, and thus the detector stability, is regulated by a computer controlled digital to analog converter (DAC) connected to the summing amplifier[22]. The DAC output signal is controlled by a software proportional-integral (PI) controller and sent into the Faraday cage via feedthrough low pass filter (ν_{cutoff}=3.4kHz).

Exponential heater pulses with a decay time adjusted to create pulses resembling particle pulses are produced by a VMI based arbitrary wave form generator board, separately for light detectors and phonon detectors. These heater pulses with a number of discrete amplitudes (energies), covering the energy range of interest, are then loaded in the local memory from where they are sent in sequences at regular time intervals. The heater pulses pass into the Faraday cage via feedthrough filters. Since the same heater pulses are used for all phonon (light) detectors, attenuators are installed in front of the summing amplifier to allow their adjustment to the dynamic range and to the heater resistance of each phonon (light) detector.

To read out the 33 detector modules, CRESST-II is using 66-channel SQUID readout system consisting of 66 SQUID sensors (Supracon), SQUID control and readout electronics (Star-Cryoelectronics) [Henry et al., 2007]. The output signal from the SQUID control electronics is amplified via symmetric differential line drivers which are placed inside the Heater-Bias unit. The SQUID signals, after passing through the Faraday cage low pass filters (ν_{cutoff}=50kHz), are further filtered through anti-aliasing filters (ν_{cutoff}=10kHz). The signal is then split in two: the actual signal, that is DC coupled to the 16-bit transient digitizer, and the trigger signal that is AC coupled (high pass filter with ν_{cutoff}=8Hz), amplified (x20) and shaped with a low pass filter with an adjustable cutoff frequency before entering a trigger unit.

The transient digitizer has a defined record length (typically 4096 channels). From the pre-trigger region of the signal, it is possible to extract the information about the baseline (SQUID output) before the pulse. The size of the pre-trigger region is chosen to have enough data for a correct determination of the baseline

[22]To suppress the noise from the switching in the DAC, a 10 s low pass filter is integrated into the summing amplifier.

level, but without an excessive increase of dead time per record. The characteristic time constants of the detectors define the duration of the pulse for a given energy deposition. Record length and sampling time are chosen such that the post-trigger region includes the full duration of the pulses in the relevant energy region.
In the second phase of CRESST the signals are digitized with independent 8 channels simultaneous sampling transient digitizers (hereafter called digitizer module). Each digitizer module has an associated trigger module. The trigger signal in one trigger module initiates the post trigger sampling cycle of all channels within the corresponding digitizer module. An internal clock synchronized with the digitizer is used to prevent another trigger on that channel until the readout of the pulse is completed and the required pre-trigger channels for the next event have been sampled. Pulses from the other detectors within the same trigger module, which arrive within half of the post-trigger period are also recorded together with the time delay with respect to the first trigger. The phonon and light detector from a single detector module are triggered independently, but read out in pairs. Whenever one of the two has a valid trigger, digitizers of both detectors are readout.
The discarding of the triggers in the trigger module that arrive after half of the post-trigger period contributes to a dead time with a half of the post-trigger region, a full pre-trigger region and a readout time for all detectors that did not trigger. For the channels that triggered the dead time has contributions from the next pre-trigger region and readout time. The accumulated dead time is measured with separate clocks for each channel.

Apart from the response to particle pulses, the data acquisition system also records the response to the periodic test pulses which are used to monitor the behavior of the detectors.
Additionally, the photomultiplier tube signals from each muon panel and the summed signal are digitized and their pulse heights recorded. The time stamps with 10 μs resolution taken for each event occurring in the detector modules and in the muon veto system allow the determination of possible coincident events.
In addition to recording the data, the DAQ handles the task of controlling the detectors as described in section 4.1.

Temperature control

As previously mentioned, the temperature reference for the detectors is the carousel, which is weakly thermally connected to the mixing chamber of the dilution refrigerator. The temperature of the mixing chamber is monitored and regulated with a four point AC resistance bridge with integrated PID[23] controller.

[23]Proportional Integral Differential.

The resistance bridge reads the resistance of a calibrated carbon resistor (speer) and sends the current into a heating resistance, both mounted on the mixing chamber. The signals from the resistance bridge are read by a multichannel digital voltmeter (DVM). During the 2007 data taking (Run 29 and 30) the mixing chamber is stabilized at a temperature of a about 7 mK with a stability of 4 μK.

Chapter 3

Detector model

A good understanding of the physics involved in the formation of the low temperature calorimeter signal allows further optimization of their performance. Here the physical processes that occur after the interaction of an incident particle in the detector absorber are described. In order to understand the specific signal shape a model of the calorimeter is developed. In this model a detector consists of several discrete components interconnected through finite thermal conductances and their contributions to the signal are taken into account. The working principle of phonon collectors that are used to enhance the temperature signal is also described. The various noise contributions and their influence on the detector response, together with the expected energy resolution are discussed in the last section.

3.1 Signal evolution

A typical CRESST detector consists of a dielectric absorber and a thin layer of superconducting material evaporated onto one of its surface serving as a thermometer.

3.1.1 Heat capacities

The heat capacities of the different detector parts play a fundamental role because they define the achievable temperature rise caused by an energy deposition.
The heat capacity of a crystalline dielectric is dominated by the lattice specific heat c_{ph}. At low temperatures it is described by the Debye model as

$$c_{ph} = \frac{12\pi^4}{5} n_a k_B \left(\frac{T}{\Theta_D}\right)^3 , \tag{3.1}$$

where k_B is the Boltzmann constant, Θ_D is the Debye temperature, n_a is the number of lattice atoms per mole. The same formula is valid for pure semiconductors at low temperatures where conduction electrons are frozen out. Due to the T^3 dependence, the phonon heat capacity is very small at low temperatures, making dielectrics and semiconductors suitable as large volume absorbers for calorimeters.
The heat capacity of the superconducting thermometer film in the normal conducting state for temperatures which are small compared to the Debye temperature Θ_D of the material, is given by the sum of the electronic specific heat and the lattice specific heat (as for other metals) [Pobell, 1992]

$$c = c_{ph} + c_e = \frac{12\pi^4}{5} n_a k_B \left(\frac{T}{\Theta_D}\right)^3 + \frac{\pi^2}{2} n_e k_B \frac{T}{T_F}\,, \tag{3.2}$$

where T_F is Fermi temperature and n_e is the number of conducting electrons per mole. The expression 3.2 can also be written in a simplified form

$$c = AT^3 + \gamma T\,, \tag{3.3}$$

where A and γ[1] are constants which depend on the material. The linear dependence of c_e causes it to dominate the heat capacity of a metal at low temperatures[2].
According to the elementary theory of superconductivity [Tinkham, 1996], in the phase transition the specific heat capacity of a superconducting film exhibits a jump given by

$$\Delta c = 1.43\gamma T_c\,, \tag{3.4}$$

where γT_c is the electronic specific heat of the normal conducting state at the critical temperature. This prediction is valid for a large class of superconductors. The heat capacity in the region of the transition, namely at the operating point of a sensor, is estimated by a linear approximation. Taking the ratio of the resistance at the operating point R_{op} to the normal conducting resistance R_n as a measure for the fraction of the film in the superconducting phase, the heat capacity at the operating point can be expressed as

$$c_{op} = c_e \left(2.43 - 1.43\frac{R_{op}}{R_n}\right). \tag{3.5}$$

Below the transition the electronic specific heat has an exponential temperature dependence, vanishing more rapidly than the electronic specific heat in the normal conducting state of the metal, whereas the lattice contribution is not

[1] γ is often called ¨ Sommerfield constant¨ .

[2] The crossing point, where the two terms are comparable, occurs at temperatures of the order of a few Kelvin [Ashcroft & Mermin, 1976].

		Tungsten	Gold	Aluminium
T_c	[mK]	15	-	1180
T_F	[K]	27000	63900	134900
Θ_D	[K]	383	162	428
γ	$[\mathrm{mJ \cdot mol^{-1} \cdot K^{-2}}]$	1.01	0.729	1.356

Table 3.1: Transition temperature, Fermi temperature, Debye temperature and Sommerfeld constant [Kittel, 1967] [Triplett et al., 1973] for metals relevant for the CRESST sensors.

influenced by the transition to the superconducting state. For temperatures below $T_c/10$ the electronic contribution becomes negligible and the heat capacity is dominated by the lattice specific heat. Table 3.1 compiles the values for metals most relevant for the CRESST sensors.

3.1.2 Energy down-conversion

In a dielectric absorber, ionizing radiation mainly looses its energy via interaction with electrons. The highly excited electrons, emitted after the absorption, initially loose their energy by interaction with other electrons and excitation of electron-hole pairs down to an energy of less than twice the energy gap in the material (see table 3.2). Below this level electrons with energies of the order of eV cannot participate any longer in the energy down-conversion and they relax within about 10 ps to the band edge mainly via the emission of optical phonons[3]. On a time scale of the order of 100 ps, optical phonons decay into acoustical phonons of about half of the Debye frequency ν_D (see table 3.2), leading to an almost monoenergetic frequency distribution. The energy released in the nuclear branch (i.e. via elastic interactions with nuclei), that becomes important for alpha particles and heavy ions and is dominant for neutrons and WIMPs, excites instead non-thermal acoustic phonons in a broad frequency range via the local deformation of the crystal lattice.
Hence, after a time of the order of 100 ps the energy released in the absorber by a generic interaction is transferred into high frequency acoustic phonons, but with a phonon spectrum dependent on the type of the interaction. These phonon populations are not in equilibrium and start to decay towards a thermal distribution. The acoustic phonons are distributed between three modes, one longitudinal (LA) and two transversal (TA). The down conversion of acoustic phonons is possible through anharmonic decay in which one phonon spontaneously splits into two lower frequency phonons respecting energy and quasi-momentum conservation.

[3]In the case of scintillating materials the emission of photons, though highly suppressed compared with the emission of phonons, is extremely important for the event discrimination.

	Al_2O_3	Si	$CaWO_4$
Θ_D [K]	1041 [a]	648 [a]	228 [b]
$\nu_D = k_B\Theta_D/h$ [THz]	≈21.7	≈13.5	≈4.7
Energy gap [eV] [eV]	8.3 [c]	1.12 [d]	5.2 [e]

Table 3.2: Debye Temperature, Debye frequency and energy gap for materials used for CRESST absorbers, [a] calculated from elastic constants [Pröbst, 2008], [b] [Gluyas et al., 1973], [c] [Bento, 2004], [d] [Ashcroft & Mermin, 1976], [e] [Mikhailik et al., ????]. The values given in the literature differ to some extent depending on the method used to derive them.

Transversal acoustic phonons occupy the lowest energetic branches. In isotropic media, where the TA branches are degenerated, TA phonons do not decay into two phonons[4]. In anisotropic media TA phonon decay though can be neglected [Tamura & Maris, 1985]. In such conditions only LA phonons can decay using the two possible channels: LA↦LA+TA and LA↦TA+TA, with a decay rate $\Gamma_{decay} \propto \nu^5$, where ν is the phonon frequency [Tamura, 1985].
Besides the decay of longitudinal phonons, all phonons scatter on isotopes present in the crystal lattice with a rate $\Gamma_{isotope} \propto \nu^4$ [Maris, 1990] and such an elastic scattering induces rapid mode conversions (TA↔LA) maintaining an occupation of modes according to the density of states, thus opening an effective decay channel for transversal phonons [Tamura, 1985].
Simulations of the time development of an initial monoenergetic phonon population of half the Debye frequency in silicon and sapphire [Pröbst et al., 1995] show that the strong frequency dependence of Γ_{decay} leads to a very rapid initial decrease of the average phonon frequency. After this time all differences in the phonon spectrum caused by energy releases in the nuclear or electronic branch are washed out. The first fast decay is followed by a much slower rate of change, consequently the phonon frequency distribution stays almost constant for about few milliseconds[5] during which phonons spread ballistically over the entire absorber filling it uniformly.

3.1.3 Energy propagation

After a few surface reflections, non-thermal phonons are uniformly distributed in the absorber. The time required to establish a uniform distribution is in the order of L/v, where L is the largest dimension of the absorber and v is the sound

[4]This is due to energy and quasi-momentum conservation that forbids the TA phonon decay in the presence of any, even small, amount of non-linearity in the dispersion relation (as is the case in real crystals) .

[5]The phonon population does not thermalize in the absorber on such a time scale.

velocity in the medium averaged over directions and modes. The non-thermal phonons are then either transmitted into the thermometer or thermalized by inelastic reflections at the crystal surfaces on a time scale of a few ms. On a perfect surface phonons are reflected elastically, but in real crystals imperfections and adsorbates also cause inelastic scattering.
The transmission probability of acoustic phonons across the absorber-thermometer interface can be calculated within the theory of anisotropic elastic continua. A calculation of the energy flux per unit area and unit time across the boundary from material 1 to material 2 ($\dot{Q}_{1\to 2}$), performed by summing over all modes and wave vectors of incident phonons [Pröbst et al., 1995], leads to

$$\dot{Q}_{1\to 2} = \left\langle \frac{E}{V} \right\rangle \frac{1}{2} \langle v_\perp \alpha \rangle, \tag{3.6}$$

where $\langle E/V \rangle$ is the average energy density[6] in the first material, $v_\perp$ is the phonon group velocity normal to the interface, α is the transmission probability and $\langle v_\perp \alpha \rangle$ is averaged over modes and wave vectors of the incident phonons.
If E/V is the thermal energy density, from equation 3.6 the heat boundary conductance G_K of thermal phonons between two materials, usually called Kapitza conductance, can be derived as

$$G_K = \frac{\dot{Q}_{1\to 2}(T+\Delta T) - \dot{Q}_{2\to 1}(T)}{\Delta T} = \frac{C}{2V} \langle v_\perp \alpha \rangle \,, \tag{3.7}$$

where C/V is the heat capacity per unit volume of the first material. Due to the cubic temperature dependence of the absorber's heat capacity (see equation 3.1), the Kapitza coupling for the absorber-thermometer interface exhibits the same dependence

$$G_K \propto T^3 \,. \tag{3.8}$$

The transmission coefficients for different metal films deposited on silicon, sapphire and $CaWO_4$ substrates, calculated by numerical methods [Pröbst et al., 1995], are shown in table 3.3. Anisotropic conditions are assumed and the films are considered as polycrystalline metals with randomly oriented single crystals.

3.1.4 Electron-phonon coupling

The electron-phonon coupling G_{ep} of electrons and phonons in the thermometer in combination with the Kapitza conductance determines the thermal coupling of the absorber to the electrons of the thermometer. The frequency and temperature

[6] Wave vectors of thermal and non-thermal phonons have the same angular distribution because surface and isotope scattering distribute them according to the density of states. Therefore the same equation 3.6 can be used for the energy transmission of thermal or non-thermal phonons by using the appropriate energy density $\langle E/V \rangle$.

Transmission from→ to	G_K/T^3 [kW· K^{-4}· m^{-2}]	$\langle v_\perp \alpha \rangle$ [m/s]	$\bar{\eta}$
Si→ W	0.440	1485.4	0.246
Al_2O_3 → W	0.430	2547.5	0.290
$CaWO_4$ → W	1.784	647.9	0.142
Al_2O_3 → Si	0.495	2933	
Si→ Al_2O_3	0.495	1668.7	

Table 3.3: Kapitza conductance G_K per T^3, $\langle v_\perp \alpha \rangle$ and effective absorption $\bar{\eta}$ for some absorber-thermometer interfaces of CRESST detectors. Parameters are calculated for the transmission of phonons across the (001) plane of silicon, the $(1\bar{1}02)$ plane of sapphire and the (001) plane of $CaWO_4$. The metals are considered to be polycrystalline with the crystals randomly oriented [Pröbst et al., 1995, Pröbst, 2008].

dependence of the electron-phonon interaction in normal conducting metals can be discussed in terms of the phonon wave vector q and the mean free path of electrons l_e.
For small phonon frequencies (thermal phonons), at low enough temperatures or in the limit where $(q \cdot l_e) \ll 1$ applies, it can be shown [Liu & Giordano, 1991, DiTusa et al., 1992] that the temperature dependence of the electron-phonon thermal coupling can be expressed as

$$G_{ep} \propto T^5. \tag{3.9}$$

At higher temperatures or in the limit $(q \cdot l_e) \gg 1$ a fourth power temperature dependence is expected.
In the temperature range relevant for the CRESST detectors ($\sim 15\,\mathrm{mK}$), the fifth power temperature dependence of the electron-phonon coupling is usually assumed [Pröbst et al., 1995]. This leads to the electron system being decoupled from the phonon system of both the thermometer and the absorber.

For non-thermal phonons $(q \cdot l_e) \gg 1$ holds and longitudinal phonons interact efficiently with the electron system of the thermometer. This is due to the electron coupling to lattice vibration via density changes. Since pure transversal phonons produce no change in density, it is expected that in metals or semiconductors with a spherical Fermi surface only longitudinal phonons couple to electrons. Assuming, for the non-thermal phonons, that the absorption in the thermometer is independent of the phonon frequency and that all transmitted LA phonons are absorbed[7] and all TA phonons do not interact, an average absorption probability $\bar{\eta}$ is calculated and listed in table 3.3.

[7]This assumption is valid only if the thermometer is thick enough to completely absorb the non-thermal phonons. Calculations of the mean free path [Pippard, 1955] suggest that longitudinal non-thermal phonons are totally absorbed in tungsten films of 2 kA thickness.

Absorbed non-thermal phonons thermalize in the thermometer and increase the temperature of its electron system. This temperature rise is measured via the consequent increase of the thermometer resistance. Due to the thermal decoupling of electrons and phonons, the electrons in the thermometer are overheated with respect to the absorber[8]. In such a situation only the heat capacity of thermometer film is relevant for the sensitivity of the detector. The absorber material does not affect the detector sensitivity through its heat capacity but only by means of its phonon transport properties (see following section).

3.2 Detector model for pulse formation

Ideal calorimeters, microcalorimeters or bolometers[9] consist of an absorber connected to a heat sink through a weak thermal link and a thermometer for measuring the temperature rise (see figure 1.5).
The theory of ideal bolometers has been developed by many authors, in particular by Mather [1982], and extended to microcalorimeters [Moseley et al., 1984]. In practice, these detectors have a complex structure with different internal parts linked together and a more realistic model is needed to describe their behavior. A rather complete theoretical analysis for the type of calorimeters used in CRESST has been proposed in Pröbst et al. [1995], where the detector system is described by a set of coupled differential thermal equations. Other analytic models of bolometers and microcalorimeters can be found in Galeazzi & McCammon [2003] and Figueroa-Feliciano [2006].

3.2.1 Calorimeter model

The model described here was developed for a calorimeter with a dielectric absorber read out by a superconducting phase transition thermometer [Pröbst et al., 1995].
Figure 3.1 is a schematic representation of a thermal model, where the detector consists of three weakly coupled thermal subsystems characterized by their heat capacity C and their temperature T. The phonon systems of the absorber and of the thermometer are thermally coupled via the Kapitza coupling G_K. The phonon and the electron systems of the thermometer are coupled by the electron-phonon coupling G_{ep}. Since the heat capacity of the phonon system of the thermometer at low temperature can be neglected (see equation 3.3), the Kapitza coupling between the two phonon systems G_K and the electron-phonon

[8]The effect of thermal decoupling between electrons and phonons is only significant for temperatures below 100 mK, where the population of non-thermal phonons has an average temperature of few K.

[9]Bolometers are low temperature detectors that measure power.

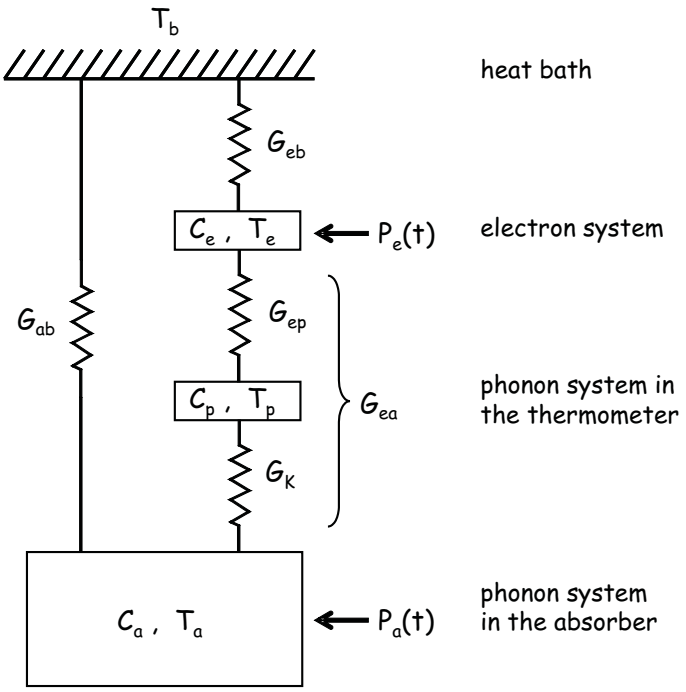

Figure 3.1: Schematic view of the thermal model of the calorimeter.

coupling G_{ep} are replaced in the model by

$$G_{ea} = \left(\frac{1}{G_{ep}} + \frac{1}{G_K} \right)^{-1} , \tag{3.10}$$

which represents a coupling between the electron system of the thermometer and the phonon system of the absorber.
The detector is coupled to the heat bath via the thermal link of the thermometer G_{eb} and directly via its mechanical mounting that can be modelled as a thermal conductance G_{ab}. As already mentioned, the thermal coupling of the detectors to the heat sink is given by the combination of gold structures and of gold bonding wires. Their thermal conductance G_{Au} can be calculated from the residual electrical resistance at low temperature via the Wiedemann-Franz law

$$G_{Au} = \frac{LT}{R} , \tag{3.11}$$

where R is the residual resistance at the temperature T and L is the Lorenz number ($L = 2.45 \cdot 10^{-8}\, W \cdot \Omega \cdot K^{-2}$).
The model assumes a uniform distribution of the non-thermal phonons within the volume of the absorber V_a immediately after the deposition of an energy ΔE. The phonons are simply subdivided into two components, thermal and

non-thermal, and the thermalization rate of non-thermal phonons is assumed to be independent of their frequency.
As already mentioned, non-thermal phonons that enter the thermometer efficiently interact with the electron system of the thermometer which, due to this interaction, experiences a time dependent power input $P_e(t)$. The thermalization of high frequency phonons in the absorber, which is a competing process to the previous one, is modelled by a power input $P_a(t)$ into the thermal phonon population. These time dependent power inputs are described as

$$P_e(t) = P_0\, e^{-\frac{t}{\tau_n}}, \qquad P_a(t) = \frac{1-\epsilon}{\epsilon} P_e(t), \tag{3.12}$$

where ϵ represents the fraction of high frequency phonons thermalized in the thermometer, P_0 is the initial power input into the thermometer ($P_0 = \epsilon\Delta E/\tau_n$) and τ_n is the effective time constant for the thermalization of high frequency phonons that is determined by the two competing phenomena of thermalization in the absorber and in the thermometer. τ_n can therefore be expressed as

$$\tau_n = \left(\frac{1}{\tau_{film}} + \frac{1}{\tau_{crystal}} \right)^{-1}, \tag{3.13}$$

where τ_{film} and $\tau_{crystal}$ are the time constants for the thermalization in the thermometer film and in the absorber crystal respectively.
The time constant $\tau_{crystal}$ is a property of the crystal and in particular of the crystal surface and is expected to scale with the ratio between the volume and the surface area of the absorber ($\tau_{crystal} \sim V_a/A_a$).
The time constant τ_{film} is given by

$$\tau_{film} = \frac{\tau_0}{\bar{\eta}}, \qquad \tau_0 = \frac{2V_a}{A\langle v_\perp \alpha \rangle} \tag{3.14}$$

with A being the area of the absorber-thermometer interface and τ_0 being the ideal thermalization time for complete thermalization in the thermometer ($\epsilon = 1$) and complete absorption of high frequency phonons transmitted into the film ($\bar{\eta} = 1$). The fraction of phonons thermalized in the thermometer

$$\epsilon = \frac{\tau_{crystal}}{\tau_{crystal} + \tau_{film}} \tag{3.15}$$

affects the duration of the power input into the electron system of the thermometer $P_e(t)$, whereas the initial power input P_0 only depends on the area of the thermometer-absorber interface and on the transmission and absorption probabilities

$$P_0 = \frac{\epsilon\Delta E}{\tau_n} = \frac{\Delta E}{\tau_{film}}. \tag{3.16}$$

The dependence of P_0 on τ_n explains the linear dependence of the detector sensitivity on the velocity of sound in the absorber material (see equation 3.14). The simple exponential time dependence of $P_e(t)$ in equation 3.12 is a consequence of the assumed frequency independence of the thermalization rate[10].

The thermal model of figure 3.1 can be described by two coupled differential equations for the temperature T_e of electrons in the thermometer and for the temperature T_a of phonons in the absorber

$$C_e\frac{dT_e}{dt} + (T_e - T_a)G_{ea} + (T_e - T_b)G_{eb} = P_e(t)\,, \tag{3.17}$$

$$C_a\frac{dT_a}{dt} + (T_a - T_e)G_{ea} + (T_a - T_b)G_{ab} = P_a(t)\,, \tag{3.18}$$

where T_b is the temperature of the heat bath.
With the initial conditions $T_a(t=0) = T_e(t=0) = T_b$, the equations have the following solution for the thermometer signal $\Delta T_e(t)$ [Pröbst et al., 1995]

$$\Delta T_e(t) = \Theta(t)[A_n(e^{-t/\tau_n} - e^{-t/\tau_{in}}) + A_t(e^{-t/\tau_t} - e^{-t/\tau_n})]\,, \tag{3.19}$$

where the step function $\Theta(t)$ takes into account the assumption of an instantaneous establishment of a homogeneous distribution of non-thermal phonons in the absorber after the energy deposition. The solution consists of two components: a non-thermal component, that originates from the direct absorption of non-thermal phonons in the thermometer film, with amplitude A_n given by

$$A_n = \frac{P_0\left(\frac{1}{\tau_{in}} - \frac{G_{ab}}{C_a}\right)}{\epsilon\left(\frac{1}{\tau_t} - \frac{1}{\tau_{in}}\right)\left(\frac{1}{\tau_{in}} - \frac{1}{\tau_n}\right)}\left(\frac{\frac{1}{\tau_t} - \frac{G_{ab}}{C_a}}{G_{eb} - \frac{C_e}{C_a}G_{ab}} - \frac{\epsilon}{C_e}\right)\,. \tag{3.20}$$

and a thermal component, caused by the temperature rise of the absorber as measured by the thermometer, with amplitude A_t given by

$$A_t = \frac{P_0\left(\frac{1}{\tau_t} - \frac{G_{ab}}{C_a}\right)}{\epsilon\left(\frac{1}{\tau_t} - \frac{1}{\tau_{in}}\right)\left(\frac{1}{\tau_t} - \frac{1}{\tau_n}\right)}\left(\frac{\frac{1}{\tau_{in}} - \frac{G_{ab}}{C_a}}{G_{eb} - \frac{C_e}{C_a}G_{ab}} - \frac{\epsilon}{C_e}\right)\,. \tag{3.21}$$

The time constants appearing in 3.19 are the effective time for thermalization of non-thermal phonons τ_n, the intrinsic thermal relaxation time of the thermometer τ_{in} and the thermal relaxation time of the absorber τ_t. The last two can be expressed as

$$\tau_{in} = \frac{2}{a+\sqrt{a^2-4b}} \qquad \tau_t = \frac{2}{a-\sqrt{a^2-4b}} \tag{3.22}$$

[10] A frequency independent τ_{film} results when the metal film is thick enough to absorb all transmitted phonons. The situation for $\tau_{crystal}$ is less clear. However the assumption of a frequency independent thermalization is justified by observation [Pröbst et al., 1995].

with

$$a = \frac{G_{ea}+G_{eb}}{C_e} + \frac{G_{ea}+G_{ab}}{C_a} \qquad b = \frac{G_{ea}G_{eb}+G_{ea}G_{ab}+G_{eb}G_{ab}}{C_eC_a}. \tag{3.23}$$

Calorimetric and bolometric mode

For CRESST detectors $C_e \ll C_a$, therefore equations 3.22 and 3.20 can be simplified as

$$\tau_{in} \approx \frac{1}{a} \approx \frac{C_e}{G_{ea}+G_{eb}} \tag{3.24}$$

$$\tau_t \approx \frac{a}{b} \approx \frac{C_a}{\frac{G_{eb}G_{ea}}{G_{eb}+G_{ea}}+G_{ab}} \tag{3.25}$$

$$A_n \approx \frac{P_0}{(G_{ea}+G_{eb})\left(1-\frac{\tau_{in}}{\tau_n}\right)\left(1-\frac{\tau_{in}}{\tau_t}\right)} = -\frac{\epsilon\Delta E}{C_e\left(\frac{\tau_n}{\tau_{in}}-1\right)\left(1-\frac{\tau_{in}}{\tau_t}\right)}. \tag{3.26}$$

At very low operating temperatures, where $G_{ea} \ll G_{eb}$, the intrinsic time constant of the thermometer τ_{in} can be controlled by the thermal conductance of the thermometer to the heat sink G_{eb}.
Two different modes of operation of the thermometer can be discussed in terms of the τ_{in}-to-τ_n ratio which controls the sign of A_n and hence the character of the non-thermal component of the signal (see equation 3.26).

A thermometer for which $\tau_{in} \gg \tau_n$ integrates the power input $P_e(t)$. The amplitude of the non-thermal component measures the total energy of the high-frequency phonons absorbed in the thermometer and is given by

$$A_n \approx -\epsilon\Delta E/C_e \tag{3.27}$$

It follows that for a given energy deposition, the heat capacity of the electron system determines the amplitude A_n. This operating mode of the thermometer is referred to as ¨calorimetric¨. In calorimetric mode the time constant τ_n defines the rise time of both the non-thermal and the thermal signal component, τ_{in} defines the decay time of the non-thermal component, while τ_t determines the decay time of the thermal component.
Light detector thermometers, used in the CRESST experiment, are optimized to work in the calorimetric mode, since their thermal coupling to the heat bath is adjusted to allow the detection of the scintillation signal with the long decay time of $CaWO_4$.

A thermometer for which $\tau_n \gg \tau_{in}$ operates in the bolometric mode, measuring the flux of non-thermal phonons. In this case the amplitude of the non-thermal component is proportional to the power input

$$A_n \approx P_0/(G_{ea}+G_{eb}). \tag{3.28}$$

The amplitude A_n is an estimate of the deposited energy in the detectors due to the proportionality of the initial power to ΔE (see equation 3.16). In bolometric mode the rise time of the non-thermal component is determined by τ_{in} and its decay time by τ_n. The rise time of the thermal component is defined by τ_n, while its decay time is defined by τ_t (see equation 3.19).
Phonon detector thermometers, used in the CRESST experiment, work in bolometric mode due to long time needed for the thermalization of the high frequency phonons.

The calorimetric and bolometric modes explained above refer to the operation of the thermometers, where the time constants of thermometer are short or long compared to the variations in the incoming non-thermal phonon flux. It should be noted that, due to the low frequency of incoming events, both light detectors and phonon detectors used in the CRESST experiment operate as calorimeters, since they can measure the energy of each single event.

3.2.2 Phonon collectors

In the calorimetric mode the amplitude of the non-thermal component for a given energy deposition is determined by the heat capacity of the electron system of the thermometer. Therefore the sensitivity of detectors can be increased by decreasing the heat capacity of the thermometer, that is decreasing the volume. Since the thickness of tungsten films is kept in the range of 2 kÅ in order to preserve the efficiency of non-thermal phonon absorption, a decrease in the heat capacity can only be achieved by decreasing the area of the thermometer. On the other hand, for detectors based upon detecting non-thermal phonons, it is imperative to collect as many of them as possible before they thermalize in the absorber. Thus a large collecting area is required. To overcome this problem and to enhance the sensitivity of detectors, the conflicting requirements on the area needed for the collection of non-thermal phonons and the heat capacity of the sensor are decoupled by means of superconducting phonon collectors.
The phonon collectors used in the CRESST detectors are large Al/W bilayer pads placed adjacent to two opposite sides of the tungsten thermometer (see figure 2.9). Due to the Al to W thickness ratio of approximately five to one, the bilayer has a transition temperature close to that of aluminium (1 K) such that its heat capacity at the operating temperature is negligible. The absorption of the high frequency phonons in such a phonon collector leads to the creation of long-lived quasi-particles which diffuse towards the thermometer, where they release their energy. The working principle of phonon collectors is illustrated in figure 3.2, and explained in more detail in the following.

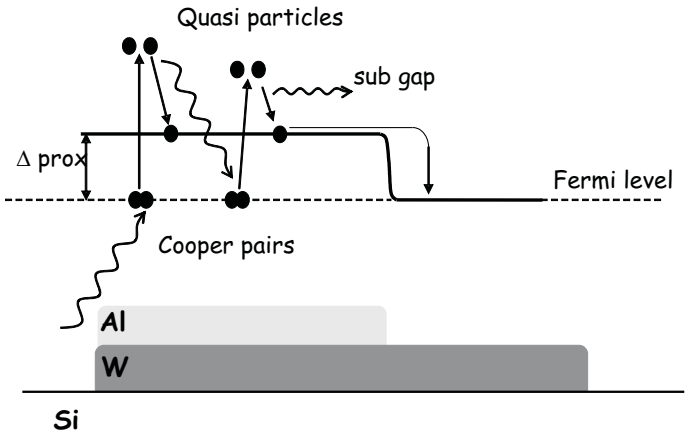

Figure 3.2: Schematic view of the working principle of phonon collectors. Figure in the top shows energy diagram for Al/W bilayer. An absorbed non-thermal phonon of energy $> 2\Delta_{prox}$ breaks a Cooper pair. The two excited quasi-particles relax towards the gap edge via emission of phonons. The emitted phonon with energy $> 2\Delta_{prox}$ will break more Cooper pairs, while the sub gap phonon is emitted back to substrate (Si in figure). Excited quasi-particles propagate diffusively through the bilayer to the tungsten film where they transfer their energy to the W electron system. Figure in the bottom shows a cross section of a Al/W bilayer.

Absorption in phonon collectors

If a non-thermal phonon of energy greater than twice the energy gap (2Δ) is absorbed in the bilayer it will break Cooper pairs and form excited quasi particles. The average phonon energies in the relevant time interval are $\bar{E}_p = h\bar{\nu} \approx 2.5\,\mathrm{meV}$ and $\bar{E}_p \approx 1.5\,\mathrm{meV}$ for sapphire and silicon respectively. The energy gap at $T = 0$ for aluminium, according to the BCS theory, is $\Delta_{Al}(T = 0) = 3.52\, k_B T_c(Al)/2 \approx 0.18\,\mathrm{meV}$, while the band gap of the proximity bilayer (Δ_{prox}) is smaller than the band gap of pure aluminium [Solymar, 1972].
The thickness of the superconducting layer needed to efficiently absorb all transmitted phonons can be estimated knowing the velocity of sound averaged over modes and the lifetime of a phonon of energy E_p due to absorption with pair breaking in the material [Kaplan et al., 1976]. In the case of pure aluminium the mean free path of phonons of energy $E_p = 2.5\,(1.5)\,\mathrm{meV} \approx 14\,(8)\Delta_{Al}$ is estimated[11] to be about $1.8\,(3.0)\,\mathrm{kÅ}$; therefore a $10\,\mathrm{kÅ}$ thick aluminium film is expected to absorb all transmitted phonons.

[11]For phonons of energy $E_p = 14\,(8)\Delta_{Al}$ the lifetime due to absorption with pair breaking is about 53(88) ps [Kaplan et al., 1976] and the group velocity averaged over modes is $3436\,\mathrm{m{\cdot}s^{-1}}$.

Quasi-particles relaxation

The quasi-particles produced after the absorption of non-thermal phonons are well above the gap edge of the bilayer ($\bar{E}_{qp} \approx (\bar{E}_p - 2\Delta_{Al})/2 \gtrapprox (3-6)\Delta_{prox}$). These highly excited quasi-particles quickly relax towards the gap edge through the emission of phonons. A detailed formulation of the rate of spontaneous phonon emission can be found in [Kaplan et al., 1976].
In the specific case of aluminium, the excited quasi-particles do not come into equilibrium with the lattice temperature within a few hundred microseconds. This is due to the slow rate of spontaneous phonon emission in aluminium in particular as the energies of the quasi-particles approach the gap edge.
As long as the energy of the emitted phonons is greater than twice the gap of the superconducting bilayer, they can break more Cooper pairs generating more quasi-particles. Once the energy of the relaxation phonons is smaller than $2\Delta_{prox}$, they cannot break pairs anymore and are re-emitted into the absorber. As a consequence, approximately half the initial energy transmitted by non-thermal phonons is lost due to sub-gap phonons.
In the process of recombination one quasi-particle combines with another one to form a pair with the emission of a phonon with energy $\geq 2\Delta_{prox}$. The recombination phonons with energy grater than $2\Delta_{prox}$ can interact with Cooper pairs and create new quasi-particles [Rothwarf & Taylor, 1967]. This increases the effective life time of quasi-particles. At temperatures well below the transition temperature of the superconductor the process of recombination is negligible [Kaplan et al., 1976]. On the other hand quasi-particle recombination has to be taken into account during the diffusion due to the possibility of trapping in sites of a reduced energy gap (e.g. caused by the presence of lattice defects or impurities) where the density of quasi-particles can be locally enhanced. In this condition the recombination of a pair would in fact lead to the emission of sub-gap phonons that are lost.
The life time of quasi-particles has been found to be extremely sensitive to film properties [Loidl et al., 2001]. Therefore, a high quality of the aluminium/tungsten bilayer which gives a fast diffusion is fundamental.

Quasi-particles diffusion

Quasi-particles excited above the gap edge have a non-vanishing group velocity v_g that allows a diffusive propagation through the film. The group velocity of quasi-particles decreases as their energy approaches the gap energy. In the limit of quasi-particles in thermal equilibrium at the detector operating temperature, that means at a temperature much lower than the transition temperature of the bilayer, the average group velocity is given in Narayanamurti et al. [1978] as

$$\langle v_g^2 \rangle \approx \frac{T}{T_c} v_F^2 \,, \tag{3.29}$$

where v_F is the Fermi velocity. Because of the long time needed for quasi-particles to relax to thermal equilibrium, the velocity given in equation 3.29 represents the lower limit for the quasi-particles group velocity that is not reached within the time scale of interest.
The quasi-particle diffusion length l_{diff} is defined by the diffusion constant D and the effective lifetime τ_q of the quasi-particles as

$$l_{diff} \sim \sqrt{D\tau_q}\,. \tag{3.30}$$

The diffusion constant, in turn, depends on the quasi-particle mean free path l_q

$$D = \frac{\langle v_g \rangle l_q}{3}\,. \tag{3.31}$$

The effective mean free path of quasi-particles is determined by the elastic scattering on impurities and lattice defects and, in the case of a film thickness comparable to l_q, by the scattering on the film surfaces.
Measurements of the quasi-particle diffusion length in an aluminium-tungsten bilayer deposited on a sapphire substrate have yielded a result of $l_{diff} \approx 1.5\,mm$[12]. The Al/W bilayer used for the measurements showed a single crystalline structure and a diffusion without significant losses has been measured over a distance of 2 mm. It is important to note, that in a superconducting film of polycrystalline structure both the quasi-particle lifetime and the diffusion constant are strongly reduced.
Once the quasi-particles have diffused into the tungsten thermometer, the energy gap of which vanishes at the transition temperature, they relax releasing their energy to the electron system of the thermometer raising its temperature. For the correct functioning of phonon collectors, a good metallic contact with the thermometer is needed. The use of aluminium-tungsten bilayers allows a good contact avoiding at the same time the structural defects in the superconducting diffusion film that are expected if it grows over the edges of the thermometer only partially overlapping the tungsten film.
As already mentioned, phonon collectors are used to enhance the sensitivity of thermometers used for light detectors. The diffusion length of quasi-particles defines the maximum size of phonon collectors. Thus, they are designed to have rectangular shape with a maximum length for diffusion of less than 1 mm. With phonon collectors employed, the quasi-particle diffusion time contributes to the light detector response time. Hence, the rise time of the non-thermal component is determined by both the phonon collection time and the quasi-particle diffusion time.

[12] A value of $D = 2.46\text{x}10^{-4} m^2/s$ and a quasi-particle lifetime of 9 ms have been found [Loidl, 1999, Loidl et al., 2001].

3.3 Noise and energy resolution

The energy resolution of a cryogenic detector is strongly affected by various noise sources. In order to optimize the design of the detector and to understand its performance it is very important to evaluate its noise, which is intimately connected to its thermal properties. Therefore, the theory of noise in bolometers and microcalorimeters is usually discussed within the detector thermal model[13].

3.3.1 Basic thermometer model

At low operating temperatures, due to the phonon-electron decoupling, the electron system of the thermometer can be considered separately from the phonon system of the thermometer and the absorber. A schematic view of the thermal and electrical circuit of the thermometer is shown in figure 3.3.

The thermal equation of the electron system without noise terms is given by

$$C_e \frac{dT_e}{dt} + P_{link}(T_e, T_{bath}) = P_e + P_{bias} + P_{heater}\,, \tag{3.32}$$

where C_e is the electronic heat capacity, T_e is the temperature of electrons, P_{link} is the power output to the cold bath, P_e is the external power input, P_{bias} is the Joule heating dissipated in the thermometer by the readout current I_f and P_{heater} is the Joule heating injected by the heater of the thermometer.

The functional form of the power output to the cold bath through the weak link is

$$P_{link}(T_e, T_{bath}) = \Pi(T_e^n - T_{bath}^n)\,, \tag{3.33}$$

where Π is a parameter dependent on the material and on the geometry of the link and n is a parameter depending on the type of coupling involved. In the CRESST devices the thermal link is provided by a gold wire or film and in this case n is equal to two[14].

The thermal conductance of the weak link is thus given by

$$G_{eb} \equiv \frac{dP_{link}}{dT_e} = n\Pi {T_e}^{n-1}. \tag{3.34}$$

According to the bias circuit of figure 3.3 (see also equation 2.1), the bias power is given by

$$P_{bias} = R_f(T_e) {I_f}^2 = \frac{R_f(T_e) {R_s}^2}{(R_f(T_e) + R_s)^2} {I_0}^2\,, \tag{3.35}$$

[13]The theory of noise for a basic model of bolometers and microcalorimeters is given in Mather [1982] and Moseley et al. [1984]. Noise analyses for some particular cases of complex microcalorimeters and bolometers can be found in Enss [2005], Galeazzi & McCammon [2003] and Figueroa-Feliciano [2006].

[14]For the case of free electrons the specific thermal conductivity (k) is proportional to the specific heat capacity (c_V) [Kittel, 1967]. Since for electrons $c_V \propto T$ and thus $k \propto T$, the power is then $P = \int k dT \propto T^2$.

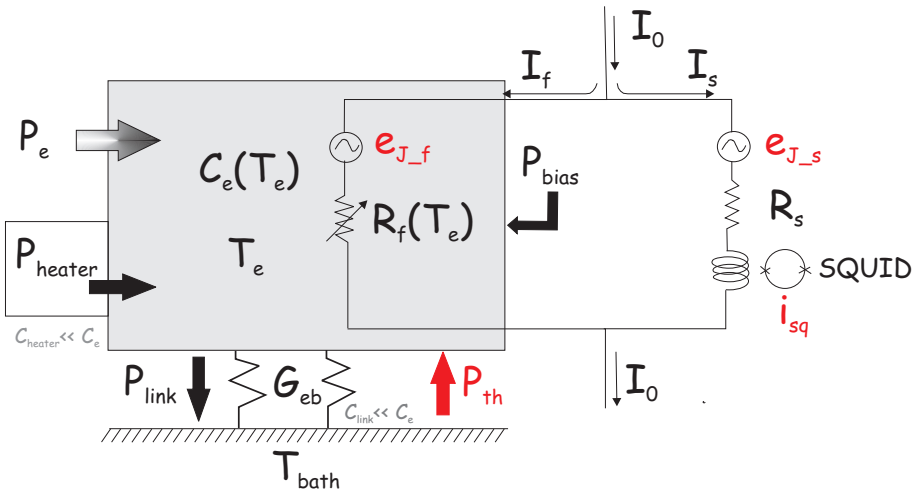

Figure 3.3: Schematic view of the thermal and electrical circuit of the thermometer. The thermometer (shaded rectangle) is characterized by the resistance R_f and the heat capacity of the electron system C_e. The biasing circuit provides the current I_f. The Joule heating from the bias current is represented as P_{bias}. P_{heater} is the Joule heating dissipated in the heater that is used to keep the thermometer at the correct operating point. The external power input (due to an event) into the thermometer is given as P_e. P_{link} is the power flow to the heat bath at temperature T_{bath} through the thermal link with a heat conductance G_{eb}. The major noise sources are drawn in red. They consist of thermal noise (P_{th}), Johnson noise of the film and shunt resistors (e_{J_f},e_{J_s}) and SQUID noise (i_{sq}). The contribution due to the inductance of the SQUID input coil is not considered.

where the thermometer resistance is taken to be only a function of its temperature[15]. The Joule heating from the heater, assuming that it is entirely absorbed in the thermometer, is simply

$$P_{heater} = R_{heater} {I_{heater}}^2 , \tag{3.36}$$

where R_{heater} and I_{heater} are the heater resistance and current.
With a constant bias and heater current and assuming no external power input, the thermometer will reach equilibrium at a temperature higher than the bath temperature. Thus, in a steady state the bias and heater power inputs are balanced by the power flow to the heat bath

$$P_{bias} + P_{heater} = P_{link} . \tag{3.37}$$

[15]The thermometer resistance may also depend on the bias current $R(T, I)$ due to critical current effects (non-ohmic thermometer behavior).

Assuming a small excursion from the equilibrium temperature ($\Delta T_e \ll T_e$) equation 3.32 can be linearized by Taylor expansion to first order in ΔT_e as

$$C_e \frac{d\Delta T_e}{dt} + P_{link} + G_{eb}\,\Delta T_e = P_e + P_{bias} - {I_f}^2 \frac{dR_f}{dT_e}\frac{R_f - R_s}{R_f + R_s}\Delta T_e + P_{heater}\,. \quad (3.38)$$

Then from equations 3.37 and 3.38 it follows

$$C_e \frac{d\Delta T_e}{dt} + G_{eb}\Delta T_e = P_e - {I_f}^2 \frac{dR_f}{dT_e}\frac{R_f - R_s}{R_f + R_s}\Delta T_e\,. \quad (3.39)$$

The solution of this equation, as in the case of a simple calorimeter model (see equation 1.16), is an exponential with the effective time constant given by

$$\tau_{eff} = \frac{C_e}{G_{eb} + {I_f}^2 \frac{dR_f}{dT_e}\frac{R_f - R_s}{R_f + R_s}} = \frac{\tau_{in}}{1 + \frac{{I_f}^2}{G_{eb}}\frac{dR_f}{dT_e}\frac{R_f - R_s}{R_f + R_s}}\,, \quad (3.40)$$

where $\tau_{in} \approx C_e/G_{eb}$ is the intrinsic time constant of the thermometer when the coupling to the absorber G_{ea} is neglected (see equation 3.24).
According to equation 3.40 the effective time response of the thermometer is influenced by the ratio of R_f to R_s and the slope of the R_f vs. T_e curve, that is always positive for SPT thermometers. The sensitivity of the thermometer is commonly parameterized with a dimensionless parameter α, that takes into account both the slope of the transition and T_e/R_f ratio as

$$\alpha \equiv \frac{T_e}{R_f}\frac{dR_f}{dT_e}\,. \quad (3.41)$$

For the same slope $\mathrm{dR_f/dT_e}$ parameter α shows an increase towards the bottom of transition curve[16]. In the small signal approximation, the transition curve is assumed to be locally linear so both the slope and α are constant for the chosen operating point.

Electro-thermal feedback

As it can be seen from equation 3.40, for $R_f \gg R_s$[17] the effective time constant is shorter than the intrinsic one. In this mode of operation, generally referred to as negative electro-thermal feedback, the external input power that warms up the thermometer and raises its resistance is removed by a reduction in Joule heating due to decrease of the current passing through the thermometer. In this

[16] The behavior of R with dependence on T and I can be then characterized by two parameters as $\alpha_T = \alpha \equiv \frac{T}{R}\frac{\partial R(T,I)}{\partial T}$ and $\alpha_I \equiv \frac{I}{R}\frac{\partial R(T,I)}{\partial I}$.

[17] If the resistance of R_s is small compared to R_f the circuit biases the thermometer with a near constant voltage bias (voltage biased thermometer) .

way the thermometer returns faster to its equilibrium and the total power in the thermometer and the bias voltage are kept constant.

For $R_f \ll R_s$[18] the effective time constant is longer than the intrinsic one. During an event the Joule heating is increased in proportion to the temperature excursion and is added to the external power (see equation 3.39). In this so-called positive electro-thermal feedback mode the current through the thermometer is kept constant.

For $R_f = R_s$ there is no feedback, the effective time constant is the intrinsic one and the Joule heating dissipated in the thermometer remains constant during an event.
For simplicity the term

$$I_f{}^2 \frac{dR_f}{dT_e} \frac{R_f - R_s}{R_f + R_s} \equiv G_{ETF}\,, \tag{3.42}$$

is defined as electro-thermal feedback term. It has the same units as thermal conductance and acts as a parallel conductance to G_{eb}.
The strength of the electro-thermal feedback depends on the bias power, on the slope of the transition curve (R vs. T) and on the ratio of thermometer and reference resistors.
The CRESST detectors are operated at a weak negative electro-thermal feedback ($R_f \gtrapprox R_s$). The small bias current of a few μA used to read out the detectors does not lead to a significant increase of the thermometer temperature. It is important to note again that the CRESST detectors are stabilized at their operating points with the help of the heater power and not with the bias power in which case a stronger ETF would take place[19].

Frequency domain

The noise is generally characterized by the noise power spectrum and therefore the following discussion is done in the frequency domain. The block diagram formalism of the control theory, which is used here, is a useful tool in modelling the frequency response of the detector keeping at the same time the physics of the model clear [Galeazzi & McCammon, 2003].
In the frequency domain equation 3.39 reads

$$\imath\omega C_e\, \Delta T_e(\omega) + G_{eb}\, \Delta T_e(\omega) = P_e(\omega) - G_{ETF}\, \Delta T_e(\omega)\,, \tag{3.43}$$

[18] In this case the reference resistor R_s provides a current bias for the film (current biased thermometer).

[19] Many groups operate the SPT thermometers in a voltage bias mode, without additional heaters. These detectors are then stabilized in the operating points above the temperature of the heat sink with the help of bias power. This results in a strong negative electro-thermal feedback and effective pulse shortening that allows an increase of the acceptable count rate [Irwin, 1995], which is not a consideration of the CRESST experiment.

The left-hand side of equation 3.43 represents the response of the thermometer, while the right-hand part is the input to the thermometer. The right side term that depends on the output (ΔT_e) is the feedback term. The solution of equation 3.43 is

$$\Delta T_e(\omega) = \frac{1}{G_{eb} + G_{ETF}} \frac{1}{1 + \imath\omega\tau_{eff}} P_e(\omega)\,. \tag{3.44}$$

The thermometer behaves as a low pass system with one pole[20] in the frequency response corresponding to the time constant τ_{eff}. Without the feedback term the thermometer would behave as a low pass system with a response with the time constant τ_{in}.

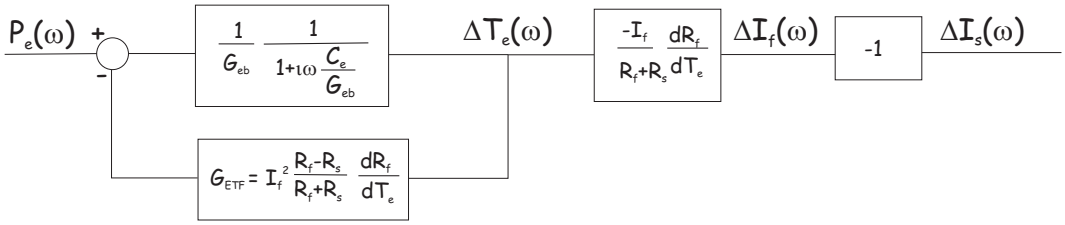

Figure 3.4: Block diagram representation of the thermometer.

The block diagram of the thermometer system, described by equation 3.43, is shown in figure 3.4. The conversion of the temperature variation ΔT_e via resistance variation and film current variation to ΔI_s, that is read out by the SQUID is also represented in the diagram (see equations 2.1 - 2.3). Then from the block diagram it follows

$$\Delta I_s(\omega) = \underbrace{\frac{1}{G_{eb} + G_{ETF}} \frac{1}{1 + \imath\omega\tau_{eff}} \frac{I_f}{R_f + R_s} \frac{dR_f}{dT_e}}_{S(\omega)} P_e(\omega)\,, \tag{3.45}$$

where $S(\omega)$ is the responsivity which is defined as the current signal measured for a given power input into the thermometer ($S(\omega) = d\Delta I_s/dP_e$).
The responsivity of the thermometer determines its theoretical spectral response to an arbitrary signal power input or to the noise power input that is introduced in the same way.
The inclusion of the different noise sources allows to estimate the size and spectral shape of the output current noise and to calculate the theoretical energy resolution of the modelled system. The output current power spectrum for a certain noise source $N(\omega)$, given as the average of the magnitude of the noise, is

$$\langle|\Delta I_N(\omega)|^2\rangle = \langle|\frac{d\Delta I_{th}(\omega)}{dN} N(\omega)|^2\rangle \qquad \left[\frac{A^2}{Hz}\right]\,. \tag{3.46}$$

[20] P_e is assumed to be instantaneous. In reality the finite time of incoming power would lead to the appearance of a second pole.

The noise, as well as the actual signal, is assumed to be a small signal so that a linear approximation is valid (see equation 3.38). The noise sources are assumed to be uncorrelated and the total output noise is found by simply adding them quadratically.

3.3.2 Noise sources

The major noise sources are shown in the block diagram of figure 3.5. They include the thermal noise due to the thermal link between the detector and the heat sink, the Johnson noise of the thermometer, the Johnson noise of the reference resistor used in the bias circuit, the noise of the read-out electronics (SQUID) and the 1/f noise introduced by the thermometer.

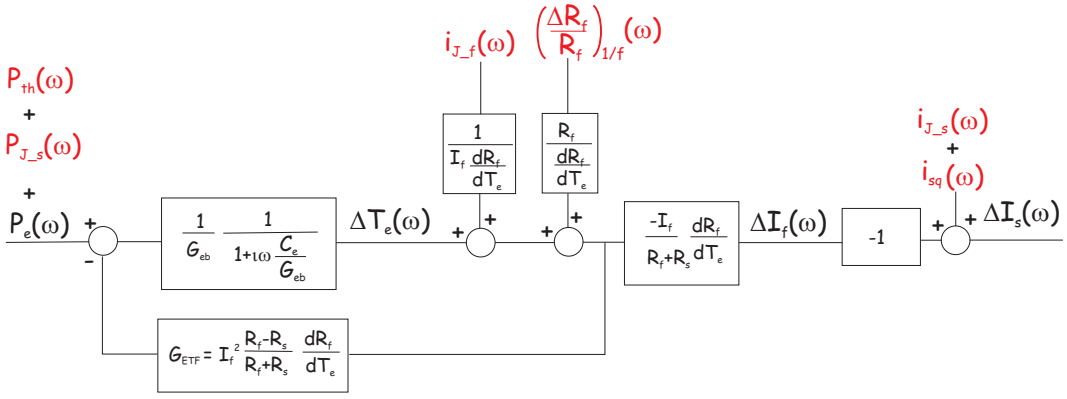

Figure 3.5: Block diagram representation of the thermometer with the various noise sources.

Thermal noise

Thermal noise (also referred to as phonon noise or Thermal Fluctuation Noise - TFN) is caused by statistical fluctuations in the energy content of the detector due to the random propagation of the energy carriers (electrons, phonons etc.) trough the thermal link between the detector and the heat bath. The thermal noise determines the ultimate limit of the achievable energy resolution because it represents a constant background noise against which the energy deposition caused by an event must be measured.
In thermal equilibrium, where the temperature of the detector is equal to the bath temperature, the amplitude of the statistical fluctuations ΔE scales as $\sqrt{C}$ (see equation 1.18) and the measured temperature signal ΔT as $1/\sqrt{C}$. It follows that the contribution of the thermal noise is more relevant for sensors

with a small heat capacity[21].
The power spectrum of the thermal noise is white with a spectral density at thermal equilibrium ($T_e = T_{bath}$) given by

$$ {P_{th\_eq}}^2 = 4k_B {T_e}^2 G_{eb} \quad \left[\frac{W^2}{Hz}\right]. \tag{3.47} $$

For a steady state, where the detector is at a higher temperature than the heat bath, the spectral density of the thermal noise depends on the thermal link properties. Assuming a diffusive thermal conductivity of the link[22] the power spectral density is given by Mather [1982] as

$$ {P_{th}}^2 = 4k_B {T_e}^2 G_{eb} \frac{2}{5} \frac{1-(\frac{T_{bath}}{T_e})^5}{1-(\frac{T_{bath}}{T_e})^2} \quad \left[\frac{W^2}{Hz}\right] \quad (T_e > T_{bath}). \tag{3.48} $$

The thermal noise appears in the form of a power component that is introduced together with the signal (P_e), as shown in figure 3.5. Therefore, the theoretical output current noise induced by P_{th} is

$$ \begin{aligned} \langle|\Delta I_{th}(\omega)|^2\rangle &= \langle|\frac{d\Delta I_{th}(\omega)}{dP_{th}} P_{th}(\omega)|^2\rangle = \langle|S(\omega)\, P_{th}(\omega)|^2\rangle \\ \langle|\Delta I_{th}(\omega)|^2\rangle &= \frac{1}{(G_{eb}+G_{ETF})^2} \frac{1}{1+\omega^2 {\tau_{eff}}^2} \left(\frac{I_f}{R_f+R_s}\right)^2 \left(\frac{dR_f}{dT_e}\right)^2 {P_{th}}^2 . \end{aligned} \tag{3.49} $$

The detector response to thermal noise is expected to have one pole related to τ_{eff}.

Johnson noise of the thermometer

Johnson noise appears as fluctuations in the voltage across a resistor due to the random motion of the electrical charges inside the resistor. The power spectrum of Johnson noise is expressed as

$$ {e_J}^2 = 4k_B T R \quad \left[\frac{V^2}{Hz}\right], \tag{3.50} $$

where T and R are temperature and resistance of the resistor respectively.
If the electro-thermal feedback of the circuit is neglected, the Johnson noise of the

[21] This is the case of light detector used in CRESST.

[22] In the diffusive limit the mean free path of the energy carriers is small compared to the length of the link. For the CRESST detectors the energy carriers are free electrons. Their mean free path at millikelvin temperatures depends on both the gold film (wire) quality and thickness and is of the order of few hundred Angstroms. This is small compared to the typical length ($\approx$ mm) of the thermal link.

thermometer itself (e_{J_f}) is modelled as a voltage fluctuation term in series with R_f that directly adds to the output current. Taking into account the ETF, the Johnson noise of the thermometer, being an integral part of the thermometer, is included in the feedback circuit [Galeazzi & McCammon, 2003]. Therefore the Johnson noise is modelled as voltage fluctuations, further read out by the circuit, but at the same time seen by the feedback as temperature fluctuations of the electron system (see figure 3.5). These temperature fluctuations have a mean value of zero and so can not affect the temperature of the thermometer. According to the block diagram the resulting output current is

$$\Delta I_{J\_f}(\omega) = e_{J\_f}\,\frac{1}{I_f\frac{dR_f}{dT_e}}\left(1-\frac{G_{ETF}}{G_{eb}+G_{ETF}}\,\frac{1}{1+\imath\omega\tau_{eff}}\right)\frac{I_f}{R_f+R_s}\,\frac{dR_f}{dT_e}\,. \quad (3.51)$$

It follows

$$\frac{d\Delta I_{J\_f}\omega)}{de_{J\_f}} = \frac{1}{R_f+R_s}\,\underbrace{\frac{G}{G_{eb}+G_{ETF}}}_{\tau_{eff}/\tau_{in}}\,\frac{1+\imath\omega\tau_{in}}{1+\imath\omega\tau_{eff}}\,, \quad (3.52)$$

$$\langle|\Delta I_{J\_f}(\omega)|^2\rangle = \frac{4k_BT_eR_f}{(R_f+R_s)^2}\left(\frac{\tau_{eff}}{\tau_{in}}\right)^2\frac{1+\omega^2{\tau_{in}}^2}{1+\omega^2{\tau_{eff}}^2}\,. \quad (3.53)$$

The detector response to the Johnson noise has one zero and one pole corresponding to τ_{in} and τ_{eff} respectively.

Johnson noise of the reference resistor

The white Johnson noise of the reference resistor R_s shows directly in the output current and can be modelled as a voltage fluctuation (e_{J_s}) term, in series with R_s, which produces a current fluctuation in the SQUID branch given by

$${i_{J\_s}}^2 = \frac{(e_{J\_s})^2}{(R_f+R_s)^2} = \frac{4k_BT_sR_s}{R_f+R_s} \quad \left[\frac{A^2}{Hz}\right], \quad (3.54)$$

where T_s is the temperature of the reference resistor. In addition the thermometer exhibits a Joule heating dissipation, due to the work done by the bias current on the Johnson noise of the reference resistor, with the form[23]

$$P_{J\_s} = -2I_fR_fi_{J\_s} = -\frac{2I_fR_fe_{J\_s}}{R_f+R_s}\,. \quad (3.55)$$

Summing both Johnson noise contributions of the reference resistors and solving the block diagram shown in figure 3.5, one obtains

$$\Delta I_{J\_s}(\omega) = i_{J\_s} - 2I_fR_f\,i_{J\_s}\,\frac{1}{G_{eb}+G_{ETF}}\,\frac{1}{1+\imath\omega\tau_{eff}}\,\frac{I_f}{R_f+R_s}\,\frac{dR_f}{dT_e}\,. \quad (3.56)$$

[23]The current fluctuations due to the Johnson noise of the reference resistor induce fluctuations of I_f and consequently a change in the Joule heating dissipation in the detector which can be written as $\Delta P_{bias} = 2I_f\Delta I_fR_f = -2I_f\,i_{J\_s}R_f$.

The derivative and the output current noise are then

$$\frac{d\Delta I_{J\_s}\omega)}{de_{J\_s}} = \frac{1}{R_f + R_s}\,\frac{\tau_{eff}}{\tau_{in}}\,\frac{1 - \frac{I_f^2}{G_{eb}}\frac{dR_f}{dT_e} + \imath\omega\tau_{in}}{1 + \imath\omega\tau_{eff}}\,, \tag{3.57}$$

$$\langle|\Delta I_{J\_s}(\omega)|^2\rangle = \frac{4k_B T_s R_s}{(R_f + R_s)^2}\left(\frac{\tau_{eff}}{\tau_{in}}\right)^2 \frac{\left(1 - \frac{I_f^2}{G_{eb}}\frac{dR_f}{dT_e}\right)^2 + \omega^2{\tau_{in}}^2}{1 + \omega^2{\tau_{eff}}^2}\,. \tag{3.58}$$

SQUID noise

Josephson junctions of dc SQUIDs have thin film shunt resistors in parallel. Their Johnson noise current affects the performances of the device by generating a white flux noise in the SQUID loop. The output current power spectrum is white and can be written as

$$\langle|\Delta I_{sq}(\omega)|^2\rangle = {i_{sq}}^2\,. \tag{3.59}$$

The dc SQUIDs used for the CRESST experiment exhibit an average noise level of i_{sq}=1.2 pA/$\sqrt{\text{Hz}}$ [Henry et al., 2007].

1/f noise

The model described here considers the ideal 1/f noise (the spectral density of which is proportional $\sqrt{1/f}$) introduced by the thermometer[24], that is described as a fluctuation in the value of the film resistance [Galeazzi & McCammon, 2003]

$$\left(\frac{\Delta R_f}{R_f}\right)_{1/f} \propto \frac{1}{\sqrt{\omega}} \quad \left[\frac{1}{\sqrt{Hz}}\right]. \tag{3.60}$$

From the block diagram 3.5 the response of the thermometer to the 1/f noise is given by

$$\langle|\Delta I_{1/f}(\omega)|^2\rangle = \frac{{I_f}^2{R_f}^2\left(\frac{\Delta R_f}{R_f}\right)^2_{1/f}}{(R_f + R_s)^2}\left(\frac{\tau_{eff}}{\tau_{in}}\right)^2 \frac{1 + \omega^2{\tau_{in}}^2}{1 + \omega^2{\tau_{eff}}^2}\,. \tag{3.61}$$

Additional noise terms

All noise spectra of the different noise terms listed above have a pole corresponding to the time constant $\tau_{squid} = L/R_{eq}$ of the bias circuit, where L is the inductance of the input circuit L_{in} plus any stray inductance and R_{eq} is the

[24]The 1/f noise can also be introduced by the SQUID.

equivalent of the two resistances R_f and R_s[25]. Additional poles in the noise spectra appear due to electronics (see subsection 2.4.2).
A more detailed noise analysis would have to take into account the complex structure of the detector. As shown in figure 3.1, a complex calorimeter consists of three weakly coupled thermal subsystems: the phonon system of the absorber, the phonon system and the electron system of the thermometer. The power fluctuations between these subsystems introduce more noise terms (Internal Thermal Fluctuation Noise - ITFN), that are not considered here. Any non-ohmic behaviour of the thermometer is neglected as well.
In addition, external disturbances like temperature fluctuations of the heat bath or vibrations and electrical interferences that reach the detector can show up as noise in the detector response. These external noise sources can be strongly reduced by a careful design of the experimental setup and by an active control of the temperature.

3.3.3 Energy resolution

The noise contribution to the detector performance is usually expressed in terms of Noise Equivalent Power (NEP).
The NEP is defined as the equivalent input power $P_e(\omega)$ to the detector that would produce the same output $\Delta I_N(\omega)$ as generated by the noise $N(\omega)$. Following equations 3.45 and 3.46, NEP can be written as

$$\Delta I_N(\omega) = S(\omega) NEP_N(\omega) \quad \mapsto \quad NEP_N(\omega) = \frac{\frac{d\Delta I_N}{dN}}{S(\omega)} N(\omega)\,, \tag{3.62}$$

where $S(\omega)$ is the reponsivity of the thermometer given in the equation 3.45. Since the noise sources are assumed to be uncorrelated, the total NEP is the sum in quadrature of the individual noise terms

$$\begin{aligned} NEP^2_{total}(\omega) &= NEP^2_{th}(\omega) + NEP^2_{J\_f}(\omega) + NEP^2_{J\_s}(\omega) + NEP^2_{sq}(\omega), \\ &= P^2_{th}(\omega) + \frac{1+\omega^2{\tau_{in}}^2}{\left(\frac{I_f}{G_{eb}}\frac{dR_f}{dT_e}\right)^2}{e_{J\_f}}^2 + \frac{\left(1-\frac{I_f^2}{G_{eb}}\frac{dR_f}{dT_e}\right)^2+\omega^2{\tau_{in}}^2}{\left(\frac{I_f}{G_{eb}}\frac{dR_f}{dT_e}\right)^2}{e_{J\_s}}^2 \\ &\quad + \frac{1+\omega^2{\tau_{eff}}^2}{\left(\frac{I_f}{G_{eb}+G_{ETF}}\frac{dR_f}{dT_e}\frac{1}{R_f+R_s}\right)^2}{i_{sq}}^2\,. \end{aligned} \tag{3.63}$$

The total NEP can be used to calculate the theoretical energy resolution, that depends on both the various noise contributions and the algorithm used for the

[25]The stray inductance leads to an increase of the total circuit inductance and of τ_{squid}. This results in a decrease of the frequency of the pole corresponding to τ_{squid}. On the other hand the feedback coil of the squid can effectively shorten the inductance of L_{in}.

data analysis. The NEP is related to the best possible energy resolution [Moseley et al., 1984] as

$$\Delta E_{rms} = \left(\sqrt{\int_0^\infty \frac{4df}{NEP_{total}(f)^2}} \right)^{-1} , \tag{3.64}$$

where $f{=}\omega/2\pi$. This relation gives the ΔE_{rms} for the estimate of the energy E, calculated with the ¨optimal filter method¨ [Szymkowiak et al., 1993].
In the optimal filter method all pulses are assumed to have the same shape given by a template event. This assumption is valid in the small pulse limit where the detector response is linear[26]. The optimal filtering method involves a least square fit in frequency space of the actual event to the template event, where the fit is weighted by the standard deviation of the noise at each frequency. The amplitude estimate of the event by the optimal filter is truly optimal if the noise is only a function of frequency (stationary noise).
In the CRESST experiment the amplitude of the event is determined by a template fit in the time domain (see chapter 4.2.1). This is equivalent to the optimal filtering method when only white noise sources are considered.
The actual energy resolution may differ from the optimal one, not only due to the presence of non-white noise terms but as well due to the limitations of the noise model presented here and due to presence of the non-stationary noise. Nevertheless, ΔE_{rms} from equation 3.64 can be considered as a good approximation of the actual energy resolution.
The integral in equation 3.64 can be solved analytically for the case of white noise sources (P_{th}, e_{J_f}, e_{J_s} and i_{SQUID}), using the following integral

$$\int_0^\infty \frac{4df}{A + B(2\pi f)^2} = \frac{1}{\sqrt{AB}} . \tag{3.65}$$

From equation 3.63 it follows,

$$A = P_{th}^2 + \frac{{e_{J\_f}}^2 + {e_{J\_s}}^2 \left(1 - \frac{I_f^2}{G_{eb}} \frac{dR_f}{dT_e}\right)^2 + {i_{sq}}^2 (R_f + R_s)^2 \left(1 + \left(\frac{G_{ETF}}{G_{eb}}\right)^2\right)}{\left(\frac{I_f}{G_{eb}} \frac{dR_f}{dT_e}\right)^2} \tag{3.66}$$

and

$$B = \frac{{C_e}^2 ({e_{J\_f}}^2 + {e_{J\_s}}^2 + {i_{sq}}^2 (R_f + R_s)^2)}{\left(I_f \frac{dR_f}{dT_e}\right)^2} . \tag{3.67}$$

Substituting the values for noise spectral densities from equations 3.48, 3.50 and 3.59, the theoretical energy resolution in terms of the full width at half maximum

[26]The pulse shape in the linear region can differ due to position dependence of the detector response. In the case of CRESST light detectors this effect can be neglected since only slight position dependence has been observed [Petricca, 2005][Frank, 2002]

(FWHM) is given by

$$\Delta E_{FWHM} = 2.355 \sqrt{\frac{4k_B T_e C_e R_f G_{eb}}{\left(I_f \frac{dR_f}{dT_e}\right)^2} \sqrt{\left(1+\frac{T_s R_s}{T_e R_f}+\frac{{i_{sq}}^2 (R_f+R_s)^2}{4k_B T_e R_f}\right)}} \times \sqrt[4]{1+\frac{T_s R_s}{T_e R_f}\left(1-\frac{I_f^2}{G_{eb}}\frac{dR_f}{dT_e}\right)^2+\frac{{i_{sq}}^2 (R_f+R_s)^2}{4k_B T_e R_f}\left(1+\left(\frac{G_{ETF}}{G_{eb}}\right)^2\right)+\frac{2}{5}\frac{1-\left(\frac{T_{bath}}{T_e}\right)^5}{1-\left(\frac{T_{bath}}{T_e}\right)^2}\frac{{I_f}^2\left(\frac{dR_f}{dT_e}\right)^2 T_e}{R_f G_{eb}}}. \tag{3.68}$$

Signal-to-noise ratio

The signal-to-noise ratio (SNR) is the most relevant parameter for the characterization of detectors. In the frequency domain SNR is defined as

$$SNR(\omega) = \left|\frac{\Delta I_{signal}(\omega)}{\Delta I_{N\_total}(\omega)}\right|. \tag{3.69}$$

Including thermal noise, Johnson noise of the film and reference resistor, according to equations 3.45, 3.49, 3.53 and 3.58, SNR is given by

$$SNR(\omega) = \frac{P_e(\omega)\frac{I_f}{G_{eb}}\frac{dR_f}{dT_e}}{\sqrt{\left(P_{th}\frac{I_f}{G_{eb}}\frac{dR_f}{dT_e}\right)^2 + {e_{J\_f}}^2(1+\omega^2{\tau_{in}}^2) + {e_{J\_s}}^2\left(\left(1-\frac{I_f^2}{G_{eb}}\frac{dR_f}{dT_e}\right)^2+\omega^2{\tau_{in}}^2\right)}}. \tag{3.70}$$

It follows that the SNR is independent of R_s and therefore of the electro-thermal feedback.

The comparison of the measured and the modelled noise spectra will be presented in the last chapter.

Chapter 4

Detector operation and data analysis

In this chapter the main experimental procedures for the detector operation and an introduction to the data analysis techniques are described.

4.1 Detector operation

For the operation of the CRESST cryogenic detector it is important to start with recording a transition of the thermometer from the normal conducting to the superconducting state in order to choose a suitable operating point. The stability of the operating point is controlled through heater pulses which are injected into the thermometer via its film heater. The energy calibration in the relevant energy range is obtained by extrapolation from the photopeak of a γ calibration source with heater pulses of different energies. Furthermore the heater pulses are injected constantly during the whole data taking in order to monitor the energy calibration when there is no calibration source installed.

4.1.1 Transition curve measurements

A measurement of the transition of the thermometer from the normal conducting to the superconducting state represents the first step in characterizing the performance of the individual detectors. The width of the phase transition in temperature, which defines the dynamical range of the thermometer, and the slope of the transition curve, which affects the sensitivity of the thermometer, are directly obtained from the measured transition curve.
Transition curve measurements are performed by measuring the SQUID output for a fixed bias current, as a function of the temperature in a neighborhood of the transition temperature of the film. In order to keep the power applied to the thermometer constant during the measurements, the bias current is switched

from $-I_0$ to $+I_0$ and half of the corresponding change of the SQUID output step represents a point of the transition curve for a bias current I_0 . This is done by feeding a square wave voltage, low pass filtered in order not to exceed the slew rate of the SQUID, to the input of the current source.
In the CRESST experiment two methods for recording transition curves are commonly used: temperature sweeps using heaters at the base plate of the cryostat (heat sink temperature sweeps) or at the detector itself (heater sweeps). Heat sink temperature sweeps of the thermometers are measurements of resistance versus temperature, where the film temperature is controlled by varying the heat sink temperature T_b via the resistance bridge for zero heating current through the film heater (see figure 4.1 left). In the heater sweeps, the film temperature is controlled by fixing the heat sink temperature and by varying the heating current through the film heater (see figure 4.1 right). Since the stabilization of the detectors during operations is achieved via the heater on the thermometers, this method is usually applied. In addition it is much easier to perform heater sweeps due to the time constants involved, which for a given thermal coupling to the base plate, roughly scales with the heat capacity of the film for heater sweeps and with the heat capacity of the mounting plate for heat sink temperature sweeps.

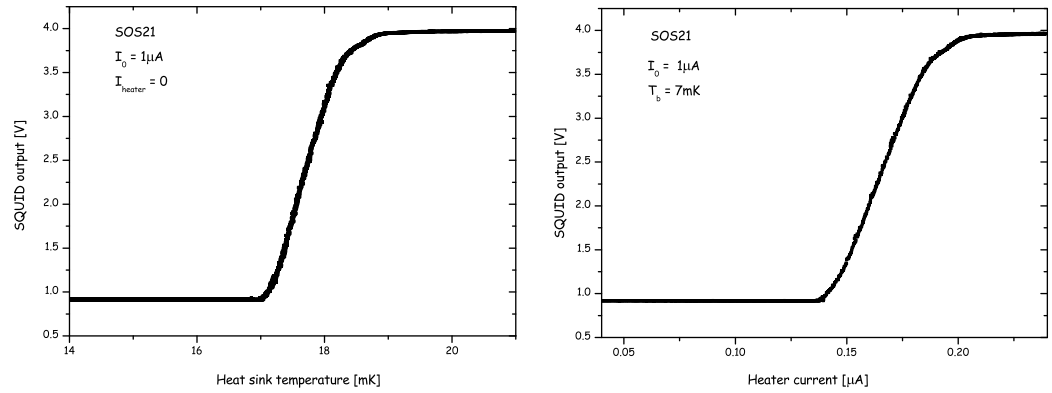

Figure 4.1: Transition curves for the light detector SOS21 recorded with a bias current of $1\,\mu A$. The left curve was recorded by varying the heat sink temperature for zero heating current through the film heater; the right curve was recorded by varying the heating power with the heat sink temperature fixed.

Operating point

The response of the thermometer at a certain operating point depends on the slope of the transition curve and on the heat capacity of the thermometer, but

also on the read out current. This can be seen from equation 3.45 which describes the responsivity of the thermometer and which, for the simplified case of no electro-thermal feedback, can be written as

$$\Delta I_s(\omega) = \overbrace{\underbrace{\frac{1}{G_{eb}} \frac{1}{1+\imath\omega\frac{C_e}{G_{eb}}}}_{\Delta T_e(P_e)} \underbrace{\frac{dR_f}{dT_e}}_{slope}}^{\Delta R_f(P_e)} \overbrace{\frac{I_0\, R_s}{(R_f+R_s)^2}}^{\Delta I_f(\Delta R_f)} P_e(\omega)\,. \tag{4.1}$$

A high bias current I_0 broadens the transition range due to the effect of the critical current. The broadening of the transition curve would decrease its slope and therefore the responsivity of the thermometer. On the other hand high read out currents increase the resistance to current conversion factor ($\Delta I_f(\Delta R_f)$) and often tend to make the transition more linear (see figure 6.3). In order to optimize the detector response, considering these aspects, transition curves of each detector are recorded for different bias currents.

Besides choosing the optimum operation point such that the detector response

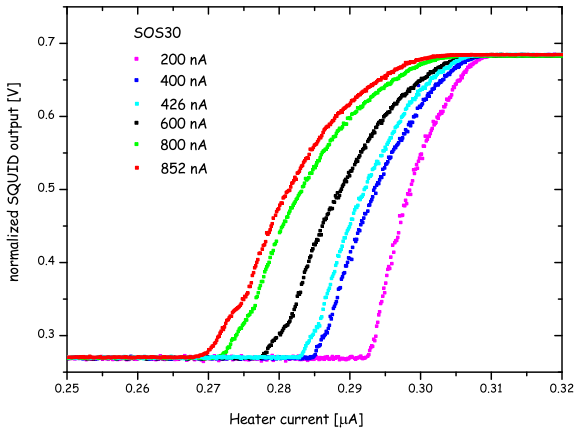

Figure 4.2: Transition curves for the light detector SOS30 measured for different bias currents I_0. The SQUID voltage output is normalized to the response of the detector with 200 nA bias current.

is maximized, the thermometer resistance at the operating point should be equal or higher than the shunt resistance in order to stay within the negative electro-thermal feedback regime to take the advantage of the self stabilizing effect on the operating point (see section 3.3.1).

4.1.2 Stability control

Once the operating points have been chosen, each detector is stabilized at its point independently of other detectors via its film heater. An excursion of the operating point due to temperature fluctuations affects the performance of the detector through its non-linear response along the transition. A typical transition of the CRESST detector has a width of few mK and a typical temperature rise for a low energy deposition is in the order of tens of μK. Hence for a stable detector response the operating point has to be constant within few μK.
Two loops, which run under computer control with a PI[1]-algorithm, are used for stability control.
A first control loop checks for deviations from the operating point by monitoring the amplitude of large heater pulses. For very large heater pulses (so called control pulses) which (partially) saturate the detector, the amplitude of the SQUID output gives a measure of how far the operating point is from the top of the transition. Deviations of the operating point are therefore identified and corrected by adjusting the control voltage applied to the heater circuit (see figure 2.15). The control pulses are injected regularly every three seconds. This rate of control pulses is chosen to monitor the stability of the operating point frequently enough and at the same time not to introduce significant dead time.
Since the SQUID output in the absence of a pulse, i.e the baseline, is also a measurement of the temperature at the detector operating point (see figure 4.1 left) this information can be used for stabilizing the operating point by monitoring and correcting baseline excursion. This is achieved with the second control loop which reads out the baseline of the detectors between pulses and regulates the control voltage applied to the heater circuit. During a pulse the baseline sampling is interrupted and the voltage is kept constant. An effect which can disturb the stabilization of the baseline is the occurrence of pulses at a rate faster than the slew rate of the SQUID, which cause flux quantum losses resulting in an incorrect SQUID output voltage. The base line control loop deals with such flux quantum losses by not responding to large jumps in the SQUID base line occurring during one sampling period.
Periods with noticeable deviations from the operating point are eliminated in the off-line data analysis.
In order to monitor the long-term stability of the operating conditions the heater is also used to inject periodic heater pulses (besides the control heater pulses). As an example, the achieved stability of the light detector SOS21 during Run30 is shown in figure 4.3 where the measured pulse height of the heater pulses is plotted as a function of time. During Run30 heater pulses of eleven different amplitudes were injected at 30 second intervals. Typical energies of the heater pulses vary from a few keV to hundreds of keV for the phonon detectors and

[1]Proportional Integral

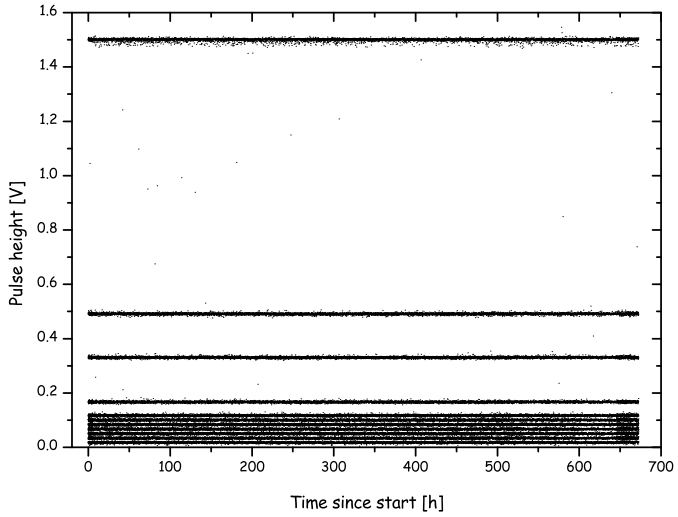

Figure 4.3: Measured pulse height of heater pulses (11 different amplitudes) of the light detector SOS21 during Run30 as a function of time (period from middle of April 2007 until end of May 2007). The operating point was mainly controlled by the control loop which monitors the amplitude of control pulses injected every 3 seconds. The detector is seen to be stable within its resolution.

from tens of eV to a few keV for the light detectors.
More importantly, heater pulses are used to extend the energy calibration from the photopeak of a γ calibration source down to the energy range of interest for Dark Matter detection and to transfer from the calibration run to the background run, as will be described in the next section. The energy injected by the heater pulses is varied to cover the whole dynamic range, with more pulses in the low energy region in order to test the trigger efficiency close to the detector threshold.

4.2 Data analysis

The data analysis begins with a computation of some simple parameters for each pulse, like estimation of the pulse height by a moving average algorithm, onset channel or baseline level for each pulse.
In addition for each pulse the time elapsed since the last muon event, the multiplicity of μ veto detector panels responding and the muon sum energy are recorded.

4.2.1 Pulse height evaluation

The correct evaluation of the pulse height, which corresponds to the energy of each pulse, is done via a template fit procedure.
A template for a given type of pulse and for the detector of interest is obtained by averaging many measured pulses in the region of small pulse height where the detector response is linear. For each detector, two templates are created, one for heater pulses and other for particle pulses. These templates are then fit to all measured pulses of a given type, with an amplitude scale factor, a base line level and an onset time as free parameters. The quality of the fit is given by the overall mean square deviation (RMS) of the measured pulse to the template.
In a Dark Matter run, where the phonon and the light detector of each detector module are read out in pairs, a so-called correlated template fit procedure is applied. In this procedure a light detector and a phonon detector template are fitted to the respective measured pulses with amplitude scale factors, base lines and a common onset of the pulses as free parameters. The quality of the correlated template fit is given by a joined RMS parameter which combines the RMS fit parameters of the phonon and the light detector signals.

The light detectors, being more sensitive, often show worse performance

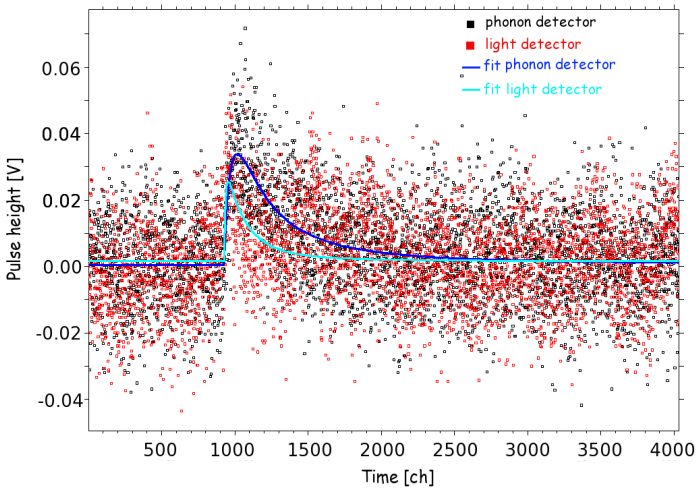

Figure 4.4: Example of the correlated fit of a low energy event in the detector module Zora/SOS21, which corresponds to an energy deposition of 3.6 keV in the phonon detector. The template was constructed by averaging pulses of the 122 keV line of a ^{57}Co calibration source.

than the phonon detectors in terms of signal to baseline noise ratio [Petricca, 2005]. In such a case the standard template fit procedure is not so efficient in estimating the pulse heights of the low energy events in the light detector due to uncertainties of the position of the onset channel. The correlated fit

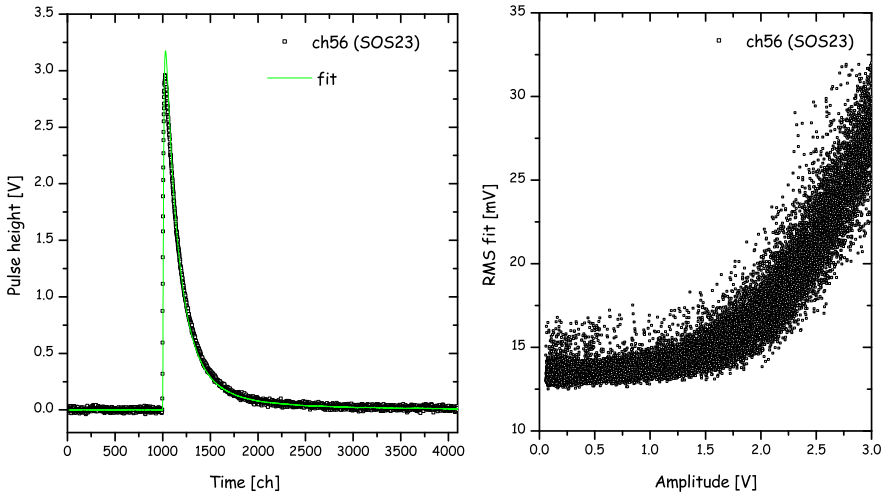

Figure 4.5: Non-truncated fit of events recorded in the light detector SOS23 during Run30 with a template obtained by averaging pulses from a region where the detector response is linear. The scatter plot shows the RMS value of the fit versus the amplitude of the pulses obtained by the fit. For pulses with amplitude below 1 V the RMS value is constant and for pulses with amplitude exceeding 1 V the RMS value starts to increase with amplitude. As it can be seen on the left figure the non-truncated fit of the pulse which is already in the nonlinear region does not agree with the data points close to the peak.

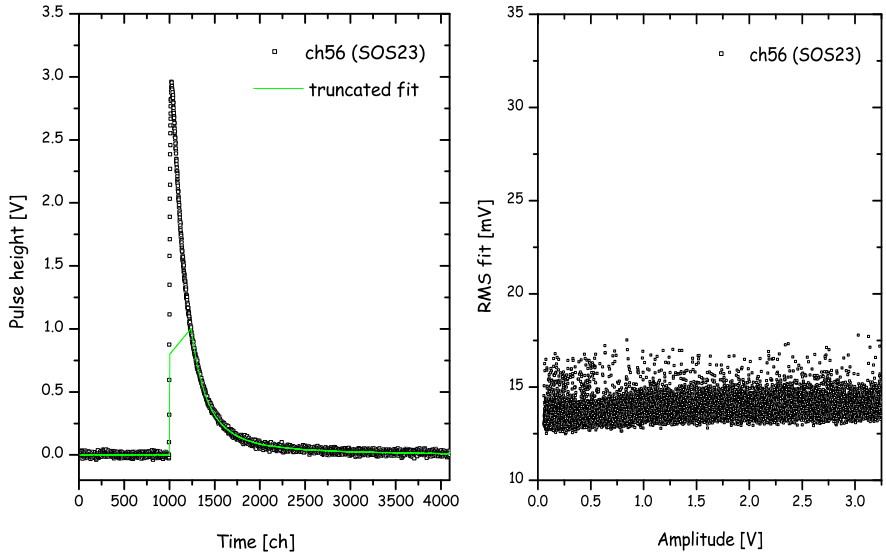

Figure 4.6: Truncated fit of events recorded in the light detector SOS23 during Run30 with a template obtained averaging pulses from a region where detector response is linear. The fit is truncated at 1 V. For pulses with amplitude below this limit the fit procedure is standard, for pulses with amplitude exceeding this limit the fit is truncated and the amplitude reconstructed from the template. As it can be seen from the scatter plot a constant RMS value of the fit is obtained. The left figure shows the truncated fit of a pulse with amplitude above 1 V.

instead allows a more accurate pulse height estimation of light detector pulses near threshold due to a more precise onset channel determination (see figure 4.4). The template fit methods as described work as long as the amplitude is in the region of linear detector response. If the response is nonlinear, the pulse shape changes with energy and the same template cannot be used over the full energy range. Therefore, for high energy pulses which approach the top of the transition curve, the part of the pulse where the response becomes reduced is excluded from the fit procedure (truncated fit) and reconstructed from the template. The quality parameter of the non-truncated template fit is used to define the range of amplitudes where the detector response is linear. As shown in figure 4.5 (right panel), the RMS value starts to increase at an amplitude of about 1V when the pulses begin to deviate from the expected pulse shape. The linear region is defined as the region with a constant RMS value. After the truncated fit is performed the data plot shows a constant RMS value in the entire range of amplitudes (see figure 4.6 right panel).
The necessary conditions for the applicability of the truncated fit technique are a high stability of the detectors at this operating points where the template has been produced and a record length long enough to contain the part of the pulse decay which is in the linear region.

4.2.2 Energy calibration

After the response of the detectors is linearized, the energy scale, for both the phonon and light channel, needs to be established.

In order to obtain an absolute energy determination for the phonon detectors, a calibration with an external source is performed. A ^{57}Co source, placed outside the cryostat, is used for this purpose since its main gamma emission lines of 122 keV and 136 keV are energetic enough to penetrate the cold box (see figure 4.7). The source is placed inside a capsule mounted on a tread, which is inserted in a plastic tube guide inside the passive shielding of the cryostat. The plastic tube guide is designed to go around the cold box allowing the adjustment of the source position for obtaining the desired count rate on all detectors. In a Dark Matter run, a calibration with ^{57}Co is performed after stable operating conditions have been reached and is repeated whenever settings have been changed.

During calibration, heater pulses of different amplitudes are injected into the thermometer. Their amplitude is determined by the template fit as described previously and then plotted as a function of the injected voltage. A comparison of the 122 keV peak of the ^{57}Co spectrum with heater pulses of similar amplitude provides an absolute calibration of the injected voltage in terms of γ energy. In order to get a reliable energy calibration the shape of the heater pulses should resemble the one of the particle pulses. The detector calibration over the whole dynamic range is obtained by fitting a polynomial function to the energy versus

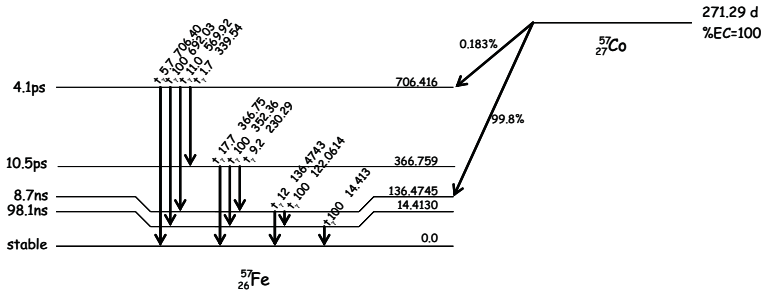

Figure 4.7: ^{57}Co decay scheme. $\dagger_\gamma$ values indicate the intensity of the line normalized to 100 for the most intense γ emitted from the level. The energies are given in keV.

pulse height sequence of all test pulses (see figure 4.8). Once this is performed, the energy of any particle pulse can be determined.
Since the test pulses are injected continuously, they provide the energy calibration throughout the entire Dark Matter run. An effect which can affect the energy calibration are pulse height changes over time due to instabilities like temperature drifts. Since there is a linear relation between energy and injected voltage of heater pulses, these variations in the pulse height are used to adjust the coefficients of the polynomial function and to correct for them.

The calibration of the light detectors follows the same procedure but the

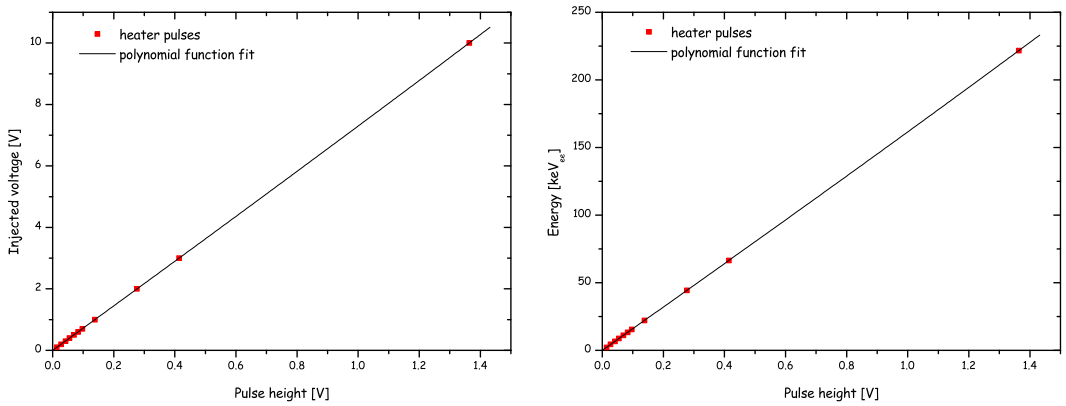

Figure 4.8: Calibration of the light detector SOS23 during Run30. Left panel: Injected voltage versus pulse height. Right panel: Energy versus pulse height. The pulse height for heater pulses is determined with the template fit. The conversion of injected heater voltage to γ energy is obtained comparing the amplitude of 122 keV γ-pulses of ^{57}Co with heater pulses of similar amplitude.

reference is provided by the light output of the scintillating crystal corresponding to an incident 122 keV γ radiation. Generally there is no absolute energy determination for light detectors. The pulse height produced in the light detector by

the absorption of 122 keV γ in the scintillating absorber is assigned the nominal value of 122 keV; the energy unit in the light channel is usually referred to as keV_{ee} (electron equivalent keV). Using this conversion, the response of the light detector is linearized through heater pulses applied to the thermometer the same way as the calibration of the phonon detector is done.
This calibration technique could be affected by a non-linear relation between the energy deposited in the scintillating crystal and its light output, yet no significant non-linearity in the relevant energy region had been observed in $CaWO_4$ crystals at room temperature [Ninković et al., 2006] and in cryogenic measurements [Angloher et al., 2005]. A slight non-linearity in the relevant energy region, compatible with the observations in [Ninković et al., 2006], has been observed in [Moszyński et al., 2005] for gamma irradiation of a $CaWO_4$ crystal at 77 K, where the light yield per energy deposited in the crystal decreases towards lower energies. Assuming a light output proportional to the energy deposit in the relevant energy region, a possible non-linearity as observed at 77 K would lead to an increased leakage of events from the electron recoil band into the nuclear recoil band and therefore would degrade the discrimination capabilities of the CRESST detector module. Such a degradation would result in an increased number of events in the WIMP acceptance region (see section 4.2.4) and thus would lead to a higher upper limit estimate for the WIMP cross section (see section 1.1.3).
Another effect which could distort the calibration, is any non-linearity in the response of the detector due to a non-smooth transition curve. The heater pulses, which are also affected by this kind of non-linearities, can be used to accurately identify such nonlinearities in the transition and to correct for them. Hence more heater pulses are always injected within the energy region of interest. Small heater pulses near the detector threshold also provide a mean to characterize and monitor the trigger efficiency.

An absolute energy calibration of light detectors is not required in order to apply the light-phonon active background discrimination technique, but it is needed for the studies of the overall light collection efficiency of the CRESST detector module and of the light detector performance. For an absolute calibration of the light detectors a very low energetic source is needed due to the high sensitivity of these detectors which are optimized to detect small amounts of scintillation light. For that purpose dedicated runs have been performed at the test facility of the Max-Planck-Institute in Munich with a ^{55}Fe X-ray source installed inside the cryostat[2]. Furthermore, in the presently ongoing Dark Matter run, very low activity (order of 1mBq) ^{55}Fe X-ray sources are mounted on a few selected light detectors.

[2]The absorption length of 6 keV X-rays in copper is about 10 μm. Thus the source could not be placed outside the cryostat.

4.2.3 Event cuts

Before any event selection, the gross exposure per detector module, which is defined as the time during which the detector module was ready to observe a WIMP induced nuclear recoil, times the detector's mass is computed.
As previously mentioned, there can be time periods during which some or all detectors are not stable enough due to large temperature fluctuations, vibrations and other noise sources. These periods are identified by an increase in the RMS value of the baseline or a deviation in the measured pulse height of the control heater pulses[3] and removed off-line, resulting in a reduced effective exposure.
Other type of event cuts that are performed include data quality cuts on parameters that are intended to remove pile-up events (like events triggered on the long tail of α pulses, which extend beyond one record length) and events where the interaction took place in the thermometers (due to their different pulse shape with respect to the pulses of events occurring in the absorber.).
As expected for a WIMP candidate event, only single scatter events (only one module responding) are accepted in the relevant energy region. Furthermore, events in coincidence with signals detected by the muon veto are rejected.

4.2.4 Acceptance regions for recoiling nuclei

The determination of the acceptance band of WIMP interactions requires the knowledge of the energy resolution of the light and phonon detectors in the relevant energy region and of the quenching factors for different recoiling nuclei. The upper boundary of the energy range of interest is given by the vanishing of the expected recoil energy spectrum in $CaWO_4$ at about 40 keV (see figure 1.4). The lower boundary of the acceptance region is defined by the discrimination threshold of the module, which corresponds to the energy where gamma and nuclear recoil bands merge (at a certain confidence level).
From the background data, the electron recoil band is determined together with the light and phonon detector resolution. Using the measured values for the quenching factor of neutron induced recoils and taking into account the resolution of the two detectors, a neutron acceptance band is determined. This is done by determining for each energy in the phonon detector the expected energy in the light detector. The uncertainty on the value of the energy in the light detector includes the phonon detector resolution (since the light detector energy scale is calibrated via the energy deposition of 122 keV γ's in the phonon detector) and the light detector resolution. Since these two contributions are independent, they

[3]The "stability cut" where periods with significant deviations from the operating point, based on the measured pulse height of the control pulse are cut from the data samples, was applied in Run28 but not in Run30.

are added quadratically[4], where the dominant term is the resolution of the light detector.
The accuracy of the procedure has been confirmed in the case of Run30 using the measured band due to neutron interactions obtained in a neutron calibration run [Angloher et al., 2008].
The same procedure, using the quenching factor measured for the tungsten recoils (see section 2.2.1), is then applied to obtain a WIMP acceptance band. Figure 4.9 shows the low energy event distribution for one detector module (Verena/SOS21) measured during the commissioning Run30 in 2007 [Lang, 2008b]. The vertical axis is the ratio of energy measured in the light channel and energy measured in the phonon channel. The horizontal axis is the energy measured in the phonon channel. The red line represents the boundary below which 90% of neutron induced nuclear recoils is expected, while the black line limits the region which is expected to contain 90% of tungsten recoils. The energy resolution of the light detector determines primarily the discrimination threshold of the detector module. The performance of the light detectors during the commissioning Run30 in 2007, particularly the achieved energy resolution, will be extensively discussed in the last chapter.

[4]The energy fluctuations in the phonon and light detectors are assumed to follow Gaussian distributions.

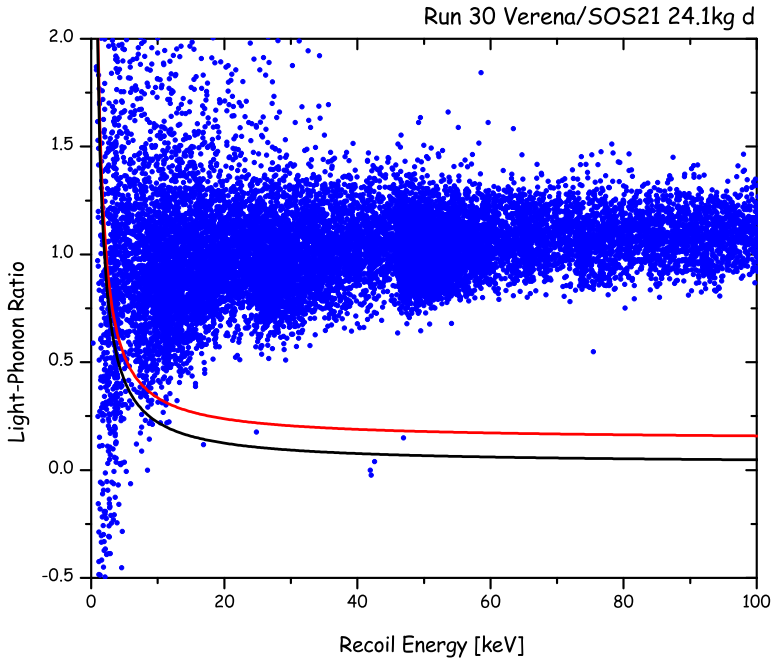

Figure 4.9: Low energy event distribution for detector module Verena/SOS21 from the data sample collected in Run30 [Lang, 2008b]. The horizontal axis represents the total energy measured by the phonon detector i.e. recoil energy. The vertical axis is the ratio of energy measured by the light detector and energy measured by the phonon detector. The energy calibration for both detectors is done in terms of γ energy, where the light detector is calibrated using the light output of the scintillating crystal corresponding to incident γ radiation as calibration reference. Therefore the ratio equals to one for the events due to γ and β interactions in the crystal. Assuming a quenching factor of 9 for nuclear recoils, the region below the red line would contain 90% of the nuclear recoils. Assuming a quenching factor of 40 for tungsten recoils, the region below the black line would contain 90% of the tungsten recoils.

Chapter 5

Light detector study

The overall light collection efficiency of the CRESST detector module and the sensitivity of the light detector thermometer are crucial parameters, which need to be optimized in order to measure the small fraction of the deposited energy which is emitted as scintillation light. With the purpose of increasing the light detection efficiency a thin superconducting lead film deposited on a sapphire substrate has been tested as an alternative light absorber to a silicon absorber. In order to analyze the effect of the thermometer layout on its sensitivity, different thermometer layouts have been compared.
All measurements of the light detector characterization were performed at the surface level testing facility at the Max-Planck-Institut in Munich using a small self-made dilution refrigerator. The cryostat is installed in a Faraday cage to isolate it from electromagnetic interferences. The data acquisition system used in the Munich facility[1] is similar to one in the Gran Sasso facility (see figure 2.15).

5.1 Thermometer layout

The standard thermometer layout of the light detector has been described in the section 2.3.2.

The first step of thermometer fabrication is the evaporation of the tungsten film onto a previously cleaned surface of the absorber. The cleaning of surfaces is necessary to obtain reproducible transition temperatures of films, ferromagnetic contaminations of the tungsten film in the order of ppm can significantly lower the transition temperature. Films are produced in an ultra high vacuum system using a tungsten single crystal with 99.99% purity as evaporation material. After deposition, tungsten films are structured to the final shape with a

[1] A detailed scheme of the data acquisition system used in the Munich facility can be found in [Petricca, 2005].

positive photolithographic process and wet chemical etching[2]. Additional photolithographic lift off processes followed by deposition steps are performed to produce aluminium and gold structures.
To meet the required surface cleanliness and radiopurity, several cleaning steps are applied during the procedure.
A detailed description of the fabrication processes is given in Frank [2002].

5.1.1 Influence of thermometer geometry on detector response

For a given absorber the sensitivity of the light detector is determined by the minimal amount of energy which its thermometer can detect.

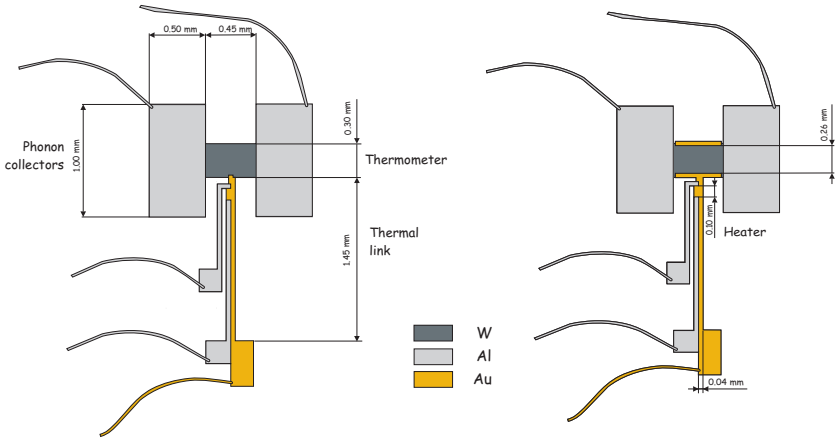

Figure 5.1: Layout of a standard light detector thermometer (left) and of a thermometer with additional gold banks (right). The dimensions given in the left panel are the same for both thermometer layouts.

The detection threshold of the thermometer is determined by the baseline noise which is the combination of different noise contributions (see section 3.3). In order to investigate the influence of the thermometer geometry on its response, a slightly modified thermometer structure with additional gold stripes (¨ banks¨) covering the edges of the tungsten film has been produced (see figure 5.1). The motivation for the deposition of normal conducting metal stripes over the tungsten film edges is their questionable quality, which is the uncontrolled result of lift off processes. The proximity effect of the normal conducting gold stripes reduces the transition temperature of the edges well below that of the remainder

[2]For tungsten etching a diluted mixture of NaH_2PO_4, NaOH and $Na_3Fe(CN)_6$ is used instead of the conventional potassium based etchants to avoid radioactive contamination by ^{40}K.

of the tungsten film resulting in well-defined edges. As observed experimentally in Hilton et al. [2001] the deposition of normal metal banks on the boundaries of an SPT has improved the smoothness of the transition curve and increased its slope.

To test this observation, two thermometers, one of standard design and the other

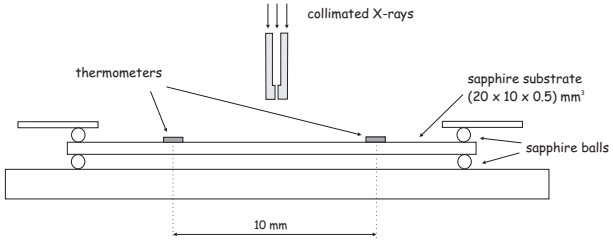

Figure 5.2: Schematic view of the setup to compare 2 thermometers with and without edge treatment (see text). The distance between the two thermometers is 10 mm. The collimated X-ray source irradiating the sapphire substrate is positioned at a distance of 5 mm from both thermometers. The diameter of the irradiation spot is estimated to be 0.5 mm.

one with additional gold banks, have been structured from the same evaporated tungsten film on the sapphire substrate (see figure 5.2). The distance between the thermometers is 10 mm. The detector is mounted in a cooper holder, which is thermally coupled to the mixing chamber by a cooper wire (0.2 mm in diameter and about 10 cm in length). The sapphire substrate is held by pressing it between seven small sapphire balls directly embedded in the copper holder, in this way providing good thermal isolation of the detector from the copper holder. As described before, the thermal coupling of the thermometers is defined by gold film structures, which are connected to isolated pads on the cooper holder by gold bond wires.

Figure 5.3 shows the transition curves of the thermometers measured with low bias current ($I_b = 150\,\mathrm{n}\mathring{A}$). Though the gold stripes on the boundaries of the W film might have narrowed the transition curve, the smoothness of the curve is not significantly improved. This hints to a variation of the transition temperature across the W film itself.

A calibration measurement was done with a collimated ^{55}Fe source irradiating the substrate at a distance of about 5 mm from both thermometers. Operating points were chosen such that they are at the same fraction of the transition (see figure 5.3). The thermometer with the additional gold banks shows a higher resistance at the top of the transition than the standard thermometer. This is due to its narrower tungsten film (0.26 mm) compared to the standard thermometer (0.3 mm).

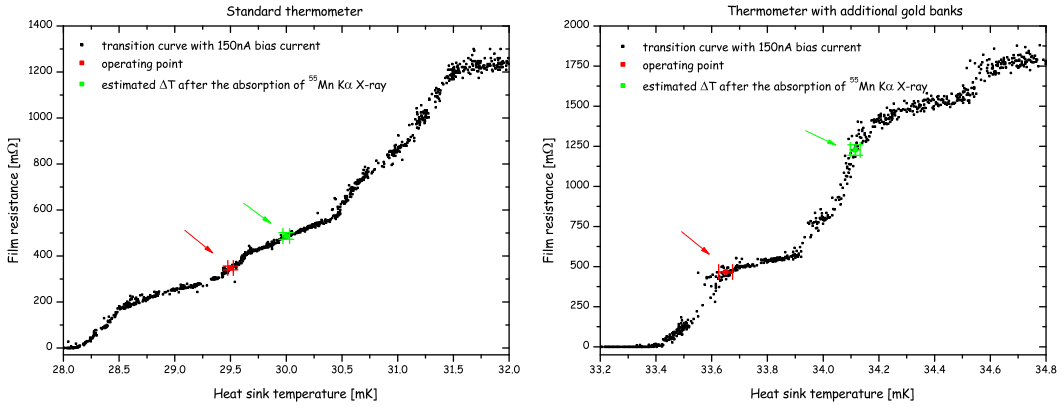

Figure 5.3: Transition curves of the two thermometers deposited on the same sapphire substrate recorded with 150 nA bias current obtained by varying the heat sink temperature. To the left is the transition curve of the standard thermometer and to the right the one of the thermometer with additional gold banks. The chosen operating points are marked in red. The estimated temperature rise after the absorption of 5.89 keV X-ray in the sapphire absorber are shown in green.

The achieved energy resolution is rather poor for both thermometers (see table 5.1) which is a consequence of the non-smoothness of the transition curves. As previously mentioned the template fit method can not be efficiently applied if the pulse shape changes notably with the measured pulse height. For both thermometers the ^{55}Mn K$_\alpha$ pulse shape is affected by the substructures in the transition curve. Therefore the resolutions achieved for the low energy heater

Thermometer layout	standard	with gold banks
FWHM of ^{55}Mn K$_\alpha$ peak [eV]	673 ± 12	460 ± 4
FWHM of low energy heater pulses [eV]	169 ± 2	196 ± 5

Table 5.1: Measured energy resolution of the ^{55}Mn Kα peak and of the low energy heater pulses (E $\sim$ 1 keV) for both thermometers biased with 150 nA. Statistical errors (1σ)for the Gaussian fit of the peaks are stated.

pulses (E $\sim$ 1 keV), which were not influenced by the shape of the transition curve, are listed in table 5.1. The thermometers show similar resolution of the low energy heater pulses. The threshold of thermometers, roughly estimated as twice the value of measured FWHM of heater pulses, is about 340 eV for standard thermometer and about 390 eV for thermometer with additional gold banks.
In an attempt to improve the resolution of the thermometers for the X-ray irradiation, another measurement with the thermometers stabilized in similar operating points is taken with a high bias current (3 μA), which is expected to smooth the transition curves. Indeed, as can be seen from figure 5.4, where the measured

spectra are shown, the achieved resolution improved. For the thermometer with the standard layout the improvement is significant. The thermometer with the gold banks shows only a slight improvement. This is due to still present substructures in the transition curves combined with the smaller dynamical range. Thus

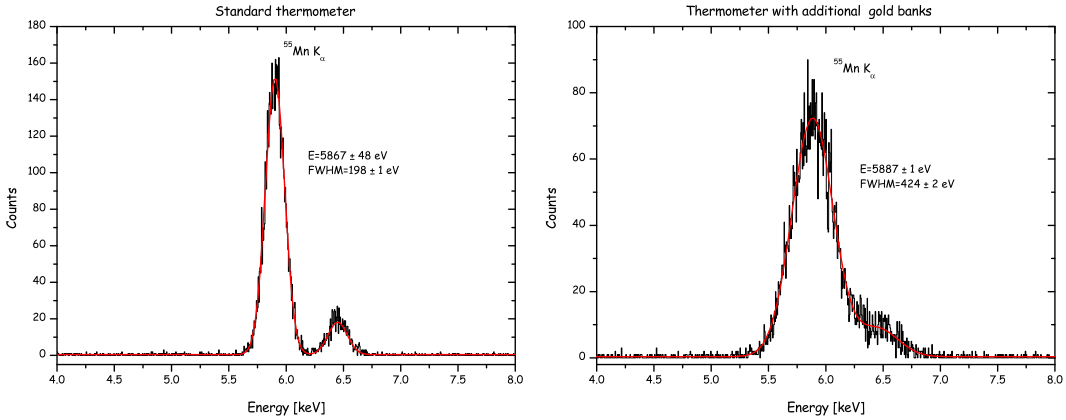

Figure 5.4: ^{55}Fe spectrum recorded with the standard thermometer (left) and the thermometer with additional gold banks (right) on the same sapphire substrate. A Gaussian fit of the two peaks is superimposed.

Thermometer layout	standard	with gold banks
FWHM of ^{55}Mn K$_\alpha$ peak [eV]	198 ± 1	424 ± 2
FWHM of low energy heater pulses [eV]	85 ± 2	86 ± 2

Table 5.2: Measured energy resolution of the ^{55}Mn Kα peak and of the low energy heater pulses ($E \sim 1\,keV$) for both thermometers biased with $3\,\mu A$. Statistical errors (1σ) for the Gaussian fit of the peaks are stated.

the measured resolutions of the low energy heater pulses for both thermometers are again compared (see table 5.2). Both thermometers show similarly improved energy resolutions for the heater pulses compared to the ones obtained from the measurement with a low bias current. The estimated energy threshold is about 170 eV for both thermometers.
Based on these measurements it follows that within the limitations imposed by the non-smooth transition curves of the two thermometers, the influence of the additional gold banks does not seem to be beneficial for the overall performance of the present thermometer of the light detector.

5.1.2 Performance of two thermometers on one substrate

The calibration measurement of the detector equipped with two thermometers was used to further investigate the overall performance of light detector thermometer.

Temperature rise

For a certain energy deposition in the substrate only a part of the energy is actually measured by the thermometer. This part is given by the fraction of non-thermal phonons which thermalize in the thermometers (see section 3.2.1). The amount of deposited energy that is detected by the thermometer is further influenced by many parameters like phonon transport properties of the absorber, size of the absorber-thermometer interface, efficiency of the phonon transmission across absorber-thermometer interface and efficiency of the quasi-particle transport from phonon collectors into the tungsten film.
For thermometers of similar sizes, produced in parallel processes on the same substrate, which is irradiated by X-rays collimated in a small spot located at a central position between the thermometers, the detected fraction of deposited energy is expected to be similar. From the calibration measurement of the above discussed thermometers, the observed temperature rise for the energy deposition of 5.89 keV is estimated. For this purpose the measurement with the low bias current is used, in which case self-heating effects can be neglected and the mixing chamber temperature can be taken as a good estimate of the thermometer temperature. The positions of the operating points are estimated by the measured pulse height of the small control pulses, while the observed pulse height of the ^{55}Mn K_α pulses determines the resulting voltage rise due to i.e the resistance change. The corresponding temperature rise is obtained directly from the measured transition curves. The heat capacity of the thermometers is estimated according to equation 3.5. The detected amount of energy is then calculated as $E=\Delta T_{op} \cdot C_{op}$. The results are given in table 5.3. As it can be seen, about 5% of the energy deposited in the sapphire substrate is measured by each thermometer. The fraction of energy which is measured by the thermometer can also be estimated according to the calorimeter model exposed in section 3.2.1 by calculating the fraction of non-thermal phonons which are thermalized in the thermometer (see equation 3.15)[3]. The thermalization time τ_{film} for the non-thermal phonons which takes into account absorption efficiency of the thermometer for the incoming non-thermal phonons is calculated according to equation 3.14 for both

[3]The assumption made here is that for an absorption event at equal distance to both thermometers, the fraction of deposited energy measured by one thermometer does not considerably affect the fraction of energy measured by other thermometer. This seems to be a reasonable assumption since from the measurement is follows that the fraction of the deposited energy detected by each thermometer is only about 5%.

Thermometer layout		standard	with gold banks
T_{op}	[mK]	29.5 ± 0.03	33.65 ± 0.03
C_{op}	[fJ·K^{-1}]	102.7 ± 0.3	109.9 ± 0.2
ΔT_{op} (5.89 keV)	[mK]	0.50 ± 0.06	0.47 ± 0.04
$E_{detected}$ (5.89 keV)	[%]	5.4 ± 0.7	5.4 ± 0.5
$\tau_{crystal}$	[ms]	~ 0.1	
τ_{film}(full thermometer area)	[ms]	~ 0.23	~ 0.24
τ_{film}(W film)	[ms]	~ 2.0	~ 2.3
ε(full thermometer area)	[%]	~ 30	~ 30
ε(W film)	[%]	~ 5	~ 4

Table 5.3: Temperature rise and fraction of energy detected in the thermometers for a 5.89 keV energy deposition in the sapphire substrate. Operating temperatures (T_{op}) and heat capacities (C_{op}) are determined as described in the text. The errors given correspond to 1σ errors of the positions of the operating points. The calculated thermalization times for the thermometers, estimated thermalization time for the substrate and estimated fractions of non-thermal phonons which thermalized in the thermometers are given in the lower part of the table. See text for explanation.

thermometers and given in table 5.3. The thermalization time of the absorber $\tau_{crystal}$ is affected by many parameters like the surface quality or the holding system and is expected to scale as the ratio between the volume and the surface area of the absorber. Hence, it can be estimated for the current absorber geometry by scaling values measured in Sisti [1999] for the large volume sapphire absorbers held by a similar holding system[4]. The calculated fractions of phonons thermalized in the thermometers do not agree with the estimated fraction of energy that is detected in the thermometers when the full thermometer area (including the phonon collectors, see figure 2.9) is considered. When only the area of the W film is taken as collection area, the collection efficiency $\varepsilon \backsimeq$ 4-5 % agrees with the measured energy fraction of 5.4 %. The observed fraction of the energy deposited in the substrate suggests that the efficiency of the phonon collectors is rather low.

Pulse shape

Following the calorimeter model of [Pröbst et al., 1995](see equation 3.19) the response of the light detector thermometer film can be described as

$$f(t) = A_n(e^{-(t-t_0)/\tau_{in}} - e^{-(t-t_0)/\tau_n}) + A_{th}(e^{-(t-t_0)/\tau_t} - e^{-(t-t_0)/\tau_n}) + b \qquad (5.1)$$

[4]The thermalization time constants of the absorbers have been obtained by fitting the measured pulses to the modelled temperature signal [Pröbst et al., 1995].

where t_0 is the onset time of the pulse, and A_n, A_{th} and b are three positive numbers representing the amplitude of the two signal components and of the baseline respectively.
The templates obtained by averaging many measured particle pulses in the low energy region for both thermometers were fitted according to equation 5.1 and the results of the fit are shown in figure 5.5. Again the data from the measurement with the low bias current were used, so that the shortening of the pulses due to the electro-thermal feedback can be neglected.
Both thermometers show a high fraction (>96%) of non-thermal phonons in the observed signal.
The decay time of the non-thermal component of the signal is defined by the heat capacity of the tungsten film and the heat conductance of the thermal link (see equation 3.24). The thermometer with additional gold stripes has shorter relaxation time τ_t than the standard thermometer. This is possibly due to an improved thermal coupling to the heat sink, since the estimated heat capacities in the operating points are similar.
The fitted rise time of the pulses τ_n can be compared to the modelled rise times

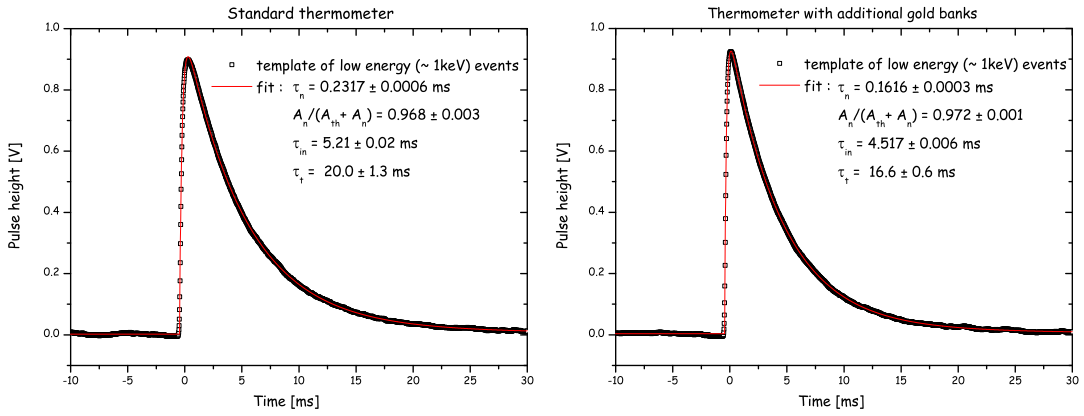

Figure 5.5: Relevant parameters resulting from the fit of template low energy events for the standard thermometer (left) and the thermometer with gold banks (right). The parameters include the rise time τ_n of the two signal components, the fraction of the non-thermal component $A_n/(A_{th} + A_n)$, the decay time τ_{in} of the non-thermal component and the decay time τ_t of the thermal component.

calculated according to equation 3.13. The modelled rise time for both thermometer, using the values from table 5.3, is expected to be in the range from ~ 0.07 ms to ~ 0.1 ms. It follows that the fitted rise time for both thermometers is longer than expected from the calorimeter model. This is due to the additional time constant, which is the time needed for the quasi-particles to diffuse into the thermometer.
In a previous work of the CRESST group [Loidl, 1999] quasi-particles have been

measured to diffuse in an aluminium-tungsten bilayer over a distance of 1 mm in a time of about 1 ms. Given the typical dimensions of the phonon collectors in the present thermometer, this would lead to a rise time of about 0.5 ms, which is longer than the fitted rise time. This difference can be ascribed to the smaller thickness and (or) worse quality of the bilayer used in this measurement than in [Loidl, 1999], which can influence the diffusion constant of the quasi-particles via their effective mean free path. As previously mentioned, the mean free path of the quasi-particles is determined by the elastic scattering on impurities and lattice defects. Additionally, in a bilayer of a thickness comparable to the quasi-particles mean free path, the effective quasi-particles mean free path is limited by the scattering on the surface[5].
Due to the complexity of the processes in the phonon collectors, the interpretations about the efficiency and quality of the phonon collectors given in this subsection require further measurements, which were not possible within the time of this thesis.

Coincident events

A scatter plot of the coincident events of the measurement with 3 μA bias current is shown in figure 5.6. The ^{55}Mn K_α and K_β X-ray peaks are clearly visible in the center of the band. The size of the collimated irradiation spot is estimated to be 0.5 mm in diameter and the estimated distance to the both thermometers is the same (5 mm).
Possible energy losses for the X-ray absorption events at the distance 5 mm$\pm$0.5mm to the thermometer would appear as a tail towards lower energies in the measured spectrum. No such effect is seen indicating no significant loss of non-thermal phonons for about 10% change in the distance from the absorption event to the thermometer. As it can be seen from figures 5.6 and 5.4 the ^{55}Mn K_α and K_β X-ray peaks have gaussian distributions in both thermometers. The worse resolution obtained by the thermometer with additional gold stripes, shows up as an elongation of the peaks along x-axis in the scatter plot.
An additional line, which is vaguely visible in the spectrum at about 8 keV, is associated with the Cu K_α X-rays induced by cosmic and environmental radioactivity. These X-rays irradiate the substrate uniformly. Events occurring near the center of the substrate cause similar fractions of energy detected in both thermometers. If an event occurs closer to one thermometer, the fraction of energy measured in that thermometer becomes larger and the fraction of energy measured in the other thermometer becomes proportionally smaller. As it

[5] In Loidl [1999] the mean free path of the quasi-particles at low temperatures in the Al/W bilayer, which was used in the measurement, was estimated to be about 1.8 μm. This is in the range of the bilayer thickness.

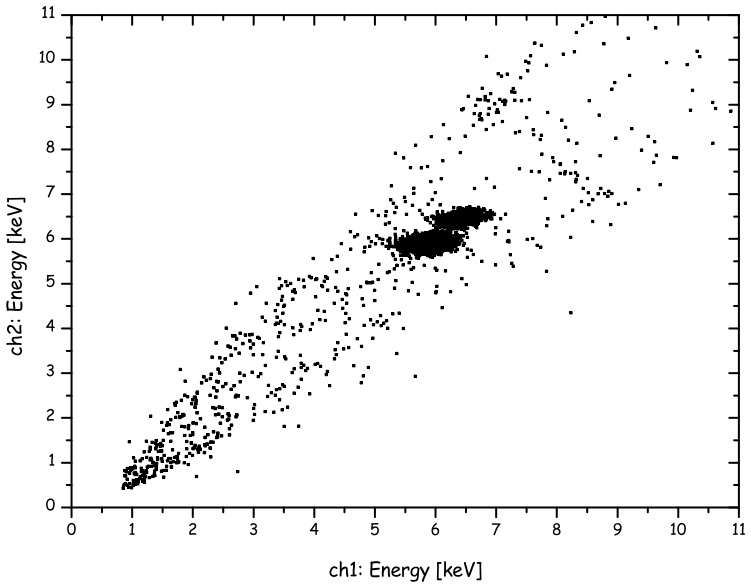

Figure 5.6: Scatter plot of the energy measured by the standard thermometer (ch2) versus the energy measured by the thermometer with additional gold banks (ch1) deposited on the same sapphire substrate. X-rays from the collimated ^{55}Fe source hit the substrate in the middle between the two thermometers.

can be seen from figure 5.6, the Cu K$_\alpha$ line is straight i.e the total energy detected by both thermometers stays constant. This suggests that there are no significant losses in the substrate for events that are up to about 15 mm away from the thermometers. This is in agreement with previous measurements in the CRESST group [Frank, 2002], where the losses in sapphire substrate for an event 20 mm away from the thermometer are estimated to be less than 2.5% of the total energy.

5.2 Light detector substrate

For a given light output of the scintillating crystal and a given reflectivity of the housing, there is a clear dependence of the light detection efficiency of the detector module on the size and absorption properties of the light detector absorber [Frank, 2002, Petricca, 2005].
With the aim of improving the light absorption of the detectors, thin lead films have been tested as alternative to silicon absorber. The performance of a sapphire light detector with a lead absorption layer was compared to that of a silicon light detector of same absorber size operated in the same setup.

5.2.1 Lead absorber on the sapphire substrate

The motivation to explore superconducting absorbers is their energy gap[6] in the order of meV, which allows much smaller excitations to be detected than with conventional semiconductors like silicon or germanium whose energy gap is in the order of eV. This is of special interest when the scintillation light is emitted in the red and near infrared spectrum, as it is in the case of scintillating sapphire crystals. Among superconductors lead absorber was chosen due to the fast relaxation time of the excited quasi-particles that should provide a fast time response of the detector. Besides lead is known to be a good X-ray absorber [Angloher et al., 2002, Bento, 2004].

Detector setup

A lead layer of $\sim$1.3 kÅ thickness and $(29\times29)\,\mathrm{mm}^2$ size was deposited on a $(30\times30\times0.45)\,\mathrm{mm}^3$ sapphire substrate on the opposite face with respect to a tungsten SPT thermometer already prepared. The thermometer layout is shown in figure 5.1 right. The deposition of the thin lead film was made in a Po-

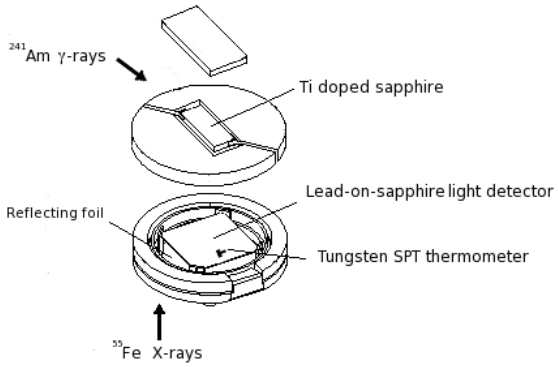

Figure 5.7: Schematic view of the setup. The titanium doped sapphire crystal and the lead-on-sapphire light detector are enclosed in a reflective housing. The light detector is illuminated by X-rays coming from an internal (inside the cryostat) ^{55}Fe source and by scintillation light coming from the sapphire crystal excited by γ-rays from an ^{241}Am external source. The light detector is read-out with a tungsten SPT thermometer.

laron SEM coating system (E5800) at room temperature using a lead target of 99.9999% purity. The thickness of the film was estimated by the weight increase of the substrate after the lead deposition.
A titanium doped sapphire $(20\times10\times5)\,\mathrm{mm}^3$ crystal with 75ppm titanium concentration was used as scintillating crystal. The crystal sides were unpolished.

[6]From another point of view metal absorbers are not suitable due to the large heat capacity compared to superconductors.

Both detectors were housed in a copper holder with Al foil used as a reflector on the side of the crystal and VM2000 foil[7] on the side of the light detector (see figure 5.7). The thermometer side of the lead-on-sapphire substrate was facing the crystal.

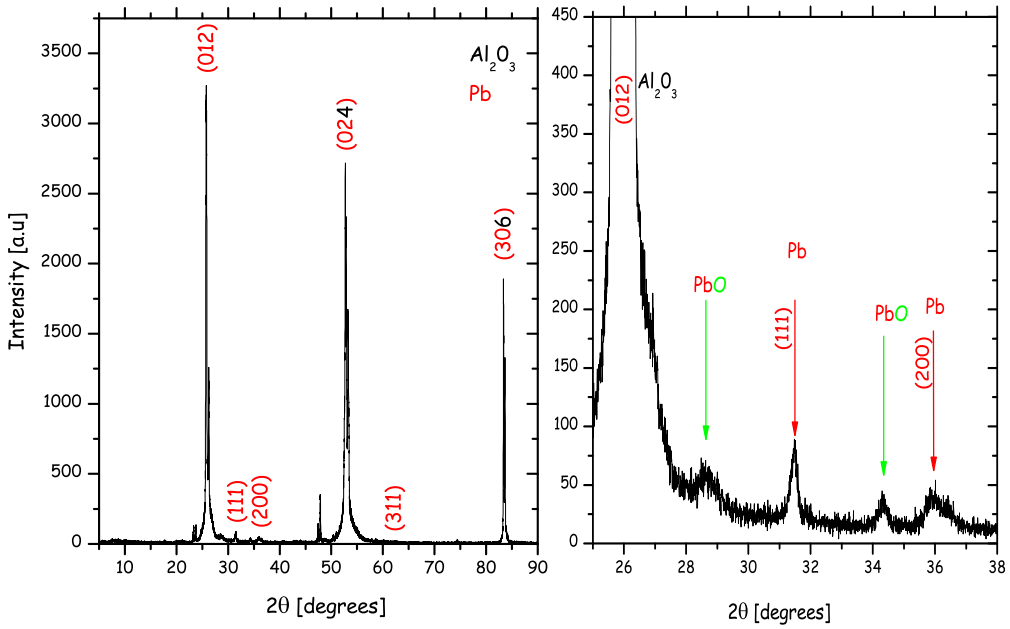

Figure 5.8: X-ray diffraction spectrum of the lead film deposited onto the sapphire substrate. The full measured spectrum is shown in the left figure, where the most intense peaks are due to the diffraction by the R-plane of the sapphire crystal. The right figure shows the region where the peaks due to the diffraction by lattice planes of the lead and lead oxide are visible. In the left figure there are additional small peaks on the left side of both sapphire diffraction peaks which are probably due to a slight misalignment of the substrate.

5.2.2 Elemental, structural and optical studies of lead film

Elemental analysis of two lead-on-sapphire samples, using an energy dispersive X-ray spectrometer (EDX), showed no significant contamination present in the films within the detection limits of the spectrometer (about 1 percent by weight).

[7] 3M Radiant Mirror Film VM2000

An X-ray diffraction (XRD) spectrum of a lead-on-sapphire sample, which is deposited under the same conditions as for the sample used in cryogenic measurement, was taken with a conventional x-ray diffractometer[8] using Cu K_α radiation (see figure 5.8). The most intense reflections are those of the sapphire substrate itself. The measured peaks of lead reveal the face-centered cubic (FCC) structure and a measured lattice constant of 4.94 ± 0.02 Å matching the lattice constant of the bulk material. According to the XRD spectrum the average grain size, estimated from observed peak widths using the Debye-Scherrer formula and neglecting any possible strain effects, is about 300 Å.

Transmission spectra[9] of the lead-on-sapphire sample were taken at wavelengths in the region between 350 nm and 1000 nm at room temperature using a Secoman Anthelie 2 Advanced spectrophotometer. The measurements were done for both the lead film and the sapphire crystal facing the light source, showing no significant difference (see figure 5.9). The sapphire substrate on average transmits above 90% in the measured region.

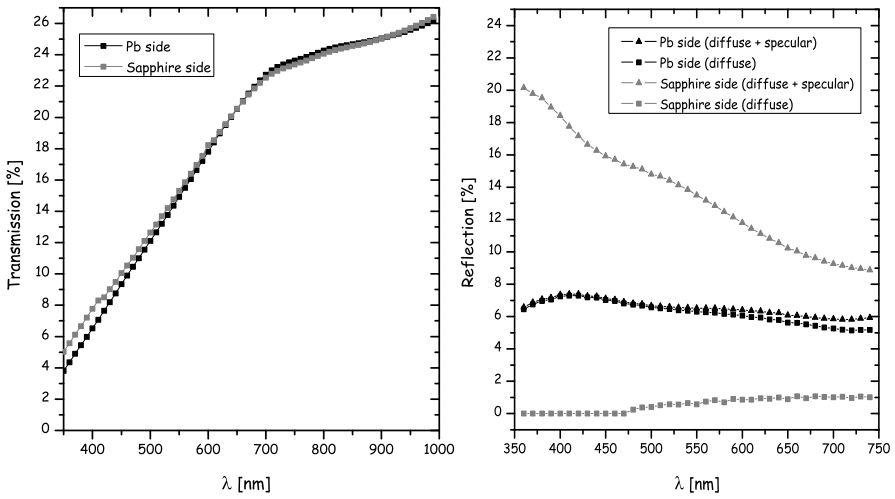

Figure 5.9: Transmission (left) and reflection spectra (right) for a lead-on-sapphire substrate measured with the lead and the sapphire side facing the light source. Transmission spectra were measured under normal incident angle and the reflection spectra were taken with an integrating sphere.

Reflectivity measurements were performed at room temperature using a Minolta CM-2500D integrating sphere spectrophotometer in the wavelength region from 360 nm to 740 nm. The total (diffuse and specular contribution) reflection spectra and the diffuse reflection spectra for the lead and the sapphire sides facing

[8]Both measurements, EDS and XRD, were done in the crystal laboratory at the Technical University of Munich in Garching.

[9]All optical measurements were carried out at the Max-Planck-Institut in Munich.

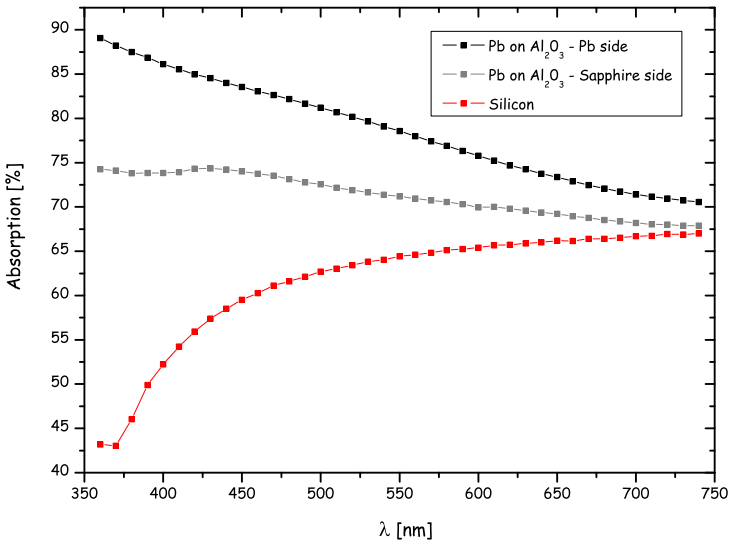

Figure 5.10: Absorption of the lead-on-sapphire substrate and the silicon substrate between 360 nm and 740 nm estimated from the combination of a transmission and a reflectivity measurement. In gray and black are the different values obtained measuring respectively on the sapphire and on the lead side, while the red curve shows the absorption of the silicon sample.

the light source are shown in figure 5.9. As it can be seen from the figure, when the lead film is directly illuminated the reflection is lower and mainly diffuse.

Absorption spectra for the lead-on-sapphire sample, calculated from the transmission and reflection spectra, are shown in figure 5.10. The absorption spectrum, obtained in the same way, for a 0.45 mm thick n-type silicon sample, which is the absorber of the light detector used for comparison, is shown in the same figure. The absorption of the lead-on-sapphire sample with both the lead directly illuminated or through the sapphire illuminated is higher than the absorption of silicon sample in the measured region of the spectrum.

The scintillation emission spectrum between 200 nm and 1000 nm of the sapphire with 75 ppm titanium concentration was measured at room temperature. The spectrum shows several emission peaks with the most prominent one centered at 750 nm with a FWHM of about 140 nm, which is due to Ti^{+3} [Luca, 2007]. Emission spectra of several sapphire crystals doped with Ti^{+3} have been measured at room temperature and at 30 K. The position of the emission peak due to Ti^{+3} does not change significantly with decreasing temperature. The lead film absorbs more strongly than the silicon substrate, as it can be seen from figure 5.10, for most of the 75 ppm titanium doped sapphire emission spectrum (the calculated absorption spectra do not cover the full region). This is due to

the higher reflectivity of silicon.

5.2.3 Performance of the lead-on-sapphire light detector

The influence of the superconducting layer on the detector pulse shape was investigated in particular for a possible decrease of the amplitude due to the energy trapped inside the layer [Rothwarf & Taylor, 1967]. Therefore the detector was calibrated with collimated X-rays from an ^{55}Fe source before and after the deposition of the lead film. The irradiation spot was of about 1 mm in diameter and placed at about 25 mm distance from the thermometer on the lead layer side of the substrate.
Figure 5.11 shows transition curves of the thermometer obtained by varying the heat sink temperature with no current through detector heater and by changing the heating current through the film heater with a stabilized heat sink temperature. As it is visible from the figure the transition curve is not smooth and a lot of substructures are present.
The operating point chosen for the measurement before the deposition of the lead film was in a very non-smooth region and the pulse shape changed with the signal amplitude (see figure 5.12 left), degrading the linearity of the detector response. Instead of applying the standard procedure (see chapter 4.2.1), the linear region of the detector response was estimated as the region where the relation between the injected voltage for the heater pulses and their pulse height, obtained by a moving average method[10], was linear. The ^{55}Mn K_α peak was at the border of the linear to the nonlinear region. The resulting ^{55}Fe spectrum is shown in figure 5.13, while the estimated resolution of the detectors are shown in table 5.4. Due to the non-linear response of the detector the results obtained should be taken with some caution.

Light Detector	WI199	WI199
Absorber	sapphire	lead-on-sapphire
FWHM for ^{55}Fe Kα peak [eV]	435±3	545±64
FWHM for heater pulse of ∼3 keV energy [eV]	326±15	837±77

Table 5.4: Measured resolution of the ^{55}Mn Kα peak and of the low energy heater pulses for the light detector WI-199 before and after lead deposition.

After the lead deposition, another calibration measurement with the ^{55}Fe source was taken but at a slightly higher operating point (see figure 5.11, left

[10]Given a certain number of channels (chosen according to the time base and the length of the pulsed) this algorithm calculates the average value among these channels and then moves the calculation by one channel at each step along the record.

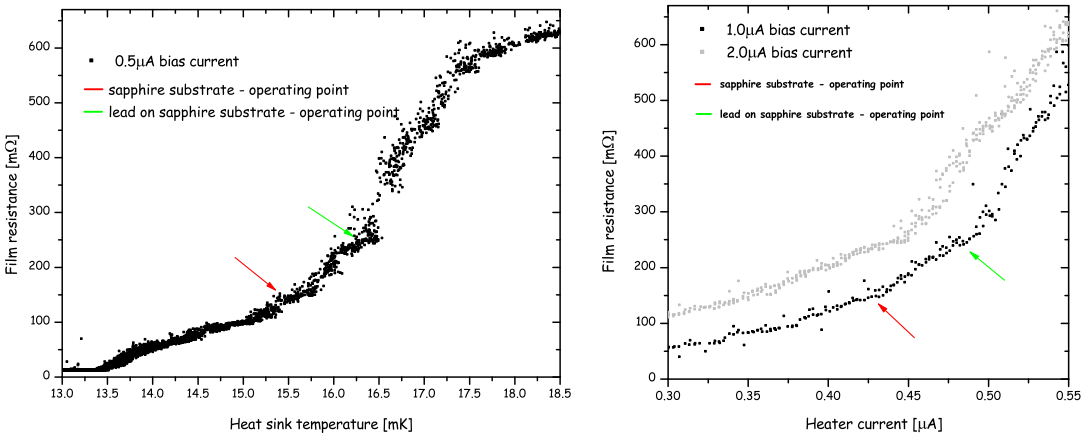

Figure 5.11: Transition curves for the light detector WI-199. The left curve was obtained by varying the heat sink temperature at a bias current of 0.5μA and 0 A heater current. The right curve was obtained by changing the heating through the film heater with 1μA and 2μA bias current.

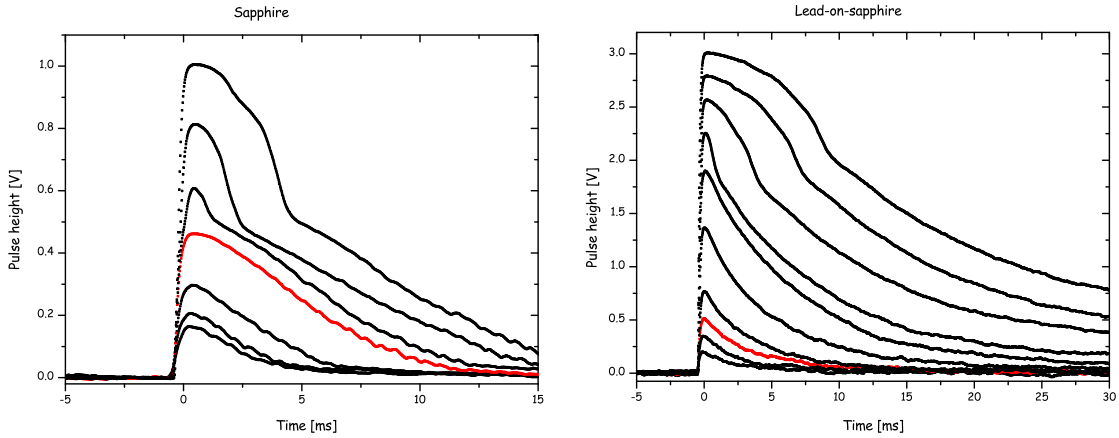

Figure 5.12: Detector response for different pulse heights for the light detector WI-199 with the pure sapphire substrate (left panel) and the lead-on-sapphire substrate (right panel). The red curve is the typical ^{55}Mn K$_\alpha$ pulse.

panel). Nonlinearities of the detector response due to substructure in the transition were not present in the energy region of interest (see figure 5.12 right panel) and the standard analysis procedure was applied. The measured spectrum is shown in figure 5.14 together with the spectrum detected while irradiating the sapphire crystal with the 60 keV γ radiation from an external ^{241}Am source. From a Gaussian fit with an exponential background of the scintillation light peak, the fraction of energy deposited in sapphire and measured in the lead-on-sapphire detector is calculated to be 2.4 % (see table 5.5). This result is a notable improvement in absorption efficiency when compared to 1.4 % which was obtained

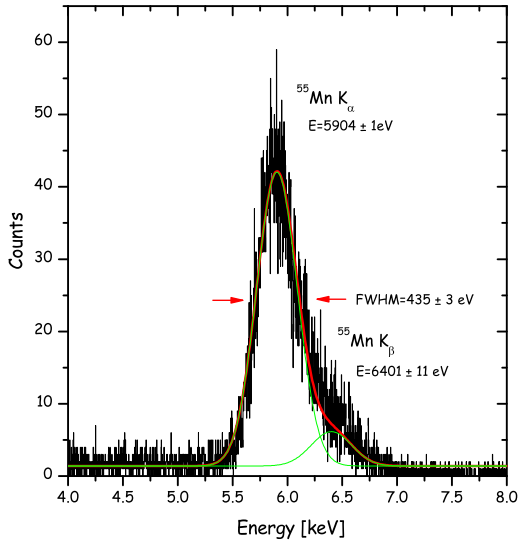

Figure 5.13: The obtained ^{55}Fe spectrum for the light detector WI-199 with the pure sapphire substrate. A Gaussian fit of the two peaks is superimposed.

with the silicon absorber in the same setup [Askin, A., 2006]. The difference is ascribed to the different absorption properties of the material used, as shown in figure 5.10.

Light Detector	Absorber	Size	Detected Light of 60 keV
BE10	silicon	$(30 \times 30)\,\mathrm{mm}^2$	1.4 %
WI-199	lead-on-sapphire	$(30 \times 30)\,\mathrm{mm}^2$	2.4 %

Table 5.5: Fraction of the energy deposited in the 75 ppm Ti doped sapphire crystal detected in the light detector for different absorber materials.

As seen from table 5.4 the resolution achieved with the sapphire detector worsen as a result of the lead deposition. Due to the different operating points in the two measurements and therefore the different gain of thermometer (slope of the transition curve) the values can not be compared directly. A simultaneous increase by a factor of two of the baseline noise and of the pulse height of X-ray absorption events due to the temperature variations around the operating point was observed during the measurement with lead-on-sapphire absorber. This indicates that the observed noise is mostly due to energy like noise sources which scale with the signal.
In addition the pulse height of events due to X-ray absorption in sapphire was significantly decreased after the lead deposition. This can not be explained only

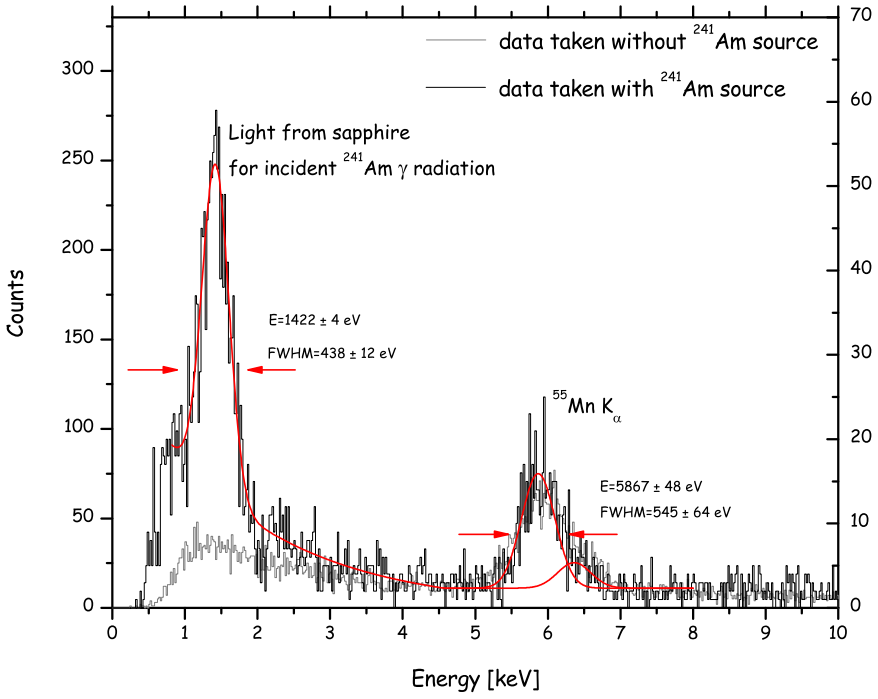

Figure 5.14: The gray solid line is X-ray spectrum of an ^{55}Fe source recorded with the lead-on-sapphire WI-199 light detector. The black solid line shows scintillation light spectrum of a ^{241}Am source shining on the sapphire titanium doped crystal in addition to the X-ray spectrum.

by the change in gain at the different operating point since the heater pulses, which are affected in the same way as particle pulses by the slope change, did not show such a decrease in this pulse height. For both measurements the same heater structure and the same set of injected heater voltages for the heater pulses was used. Therefore the amplitude of the particle pulses, before and after the lead deposition, should be about the same. Figure 5.15 illustrates the effect showing the templates of ^{55}Mn K$_\alpha$ events and the templates of heater pulses for 0.1V injected heater voltage before and after the lead film deposition. In order to account for different squid settings and different slope of the transition curve, the vertical axis was scaled appropriately using squid transfer coefficients and normalized to the heater pulse amplitude in both cases. As can be seen in figure 5.15, the pulse height of the ^{55}Mn K$_\alpha$ template is decreased by a factor of about three after the lead film deposition.

In order to understand this behavior and keeping in mind that there are many factors influencing the light detector performance, a qualitative interpretation of the observations will be discussed in the following paragraphs.

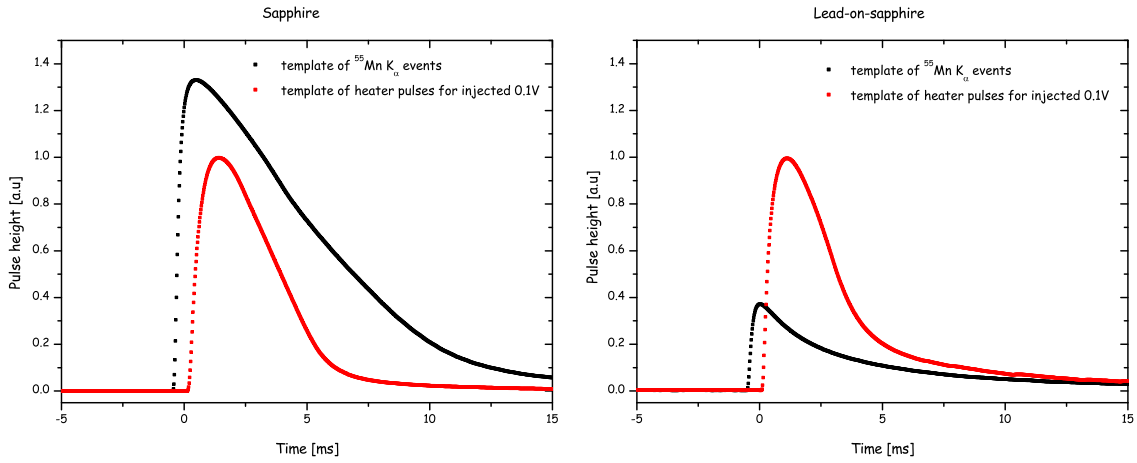

Figure 5.15: The left and right figures show the templates of ^{55}Mn K$_\alpha$ events and the templates of heater pulses for 0.1V injected heater voltage before and after the lead film deposition respectively. In order to account for the different slope of the transition curves at the different operating points of the measurements, the vertical axis is normalized to the heater pulse amplitude. The pulse height of ^{55}Mn K$_\alpha$ template is decreased by a factor of about three after the lead film deposition.

The light detector response

The template obtained by averaging many measured particle pulses in the low energy region for the light detector with a pure sapphire absorber was fitted according to equation 5.1 and the results of the fit are shown in figure 5.16 (top panel). For comparison the fitted templates for ^{55}Mn K_α X-ray absorption and scintillation light absorption measured with the light detector after the lead deposition are presented in the bottom panel of the same figure.

Discussion

After a scintillation photon (about 2 eV energy) is absorbed in the superconducting Pb-layer, which has an energy gap at zero temperature of 0.17 meV [Zehnder, 1995], it breaks Cooper pairs producing excited quasi-particles. Similar to the energy down-conversion process in the superconducting aluminum (see section 3.2.2), these quasi-particles will relax by phonon emission and recombine emitting recombination phonons. Phonons with energy $> 2\Delta$ can break other Cooper pairs and create new quasi-particles inside the lead, while phonons with $\leq 2\Delta$ might be transmitted across the lead/sapphire boundary, with transmission coefficients determined by the acoustic mismatch. Recombination phonons with energy greater than 2Δ can again break other Cooper pairs [Rothwarf & Taylor, 1967]. This process extends the intrinsic life time of quasi-particles and, combined with the reflection of the recombination phonons at the boundary of

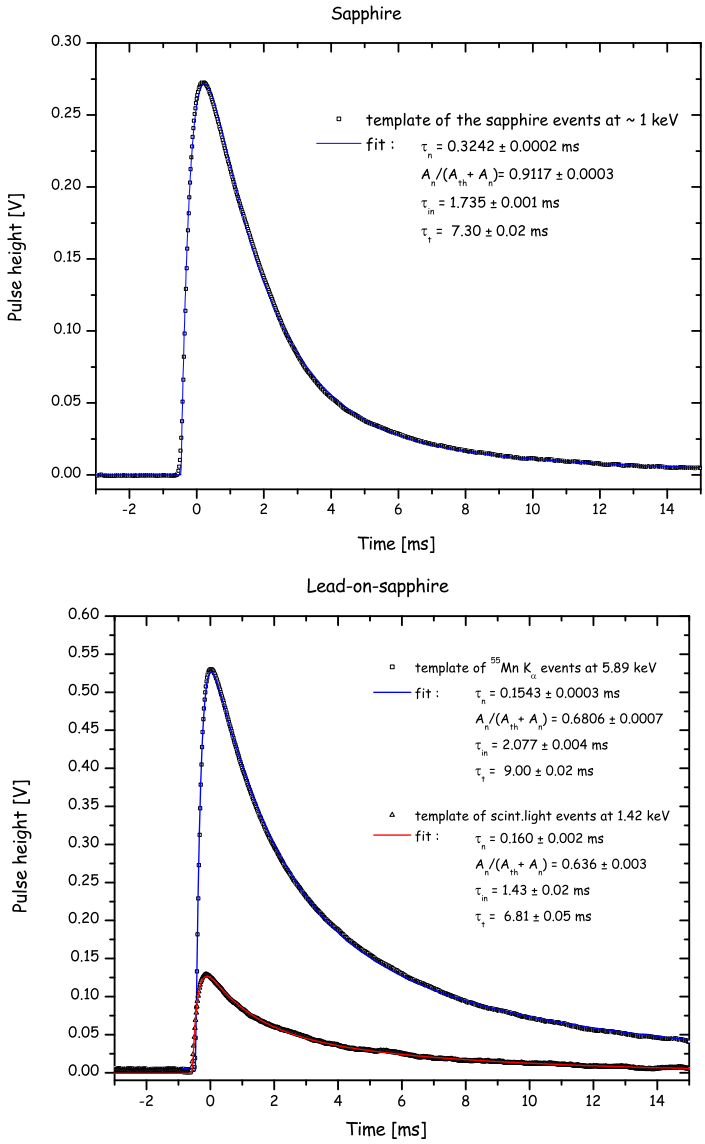

Figure 5.16: Relevant parameters resulting from the fit of particle interactions in the pure sapphire absorber (top) and in the lead-on-sapphire absorber (bottom). The parameters include rise time τ_n of the two signal components, fraction of the non-thermal component $A_n/(A_{th} + A_n)$, decay time τ_{in} of the non-thermal component and decay time τ_t of the thermal component.

the sapphire, results in a delayed heat flow to the thermometer which increases the rise time of the pulses. The delay of the "2Δ-phonons" produced in lead is primarily determined by the effective lifetime of quasi-particles which has been estimated to be $\tau_{qp} = 89.5 \pm 1.2\mu s$ for the case of a round (1 mm diameter and

2μ m thick) lead film on a $(20 \times 10 \times 5)\,\mathrm{mm}^3$) sapphire substrate at a temperature of 20 mK [Bento, 2004]. In the same measurement, the observed rise time of pulses due to X-ray absorption in this lead film was about 180 μs.

For the events in the light detector from an ^{55}Fe source, the attenuation length of a 6 keV X-ray is equal to 34 μm in sapphire and 1.9 μm in lead [CXRO, 2008]. Since the lead layer is only about 0.1 μm thick the absorption of X-rays occurs mainly in the sapphire.
After the X-ray absorption, a very rapid down-conversion of the deposited energy occurs resulting in a population of high frequency phonons with half of the Debye frequency, which is about 10 THz for sapphire. These phonons quickly undergo anharmonic decay with a mean free path of about 0.1 μm in sapphire. Following a simple model in which the high frequency phonons convert down to phonons with half of the frequency, the second generation of phonons have about 5 THz and a mean free path before anharmonic decay in the range of 1.6 to about 30 μm [Poelaert et al., 1996]. Thus many of these high frequency phonons have an energy higher than twice the energy gap of lead (2Δ-phonons of lead have the frequency of about 2 THz). After these phonons reach the lead/sapphire interface and are transmitted into the lead they will break Cooper pairs inside the lead and produce excited quasi-particles. As a consequence, part of energy deposited by X-ray absorption is delayed by the lifetime of the quasi-particle in the superconductive lead and therefore no significant difference in the rise time of the X-ray absorption and scintillation light absorption is to be expected. This disagree with observation (see figure 5.16 bottom panel).
The down-conversion in energy in the sapphire substrate continues until the energy of the phonons becomes low enough such that their mean free path is longer than the thickness of the substrate. Then their effective mean free path can be approximated by the substrate thickness. In a sapphire crystal, phonons with a frequency lower than 1 THz have a mean free path against anharmonic decay in the millimeter range [Poelaert et al., 1996]. The population of these non-thermal phonons spreads around the substrate with the speed velocity of sound, having multiple reflections at the surface. On a perfect surface the phonons are reflected specularly, but in a real crystal imperfections and adsorbates can cause diffuse reflections. Most of these reflections are elastic and contribute to a uniform phonon distribution in the crystal. On the other hand inelastic reflections through surface excitations result in the thermalization of the phonons.
As seen from table 5.6 approximately 72% of the phonons incident at the sapphire/lead interface are transmitted into the lead layer and only about 1% are transmitted at the lead/sapphire interface. This means that a phonon has to undergo many reflections inside the lead layer in order to be transmitted back to the sapphire. When compared to the pure sapphire absorber this results in an increased probability for thermalization. In addition the losses of non-thermal phonons due to inelastic scattering on the surface depends on the quality of the

Transmission from→ to	$\langle\alpha\rangle$ [%]	G_K/T^3 [kW· K^{-4}· m^{-2}]
$Al_2O_3 \rightarrow$ Pb	71.56	1.88
Pb→ Al_2O_3	0.96	0.54

Table 5.6: Parameters numerically calculated according to Pröbst et al. [1995] for the transmission of phonons across the $(1\bar{1}02)$ plane of sapphire into polycristalline lead film with the crystals randomly oriented. Total transmission coefficient $\langle\alpha\rangle$ (averaged over modes and wave vectors of the incident phonons) and Kapitza conductance G_K per T^3.

material and for a polycristalline lead layer with the naturally grown lead-oxide[11] they are expected to be higher than for a sapphire monocrystal[12].
As a consequence, for the lead-on-sapphire absorber compared to the pure sapphire absorber, the number of non-thermal phonons that reach the thermometer is expected to decrease and the number of thermal phonons to increase. The experimental values obtained by fitting the template for the low energy events in the case of pure sapphire absorber and templates for the ^{55}Mn K_α and scintillation light events in the case of lead-on-sapphire absorber, confirm this expectation (see figure 5.16). The ratio of the non-thermal to thermal component is significantly smaller in the case of lead-on-sapphire substrate for both fitted templates (68.1 and 63.6%) than for low energy events in the pure sapphire absorber (91.2 %). Furthermore, according to the values obtained from the fit, the pulses after the deposition of the Pb-layer have a rise time faster by a factor of 2. As previously discussed (see section 3.2.2), the rise time in the light detector thermometer is mostly determined by the thermalization time of the non-thermal phonons in the substrate and by the quasi-particle diffusion time in the phonons collectors . Since the same thermometer was used in both measurements, this result points to a faster thermalization of non-thermal phonons in the lead-on-sapphire substrate, as expected from the model discussed.

Superconducting Pb-layers are suitable as absorbers for the scintillation light of the sapphire crystal. Despite the strong reduction in pulse amplitude after the Pb-layer deposition it is possible to see that the fraction of detected scintillation light is larger than with Si substrates. These results agree with optical measurements at room temperature. Energy resolution seems to worsen after the deposition of the lead absorption layer, but due to the non-smooth transition

[11]Since the cryogenic, optical and structural measurements described here were performed some months after the Pb-layer deposition the naturally grown lead-oxide is expected to be present.

[12]An increase of losses of non-thermal phonons has also been observed after the deposition of a silicon absorption layer on a sapphire substrate [Frank, 2002].

curve of the thermometer this can not be clearly stated. The faster rise time of the pulses after the lead layer deposition indicates an increase of losses at the surface of the substrate. The reduction of the signal can be explained by the combined effect of the lifetime of quasi-particles in Pb and a low transmission of phonons from lead to sapphire. Possible ways to improve the phonon transmission are the inclusion of a layer of appropriately chosen material between the sapphire and Pb-layer or by using another substrate. In addition superconducting Nb-layers on the sapphire substrate are being tested, which have a transmission coefficient five time larger than for Pb-layers [**?**].

Another route to improve the discrimination power of the combined measurement of scintillation light and phonons is to avoid the degradation of scintillation light output of $CaWO_4$ crystal in the process of tungsten film deposition at high temperatures ($\sim 450°C$). This can be achieved by producing thermometers on small $CaWO_4$ samples which are then glued to the big crystals [Kiefer, M., 2007].

Chapter 6

Light detector performance in Gran Sasso

After the major upgrade of the CRESST setup a commissioning runs was performed. Three detector modules could be operated in this commissioning run (Run30) in the period March to November 2007. In this chapter the overall performance of the light detectors during Run30 will be presented.

6.1 Light detector layout and operation

The detector modules were mounted as described in section 2.3. The three $CaWO_4$ crystals named, Verena, Zora and Quedlina were associated with light detectors SOS21, SOS23 and SOS30 respectively. All 3 light detectors had silicon-on-sapphire (SOS) round substrates (ø 40mm) as detector absorber.

6.1.1 Thermometer layout

The two different thermometer layouts of the light detectors that were operated in Run30 are shown in figure 6.1 and their relevant parameters are summarized in table 6.1.

Light detector SOS30 has a thermometer with a three times larger tungsten film area compared to the standard geometry previously described. The motivations for this choice are: the increase of the quasi-particle collection efficiency by prolonging the border between the W film and Al/W bilayers and the enlargement of the total phonon collection area.

Thermometer fabrication

The tungsten films of all light detectors operated in Run30 were produced by electron-beam evaporation of a tungsten single crystal with 99.99% purity in high

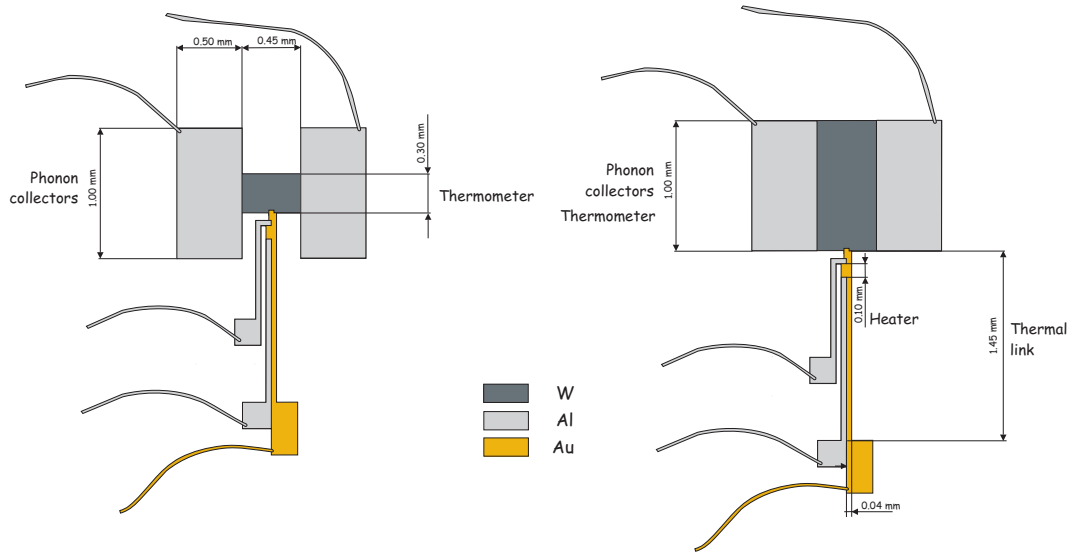

Figure 6.1: Layout of a standard light detector thermometer used in the second phase of CRESST (left) and of a thermometer with three times bigger tungsten film (right). The dimensions that are the same for both thermometers are depict only once.

Light detector	**SOS21**	**SOS23**	**SOS30**
Partner phonon detector	Verena	Zora	Quedlina
Substrate	Silicon-on-sapphire		
Size	ø 40 mm, d=0.46 mm		
Thermometer	deposited on the sapphire side		
Layout	fig. 6.1 left	fig. 6.1 left	fig. 6.1 right
Collection area [mm^2]	1.14	1.14	1.45
W film area [mm^2]	0.45×0.3	0.45×0.3	0.45×1.0
W film thickness [Å]	1300±100	1300±100	1300±100
Al/W bilayer [mm^3]	$2\times1\times0.5\times1.13\cdot10^{-3}$		
Au/W heater area [mm^2]	0.1×0.04		
Au/W thermal link area [mm^2]	∼1.2×0.04	∼1.45×0.04	∼1.45×0.04
Au/W thickness[Å]	1000±100	1000±100	800±100

Table 6.1: Relevant parameters of the light detectors operated in Run30.

vacuum system at the Technical University of Munich [Pfister, 2006]. During this process the substrates were heated to about 450 °C to ensure a good growth of the metal film. The thickness of the tungsten films is ∼1300 kÅ.
The thermometer is structured following the standard procedure described in

section 5.1.

6.1.2 Transition curves

Figure 6.2 depicts the transition curves of the light detectors for 1 μA bias current, obtained by slowly ramping the temperature of the mixing chamber with no heating current through detector heater. The carousel, which is the temperature reference for the detectors, is, as previously mentioned, only weakly coupled to the mixing chamber. To minimize the temperature gradient between the mixing chamber and the carousel, the temperature of the mixing chamber was slowly ramped within 10 hours from from 21.5 mK to 7 mK. The temperature of the thermometers is always higher than the temperature of the carousel due to self heating of the films (see equation 3.37). Additionally it can not be excluded that the temperature of the detector holder was higher than the mixing chamber temperature due to the Cu heat leak[1].
As can be seen from figure 6.2, the transition temperatures of all detectors are in the range of 14 mK to 18 mK (mixing chamber temperature) with a width of 1.5 mK to 4 mK. The resistance of the thermometer is calculated as

$$R_f = R_s \frac{I_s}{I_0 - I_s}\,, \tag{6.1}$$

where R_s is the reference resistance, I_0 is the current applied to the bias circuit and I_s is the current in the input coil branch which is proportional to the measured signal (see equation 2.4). The error of the evaluated resistance is estimated to be about 10%. This is mostly due to the uncertainty of about 2% in the values of the SQUIDs input couplings[2] (current to flux transfer coefficients) which affects the evaluation of I_s.
SOS21 and SOS23 show a resistance of about 300 mΩ in the normal conducting state, while SOS30 shows a resistance of about 100 mΩ as expected because of its 3 times wider W film. The nonzero value of the resistance of all 3 films in the superconducting region points to a residual resistance in series with the thermometers, probably due to a imperfect contact to the readout circuit.

In addition to the heat sink temperature sweeps, heater sweeps with different bias currents have been measured. Figure 6.3 shows heater sweeps for a wide range of bias currents for detector SOS23. The heater input voltage shown on the x axis is the parameter which is directly set during the measurements. It is proportional to the heater power applied to the thermometer (see section 2.4.2). The corresponding heater current is also shown in figure 6.3. The transition

[1] The heat leak in Cu originates from the ortho-para conversion of H_2 molecules of enclosed gas bubbles.

[2] The uncertainty in the value of resistance due the uncertainty of the SQUID transfer functions depends on the amplification range of the SQUID during measurements.

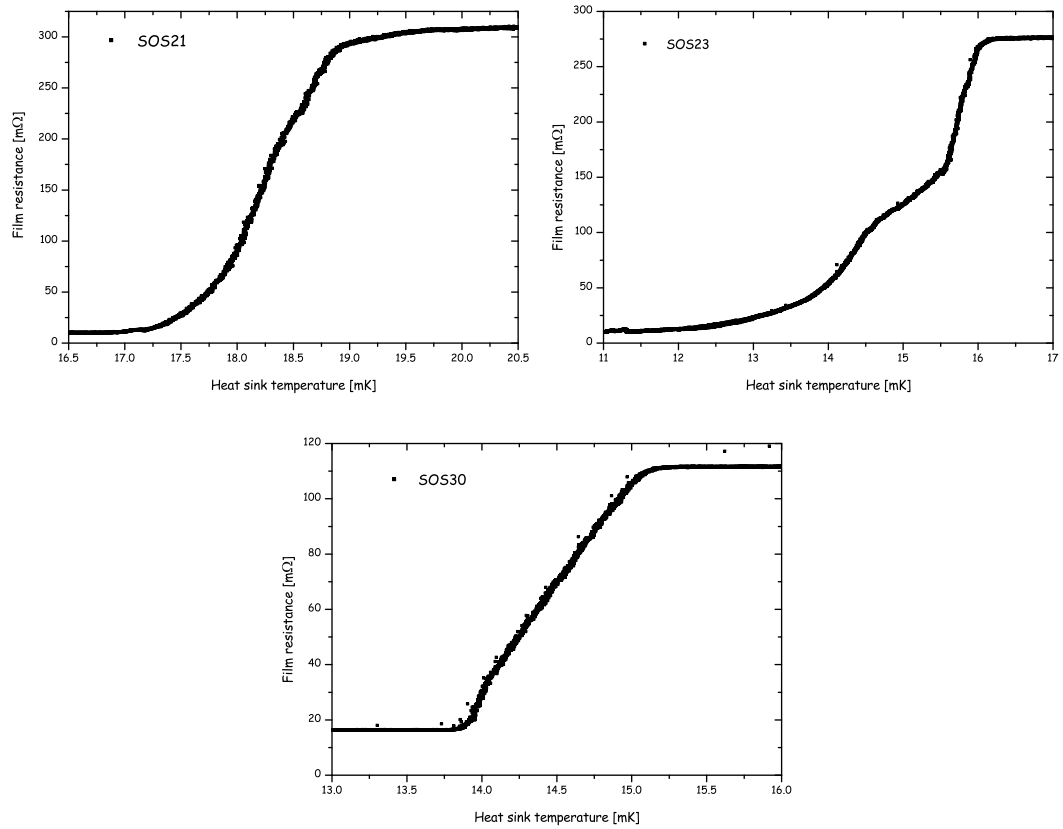

Figure 6.2: Transition curves for the three light detectors SOS21, SOS23 and SOS30 measured with 1 μA bias current. The heat sink temperature is read out with a carbon resistor mounted at the mixing chamber of the cryostat.

curve becomes smoother as the current increases from 30 nA to 7.144 μA. This improves the linearity of the detector response which is, as previously discussed, needed for the correct evaluation of the pulse height. The broadening of the transition and the shift towards lower heater input voltage when bias current is increased is due to the critical current effect.
The heater sweeps for the light detectors SOS21 and SOS30 are shown in figures 4.1 and 4.2. The bias current used for the detectors SOS21 and SOS23 during Run30 was 7.144 μA, while SOS30 was operated with 2 μA.

6.1.3 Operating point

The main requirements for a good operating point are: the linearity of the detector response (the smoothness of the transition curve), the steepness of the curve to obtain a high sensitivity and the dynamical range fulfilling the experimental needs (determined by the position of the operating point within the transition

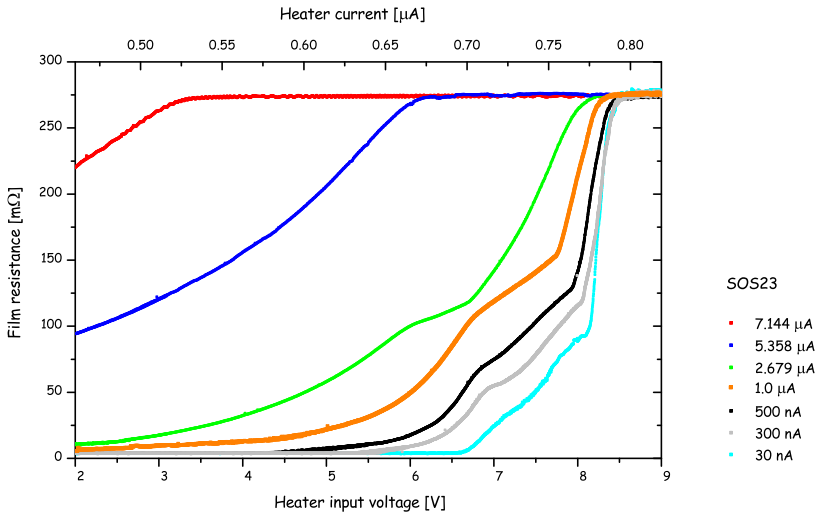

Figure 6.3: Measured transition curves for the light detector SOS23 with bias currents ranging from 30 nA to 7.144 μA obtained by varying the heater current through the film heater. The mixing chamber was stabilized at 7 mK.

combined with the heat capacity of the film and the slope of the curve).
In order to find the optimal operating point heater pulses of different amplitudes have been injected during the sweep of the heater current. They probe different regions around the operating point according to their energy. In this way, for the desired energy range, an operating point with a certain slope and a linear response, which ideally does not change for small variations around the point, can be determined. Additionally, in order to apply the stability control algorithm based on the pulse height of large heater pulses (described in section 4.1.2), the pulse height of the highest heater pulses should be sensitive to small temperature variations at the the operating point.

Figure 6.4 shows the voltage response to the various heater pulses in a broad range of injected voltages (corresponding to a broad range of energy) as a function of the heater input voltage for the light detector SOS23. The vertical red dashed line indicates the chosen operating point. As can be seen from figure 6.4, for this operating point small heater pulses have a rather temperature independent response. On the other hand the pulse height of the highest heater pulse (control heater pulse) changes with the heater input voltage indicating the change of slope at the top of the transition curve, making the stability control possible.
Using this method it is possible to obtain detailed information about the overall response of the detector which cannot be easily obtained from transition curves.

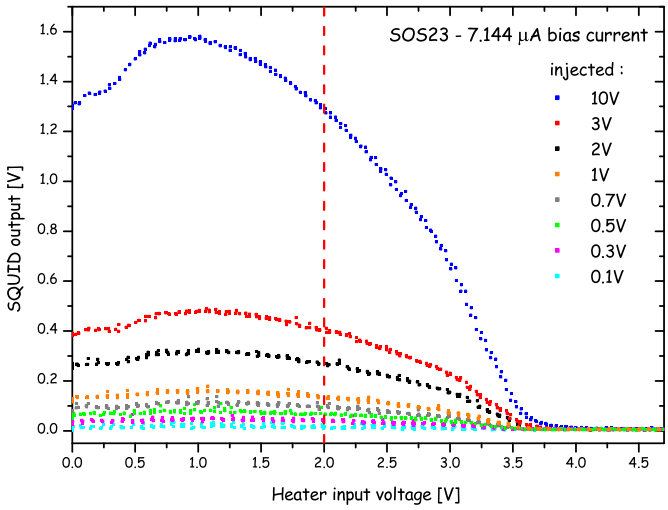

Figure 6.4: Voltage response to heater pulses of different energies as a function of heater input voltage for the light detector SOS23 with 7.14 μA bias current.

The difference can be clearly seen by comparing figure 6.4 and figure 6.5.
As can be seen from figure 6.4, the measured pulse height of control heater pulses is constant for the heater input voltage in the range from about 0.8 V to about 1 V and it decreases for heater input voltage less than 0.8 V. This points to the presence of substructures in the transition curve. From the curve in figure 6.5 these features can not be so clearly interpreted. The insert in figure shows an enlarged view for the heater input voltage below 1 V. The non-smoothness of the curve is visible but to determine which operating point is the optimal one is rather difficult.
The control heater pulses for the detector SOS21 were only slightly saturated. This choice is a compromise between the need of heater pulses covering the full dynamical range of the detector and the minimal accurate amplitude of injected heater pulses for a chosen output range of the Heater-Bias electronics. The control pulses of the light detector SOS23 were similarly only slightly saturated, while in the case of SOS30, due to a narrower transition curve (see figure 6.2) and possibly due to the lower bias current, the control pulses were completely saturated.
In order to optimize the response of detector in the energy range of interest, a gamma calibration is performed before the detectors are stabilized using a ^{57}Co source to illuminate the detectors, as described in section 4.2.2.

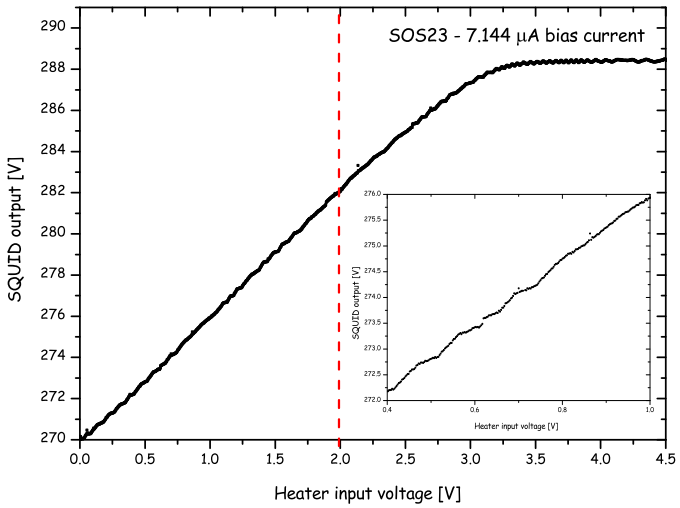

Figure 6.5: Measured transition curve for the light detector SOS23 with bias current of 7.144 μA obtained by varying the heater current through the film heater. The insert shows a region for heater input voltage from 0.4 V to 1 V. The SQUID voltage output, is increased by a factor of one hundred to allow the direct comparison with the scale of heater pulses in figure 6.4, where a different operating range of the SQUID was used.

6.2 Results

Since only about 1% of the energy deposited in $CaWO_4$ by γ or β interaction can be detected as scintillation light, the performance of light detectors is a critical issue for the light-phonon active background discrimination at energies relevant for WIMP searches.

6.2.1 Light detector energy resolution

The energy resolution of the light detector plays an important role in the performance of a detector module because it determines the discrimination threshold. The resolution of the light detector defines in fact the width of the different bands corresponding to the various types of interactions in the scintillating absorber and therefore the energy where they merge and the efficiency of the discrimination drops.

Figure 6.6 (left panel) shows the energy spectrum measured with phonon detector Verena during the ^{57}Co gamma calibration. The good energy resolution of the phonon detector ($\sim 1\%$) is used to define a region which contains the 122 keV

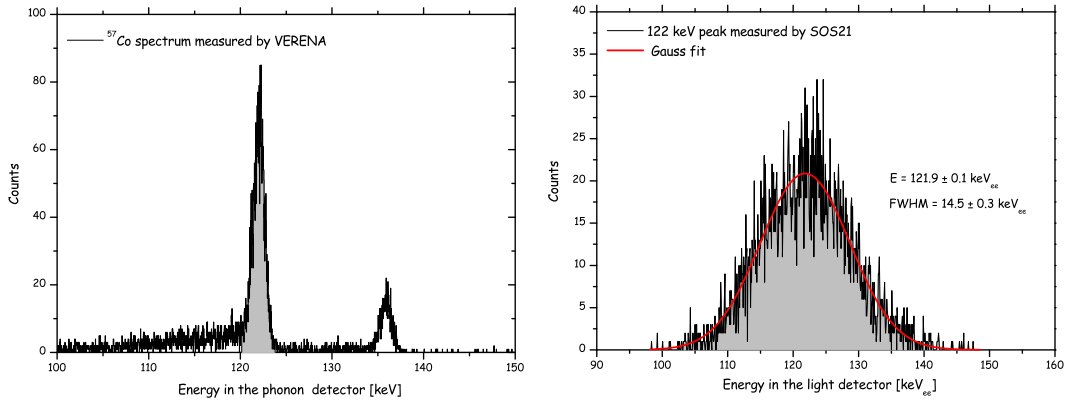

Figure 6.6: ^{57}Co gamma calibration spectra of the phonon detector Verena (left panel). The shaded region indicates the 122 keV γ line. The 122 keV peak as seen in the light detector SOS21 with the Gaussian fit of peak superimposed, is shown in the right panel.

γ line. The corresponding peak as seen in the light detector SOS21 with a resolution of about 12% is presented in the same figure to the right.
Table 6.2 summarizes the measured energy resolution of the light detectors which were operated in Run30 (SOS21, SOS23 and SOS30) and in Run28 (BE13 and BE14). Besides the widths of the ^{57}Co lines at 122 keV and 136.5 keV (as seen in the light detector), the energy resolution for the W K_α and W K_β escape peaks from the 122 keV line and the W K_α escape peak from the 136.5 keV line is given in the same table.
The resolution of the gamma emission peak at 46.54 keV due to ^{210}Pb contamination, which has been observed in the background data samples during Run28 and Run30 is also shown in the table. The 46.5 keV gamma emission is accompanied with the beta spectrum of the ^{210}Pb decay to ^{210}Bi which extends up to 63.5 keV. The measured energy spectrum due to ^{210}Pb contamination depends on whether the contamination is external or internal with respect to the $CaWO_4$ absorber. For an external ^{210}Pb contamination, as it was the case in Run28, the beta spectrum is not visible and the position of the gamma peak can be precisely determined [Angloher et al., 2005]. In Run30 the gamma peak was not well represented by a Gaussian since the beta spectrum was superimposed due to a mostly internal ^{210}Pb contamination. Hence, the measured widths of the 46.5 keV gamma emission line in the light detectors SOS21, SOS23 and SOS30 might be slightly overestimated.
It should be noted that the light detectors operated in Run28 have a 30×30 mm^2 pure silicon wafer as absorber in comparison to the circular (40 mm diameter) silicon-on-sapphire absorbers for the light detectors operated in Run30. The thermometer layout did not change significantly from Run28 [Petricca, 2005] to

Light detector	**SOS21**	**SOS23**	**SOS30**	**BE13**	**BE14**
Partner phonon detector	Verena	Zora	Quedlina	Daisy	Julia
FWHM at 136.5 keV [keV$_{ee}$]	15.7±0.6	21.1±0.5	15.5±1.0	24.9±2.6	30.4±2.3
FWHM at 122 keV [keV$_{ee}$]	14.5±0.3	18.0±0.3	15.6±0.4	23.8±2.2	26.4±3.0
FWHM at 78 keV [keV$_{ee}$]	11.0±2.4	11.2±0.9	-	-	-
FWHM at 63 keV [keV$_{ee}$]	9.4±1.0	10.9±0.4	11.8±1.9	14.7±2.7	19.6±6.2
FWHM at 55 keV [keV$_{ee}$]	10.8±1.6	10.5±0.8	10.7±3.3	9.2±4.8	-
FWHM at 46.5 keV [keV$_{ee}$]	12.3±0.5	17.4±1.2	14.1±1.1	10.5±1.2	8.8±2.0

Table 6.2: Energy resolution of the light detectors used in Run28 (BE13 and BE14) and in Run30 (SOS21, SOS23 and SOS30) for monochromatic gamma rays in the energy range from 46.5 keV to 136.5 keV (referred to the energy deposition in the phonon detector). Statistical errors (1σ) for the Gaussian fit of the peaks are given.

Phonon detector	**Verena**	**Zora**	**Quedlina**	**Daisy**	**Julia**
Partner light detector	SOS21	SOS23	SOS30	BE13	BE14
FWHM at 661 keV [keV]	12.3	15.03	12.1	13.6	13.9
Normalized light output [%]	108.6	93.2	105.3	96.7	89.5

Table 6.3: Energy resolution of the ^{137}Cs line for different $CaWO_4$ crystals measured with a photomultiplier at room temperature [Ninković, 2005][Ninković, 2007][Petricca, 2007]. The light output is given normalized to the light output of a chosen $CaWO_4$ crystal, which is used as reference. The errors are smaller than the stated precision.

Run30. Light detector absorbers of different materials and sizes, besides having different absorption efficiency for the scintillation light, can also introduce different energy losses (e.g. due to different surface quality). However, in a comparison of the performance of the silicon-on-sapphire light detector and the silicon light detector in the same setup in Petricca [2005], both light detectors performed similarly in terms of achieved energy resolution for scintillation light and of the amount of detected scintillation light for a given energy deposition in the $CaWO_4$ crystal[3].

The observed resolution of a light channel when used in a detector module reflects not only the performance of the detector itself but also fluctuations of the light production and collection. The achieved energy resolution in a low temperature measurement is comparable to the values (see table 6.3) obtained at room

[3]In Petricca [2005] the silicon light detector measured about 20% more light than the silicon-on-sapphire light detector. This was due to the choice of $ZnWO_4$ as scintillator. $ZnWO_4$ crystals emit at higher wavelengths than $CaWO_4$ crystals, where the absorptions of silicon-on-sapphire absorber is decreased by about 20%.

temperature using a photomultiplier tube to detect the scintillation light due to the absorption of 661 keV photons (^{137}Cs source) in $CaWO_4$ crystals [Ninković, 2005, 2007, Petricca, 2007]. As can be seen from tables 6.2 and 6.3, the energy resolution obtained with the light detector depends on the scintillating crystal sample. In both measurements at room temperature and at low temperature the best resolution was obtained with the crystals Verena and Quedlina.

6.2.2 Energy dependence of the light detector resolution

As can be seen from the values in table 6.2, the energy resolution of the light detector measured for monoenergetic γ's shows an energy dependence. In order to investigate the orgin of this energy dependence, the light detector energy resolution is parameterized as

$$\Delta E_{rms} = \sqrt{A_0^2 + A_1 E_{pd} + A_2 E_{pd}^2}\,, \tag{6.2}$$

where three independent sources of noise are taken into account and are thus added quadratically:

$\boldsymbol{A_0}$: The contribution of the baseline noise of the detector, which arises from a combination of detector thermal fluctuations, electrical noise of the resistors and SQUID noise.

$\boldsymbol{A_1}$: The term describes the Poisson photon counting fluctuations and thus scales as the square root of the number of the energy carriers. For the case of the light detectors the energy carriers are scintillation photons carrying a constant fraction of E_{pd}.

$\boldsymbol{A_2}$: The term is due to a position dependent light detection efficiency of the detector module which can arise from a dependence of the light output on the position of the energy deposition within the $CaWO_4$ crystal or from a non-uniform response of the light detector, and may also account for further effects contributing to fluctuations proportional to E_{pd}.

The light detectors are calibrated with the scintillation light from the $CaWO_4$ crystals and therefore the energy parameter E_{pd} appearing in equation 6.2 corresponds to the energy measured in the phonon detector. Since nuclear recoils induced by neutrons and WIMPs are expected to be distributed uniformly in the crystal volume, the energy dependence of the resolution of the light detectors should be extracted from data corresponding to an uniform irradiation of the crystals. For this reason data from a ^{232}Th calibration during Run28 have been used. The low energy continuum in this data is due to Compton scattered

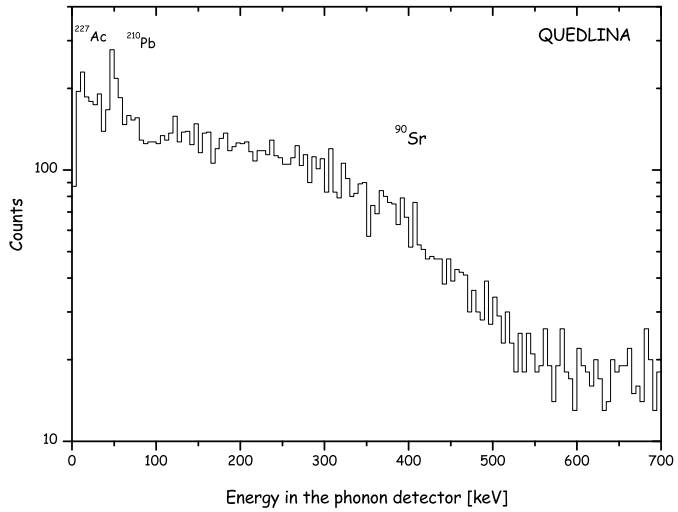

Figure 6.7: The background spectrum measured by the phonon detector Quedlina during Run30. The main features of the spectrum are due to ^{90}Sr, ^{210}Pb and ^{227}Ac contaminations of the crystal.

high energetic γ rays which interact rather uniformly within the crystal. During Run30 no ^{232}Th calibration data were taken. Instead, the measured band of background counts, associated with γ and β interactions inside the crystal, is used. This is not optimal, since it implicitly assumes that the low energy continuum is due to γ and β interactions homogeneously distributed within the volume of the $CaWO_4$ crystal, which may be not true as e.g. in the case of ^{210}Pb contamination. Nevertheless it is still a valid assumption since the major part of the low energy continuum in Run30 was due to ^{227}Ac and ^{90}Sr contaminations of the $CaWO_4$ crystals, which in all probability are uniformly distributed within the volume of the crystal. Figure 6.7 shows the measured background spectrum for the crystal Quedlina where the ^{90}Sr β spectrum with an end point of 546 keV is the dominant contribution.
To exclude the effects of electromagnetic interferences or grounding problems, which intermittently occurred during the commissioning Run30, data samples with a constant baseline noise for both light and phonon detector in the same detector module have been chosen for the following analysis.
The resolution of the light detectors is extracted from the measured background data in the energy range specified in table 6.4. The first requirement for the chosen energy range was the linearity of the thermometer response. In this way eventual spreading of the points in the spectrum of the light detector due to the fit procedure is avoided. The scaling of the template event for fitting pulses of energy much higher than the template, implies also a corresponding scaling of

any non-averaged noise[4] in the baseline of the template. This, combined with the truncation of fit, might cause uncertainties in the evaluated pulse height.

In addition, in the specified energy range, the widths of the heater pulses was

Light detector	**SOS21**	**SOS23**	**SOS30**	**BE13**	**BE14**
Energy range [keV$_{ee}$]	0-140	0-70*	0-140	0-140	0-140
Heater pulses Cnts per pulse	∼5700	∼6500	∼700	∼600	∼600
Energy [keV$_{ee}$]	10.77±0.01	2.23±0.01	5.76±0.08	5.79±0.03	3.65±0.06
FWHM [keV$_{ee}$]	2.28±0.02	1.78±0.02	3.2±0.2	1.3±0.1	2.6±0.1
Energy [keV$_{ee}$]	21.65±0.01	4.61±0.01	11.87±0.07	11.65±0.03	15.5±0.1
FWHM [keV$_{ee}$]	2.27±0.03	1.75±0.02	3.2±0.2	1.38±0.06	4.2±0.5
Energy [keV$_{ee}$]	32.63±0.01	6.95±0.01	18.16±0.07	17.61±0.03	21.98±0.09
FWHM [keV$_{ee}$]	2.33±0.03	1.70±0.02	3.2±0.2	1.62±0.08	4.8±0.2
Energy [keV$_{ee}$]	43.64±0.01	11.68±0.01	29.96±0.08	35.66±0.03	44.5±0.1
FWHM [keV$_{ee}$]	2.31±0.03	1.70±0.02	3.1±0.2	1.56±0.05	4.1±1.2
Energy [keV$_{ee}$]	54.65±0.01	16.37±0.01	36.02±0.07	47.74±0.03	59.6±0.1
FWHM [keV$_{ee}$]	2.23±0.03	1.75±0.02	3.0±0.2	1.55±0.05	4.1±1.7
Energy [keV$_{ee}$]	65.73±0.01	23.40±0.01	42.09±0.07	59.80±0.03	74.9±0.1
FWHM [keV$_{ee}$]	2.31±0.03	1.79±0.02	3.0±0.2	1.57±0.05	5.2±0.3
Energy [keV$_{ee}$]	76.82±0.01	46.87±0.01	59.75±0.07	120.23±0.03	150.4±0.1
FWHM [keV$_{ee}$]	2.36±0.03	1.81±0.02	2.9±0.2	1.46±0.05	4.7±0.2
Energy [keV$_{ee}$]	110.31±0.01	70.21±0.01	120.81±0.08	178.75±0.03	223.72±0.08
FWHM [keV$_{ee}$]	2.43±0.03	1.82±0.02	3.2±0.2	1.54±0.05	4.4±0.2
$\langle$**FWHM**$\rangle$ **[keV$_{ee}$]**	2.31±0.01	1.87±0.01	3.4±0.1	1.54±0.02	4.7±0.1
$\langle\sigma\rangle$ **[keV$_{ee}$]**	0.980±0.004	0.794±0.004	1.43±0.05	0.66±0.01	2.01±0.03

Table 6.4: Resolution of heater pulses of different energies in the energy range used for the extraction of the light detectors' energy resolution. Statistical errors (1σ) for the Gaussian fit of the peaks are given.*The energy range of light detector SOS23 was limited to this energy region because the highest injected heater pulse within the linear region corresponded to 70 keV$_{ee}$.

constant supporting the correct choice of the used energy interval. The heater pulses are directly injected into the thermometer. Hence, their energy resolution is mainly determined by the baseline noise. A possible worsening of the

[4]A template event derived from a limited number of pulses may still contain same noise, that was not averaged. This depends on the time period (frequency) of the noise with respect to duration of the pulses, where low frequency noise terms are more likely not be averaged away.

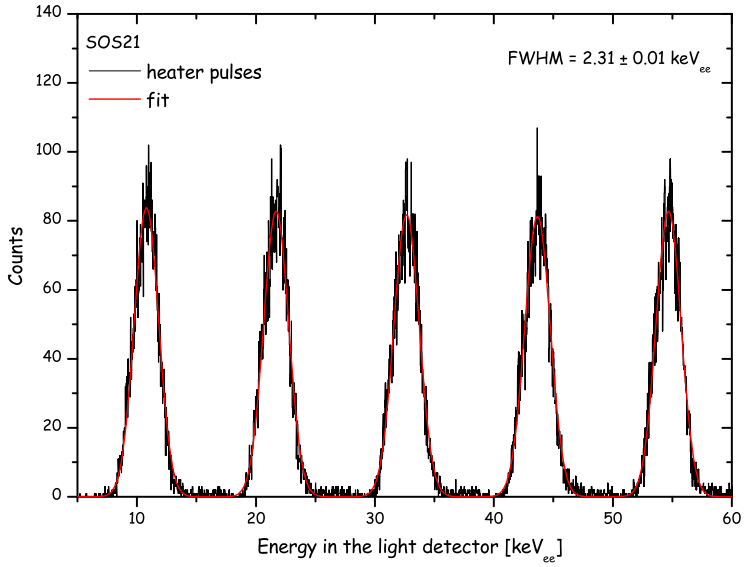

Figure 6.8: Heater pulses of different energies measured by the light detector SOS21. Gaussian fit with a common width is superimposed.

resolution of the heater pulses within the region of linear response of the thermometer might therefore indicate local non-smoothness of the transition curve. The resolution of the heater pulses of different energies in the specified energy range for the extraction of the light detector resolution is given in table 6.4. The averaged energy resolution obtained by simultaneously fitting the heater pulses with a Gaussian of common width for all peaks (see figure 6.8) is also given in the same table.
In the case of SOS23 the corresponding energy range was limited to 70 keV$_{ee}$, because in the linear range heater pulses were only available up to this energy. Using a large energy range would have in fact required assuming a smooth transition without having heater pulses to probe it.
The resolution of the light detector is extracted using the following procedure.

For each detector module a scatter plot of energy in the light detector versus energy in the phonon detector is fitted with a second order polynomial passing through zero (see figure 6.9 upper left). In this way a correspondence between energy deposited in phonon detector and energy measured in light detector is obtained. The full energy region is divided in energy bins. The weight of the data points in each bin is calculated from the standard deviation of the data points from the fitted line in this energy bin. The second order polynomial fit is performed instead of a linear fit, to take into account eventual non-linearities in the light output of the $CaWO_4$ crystals. As can be seen in table 6.5, which gives the coefficients of the fit, the second order coefficient a_2 is small with respect to the first coefficient a_1 indicating a rather linear light output in the chosen energy

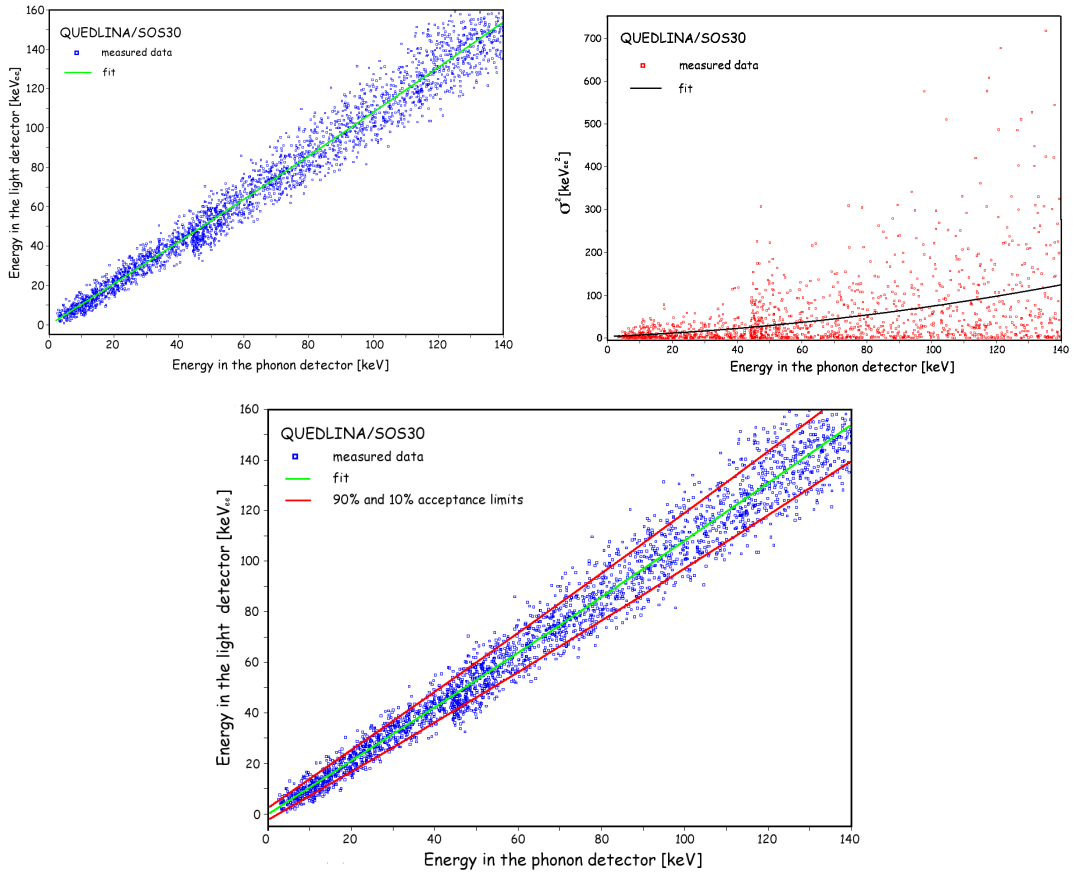

Figure 6.9: Figure on the left shows the energy in the light detector SOS30 versus energy in the phonon detector Quedlina fitted with a polynomial function through zero. In figure on the right the squared standard deviation from the polynomial fit is plotted as a function of energy in the phonon detector together with a fit according to the parametrization given in equation 6.2. 90% and 10% acceptance limits (i.e. 90% of the data points are below upper and 10% below the lower curve), derived from the polynomial fit of the squared standard deviation are shown in figure at the bottom.

region.

For each data point in the scatter plot the deviation from the fitted line is calculated. The square of these deviations of all points is then fitted with equation 6.2 (see figure 6.9 on the right). A quality of the fit can be checked visually in figure 6.10, where the squared deviations averaged in energy bins are plotted together with the fit function. Good agreement is observed. Table 6.6 summarizes the parameters A_0, A_1 and A_2 of equation 6.2 obtained by the fit.

For all light detectors the value of the parameter A_0, which represents the energy resolution at zero energy, agrees with the energy resolution of the heater pulses (see table 6.4). This is expected as the resolution of the detector at zero energy

Light detector	**SOS21**	**SOS23**	**SOS30**	**BE13**	**BE14**
Partner phonon detector	Verena	Zora	Quedlina	Daisy	Julia
Energy range [keV$_{ee}$]	0-140	0-70	0-140	0-140	0-140
a_1 [1/keV$_{ee}$]	0.98	0.94	1.04	0.90	0.89
a_2 [1/keV$_{ee}$]^2	0.0013	0.0036	0.00045	0.00024	0.00065

Table 6.5: Coefficients of the second order polynomial fit through zero of the energy in the light detector as a function of energy in the phonon detector in the energy range used for extraction of the light detectors energy resolution. The first coefficient would have value one and the second coefficient would be zero if it were an ideal detector module having a strictly linear relation between light and phonon measurements. The fit errors are smaller than the stated precision.

is limited by its baseline noise. To correctly evaluate the parameter A_0 is important, since it limits the energy resolution of the light detector in the energy region, which is relevant for WIMP search. The values of the coefficients A_1 and A_2 will be discussed later.

The validity of the described procedure is finally checked by comparing the ob-

Light detector	**SOS21**	**SOS23**	**SOS30**	**BE13**	**BE14**
Energy range [keV$_{ee}$]	0-140	0-70	0-140	0-140	0-140
A_0 [keV$_{ee}$]	1.0±0.1	1.1±0.3	1.9±0.4	0.7±0.5	1.9±0.4
A_1 [keV$_{ee}$]	0.29±0.04	0.33±0.08	0.32±0.08	0.34±0.05	0.36±0.08
A_3	0.0092±0.0004	0.012±0.001	0.0039±0.0006	0.0025±0.0003	0.0041±0.0005

Table 6.6: Coefficients of the parametrization of the light detector resolution given in equation 6.2. Statistical errors (1σ) are given.

served energy resolution for some monochromatic lines present in the spectra and the energy resolution calculated (at the same energy deposition in the phonon detector) by using the values of the fit parameters of table 6.6. Figure 6.11 shows both fitted and observed energy resolution of the light detectors, operated in Run30 and Run28, in terms of FWHM versus energy in the phonon detector. As can be seen from the figure 6.11, for the light detectors SOS21 and SOS23 the energy resolution obtained by the fit and the energy resolution extracted from calibration peaks notably disagree above 50 keV with the fit showing a much steeper increase with energy. For light detector SOS30 the disagreement is less pronounced, while for light detectors BE13 and BE14 the values agree within the errors. The reasons for such a discrepancy for the light detectors operated in Run30 are still under investigation. As visible in figure 6.11 the energy resolution obtained by the fit (red dots in figure 6.11) shows similar energy dependence for

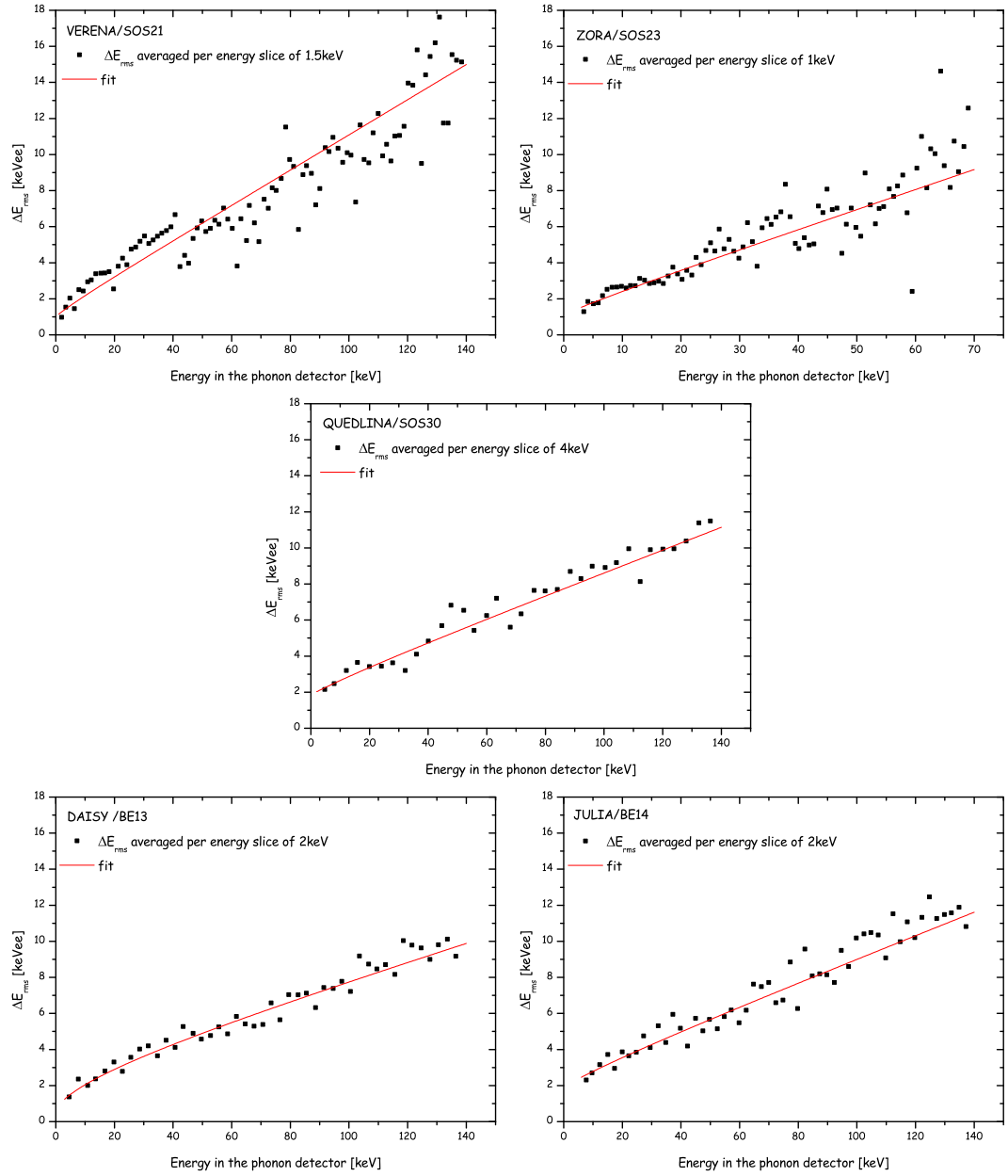

Figure 6.10: Resolution (σ value) of the light detectors in Run28 and Run30 as a function of energy deposited in the phonon detector. The scatter points are standard deviations per specified energy slice from the polynomial fit of energy in the light detector versus energy in the phonon detector. The full line represents the fit according the the parametrization given in equation 6.2.

all light detectors in Run28 and in Run30, while it is the measured resolution of gamma peaks present in spectra (black dots in figure 6.11) which shows different energy dependence in Run30 and in Run28. A possible explanation is given in

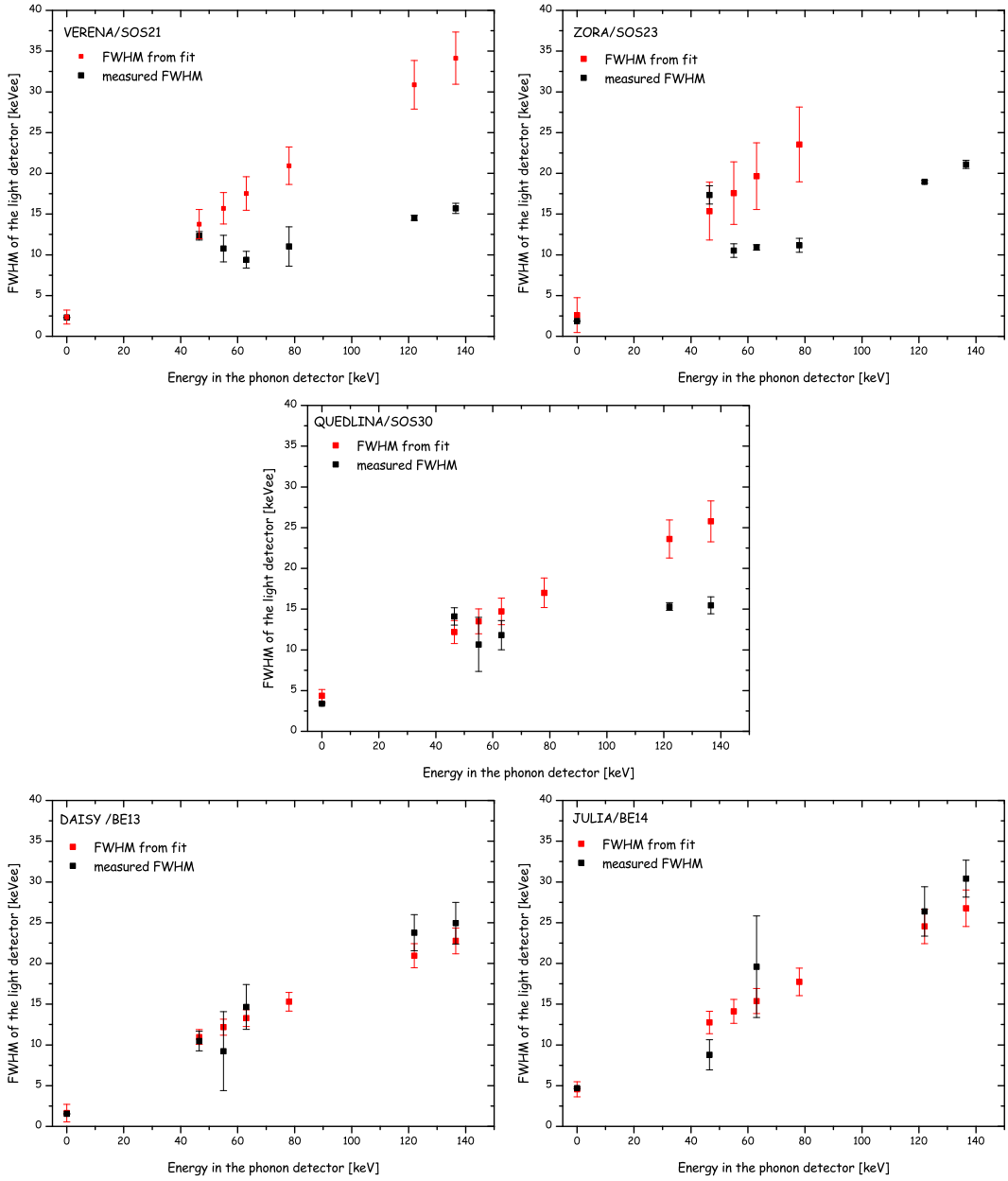

Figure 6.11: The observed resolution (FWHM) of the light detectors compared to the calculated one according to the parametrization 6.2 using values of the fit coefficients from table 6.6 in the energy range which has been used for the extraction of their energy resolution.

the following subsection.

Uniformity of the light output

Due to the high refraction index and to the cylindrical geometry of the $CaWO_4$ crystals, a scintillation photon can undergo many reflections inside the crystal before it hits the surface at an angle that allows it to escape. The competing processes of elastic scattering and absorption in the crystal determine the fraction of photons which escape the crystal i.e. the light output. The cylindrical shape of the crystals can lead to a radially position dependent light output due to different incident angles of the emitted scintillation photon on the crystal surface for energy depositions at different distances from the center. According to simulations of the CRESST detector module in Frank [2002] about 60 % of scintillation photons emitted on the axis of the crystal escape the crystal, while of the photons emitted close to the cylinder wall only about 25 % leave the crystal[5]. As a consequence of such a spatial dependence, uniformly irradiating a crystal would result in an observed non-Gaussian distribution in a light detector. Taking into account that the outer shell of the cylindrical crystal has bigger volume and lower light output with respect to the central part, the light distribution for a given uniform energy deposition in the crystal will be shifted down to the light output corresponding to the energy deposition in the outer shell, with a tail towards the higher light output due to the energy deposition in the inner part of the cylinder. As can be seen from figure 6.12 this spatial effect is not so pronounced, but is present.
The measured values of light detectors' energy resolution at different energies which are plotted in figure 6.11, are mainly obtained from the gamma calibration measurement. In Run30 the ^{57}Co calibration source was mostly irradiating the crystals at their cylindrical surface leading to photon absorption near the crystal surface since the attenuation length for the 122 keV gamma is less than 1mm in $CaWO_4$ [XCOM, 2008]. Hence the observed disagreement can possibly be explained by reduced escape probability from near the surface compared to the rather uniform interactions within the crystal volume like in case of ^{90}Sr internal contamination. In addition, due to the fact that γ rays from the calibration source probe only a small part of the crystal volume the resolution obtained from the calibration data is better in comparison to the one from the background data which is subject to position dependencies of the scintillation light output. To illustrate this, the background data used for extracting the energy resolution and the gamma calibration data for the detector module Verena/SOS21 are plotted together in figure 6.12 on the left. The combined background and gamma calibration data for the detector module Daisy/BE13 are plotted in figure 6.12

[5]Roughening of the crystal surface facing the light detector significantly reduces the spatial effect by allowing the scintillation light to leave the crystal after fewer reflections [Ninković, 2005].

on the right. In Run28 the calibration source was mainly illuminating the surface of the crystal carrying the thermometer leading to a more uniform radial excitation of the crystal and thus more uniform distribution of scintillation light leaving the crystal. Consequently, the gamma lines from the calibration source show the same width as the background γ-β band.

An additional argument for this interpretation is the observed resolution for the

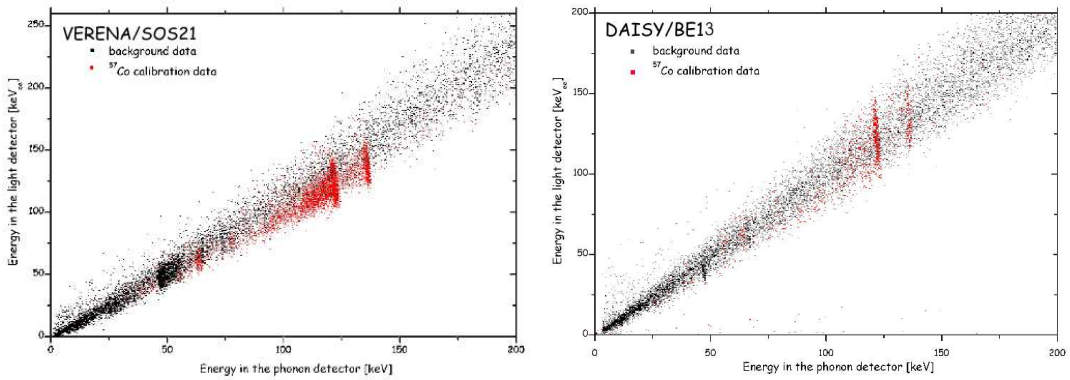

Figure 6.12: The background data and the gamma calibration data are compared in the scatter plots of energy in the light detector versus the energy in the phonon detector for the detector modules Verena/SOS21 (left) and Daisy/BE13 (right). In figure to the left, the lines from the ^{57}Co source show a lower light output and less spreading with respect to the γ-β band from the background data. The ^{57}Co was illuminating the crystal on the cylinder surface. This behavior is not visible in figure to the right, where the ^{57}Co source was illuminating the flat surface.

parasitic 692 keV γ line from the ^{57}Co calibration source (see figure 4.7) which has the same width as the background γ-β band (see figure 6.13). Since the attenuation length for the 692 keV gamma is about 2 cm in the $CaWO_4$ [XCOM, 2008], the crystal is more uniformly irradiated along its radius.

However this explanation might not be able to fully explain the observed lower position of lines due to ^{210}Pb and ^{227}Ac contaminations of the crystal with respect to other measured points in the γ-β band from Run30 as seen in figure 6.12 (left panel). Since the ^{210}Pb contamination is mainly internal and therefore is expected to be homogeneously distributed within the crystal, the 46.5 keV line should have a similar width and mean as the γ-β band[6]. Similarly the γ lines due to an ^{227}Ac contamination of the crystals at 9.3 keV and 24.5 keV with the associated β spectrum with end point at 44.8 keV are also positioned lower than the rest of the γ-β band. According to the interpretation given above the lower position of these lines can be explained only if the contamination sources are located inside of the crystal but close to its surface. This assumption is not

[6]In Run28 where the ^{210}Pb contamination was external the expected behavior (see figure 6.12 on the right) is observed.

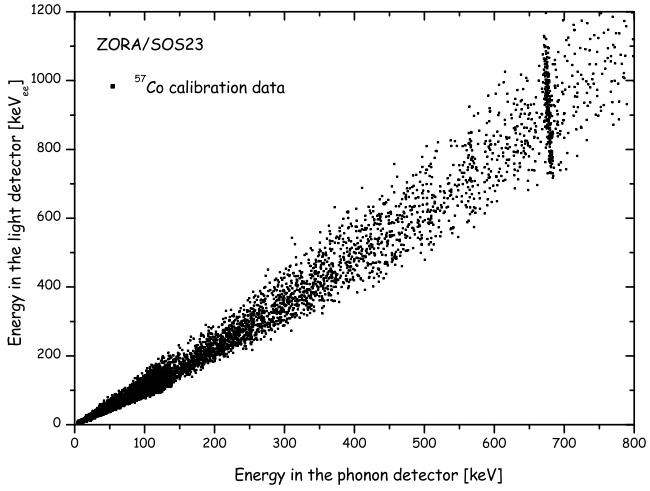

Figure 6.13: Scatter plot of energy in the light detector versus the energy in the phonon detector showing the gamma calibration data for the detector module Zora/SOS23 up to 800 keV energy deposition in the phonon detector. The gamma line at 692 keV from the ^{57}Co calibration source has the same width in the light channel as the background band due to γ-β interaction within the $CaWO_4$ crystal.

easily checked, however it appears rather unlikely. Still, the confirmation or the disproof of the given explanation is possible using the lines of the background spectrum which are due to the cosmic activation of the tungsten nuclei since this is a process which is certainly uniform within the crystal volume. If the γ lines due to the cosmic activation of the tungsten show the same width in the light channel as the γ-β band, the above given explanation seems more plausible. The analysis of these data is still in progress [Lang, 2008a].
Another geometrical effect which might contribute to a spatially dependent light output of the crystals comes from the presence of chamfered edges on the crystals which facilitate an easier and safer handling[7]. A series of measurements were performed at room temperature recording the scintillation light from the $CaWO_4$ crystals, irradiated with a small α source positioned centrally on one crystal surface, with photographic films placed directly below the crystal [Ninković, 2007]. For crystals with chamfered edges and all surfaces polished it was observed that the light mostly leaves the crystal through the chamfers forming a ring structure with outer diameter slightly bigger than the crystal diameter. Roughening of the crystal surface facing the light detector improved the homogeneity of the

[7] $CaWO_4$ material is rather brittle and sharp edges are easily damaged. This is prevented by beveling the edges of the crystals at 45°.

light output as expected but the ring structure, though not intense, seems to be still present. Considering the phonon detectors operated in Run28 and Run30, Daisy and Julia have no chamfers on the surface facing the light detector and very small ones on the opposite surface; Quedlina has small chamfers, less than 0.5 mm in length, on both surfaces; Verena has chamfers of 1 mm length on the thermometer side and 0.5 mm on the light detector side and Zora has chamfers with length of 1.2 mm on both sides of the cylinder. All crystals have the surface facing the light detector roughened. As can be seen from figure 6.11 it is for the detector modules where the phonon detector has longer chamfers (Verena, Zora) that the disagreement between the fitted and the measured energy resolution of the light detector is stronger. In addition these detector modules show the highest values of the coefficient A_2 in the parametrization of the energy resolution of the light detector (see table 6.6) that also points to a stronger position dependence of the light detection efficiency. However at this point, due to the small number of detectors which could be analyzed, it can not be claimed that the chamfered edges cause an observable effect on the distribution of the light output.

Fraction of deposited energy measured by the light detector

The coefficient A_1 of the parametrization 6.2 of the light detector energy resolution quantifies the term which describes the statistical fluctuations in the number of the scintillation photons measured by the light detector. Hence it can be used to estimate the amount of scintillation light for a given energy deposition in the $CaWO_4$ crystal, which is detected by the light detector.
For an energy deposition E_{pd} in the phonon detector the actual energy measured in the light detector E_{ld} is given as

$$E_{ld}[keV] \;=\; L[\%] \cdot E_{pd}[keV] = \; L[\%] \cdot E_{ld_{ee}}[keV_{ee}], \tag{6.3}$$

where L, which is the unknown, is the fraction of the energy deposited in the crystal, that is measured by the light detector and $E_{ld_{ee}}$ is the energy in the light detector corresponding to the energy deposition in the phonon detector. According to the energy calibration for an electron recoil event there is a one-to-one correspondence between E_{pd} and $E_{ld_{ee}}$.
On the other hand, E_{ld} can be written as

$$E_{ld}[keV] \;=\; N_{ph} \cdot E_{\nu}[keV], \tag{6.4}$$

where E_ν is the average energy of the absorbed scintillation photons and N_{ph} in their number. The statistical fluctuations of E_{ld} is then given as

$$\Delta E_{ld}[keV] \;=\; \sqrt{N_{ph}} \cdot E_{\nu}[keV] = \; \sqrt{E_{ld}[keV] \cdot E_{\nu}[keV]}. \tag{6.5}$$

The coefficient A_1 is modelled as

$$A_1 = \Delta E^2_{ld_{ee}}[keV^2_{ee}]/E_{ld_{ee}}[keV_{ee}]\,, \tag{6.6}$$

where both the standard deviation Δ $E_{ld_{ee}}$ and the energy $E_{ld_{ee}}$ measured in the light detector are given in terms of the energy deposition in the phonon detector (in keV_{ee}). Expressing equation 6.6 in units of absolute energy absorbed in the light detector using equations 6.3 and 6.5, the coefficient A_1 can be written as

$$A_1 = E_\nu[keV]/L. \tag{6.7}$$

Using the values of the coefficient A_1 given in table 6.6 and $E_\nu \approx 3\,eV$ for $CaWO_4$, it follows that the fraction of total energy deposited in the crystal which is detected by light detectors is about 1% for all detector modules considered here. This is in agreement with a previous measurement with a 4 cm cylindrical $CaWO_4$ crystal in the similar setup, where the fraction of deposited energy measured by the light detector was found to be 1.3 % [Frank, 2002].

6.2.3 Pulse shape

Figure 6.14 shows the quality of the template fit (RMS value) to the pulses observed in the light detector versus the energy measured in the phonon detector for detector module Zora/SOS23. Two classes of light detector events are clearly distinguished by the RMS value of the template fit.
The horizontal band of events with a small RMS value of the fit for a wide range of energy depositions in the phonon detector corresponds to γ or β interactions within the $CaWO_4$ crystal. The template for the fit is obtained by averaging pulses from the ^{57}Co 122 keV_{ee} scintillation peak and obviously give the best fit for scintillation events. The vertical band of events with no energy deposition in the phonon detector is due to direct γ or β interactions within the light detector or to absorption of the very fast scintillation light emitted by the scintillating polymeric foil or by the plastic scintillator rings. These events have pulse shapes different from the template used for fitting as indicated by the higher value of the RMS of the fit.
Another group of events with about 100 keV energy deposition in the phonon detector can be seen above the main band of the $CaWO_4$ scintillation events. They are due α-decays of a ^{210}Po contamination in the vicinity of the crystal (see section 1.2.3). When the α particle moves away from the detector only the energy of the recoiling ^{206}Pb nucleus ($\sim$100 keV) is detected by the phonon detector. Additional light from the associated α particle that escapes the crystal and hits the scintillating foil or ring shifts these events above the main band due to their much faster time response with respect to $CaWO_4$ which results in a worse quality of the fit.

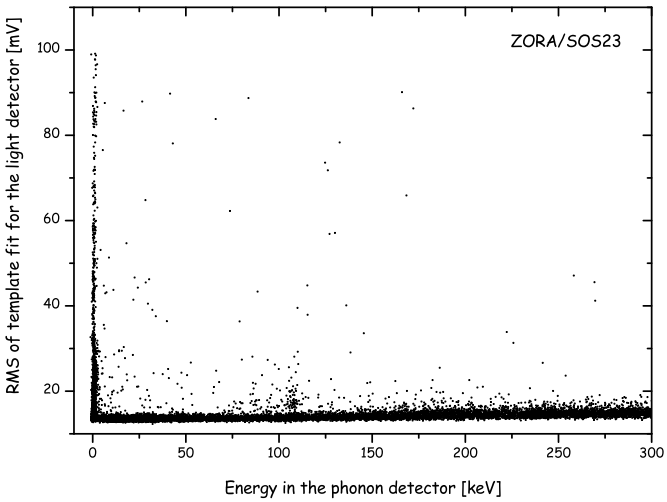

Figure 6.14: Scatter plot of the RMS value of the template fit in the light detector versus the energy detected by the phonon detector for the detector module Zora/SOS23. The template for the fit was obtained by averaging pulses from the 122 keV$_{ee}$ scintillation peak. The best fit is obtained for pulses which are due to scintillation light events (horizontal band at low RMS value). Events due to direct energy depositions in the light detector with no energy deposition in the phonon detector show much worse quality of the fit. The additional group of events with about 100 keV energy deposition in the phonon detector, located above the main band, is due to ^{210}Po contamination in the vicinity of the crystal.

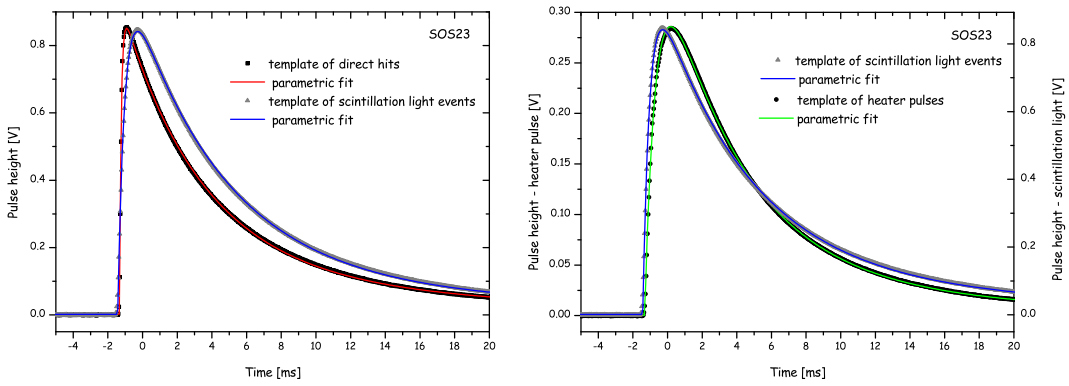

Figure 6.15: The figure on the left compares a template of direct hit events and a template of scintillation light events for light detector SOS23. The figure on the right compares a template of the scintillation light events and a template of heater pulses for the same detector. For all templates the parametric fit is also shown.

In figure 6.15 on the left are shown the templates of direct hit events and of scintillation light events with similar pulse height for the light detector SOS23.

The longer rise time of the template of scintillation light events is due to the long scintillation decay time in $CaWO_4$ crystals [Ninković, 2005].
In order to obtain parameters which characterize the specific pulse shape, the templates have been fitted according to equation 5.1 (parametric fit). The fitted pulse shapes for the light detector SOS23 are shown in figure 6.15 together with the templates. The results of the parametric fit for the light detectors operated in Run30 are given in table 6.7. Time constants τ_n for the collection of the non-thermal phonons estimated from the calorimeter model described in section 3.2.1 are presented in the same table.

Direct hits

As seen in table 6.7, the light detectors SOS21 and SOS23 show a fast fitted rise time τ_n for direct hit events as expected from the calorimeter model for the thermometer without collectors (see section 3.2.1). In this case the rise time of the pulses is largely given by the time constant $\tau_{crystal}$ for thermalization of non-thermal phonons in the absorber crystal. This indicates that either the quasi-particle diffusion time in the phonon collectors is much faster than $\sim 0.5\,\mathrm{ms}$, which is the diffusion time expected from earlier measurements [Loidl, 1999], or that the quasi-particle lifetime due to a worse quality of Al/W bilayer (see section 5.1.2) is much shorter than expected and the phonon collectors are rather inefficient. The light detector SOS30 shows a much longer rise than the one calculated from the calorimeter model, as expected if the rise time is dominated by the additional time constant for the diffusion of the quasi-particles. The reason for the different behavior of SOS30 might be due to the larger interface between phonon collectors and tungsten film or to a different quality of the Al/W bilayer.
The fitted decay time of the non-thermal component of the signal τ_{in} shows quite different values for the three light detectors. There are several reasons for this behavior: different length or thickness of the structured thermal link which influences the thermal coupling of the thermometer to the heat bath; different resistance value of the thermometer and the steepness of the transition curve at the chosen operating point which may affect the strength of the negative electrothermal feedback.
Table 6.7 also lists the resistances at the operating points R_{op} for the light detectors, which are estimated from the measured pulse height of the completely saturated high energy particle pulses. For each light detector, the temperature of the mixing chamber T_{MC} for zero heating current through film heater, which corresponds to its estimated R_{op}, is obtained from heat sink temperature sweep. The temperatures of the thermometers in the operating points T_{op} are then roughly estimated from measured T_{MC} taking into account the slight difference between

Light detector	**SOS21**	**SOS23**	**SOS30**
Direct hit events $\sim 120\text{keV}_{ee}$			
τ_n [ms]	0.078 ± 0.001	0.1009 ± 0.0001	0.452 ± 0.002
τ_{in} [ms]	1.46 ± 0.01	4.536 ± 0.003	9.54 ± 0.02
τ_t [ms]	7.43 ± 0.04	17.55 ± 0.04	40.7 ± 0.5
$A_n/(A_{th}+A_n)$ [%]	65.2 ± 0.3	84.11 ± 0.05	91.1 ± 0.2
Scintillation light absorption events $\sim 120\text{keV}_{ee}$			
τ_n [ms]	0.337 ± 0.001	0.3947 ± 0.0002	0.8499 ± 0.0004
τ_{in} [ms]	2.39 ± 0.02	5.316 ± 0.002	11.48 ± 0.004
τ_t [ms]	10.09 ± 0.05	21.83 ± 0.03	58.1 ± 0.1
$A_n/(A_{th}+A_n)$ [%]	68.3 ± 0.2	88.04 ± 0.03	91.77 ± 0.02
Heater pulses			
τ_n [ms]	0.1968 ± 0.0004	0.6312 ± 0.0003	0.8327 ± 0.0003
τ_{in} [ms]	1.243 ± 0.002	4.521 ± 0.003	4.43 ± 0.003
τ_t [ms]	7.46 ± 0.05	14.55 ± 0.03	13.94 ± 0.04
$A_n/(A_{th}+A_n)$ [%]	94.58 ± 0.03	88.03 ± 0.05	74.70 ± 0.04
Rise time from the calorimeter model			
$\tau_{crystal}$ [ms]	~ 0.1		
τ_0 [ms]	0.4	0.4	0.3
τ_{film} [ms]	1.3	1.3	1.0
τ_n [ms]	~ 0.09	~ 0.09	~ 0.09
Estimated operating point			
R_{op} [mΩ]	~ 180	~ 230	~ 60
T_{MC} (I_{heater}=0) [m K]	~ 18.3	~ 15.7	~ 14.5
T_{op} [m K]	~ 22	~ 20	~ 17.5
C_{op} [fJ/K]	~ 65	~ 55	~ 140

Table 6.7: Relevant parameters obtained by the parametric fit of the templates made for direct hit events, scintillation light events and heater pulses for light detectors SOS21, SOS3 and SOS30. They include the rise time τ_n of the two signal components, the fraction of the non-thermal component $A_n/(A_{th} + A_n)$, the decay time τ_{in} of the non-thermal component and the decay time τ_t of the thermal component. The errors given are 1σ errors of the fit. The rise time of the direct hit events calculated from the calorimeter model and estimated temperature, resistance and heat capacity of thermometers in the operating points are also listed. See text for explanation.

the temperature of the carousel and the mixing chamber of ~ 3 mK (obtained from the Run31 where an additional thermometer is mounted on the carousel) and the self-heating of the film. Heat capacities in the chosen operating points

C_{op} are estimated using equation 3.5. These estimates should be taken only as approximate values due to uncertainties in the measurements of the transition curves. Nevertheless they are accurate enough for a qualitative understanding of the different decay times obtained by the fit for the different light detectors.
As can be seen from table 6.7 heat capacities at the chosen operating points for SOS21 and SOS23 are similar. Taking into account that the resistances at their operating points are also similar and that they were both biased with 7.144μA, it is expected that the negative electro-thermal feedback has similar strength. Therefore the shorter relaxation time τ_{in} of SOS21 is plausibly due to the shorter thermal link (see table 6.1) which results in a stronger thermal coupling of the detector to the heat bath. SOS30 has larger heat capacity than the other light detectors and also a weaker thermal coupling due to a thinner thermal link (see table 6.1), which both lead to a longer relaxation time of the non-thermal component.
The fitted decay time of the thermal component τ_t shows the same trend as the decay time of the non-thermal component τ_{in}. This behavior is due to the fact that both thermometer and absorber relax to an equilibrium state mostly through the thermal link of the thermometer, and both relaxation times are affected by the strength of its thermal conductance G_{eb} (see equation 3.25 for τ_t). Though the absorber also relaxes via its direct thermal coupling to the heat bath, this coupling is expected to be negligible due to the holding system in use which minimizes the contact surface (see section 2.3.3).
As visible in table 6.7 the dominant part of the signal measured by the thermometers of the light detectors is due to the non-thermal component A_n, which corresponds to the rise of the thermometer temperature caused by the absorption of non-thermal phonons in the film. For a given energy deposition in the absorber of the light detector, only a relatively small fraction of non-thermal phonons is absorbed in the thermometer. The rest of the non-thermal phonons thermalizes in the absorber causing its temperature rise, which corresponds to the thermal component of the signal. Since the thermometer is thermally coupled both to the heat sink with a thermal conductance G_{eb} and to the absorber with a thermal conductance G_{ea} (see figure 3.1), a part of the energy contained in the non-thermal component, which depends on the ratio of these thermal conductances, is transferred back to the absorber. This adds to the thermal component of the signal. Finally it should be noted that the thermal component of the signal measured by the thermometer is only a fraction of the actual temperature rise of the absorber due to the presence of the thermal coupling of the thermometer to the heat bath[8].
Light detectors SOS21 and SOS23 have substrates of the same material and size

[8]For an isolated system consisting of the substrate and the thermometer the same temperature rise, after thermal equilibrium is achieved, would be observed in both subsystems.

and also thermometers with the same layout. Therefore the fraction of non-thermal phonons which is absorbed in the thermometers is expected to be the same for both detectors. The observed difference is due to a different thermal coupling of their thermometers. The thermometer of light detector SOS21 has a stronger thermal coupling to the heat bath, but also a much stronger thermal coupling to the absorber due to a higher operating temperature (see equations 3.8 and 3.9). This means that for the light detector SOS21 more energy of the non-thermal component is transferred back to the substrate contributing to the thermal signal. SOS30 shows the highest fraction of the non-thermal component in the measured signals. This is plausibly due to the larger area of its thermometer which results in a higher fraction of non-thermal phonons thermalizing in the thermometer. Moreover, due to the lower operating temperature, the thermal coupling to the absorber (G_{ea}) is weaker than in the case of SOS21 and SOS23, despite the larger volume of the tungsten film. This leads to a smaller reflux of non-thermal phonons to the absorber.

Scintillation light events

For all light detectors the rise time of the scintillation light events is about 0.3 ms longer than that of the direct hit events, reflecting the rather long decay time of the $CaWO_4$ scintillation pulse at the operating temperatures.
The emission of the $CaWO_4$ crystals is usually characterized by two scintillation time constants [Ninković, 2005]. The time constant of the fast component, that is making up about 70 % of the emitted light, is estimated to be about 0.3 ms and the time constant of the slow component is about 2.5 ms at 20 mK [Di Stefano et al., 2003][Westphal et al., 2006]. Hence the observed prolongation of the decay time of the non-thermal component (see table 6.7) could therefore be ascribed to the slow component of the scintillation light which is emitted on a time scale which is of the same order as the relaxation time of the thermometers.
Light detector SOS21, due to its short decay time of the non-thermal component, was not performing completely as a calorimeter[9], since it did not fully integrate the energy of the scintillation light. The other two light detectors were able to fully integrate the energy of the incoming scintillation light.
The fraction of the non-thermal component is expected to be the same for both direct hit events and scintillation events. The slight difference in the light detectors SOS21 and SOS23 is thus attributed to systematics possibly introduced by the fit or by the different quality of the templates used[10].

[9] This refers to the performance of the detector and not of its thermometer, which is operated in the calorimetric mode (see section 3.2.1).

[10] The parametric fit is modelled for an instantaneous energy deposition and applying it to the slow scintillation light events might lead to slight differences in the values of parameters. In addition a different number of pulses averaged to obtain templates results in their different quality due to a better or worse averaging of noise terms.

Heater pulses

The templates of the scintillation light events and of the heater pulses for light detector SOS23 are compared in figure 6.15 on the right. The parameters obtained by the parametric fit of the templates of the heater pulses for all light detectors are listed in table 6.7. The rise time of the heater pulses is determined by the duration of the power input, that is predefined in the wave form generator board (see section 2.4.2). Their decay times both for the non-thermal and the thermal component of the signal τ_{in} and τ_t, respectively should be similar to those of the direct hit events. This is observed for light detectors SOS21 and SOS23, while the heater pulses of the light detector SOS30 show relaxation times about a factor of two to three smaller for both components. Since the heater pulses are directly injected into the thermometer via the film heater, the thermal component of the heater signal is solely due to the part of injected power which is transferred back to the absorber. Thus, the non-thermal component A_n is expected to be higher than for direct hit events, as observed for SOS21 and SOS23. Again, light detector SOS30 shows a quite different behavior. The reason for this is not understood, but might be related to the specific properties of its thermal link. Due to the specific position of the heater film (see figure 6.1), heat dissipated in it is shared between the tungsten film and the thermal link according to the strength of their thermal couplings to the heat bath. Hence, for the same rise of temperature in the tungsten film, more power is flowing across the thermal link in the case of heater pulses than for particle pulses. This can lead to a slightly higher temperature of the thermal link during the process of relaxation of heater pulses and, in case of a thermal link which notably changes thermal conductivity with temperature, this can result in a shorter relaxation time. One possibility this to occur is in case of partially superconducting thermal links. Since the thermal links of all light detectors operated in Run30 are gold-tungsten bilayers (the tungsten is used as adhesion layer) it cannot be excluded that they were partially superconducting due to proximity effects[11].

6.2.4 Optimal operation point

As previously mentioned for a suitable operating point various conditions need to be matched. The most import criterion considering the overall performance of the detector is the achieved signal-to-noise ratio.
In order to investigate the influence of the chosen operating point on the signal-to-noise ratio, a series of measurements was performed at different operating points. For practical reasons the signal-to-noise ratio was measured for heater

[11] In the course of detector fabrication some thermal links and heater films have been observed to be unexpectedly superconducting due to proximity effects. This behavior was systematically investigated during the fabrication of light detector for the following Run31 and was solved by skipping the deposition of the tungsten adhesion layer [Huff, 2007].

pulses of given injected energy and not for particle pulses.
For these measurements light detector SOS23 was chosen, because it has shown a more stable behavior than SOS21 and SOS30. The measurements were performed with two different bias currents (1.0 μA and 7.144 μA).

Measurement with 1.0 μA bias current

Figure 6.16 to the left shows the transition curve with 1.0 μA bias current, obtained by sweeping the heater voltage applied to the heater circuit. This changes the temperature of the thermometer, because the heater is thermally linked to the film[12]. The marked locations on the transition curve indicate operating points where the measurements were taken.

In addition, the response of light detector SOS23 for three different heater

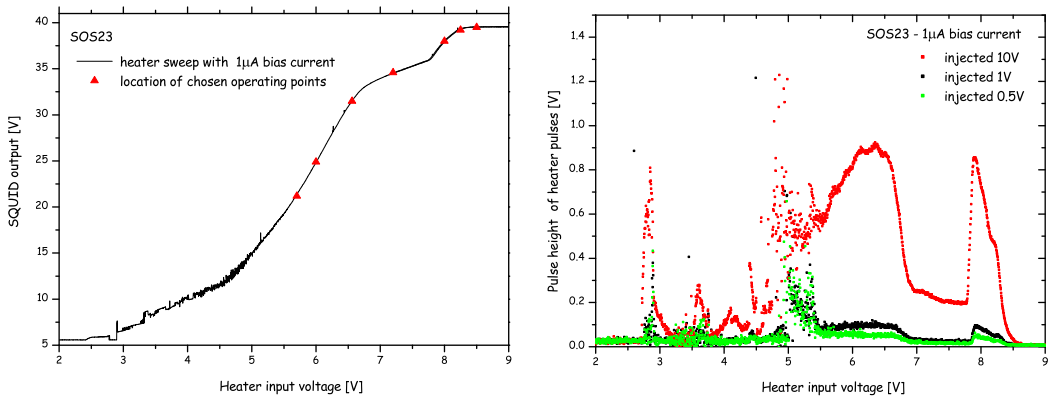

Figure 6.16: The figure on the left shows the transition curve for light detector SOS23 obtained by sweeping the applied heater voltage. The marked positions on the transition curve indicate the operating points where the measurements have been taken. The figure on the right shows the observed pulse height of three different heater pulse amplitudes along the phase transition of the thermometer. The detector was biased with 1.0 μA. Due to different SQUID operating ranges, the SQUID output in the left panel was scaled by a factor of ten in order to be compatible with the scale of the pulses in the right panel.

pulses was recorded as a function of the applied heater voltage. As can be seen from figure 6.16 right, the measured pulse height spectra of the heater pulses show a lot of structures which is not so easily recognized in the transition curve. All heater pulses show an unstable response below about 5.5 V of applied heater voltage. The non-smoothness of this part, which corresponds to the very bottom of the transition, is also visible on the transition curve. This behavior is not well

[12]When it is mentioned, sweeping of the applied voltage in fact is a sweep of the temperature of the thermometer.

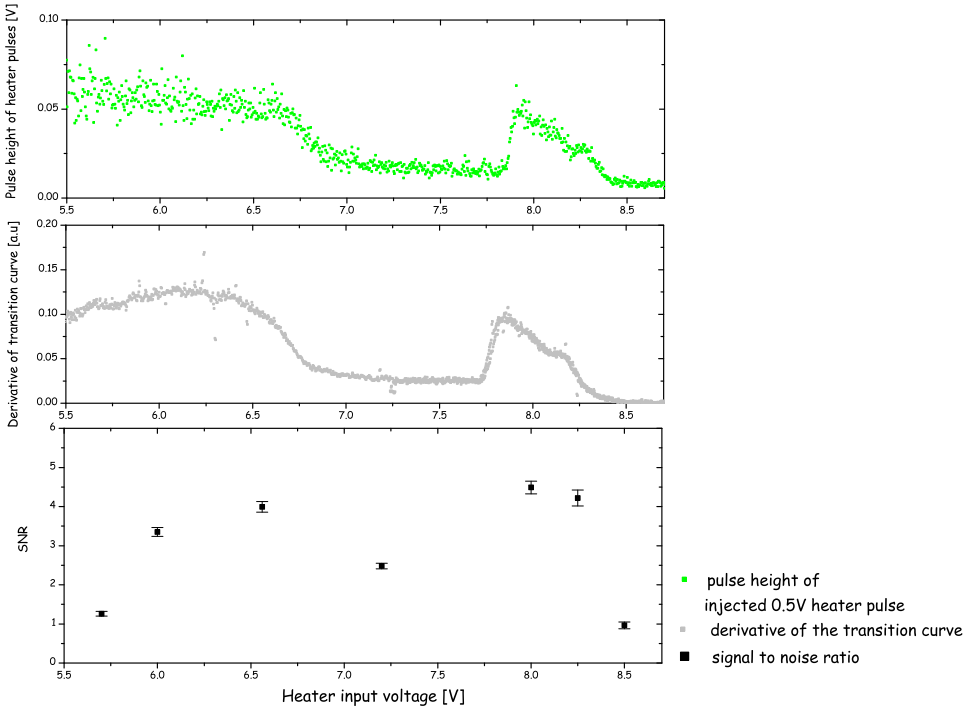

Figure 6.17: The pulse height of injected 0.5 V heater pulse (top) and the slope of the heater sweep transition curve (middle) as a function of applied heater voltage for light detector SOS23. The observed signal-to-noise ratio (with 1σ errors) for heater pulses of injected 0.5 V at different values of heater voltage is plotted in the bottom figure. The detector was biased with 1.0 μA.

understood, but it is quite common for SPTs and many experimental groups have observed large noise when detectors are operated in the lower part of the transition (see for example [Lindeman et al., 2002][Fujimoto et al., 2002]).
To illustrate that the behavior of the heater pulses as a function of applied heater voltage actually reflects the shape of the transition curve, the measured pulse height for injected heater pulse of 0.5 V along the transition curve is compared to the derivative of the transition curve in figure 6.17. A change of the slope of the transition curve translates into a change of the pulse height of injected heater pulses.
At each chosen operating point the light detector SOS23 was stabilized and its response to the heater pulses of injected 0.5V was recorded. The small injected energy of the heater pulse, which corresponds to $21.00 \pm 0.04\,\mathrm{keV}_{ee}$ according to the gamma energy calibration, was chosen to probe locally the effect of the slope of the transition curve without being affected by the presence of substructures. During the measurements triggering was done by the partner phonon detector Zora, which was kept at a fixed operating point. The signal-to-noise ratio (SNR)

is calculated as the ratio of pulse height and FWHM of the peak due to the heater pulse.
The results of measurements are summarized in the bottom panel of figure 6.17, where the measured SNR is shown as a function of the applied heater voltage. The value of the resistance at each operating point expressed as the percentage of the normal conducting resistance is given in table 6.8. For the operating points in the upper part of the transition (sp1 to sp5 in table 6.8) the measured SNR follows the slope of the transition curve, indicating that the signal is strongly affected by the slope of the transition. This is expected due to the fact that some components of the noise do not scale with the slope as discussed in subsection 6.2.5. Nevertheless for the two operating points positioned low in the transition (sp6 to sp7 in table 6.8), despite the steep slope of the transition curve, the observed signal-to-noise ratio is notably decreased. This is ascribed to a significant increase of the noise which then limits the performance of the detector.
The best SNR for heater pulses of about 20 keV$_{ee}$ was achieved at the point (sp3) corresponding to 8 V applied heater voltage. At this operating point the thermometer has a resistance which is about 60% of the normal conducting resistance (see table 6.8) and the slope of the transition curve at this point is one of the steepest.

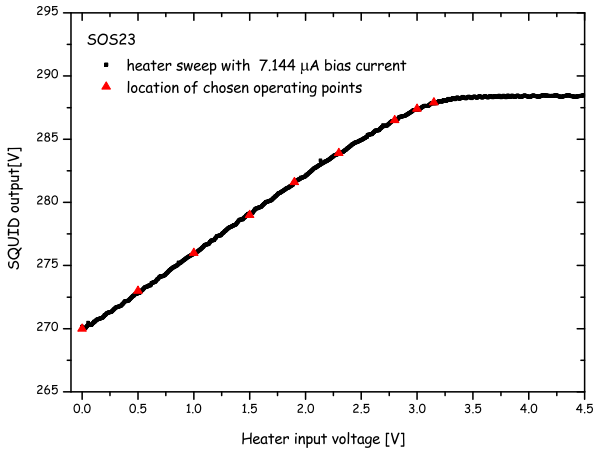

Figure 6.18: Transition curve for light detector SOS23 obtained by sweeping the applied heater voltage. The marked positions on the transition curve indicate where the measurements of the detector response to injected heater pulses have been taken. The detector was biased with 7.144 μA. Due to different SQUID operating ranges, the SQUID output was scaled by a factor of hundred in order to make it compatible with the scale of the heater pulse presented in figure 6.19.

Measurement with 7.144 μA bias current

The same set of measurements have also been performed with 7.144 μA bias current, which was the standard bias current for light detector SOS23 during Run30. The 9 positions of operating points where the measurements were taken

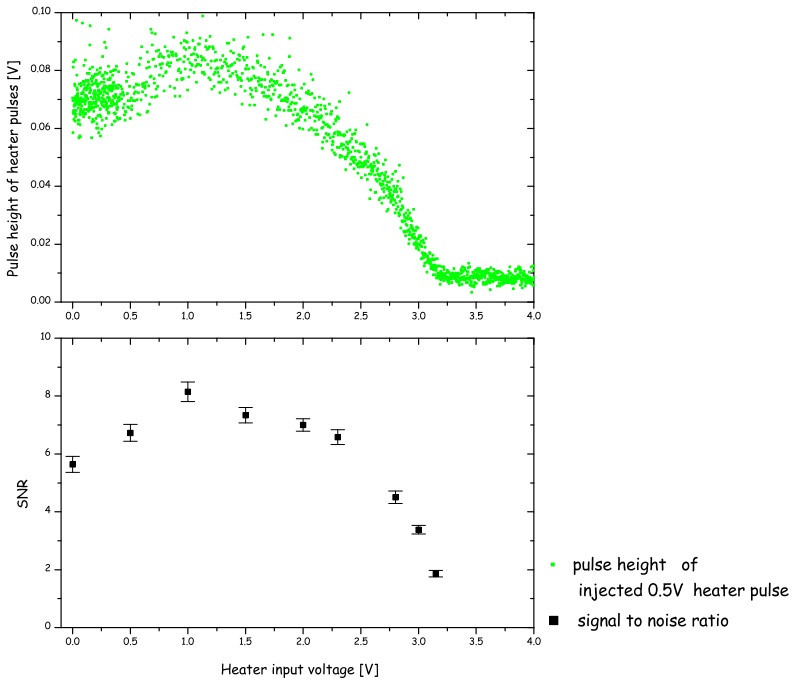

Figure 6.19: Figure compares the pulse height of injected 0.5 V heater pulses (top panel) and observed signal-to-noise ratio (with 1σ errors) (bottom panel) as a function of applied heater voltage for light detector SOS23. The detector was biased with 7.144 μA.

are marked in figure 6.18, showing the transition curve of SOS23. Figure 6.19 shows the measured SNR for heater pulses of 20 keV_{ee} and the measured pulse height of the same heater pulses versus the applied heater voltage. The observed SNR follows the change in the pulse height of the heater pulse, which can be taken as an estimate of the change of the slope of the transition curve. The operating point corresponding to 1.0 V of applied heater voltage shows the best SNR, while the standard operating point of SOS23 during Run30 at 2.0 V shows a slightly worse performance in this respect. It should be noted that this study allows to find the optimal points of operation for particle interactions with an energy deposited similar to the energy of injected heater pulse. To find an optimal point for other values of energy deposited similar measurements should be performed with heater pulses in that energy range.

6.2.5 Noise spectra

In addition to the response of light detector SOS23 on the injected heater pulses, samples of baseline noise were recorded at the locations marked on the transition curves for both bias currents (see figures 6.16 and 6.18).
For a bias current of 1.0 μA the baseline noise is obtained from measurements with a record length of 8192 channels with a sampling time of 20 μs to allow accurate measurements of noise spectra up to the cut-off frequency of the anti-aliasing filter which was set at 10 kHz during Run30. Figure 6.20 contains the

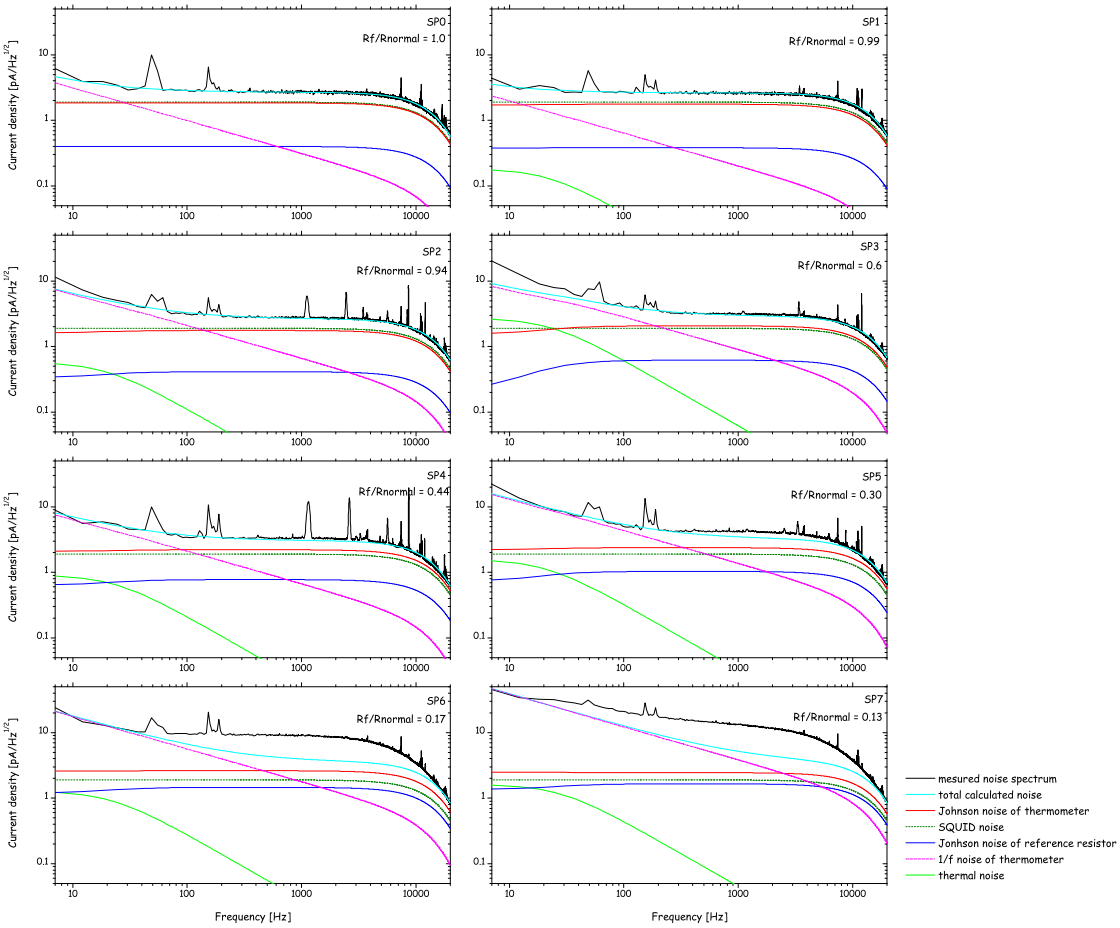

Figure 6.20: Measured noise spectra for light detector SOS23 at different operating points. Calculated and also shown are: Johnson noise in the thermometer, Johnson noise in the reference resistor, thermal noise, SQUID noise and *1/f* noise in the thermometer is also plotted.

measured noise spectra for light detector SOS23 when biased with 1.0 μA at different operating points. The calculated current noise due to Johnson noise in the thermometer, Johnson noise in the reference resistor, thermal noise, SQUID

noise and 1/f noise, according to the model described in section 3.3, is also plotted in the same figure. The numerical values of the parameters of the model used to compute the current noise are given in table 6.8.
The resistance of the thermometer R_f at different operating points and corresponding temperature of the mixing chamber T_{MC} for zero heating current through the film heater are obtained using the measured heat sink sweeps and heater sweeps transition curves. The error on the resistance values is estimated to be about 10 % due to uncertainties of the SQUID transfer function as previously mentioned. The temperature of the thermometer T_e is estimated from data obtained in the presently ongoing Run31, where an additional thermometer, heat sinked at the carousel, shows a slight difference (~ 3 mK) between carousel and mixing chamber temperature. Self-heating of the thermometer due to a bias current of 1.0 μA is estimated to be less than 1 mK for all operating points.
As discussed in section 6.2.3, heater pulses and particle pulses show the same relaxation times. Hence, the effective decay time of the non-thermal component of the signal τ_{eff} is obtained by fitting the template of the injected 0.5 V heater pulses according to equation 5.1 for each operating point. From the calculated heat capacity C_{op} (using equation 3.5) and the fitted effective relaxation time of the thermometer, the effective thermal coupling of thermometer to the heat bath G_{eff} is obtained from equation 3.24. The intrinsic relaxation time τ_{in} was then estimated by subtracting the additional thermal coupling due to electro-thermal feedback G_{ETF} from the effective thermal coupling.
The slope of the transition curve was obtained by differentiating the measured transition curve and is very rough estimate since the temperature on the x-axis is the one of the mixing chamber and not of the thermometer. These two temperatures do not change in the same way along the transition, for example due to the dependence of the electro-thermal feedback term and of the self-heating effect on the position in the transition curve. For the modelling presented here these effects were neglected.
During the data taking the mixing chamber was stabilized at 7 mK, while detector was stabilized at different operating points by applying different heater currents through the film heater (indicated in table 6.8 by different values of heater voltage). The temperature of the reference resistors was assumed to be the same as the one of the mixing chamber.
The SQUID noise term was estimated from the noise spectrum measured above the transition, where only Johnson noise of the thermometer, Johnson noise of the reference resistor and SQUID noise are present[13].
The *1/f* noise was modelled according to equation 3.61. The amplitude of the *1/f* noise was varied to obtain the best matching with the measured spectra. The values of this parameter are given in table 6.8.

[13]The value of SQUID current noise estimated here is higher than the average value given in Henry et al. [2007], but is still compatible with the measurements.

For the different operating points the measured noise ranges from 2.7 pA/$\sqrt{Hz}$

Spectrum	**sp0**	**sp1**	**sp2**	**sp3**	**sp4**	**sp5**	**sp6**	**sp7**
Heater voltage [V]	-	8.50	8.25	8.00	7.2	6.56	6.00	5.7
R_f/R_{normal}	1	0.99	0.94	0.60	0,.44	0.30	0.17	0.13
$T_{MC}(I_h=0)$[mK]	∼16.4	∼16.2	∼16	∼15.7	∼15	∼14.4	∼14	∼13.6
T_e [mK]	∼20	∼20	∼19.5	∼19.5	∼19.0	∼18.5	∼18.0	∼17.5
R_f [mΩ]	270±27	268±26	255±26	160±16	120±13	80±8	50±5	35±5
τ_{eff} [ms]	-	7.5±1.2	8.4±0.2	7.1±0.1	6.9±0.3	7.8±0.1	7.4±0.2	5.8±0.3
slope [mΩ/mK]	-	∼10	∼30	∼90	∼20	∼20	∼9	∼10
C_{op} [fJ/K]	38±10	38±21	41±21	60±22	67±23	75±23	82±24	84±24
G_{eff}[pW/K]	-	5.1±3.7	4.8±2.7	8.3±3.3	9.8±3.8	9.7±3.1	11.1±3.5	14.5±4.8
τ_{in} [ms]	-	7.7±10.0	9.2±10.7	9.6±9.5	7.3±5.7	8.4±5.8	7.5±4.7	5.7±3.6
G_{eb}[pW/K]	-	4.9±3.7	4.4±2.8	6.2±3.7	9.2±3.9	8.9±3.3	11.0±3.7	14.7±5.0
G_{ETF}[pW/K]	-	0.12±0.03	0.40±0.08	2.16±0.46	0.62±0.15	0.74±0.20	0.11±0.12	-0.19±0.18
R_{shunt} [mΩ]	40	40	40	40	40	40	40	40
T_{shunt} [mK]	7.0	7.0	7.0	7.0	7.0	7.0	7.0	7.0
i_{sq} [pA/$\sqrt{Hz}$]	1.9	1.9	1.9	1.9	1.9	1.9	1.9	1.9
1/f amplitude	$5{\cdot}10^{-8}$	$2{\cdot}10^{-8}$	$2{\cdot}10^{-7}$	$2{\cdot}10^{-7}$	$8{\cdot}10^{-8}$	$2{\cdot}10^{-7}$	$3{\cdot}10^{-7}$	$2{\cdot}10^{-6}$

Table 6.8: Relevant parameters used for calculating the current noise for light detector SOS23 when biased with 1.0 μA. See text for explanation.

to 15 pA/$\sqrt{Hz}$ at frequencies between 200 Hz and 2 kHz. The noise is fairly constant across most of the bandwidth of the measured spectra with the exception of the spectra taken near the bottom of the transition. The cuts off of the noise spectra is at 10 kHz due to the anti-aliasing filter. The contributions of the thermal noise are small compared to other noise sources expect for the operating point with high value of the slope of the transition curve. This is expected since the thermal noise scales as the signal, i.e. it depends on the slope of the transition curve (see equation 3.49). The small contribution of the thermal noise to the total calculated noise leads to the conclusion that it is the Johnson noise in the thermometer, SQUID noise and *1/f* noise that limit the performance of the detector. The Johnson noise in the thermometer and SQUID noise are more dominant in the high frequency part of the spectra, while the *1/f* noise term dominates the low frequency part of the spectra. As can be seen from table 6.8, the amplitude of the *1/f* increases as the resistance of the operating point decreases and seems to be also correlated with the slope of the transition curve (although there are not enough results to make a definite statement). For CRESST detectors the effect of electro-thermal feedback in not very significant,

as indicated with a small value of G_{ETF} in table 6.8.
The modelled spectra agree well with the data in the upper part of the transition (see figure 6.20 sp0 to sp5). For the two operating points where the thermometer was stabilized below 30 % of the normal resistance (sp6 and sp7) the measured noise is much larger that the theoretical one. The SNR at these two operating points is low, as described in the previous section (see figure 6.17). The excess of the measured noise is present both in the low frequency part, as indicated by a higher value of the amplitude of the *1/f* noise in table 6.8, and in the high frequency part of the spectra, as seen in figure 6.20.
According to Enss [2005] excess low frequency noise seems to be correlated with the so called "excess electrical noise", which has the same frequency dependence as Johnson noise. There are many theories proposed to explain the origin of excess electric noise in the superconducting transition, while the origin of *1/f* noise is still not understood. As mentioned in Enss [2005], possible factors that contribute to the excess noise are current-dependent resistance of the thermometer or non-equilibrium effects since the thermometers are operated out of equilibrium. Some sources of excess noise can be reduced by a careful detector design, e.g the boundary conditions of the thermometer are found to influence the excess electrical noise.
In order to investigate the origin of the excess of observed noise in the lower part of transition curve, more systematic studies and more detailed noise modelling are needed.

The theoretical energy resolution of thermometer calculated with the optimal filter method according to equation 3.68 was compared to the energy resolution measured for the heater pulses, which is determined by the baseline noise. For the case of the white band noise these two resolutions should agree due to the equivalence of the template fit method in the time domain and of the optimal filtering method in the frequency domain (see section 3.3.3). Using parameters from table 6.8, theoretical resolution (FHWM) of about 1 - 2 eV was computed for an operating point in the upper part of transition at 94 % of the normal conducting resistance. The resolution (FWHM) of the injected heater pulse was measured to be 3.19 ± 0.04 keV$_{ee}$[14]. Assuming that about 1 % of the energy deposited in $CaWO_4$ is detected as scintillation light and that thermometer measures at most about 5 % of the energy deposited in the light detector absorber (see table 5.3), this value translates into energy resolution in the order of eV. Theoretical and observed resolution agree, but it should be noted that there are additional noise terms, which are not taken into account by the optimal filter method like the *1/f* noise term. This noise term significantly contributes to the baseline noise as is

[14]The noise measurements were performed at the end of Run30 where the performance of all detectors had worsened with respect to the data set considered in section 6.2.1. Therefore the observed resolution of heater pulses for light detector SOS23 is about twice the value given in table 6.4.

visible from the measured noise spectra of the detector.
Noise spectra of the light detector SOS23 measured in different operating points for the 7.144 μA bias current are shown in figure 6.21. The record length used in this measurements was 16384 channels with 40 μs time base[15]. This allowed the noise measurements down to the low frequency region. As can be seen from figure 6.21 the noise in the low frequency part is dominated by the *1/f* noise and the peaks due to electromagnetic interferences. Figure 6.22 compares the signal spectrum of 0.5 V heater pulse and noise spectrum at the operating point which corresponds to 2 V applied heater voltage (standard operating point for SOS23 in Run30). The signal-to-noise ratio for this operating point is 7 (see figure 6.19). As seen from figure 6.22 the performance of the detector is influenced by the presence of the *1/f* noise and pick-up noise.

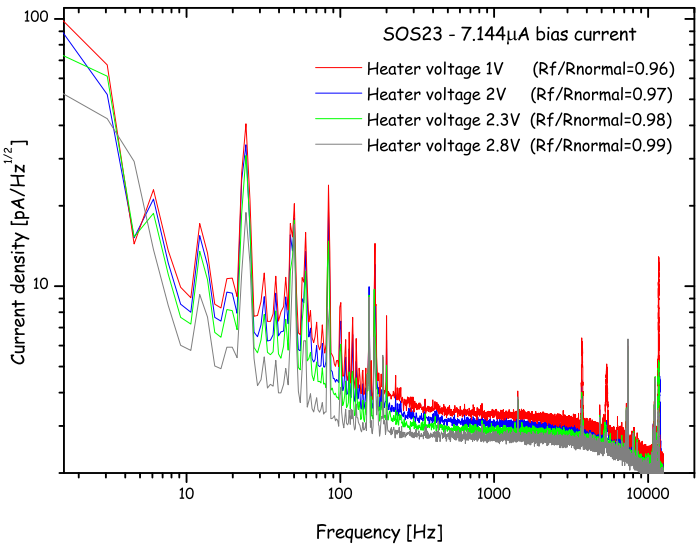

Figure 6.21: Measured noise spectra for light detector SOS23 at different operating points when biased with 7.144 μA.

The comparison of measured baseline noise spectra with the calculated ones revealed that the dominant noise source for the low frequency part of the spectra, which is the relevant one considering the time structure of the light detectors signals, is the *1/f* noise. Moreover the measured noise spectra show the presence of external pick-up noise (emi) also in the same frequency region. In order to improve the performance of the detectors several tests (reanalyzing of the

[15]Since the anti-aliasing filter was set to 10 kHz the choice of 40 μs sampling time resulted in a slight aliasing of the frequencies higher than the sampling frequency.

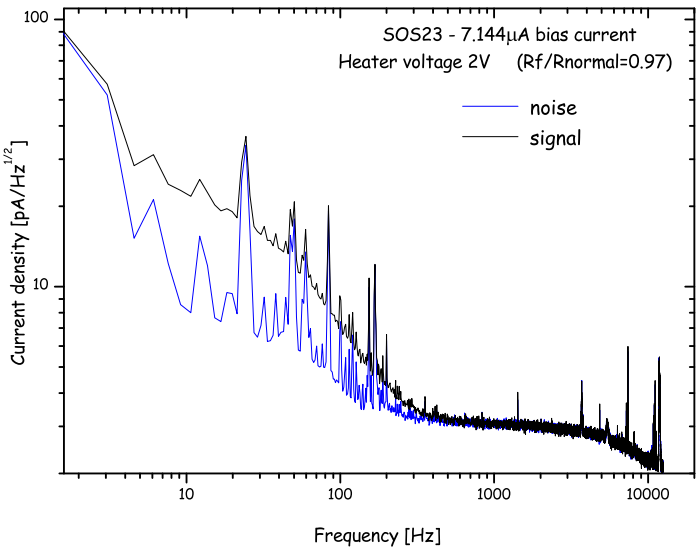

Figure 6.22: Signal spectrum of injected 0.5 V heater pulse and noise spectrum measured for light detector SOS23 at the operating point which corresponds to 2 V applied heater voltage. The detector is biased with 7.144 μA.

grounding scheme, improved shielding of the cables, rearrangement of the electronic circuits) have been carried out and are still going on with the aim of suppressing or reducing possible sources of electro-magnetic interferences.

Chapter 7

Conclusion and Perspectives

The CRESST-II experiment is searching for WIMPs via their elastic scattering off tungsten nuclei in scintillating $CaWO_4$ target crystals. Since the energy transferred to the tungsten nuclei steeply rises towards lower energies and extends only up to about 40 keV, a low energy threshold of the detectors is of utmost importance. Detector modules developed for CRESST-II consist of a 300 g scintillating $CaWO_4$ crystal operated as a cryogenic calorimeter (phonon detector) in coincidence with a second, much smaller cryogenic calorimeter (light detector) for the detection of the scintillation light. Both detectors are read out by tungsten superconducting phase transition thermometers. Measuring simultaneously the phonon and scintillation light signal, the CRESST-II detector modules are able to discriminate nuclear recoils, in particular tungsten recoils as expected from WIMP interactions, from radioactive γ and β backgrounds down to recoil energies of about 10 keV. Only about 1% of the energy deposited in the $CaWO_4$ crystal by γ or β interactions can be detected as scintillation light. Therefore, the sensitivity of the light detectors is a most critical issue for the efficient background discrimination at energies relevant for WIMP searches.

At focus of this work was the development of cryogenic light detectors for the measurement of the $CaWO_4$ scintillation light as well as a thorough investigation of their performance.

In order to study the influence of the tungsten film edge quality on the thermometer performance, tests have been performed comparing the standard design with a thermometer with well-defined edges. These edges were obtained by additional gold structures deposited on top of the tungsten film edges. The results showed practically no improvement, possibly due to limitations imposed by the non-smoothness of the transition curves for both thermometers.

Compared to the standard silicon absorber, significantly improved absorption of the light detector substrate has been achieved using a thin superconducting lead layer which was deposited on the sapphire substrate. Yet, the combined

effect of the comparatively low transmission of phonons from lead to sapphire and the increase of losses of non-thermal phonons at the surface of the lead film resulted in a strong reduction of the pulse amplitude and consequently in a degradation of the energy resolution. Additional tests with other superconducting absorption layers that would better match the needs of the experiment are in progress.

In the course of this work three light detectors with silicon-on-sapphire absorbers (SOS) have been operated for the first time in CRESST-II detector modules in the Gran Sasso setup during the commissioning Run30. Their performance has been compared to the one of the silicon light detectors used during the prototyping phase of the CRESST-II experiment (Run28). Besides the change of the light detector absorbers from Run28 to Run30, the thermometer geometry of the light detector also slightly changed. The $CaWO_4$ crystals used in both runs have a comparable light output, but the light collection efficiency of the reflective housing is expected to be improved in Run30: This is due to the care taken that all the parts of the holder which extend into the reflective housing have a highly reflective surface.
The SOS light detectors show a comparable performance with respect to the silicon light detectors in terms of achieved energy resolution at zero energy (about 20 eV) and the estimated amount of detected light for a given energy deposited in the $CaWO_4$ crystal (about 1 %). This indicates that, besides the light collection efficiency which concerns both light detector absorber and reflecting housing, the light output of the scintillating crystal is a crucial parameter in the overall light detection efficiency. For this reason, further improvement of the light output of the $CaWO_4$ crystals is actively pursued.
In order to determine the major noise sources which contribute to the baseline noise of the light detectors and thus limit their energy resolution at zero energy, noise spectra were recorded at different operating points. The Johnson noise in the thermometer, the SQUID noise and the $1/f$ noise in the thermometer were found to be the dominant noise sources. In addition, a new method has been developed which allows to locate the optimal point for stabilizing detectors within the thermometer phase transition. It has been validated by measuring the signal-to-noise ratio at various points of the transition.
The energy dependence of the light detector resolution was studied in the relevant energy range showing a square root energy dependence as expected for an energy resolution limited by statistical fluctuations in the number of detected scintillation photons. The presence of a much weaker component of linear energy dependence points to a position dependent light detection efficiency of the detector module. This may be the result of a slight dependence of the $CaWO_4$ light output on the position of the energy deposition within the crystal.

The CRESST-II experiment, after a major upgrade which included the installation of a neutron shielding, a muon veto system, a mounting system and a readout for 33 detector modules, has operated three detector modules during the commissioning Run30. The data collected with two detector modules during this commissioning phase yielded an upper limit for the WIMP-nucleon elastic scattering cross section shown in figure 7.1 [Angloher et al., 2008]. Despite the brief exposure of a small detector mass, the powerful background discrimination capability of the CRESST-II detector modules lead to a competitive result already during commissioning.

In April 2008, CRESST-II has started another run with more detector modules installed. In this run an absolute energy calibration of the light detectors will be performed to determine the overall light collection efficiency of the CRESST-II detector modules. Since the $CaWO_4$ crystals employed in this run have significantly higher light outputs than the ones operated in Run28 and Run30, enhanced discrimination capabilities are expected.

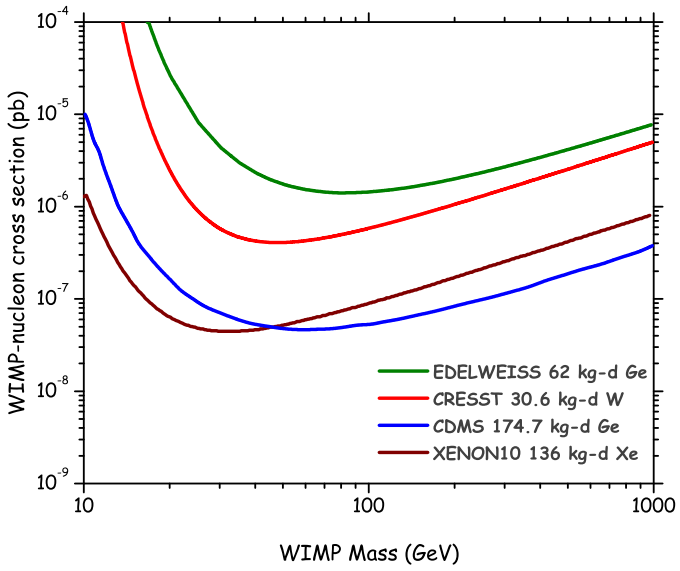

Figure 7.1: The preliminary limits from the CRESST-II experiment on the spin-independent WIMP-nucleus elastic scattering cross section (normalized per nucleon) obtained from the data sample of Run30 as a function of the WIMP mass [Angloher et al., 2008]. For comparison, current limits from several other leading direct detection experiments are shown. The regions above the curves are excluded with 90% C.L.

Bibliography

Ahmed, Z., Akerib, D. S., Attisha, M. J., et al. Status of the Cryogenic Dark Matter Search Experiment. Journal of Low Temperature Physics, 151:800–805, 2008

Akerib, D. et al. (CDMS Collaboration), Exclusion limits on the WIMP-nucleon cross section from the first run of the Cryogenic Dark Matter Search in the Soudan Underground Laboratory. Phys. Rev. D, 72(5):052009–+, 2005, astro-ph/0507190

Akerib, D. S., Bailey, C. N., Bauer, D. A., et al. Present Status of the Super-CDMS program. Journal of Low Temperature Physics, 151:818–823, 2008

Alner, G. J., Araújo, H. M., Bewick, A., et al. First limits on WIMP nuclear recoil signals in ZEPLIN-II: A two-phase xenon detector for dark matter detection. Astroparticle Physics, 28:287–302, 2007, arXiv:astro-ph/0701858

Altmann, M. et al., 2001, Update of the Proposal to the LNGS for a Second Phase of the CRESST Dark Matter Search

Angle, J., Aprile, E., Arneodo, F., et al. First Results from the XENON10 Dark Matter Experiment at the Gran Sasso National Laboratory. Physical Review Letters, 100(2):021303–+, 2008, arXiv:0706.0039

Angloher, G., Bucci, C., Christ, P., et al. Limits on WIMP dark matter using scintillating $CaWO_4$ cryogenic detectors with active background suppression. Astroparticle Physics, 23:325–339, 2005, arXiv:astro-ph/0408006

Angloher, G., Huber, M., Jochum, J., et al. Energy resolution ΔE=12 eV at 5.9 keV for lead absorber coupled to a single Al-STJ via phonons. Low Temperature Detectors, 605:23–26, 2002

Angloher, G. et al. Limits on WIMP dark matter using sapphire cryogenic detectors. Astropart. Phys., 18:43–55, 2002

Angloher, G. et al. Results from the Commissioning Run of the CRESST-II Dark Matter Search. in preparation, 2008

Aprile, E., Dahl, C. E., de Viveiros, L., et al. Simultaneous Measurement of Ionization and Scintillation from Nuclear Recoils in Liquid Xenon for a Dark Matter Experiment. Physical Review Letters, 97(8):081302–+, 2006, arXiv:astro-ph/0601552

Aprile, E., Giboni, K. L., Majewski, P., et al. Scintillation response of liquid xenon to low energy nuclear recoils. Phys. Rev. D, 72(7):072006–+, 2005, arXiv:astro-ph/0503621

Arpesella, C. Background Measurements at Gran Sasso Laboratories. Nuclear Physics B (Proc. Suppl.), 28A:420, 1992

Ashcroft, N. W. & Mermin, N. D. Solid State Physics, Holt-Saunders International Editions, 1976

Askin, A. Light Yield Investigation of Titanium Doped Al_2O_3 Crystals for CRESST Dark Matter Search, Master's thesis, Fachbereich Physik der Universität Siegen, 2006

Battaglia, G., Helmi, A., Morrison, H., et al. The radial velocity dispersion profile of the Galactic halo: constraining the density profile of the dark halo of the Milky Way. Mon. Not. R. Astron. Soc., 364:433–442, 2005, arXiv:astro-ph/0506102

Baudis, L. Direct Detection of Cold Dark Matter. ArXiv e-prints, 711, 2007, 0711.3788

Bavykina, I., Angloher, G., Hauff, D., et al. Investigation of $ZnWO_4$ Crystals as Scintillating Absorbers for Direct Dark Matter Search Experiments. IEEE Transactions on Nuclear Science, 55:1449–1452, 2008

Bavykina, I., Christ, P., Huff, P., et al. Interpretation of light-quenching factor measurements. Astroparticle Physics, 28:489–493, 2007, arXiv:0707.0766

Begeman, K. G., Broeils, A. H., & Sanders, R. H. Extended rotation curves of spiral galaxies - Dark haloes and modified dynamics. Mon. Not. R. Astron. Soc., 249:523–537, 1991

Behnke, E., Collar, J. I., Cooper, P. S., et al. Spin-Dependent WIMP Limits from a Bubble Chamber. Science, 319:933–, 2008, arXiv:0804.2886

Bellotti, E. et al. New Measurement of Rock Contaminations and Neutron Activity in the Gran Sasso Tunnel. INFN/TC-85/19, : , 1985

Bento, A. Aspects of the performance of low temperature calorimeters for X-ray spectroscopy with high detection efficiency, PhD thesis, University of Oxford, 2004

Bernabei, R., Belli, P., Cappella, F., et al. First results from DAMA/LIBRA and the combined results with DAMA/NaI. ArXiv e-prints, 804, 2008, 0804.2741

Bertone, G. Dark Matter: A Multidisciplinary Approach. ArXiv e-prints, 710, 2007, 0710.5603

Binney, J. & Tremaine, S. Galactic Dynamics, Princeton University Press, 1987

Birks, J. B. Theory and Practice of Scintillation Counting, Pergamon, 1967

Blasse, G. & Bokkers, G. Low-Temperature Decay-Time Measurements on the Luminescence of Calcium Tungstate. J. Solid State Chem., 49:126–128, 1983

Boerner, G. The early universe : facts and fiction, The early universe : facts and fiction, 4th ed. By G. Boerner. Astronomy and astrophysics library. Berlin: Springer, 2003., 2003

Bottino, A. et al. Exploring the Supersymmetric Parameter Space by Direct Search for WIMPs. Phys. Lett. B, 402:113, 1997

Broniatowski, A., Defay, X., Juillard, A., et al. Cryogenic Ge Detectors with Interleaved Electrodes: Design and Modeling. Journal of Low Temperature Physics, 151:830–834, 2008

Brunoldi, M. et al., 2007, Study of the Optical Properties of the Mirrors of the Directional Optical Module for the Nemo Neutrino Underwater Telescope, LNF-SIS Publication TC 07 / 9, INFN

Bucci, C., 2007, private communication

Bühler, M. et al. Status and Low Background Considerations for the CRESST Dark Matter Search. Nucl. Instr. and Meth. A, 370:237, 1996

Calleja, A., Coron, N., García, E., et al. Recent Performance of Scintillating Bolometers Developed for Dark Matter Searches. Journal of Low Temperature Physics, 151:848–853, 2008

CDMS Collaboration. A Search for WIMPs with the First Five-Tower Data from CDMS. ArXiv e-prints, 802, 2008, 0802.3530

Chantelauze, A. Status of the EDELWEISS-2 Dark Matter Search. ArXiv e-prints, 710, 2007, 0710.5849

Chardin, G. Dark Matter Direct Detection. in "Cryogenic Particle Detection", (Springer, Heidelberg, 2005), 2004, astro-ph/0411503

Clarke, J., 1989, in Proceedings of the IEEE, Vol. 8

Clowe, D., Bradač, M., Gonzalez, A. H., et al. A Direct Empirical Proof of the Existence of Dark Matter. Astrophys. J., Lett., 648:L109–L113, 2006, arXiv:astro-ph/0608407

Coppi, C., 2007, private communication

Cribier, M., Pichard, B., Rich, J., et al. The muon induced background in the GALLEX experiment. Astroparticle Physics, 6:129–141, 1997

CXRO, 2008, Center for X-ray optics, http://www-cxro.lbl.gov/

Di Stefano, P. et al. Textured Silicon Calorimetric Light Detector. Journal of Applied Physics, 94(10):6887, 2003

Dietsche, W. & Kinder, H. Spectroscopy of Phonon Scattering in Glass. Phys. Rev. Lett., 43(19):1413–1417, 1979

DiTusa, J. F. et al. Role of phonon dimensionality on electron-phonon scattering rates. Phys. Rev. Lett., 68:1156–1159, 1992

Enss, C. Cryogenic Particle Detection, Springer-Verlag, 2005

Figueroa-Feliciano, E. Complex microcalorimeter models and their application to position-sensitive detectors. Journal of Applied Physics, 99:4513–+, 2006

Formaggio, J. A. & Martoff, C. J. Backgrounds to Sensitive Experiments Underground. Annual Review of Nuclear and Particle Science, 54:361–412, 2004

Frank, T. Development of Scintillating Calorimeters for Discrimination of Nuclear Recoils and Fully Ionizing Events, PhD thesis, Technische Universität München, 2002

Fujimoto, R., Mitsuda, K., Iyomoto, N., et al. Status of X-ray microcalorimeter development at ISAS. Low Temperature Detectors, 605:231–234, 2002

Gaitskell, R. J. Direct Detection of Dark Matter. Annual Review of Nuclear and Particle Science, 54:315–359, 2004

Galeazzi, M. & McCammon, D. Microcalorimeter and bolometer model. J. Appl. Phys., 93:4856, 2003

Garcia-Bellido, J. Cosmology and Astrophysics. ArXiv Astrophysics e-prints, 2005, astro-ph/0502139

Gates, E. I., Gyuk, G., & Turner, M. S. The Local Halo Density. Ap. J. L., 449: 123, 1995

Gluyas, M., Huges, F. D., & James, B. The Elastic Constants of Calcium Tungstate. J. Phys. D: Appl. Phys., 6:2025–2037, 1973

Green, A. M. Calculating Exclusion Limits for WIMP Direct Detection Experiments without Background Subtraction. Phys. Rev. D, 65:023520, 2002

Henry, S., Bazin, N., Kraus, H., et al. The 66-channel SQUID readout for CRESST II. Journal of Instrumentation, 11:3–+, 2007

Hilton, G. et al. Microfabricated transition-edge X-ray detectors. IEEE Transactions on Applied Superconductivity, 11:467–565, 2001

Huff, P., 2007, private communication

Irwin, K. D. An application of electrothermal feedback for high resolution cryogenic particle detection. Applied Physics Letters, 66:1998–2000, 1995

Jagemann, T., Feilitzsch, F. V., Hagn, H., et al. Measurement of nuclear recoil quenching factors in $CaWO_4$. Astroparticle Physics, 26:269–281, 2006

Jagemann, T., Jochum, J., & Feilitzsch, F. V. Neutron scattering facility for the measurement of nuclear recoil quenching factors. Nuclear Instruments and Methods in Physics Research A, 551:245–260, 2005

Jungman, G., Kamionkowski, M., & Griest, K. Supersymmetric Dark Matter. Phys. Rep., 267:195, 1996

Kaplan, S. B. et al. Quasiparticle and phonon lifetimes in superconductors. Phys. Rev. B, 14(11):4854–4873, 1976

Kerr, F. J. & Lynden-Bell, D. Review of galactic constants. Mon. Not. Roy. Astron. Soc., 221:1023, 1986

Kiefer, M. Optimierung szintillierender Tieftemperaturkalorimeter fr den direkten Nachweis von Teilchen der Dunklen Materie, Master's thesis, Bayerische Julius-Maximilians-Universitt Wrzburg, 2007

Kittel, C. Introduction to Solid State Physics, Third edn., John Wiley and Sons, 1967

Komatsu, E., Dunkley, J., Nolta, M. R., et al. Five-Year Wilkinson Microwave Anisotropy Probe (WMAP) Observations: Cosmological Interpretation. ArXiv e-prints, 803, 2008, 0803.0547

Koshiba, M. Observational neutrino astrophysics. Phys. Rep., (220):229–381, 1992

Kraus, H., Bauer, M., Bavykina, I., et al. EURECA – the European Future of Dark Matter Searches with Cryogenic Detectors. Nuclear Physics B Proceedings Supplements, 173:168–171, 2007

Lang, R., 2008, private communication

Lang, R. F. -, PhD thesis, Technische Universität München, 2008, in preparation

Lang, R. F. The CRESST-II Experiment. ArXiv e-prints, 805, 2008, 0805.4705

Lewin, J. D. & Smith, P. F. Review of Mathematics, Numerical Factors, and Corrections for Dark Matter Experiments based on Elastic Nuclear Recoil. Astropart. Phys., 6:87, 1996

Lindeman, M. A., Brekosky, R. P., Figueroa-Feliciano, E., et al. Performance of Mo/Au TES microcalorimeters. Low Temperature Detectors, 605:203–206, 2002

Lita, A. et al. Tuning of tungsten thin tilm superconducting transition temperature for fabrication of photon nubmer resolving detectors. IEEE transactions on applied superconductivity, 15(2), 2005

Liu, J. & Giordano, N. Electron-phonon scattering times in thin Sb films. Phys. Rev. B, 43:3928–3932, 1991

Loidl, M. Diffusion und Einfang von Quasiteilchen, PhD thesis, Ludwig-Maximilians-Universität, München, 1999

Loidl, M. et al. Quasiparticle diffusion over several mm in cryogenic detectors. Nucl. Instr. and Meth. A, 465:440–446, 2001

Luca, M. Sapphire scintilation tests for cryogenic detectors in the EDELWEISS dark matter search, PhD thesis, lUniversit Claude Bernard Lyon-I, 2007

Majorovits, B., 2007, private communication

Majorovits, B., Kader, H., Kraus, H., et al. Production of Low-background CuSn6-Bronze for the CRESST Dark-Matter-Search Experiment. Applied radiation and isotopes, 2008, submitted to the journal

Maris, H. J. Phonon propagation with isotope scattering and spontaneous anharmonic decay. Phys. Rev. B, 41(14):9736–9743, 1990

Marnieros, S., Berge, L., Broniatowski, A., et al. Surface Event Rejection of the EDELWEISS Cryogenic Germanium Detectors Based on NbSi Thin Film Sensors. Journal of Low Temperature Physics, 151:835–840, 2008

Mather, J. C. Bolometer noise: nonequilibrium theory. Applied Optics, 21(6): 1125–1129, 1982

Mather, J. C., Fixsen, D. J., Shafer, R. A., Mosier, C., & Wilkinson, D. T. Calibrator Design for the COBE Far-Infrared Absolute Spectrophotometer (FIRAS). Astrophys. J., 512:511–520, 1999, arXiv:astro-ph/9810373

Meunier, P. et al. Discrimination between Nuclear Recoils and Electron Recoils by Simultaneous Detection of Phonons and Scintillation Light. Appl. Phys. Lett., 75(9):1335, 1999

Mikhailik, V. B., Kraus, H., Henry, S., & Tolhurst, A. J. B. Scintillation studies of $CaWO_4$ in the millikelvin temperature range. Phys. Rev. B, 75(18):184308–+, 2007

Mikhailik, V. B., Kraus, H., Wahl, D., et al. ????

Milgrom, M. A Modification of the Newtonian Dynamics as a Possible Alternative to the Hidden Mass Hypothesis. Ap. J., 270:365–370, 1983

Moseley, S. H., Mather, J. C., & McCammon, D. Thermal detectors as x-ray spectrometers. J. Appl. Phys., 56(5):1257–1262, 1984

Moszyński, M., Balcerzyk, M., Czarnacki, W., et al. Characterization of $CaWO_4$ scintillator at room and liquid nitrogen temperatures. Nuclear Instruments and Methods in Physics Research A, 553:578–591, 2005

Mott, N. & Davies, J. ????

Nagel, U., Nowak, A., Kellner, E., et al. Use of proximity effect in iridium-gold superconducting phase transition thermometers. Journal of Low Temperature Physics, 93:543–548, 1993

Narayanamurti, V. et al. Quasiparticle and phonon propagation in bulk, superconducting lead. Phys. Rev. B, 18(11):6041–6052, 1978

Nikolodi, D. Calibration system for the muon veto scintillators employed in the CRESST-II dark matter search experiment., Master's thesis, Universita degli studi di Trento, 2006

Ninković, J. Investigation of $CaWO_4$ Crystals for Simultaneous Phonon-Light Detection in the CRESST Dark Matter Search, PhD thesis, Technische Universität München, 2005

Ninković, J., 2007, private communication

Ninković, J., Christ, P., Angloher, G., et al. New technique for the measurement of the scintillation efficiency of nuclear recoils. Nuclear Instruments and Methods in Physics Research A, 564:567–578, 2006, arXiv:astro-ph/0604094

Peccei, R. & Quinn, H. CP Conservation in the Presence of Pseudoparticles. Phys. Rev. Lett., (38):1440, 1977

Penzias, A. A. & Wilson, R. W. A Measurement of Excess Antenna Temperature at 4080 mc/s. Ap. J., 142:419–421, 1965

Petricca, F. Dark Matter Search with Cryogenic Phonon-Light Detectors, PhD thesis, Ludwig-Maximilians-Universität München, 2005

Petricca, F., 2007, private communication

Pfister, S. Reproducilbe Production of Superconducting Thin Films as Detector Components for the CRESST Experiment, Master's thesis, Technische Universität München, 2006

Pippard, A. B. Ultrasonic Attenuation in Metals. Philos. Mag, 46:1104–1114, 1955

Pobell, F. Matter and Methods at Low Temperatures, Springer-Verlag, 1992

Poelaert, A., Erd, C., Peacock, A., et al. X-ray detection by superconducting tunnel junctions via phonon propagation in the substrate. Journal of Applied Physics, 79:7362–7369, 1996

Pröbst, F., 2008, private communication

Pröbst, F. et al. Model for Cryogenic Particle Detectors with Superconducting Phase Transition Thermometers. J. of Low Temp. Phys., 100:69, 1995

Rose-Innes, A. C. & Rhoderick, E. H. Introduction to Superconductivity, Vol. 6 of International series in solid state physics, 2nd edn., Pergamon Press, 1978

Rothwarf, A. & Taylor, B. N. Measurement of Recombination Lifetimes in Superconductors. Physical Review Letters, 19:27–30, 1967

Sanglard, V. et al. Final results of the EDELWEISS-I dark matter search with cryogenic heat-and-ionization Ge detectors. Phys. Rev. D, 71(12):122002–+, 2005, arXiv:astro-ph/0503265

Schäffner, K., 2007, private communication

SDDS, 2008, Sloan Digital Sky Survey (SDSS), web link http://www.sdss.org/

Shutt, T., Emes, J., Haller, E. E., et al. A solution to the dead-layer problem in ionization and phonon-based dark matter detectors. Nuclear Instruments and Methods in Physics Research A, 444:340–344, 2000

Simon, E., Bergé, L., Broniatowski, A., et al. SICANE: a detector array for the measurement of nuclear recoil quenching factors using a monoenergetic neutron beam. Nuclear Instruments and Methods in Physics Research A, 507: 643–656, 2003, arXiv:astro-ph/0212491

Sisti, M. CRESST – a Cryogenic Experiment for Dark Matter Search, PhD thesis, Ludwig-Maximilians-Universität München, 1999

Solymar, L. Superconductive Tunneling and Applications, Chapman and Hall, 1972

Springel, V., White, S. D. M., Jenkins, A., et al. Simulations of the formation, evolution and clustering of galaxies and quasars. Nature, 435:629–636, 2005, arXiv:astro-ph/0504097

Stark, M. Detektoren mit effizienter und shneller Phononensammlung für das CRESST-Experiment, PhD thesis, Technische Universität München, 2005

Szymkowiak, A. E., Kelley, R. L., Moseley, S. H., & Stahle, C. K. Signal processing for microcalorimeters. Journal of Low Temperature Physics, 93:281–285, 1993

Tamura, S.-i. Spontaneous decay rates of LA phonons in quasi-isotropic solids. Phys. Rev. B, 31, 1985

Tamura, S.-i. & Maris, H. J. Spontaneous decay of TA phonons. Phys. Rev. B, 31(4):2595–2598, 1985

Tinkham, M. Introduction to Superconductivity, 2nd edn., McGraw-Hill, 1996

Tovey, D. et al. A New Model Independent Method for Extracting Spin-Dependent (Cross Section) Limits from Dark Matter Searches. Phys. Lett. B, 488:17–26, 2000

Triplett, B. B. et al. Critical Field for Superconductivity and Low-Temperature Normal-State Heat Capacity of Tungsten. J. of Low Temp. Phys., 12:499–518, 1973

WARP Collaboration. First results from a dark matter search with liquid argon at 87 K in the Gran Sasso underground laboratory. Astroparticle Physics, 28: 495–507, 2008, astro-ph/0701286

Westphal, W., Coppi, C., Feilitzsch, F. V., et al. Detector calibration measurements in CRESST. Nuclear Instruments and Methods in Physics Research A, 559:372–374, 2006

Wulandari, H., Jochum, J., Rau, W., & von Feilitzsch, F. Neutron Background Studies for the CRESST Dark Matter experiment. Preprint, hep-ex/0401032, 2004

Wulandari, H., Jochum, J., Rau, W., & von Feilitzsch, F. Neutron Flux at the Gran Sasso Underground Laboratory Revisited. Astropart. Phys., 22:313–322, 2004

XCOM, 2008, XCOM: Photon Cross Sections Database, http://physics.nist.gov/PhysRefData/Xcom/Text/XCOM.html

Xue, X. ., Rix, H. ., Zhao, G., et al. The Milky Way's Circular Velocity Curve to 60 kpc and an Estimate of the Dark Matter Halo Mass from Kinematics of ˜2500 SDSS Blue Horizontal Branch Stars. ArXiv e-prints, 801, 2008, 0801.1232

Yao, W.-M., Amsler, C., Asner, D., et al. Review of Particle Physics. Journal of Physics G, 33:1+, 2006, http://pdg.lbl.gov

Yellin, S. Finding an upper limit in the presence of an unknown background. Phys. Rev. D, 66:032005, 2002

Young, B. A., Saab, T., Cabrera, B., et al. Measurement of Tc suppression in tungsten using magnetic impurities. Journal of Applied Physics, 86:6975–6978, 1999

Zehnder, A. Response of superconductive films to localized energy deposition. Phys. Rev. B, 52:12858–12866, 1995

Zwicky, F. Die Rotverschiebung von extragalaktischen Nebeln. Helv. Phys. Acta, 6:110–127, 1933

Acknowledgments

I want first to express my gratitude to Dr. Franz Pröbst for giving me the opportunity to accomplish this thesis and more importantly for advising me and for sharing his enormous knowledge with me. To Prof. Dr. Rainer Kotthaus I am very grateful for the excellent guidance and support during the last part of my thesis. I must say that I am very sorry for not having him advise me for full period of the thesis. Federica helped me in so many aspects of my work and life that I do not even want to try to express my gratitude in this way. I really enjoy working with her. We know each other for 4 years and I am still amazed how sharp her brain is. Antonio, besides Federica and Franz, is the person to be blamed for most of great ideas that made possible this work to be finished. Many thanks to mister Bento for sharing his clear and simple explanations of many complicated problems. Veliko hvala Jeleni for constantly supporting me and helping me with the work even though she has changed the research field. Vielen, vielen Dank to Hans for helping me in numerous occasions with work and even more with outside-of-work problems. I enjoyed all our conversations. Goran is responsible for all of this happening, since he sent me here at the first place. Puno hvala od serpasa. Vincent taught me that work can be productive and amusing at the same time. Many thanks from the crazy c*w. Grazie to Cristina to try to teach me that one can stay cool, quite relaxed and extremely efficient in work (somehow it did not work out with me :-)). Gode is the most enthusiastic person about the physics I know. Ok, Rafael as well but in a different way. Special thanks to Rafael for trying to make our group more efficient. Thanks to Patrick for all great and successful discussions about the work and all great but unsuccessful (since we both still keep our initial opinion) discussions outside the work ;-). I wish to thank Irina for teaching me that one should never give up fighting for its own place. Many thanks to Dieter for helping all of us in so many occasions. Thanks to Michael for not leaving out the fun after (or during) the work and for approaching problems from different perspective than others leading to inspirative atmosphere. Karolina is just great. She is blushing now but this is true. Danke schöne Frau für alles. Thanks to Jens for all discussions with clear statements, problems or solutions and for being so serious and funny at the same time. Thanks to Wolfgang for creative criticism. I am also thankful to all the members of CRESST group at TUM, workshop at MPI, Dr. Leo Stodolsky and Carlo Bucci for always willing to help our group.
Grazie to Stefano for being with me all this time, is still and hopefully will be in future. Special thanks to all friends here, there and somewhere in the world for being my friends. Finally, I want to write to my family hvala.